TESI DI DOTTORATO IN COTUTELA

UNIVERSITA' DEGLI STUDI DI ROMA TOR VERGATA E UNIVERSITA' DI BORDEAUX

FACOLTA' DI SCIENZE MATEMATICHE, FISICHE E NATURALI

Corso di dottorato di Matematica

CICLO XXX

a.a. 2017/2018

Mathematical Modeling of enhanced drug delivery by mean of Electroporation or Enzymatic treatment

Manon DEVILLE

Docente guida Roberto NATALINI / Clair POIGNARD

Coordinatore Andrea Braides

Title : Mathematical Modeling of enhanced drug delivery by mean of Electroporation or Enzymatic treatment.

Abstract : This PhD thesis is devoted to the mathematical modeling and simulation of two existing physical methods to overcome the biological barriers to drug delivery. In the first part, several ways to model electroporation are considered, from the cell scale to the tissue scale. Existing phenomenological models of tissue electroporation are presented and numerically compared. Then a macroscopic model of electroporation is derived from a well-established model of cell elecroporation using homogenization techniques. In the second part, a new poroelastic model for the flows in biological tissues is presented to account for tissue degradation after an enzymatic treatment. To finish, an optimization algorithm is suggested in attempt to determine an optimal protocol when considering enzyme based therapies.

Keywords : modeling, simulation, drug delivery, electroporation, homogenization, enzymatic treatment, optimization

---

Institut de Mathématiques de Bordeaux (IMB) - UMR 5251
351, cours de la Libération, 33405 Talence (France)

Istituto per le Applicazioni del Calcolo "M. Picone"
Consiglio Nazionale delle Ricerche
Via dei Taurini 19, I-00185, Roma (Italy)

Titre : Modélisation de l'administration de médicaments par électroporation ou suite à un traitement enzymatique.

Résumé : Cette thèse présente des travaux concernant la modélisation mathématique de deux méthodes physiques existantes pour surmonter les barrières biologiques s'opposant à l'administration efficace de médicaments. Dans la première partie, plusieurs manières de modéliser l'électroporation sont exposées, aux échelles tissulaire et cellulaire. Des modèles phénoménologiques existants d'électroporation tissulaire sont présentés et comparés numériquement. Puis un modèle macroscopique d'électroporation est déduit d'un modèle d'électroporation cellulaire bien établi en utilisant des techniques d'homogénéisation. Dans la seconde partie, un nouveau modèle poroélastique est introduit pour décrire les écoulements dans un tissu biologique. Celui-ci prend en compte la dégradation tissulaire consécutive à un traitement par enzyme. Pour finir, un algorithme d'optimisation est proposé dans le but de déterminer un protocole optimal pour effectuer un traitement enzymatique.

Mots clés : modélisation, simulation, administration de médicaments, électroporation, homogénéisation, traitement enzymatique, optimisation

---

Institut de Mathématiques de Bordeaux (IMB) - UMR 5251
351, cours de la Libération, 33405 Talence (France)

Istituto per le Applicazioni del Calcolo "M. Picone"
Consiglio Nazionale delle Ricerche
Via dei Taurini 19, I-00185, Roma (Italy)

Titolo : Modellizzazione della somministrazione di farmaci tramite elettroporazione o usando un trattamento enzimatico.

Sintesi : Questa tesi di dottorato presenta dei lavori relativi alla modellizzazione matematica di due metodi fisici esistenti per sormontare le barriere biologiche che si oppongono alla somministrazione efficace di farmaci. Nella prima parte, diversi modi di modellizzare l'elettroporazione sono esposti, sia alla scala del tessuto che della cellula. Alcuni modelli fenomenologici esistenti di elettroporazione tissutale sono presentati e confrontati numericamente. Inoltre un modello macroscopico di elettroporazione è ottenuto da un modello a scala cellulare consolidato usando tecniche di omogeneizzazione. Nella seconda parte, un nuovo modello poroelastico è introdotto per descrivere il flusso in tessuti biologici. Questo modello tiene conto della degradazione del tessuto dopo un trattamento enzimatico. Per finire, un algoritmo di ottimizzazione è proposto allo scopo di determinare un protocollo ottimale per effettuare un trattamento enzimatico.

Parole chiave : modellizzazione, simulazione, somministrazione di farmaci, elettroporazione, omogeneizzazione, trattamento enzimatico, ottimizzazione

---

Institut de Mathématiques de Bordeaux (IMB) - UMR 5251
351, cours de la Libération, 33405 Talence (France)

Istituto per le Applicazioni del Calcolo "M. Picone"
Consiglio Nazionale delle Ricerche
Via dei Taurini 19, I-00185, Roma (Italy)

Contents

Introduction

0.1 Prelude

This PhD thesis is the result of three years of research at the Institut de Mathématiques de Bordeaux (Bordeaux, France), within the INRIA team MONC (Mathematics for ONCology), under the supervision of Clair Poignard. This work was equally supervised by Roberto Natalini, in the framework of a cotutelle with Universitá di Tor Vergata (Rome, Italy).

I was partly granted by Université Franco-Italienne (project VINCI C2-25), INdAM, the Plan Cancer DYNAMO (Inserm 9749) and the Plan Cancer NUMEP (Inserm 11099).

This document deals with the modeling of physical methods in order to overcome the biological barriers to drug delivery. Before reaching their target, therapeutic agents face a complex series of biological barriers. We focused on two of these barriers, along with the strategies existing to overcome them. First, the extracellular matrix (ECM) can generate diffusive hindrance and/or jeopardize transcapillary transport, especially in the case of solid tumors. Enzyme-based therapies can be used to degrade the ECM in order to improve the penetration of therapeutic molecules. Secondly, the cell membrane is the main obstacle to the free diffusion of macromolecules into the intracellular compartment. Electroporation, which consists in applying short electric pulses in order to disrupt the cell membrane can be used to facilitate the uptake of large molecules. The mathe-

matical modeling done during the PhD of these two physical methods uses partial differential equations (PDEs) and their numerical approximation. The goal is to retrieve the experimental observations with the models in order to justify their use to optimize future protocols of drug delivery by mean of electroporation and/or enzymatic treatment.

In order to introduce the two modeling themes involved in this document, this introducing chapter presents hereunder the biological background behind our study. The main biological barriers to drug delivery are presented along with a non exhaustive overview of the physical methods to increase drug penetration and uptake in tissues. Then the organisation of this document is detailled, with an overview of the main obtained results.

0.2 Biological background : enhancing penetration of therapeutic molecules in biological tissues

0.2.1 Biological barriers to drug delivery

Before reaching their target, therapeutic agents face a complex series of biological barriers (see Figure 1). These obstacles include degradation and/or clearance, the vascular wall, the extracellular matrix, the cell membrane and potentially the intracellular medium. In addition to the substantial challenges presented by each individual biological barrier, it is important to note that they depend on factors, such as the pharmacokinetics, the administration route (direct injection versus intravenous) and the target tissue (cancer versus normal tissue) [89].

0.2.1.1 The cell membrane

The cell membrane is a physical barrier that separates the intracellular components from the extracellular environment. It is the main physical barrier encountered by macromolecules, along with the nuclear envelope. It is composed of two

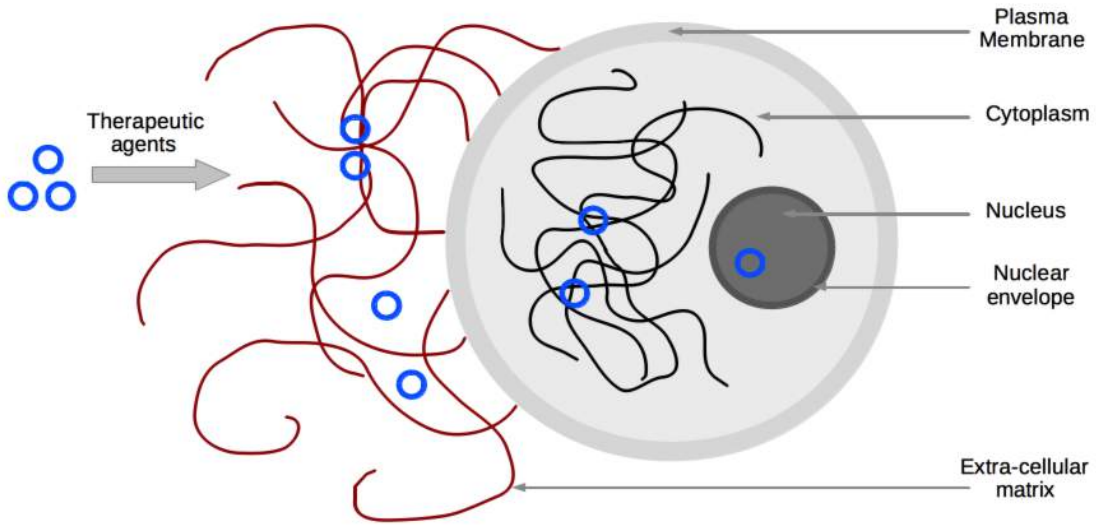

Figure 1: After its injection into the target tissue, a therapeutic agent encounters biological barriers from extracellular environment toward the interior of the target cell.

main classes of molecules, proteins and lipids [49] (see Figure 2).

Membrane Lipids. The fundamental building blocks of all cell membranes are phospholipids, which are amphipathic molecules, consisting of two hydrophobic fatty acid chains linked to a phosphate-containing hydrophilic head group. Because their fatty acid tails are poorly soluble in water, phospholipids spontaneously form bilayers in aqueous solutions, with the hydrophobic tails buried in the interior of the membrane and the polar head groups exposed on both sides, in contact with water. Such phospholipid bilayers form a stable barrier between two aqueous compartments and represent the basic structure of all biological membranes [36].

Membrane Proteins Proteins can either be inserted into the lipid bilayer or associated with the membrane indirectly, by protein-protein interactions. While phospholipids provide the basic structural organization of membranes, membrane proteins carry out the specific functions of the different membranes of the cell [36].

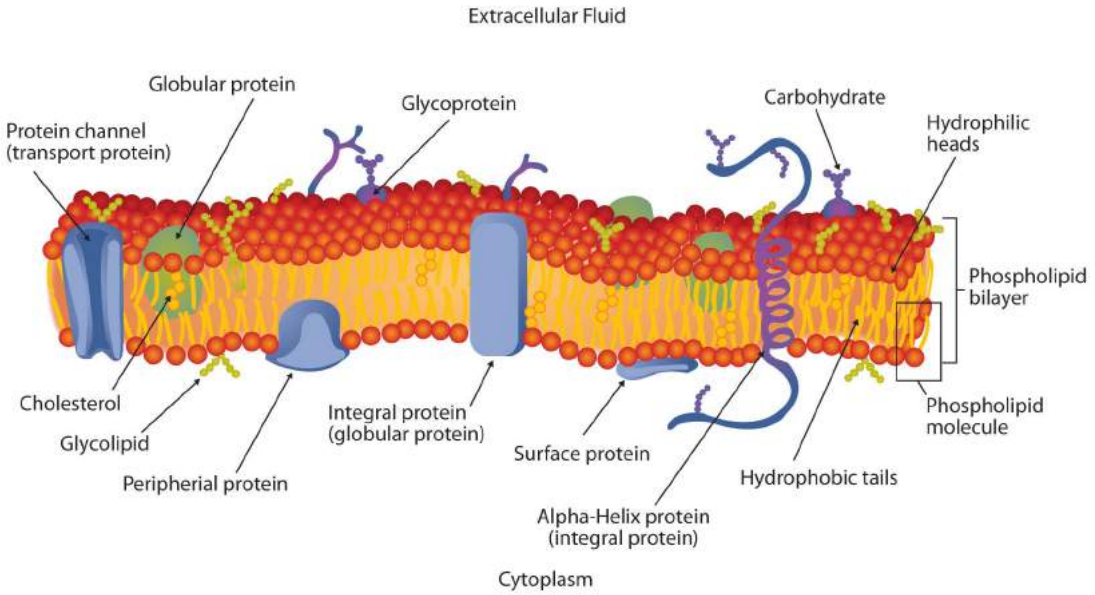

Figure 2: Schematic representation of a membrane portion.

Transport across Cell Membranes Exchanges between intracellular and extracellular compartments are limited by the plasma membrane. The entry of a substance in a cell depends on the properties of the membrane and the substance (ion or molecule) itself. From here, a fundamental concept emerges: plasma membranes are selectively permeable [89]. Lipid bilayers are permeable only to small uncharged molecules. Ions and most polar molecules are transported across cell membranes by specific transport proteins [36] (see Figure 3).

Intracellular Transport The cytosol is a region with a high level of molecular crowding due to the presence of the cytoskeletal network, organelles, and a high concentration of macromolecules. Transport or diffusion in such crowded media, especially for high molecular weight drugs, is generally described as hindered diffusion. Thus, some molecules that enter the intracellular space cannot diffuse freefly towards the various subcellular regions of interest. Instead, the molecule may be subject to active transport within the cell [89]. For instance, plasmids transport is a combination of very slow free diffusion and active transport along

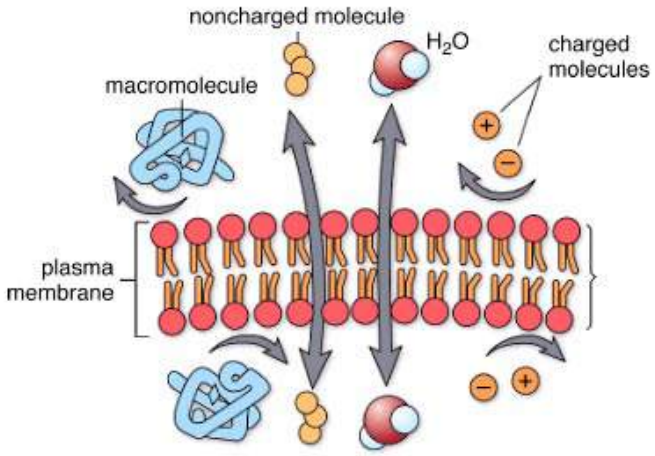

Figure 3: Transport of molecules accross the plasma membrane: schematic representation of membrane selective permeability.

microtubules. Recent studies demonstrate that while the cytoskeleton acts as a barrier to DNA plasmids movement in the cytoplasm, the microtubule network is required for plasmid trafficking directed towards the nucleus [103]. The role of cytoskeleton in intracellular DNA transport has been addressed in Notarangelo's PhD thesis [94], and a mathematical model for transport of DNA plasmids from the external medium up to the nucleus by electroporation was proposed in [73].

0.2.1.2 The extracellular space

The interstitial space which surrounds the cells, called the extracellular space, contains a complex and dynamic network of macromolecules, polysaccharides and glycosaminoglycans, fibrous proteins, salts and water, known as the extracellular matrix (ECM) [49]. Table 1 provides a list of several common ECM components and where they are most abundantly found in the body [121].

The ECM provides mechanical support and determines the mechanical properties of the tissue. The physical, topological, and biochemical composition of the ECM is tissue-specific and markedly heterogeneous. The main fibrous ECM proteins are collagens, elastins, fibronectins and laminins. Proteoglycans, to which characteristic glycosaminoglycan chains are attached, fill the majority of the ex-

ECM component	Characteristics	Localization in body
Collagens		
I	>300-nm-long fibrils	Skin, tendon, bone, ligaments, dentin, interstitial tissues
II	>300-nm-long fibrils	Cartilage, vitreous humor
III	>300-nm-long fibrils	Skin, muscle, blood vessels
IV	Sheet forming	Basal lamina
Proteoglycans	Polysaccharides (glycosaminoglycans) attached to protein cores	Cartilage and cell surfaces, basal lamina
Fibrin	Strong fibrillar protein capable of polymerizing quickly, blood clots	Wounds and provisional matrix. Sometimes found in the tumor periphery and often used in tissue engineering
Elastin	Highly extensible protein that gives tissue elastic recoil after stretch	Blood vessels, lung, skin, and connective tissue
Laminin	Adhesive protein that glues together basal lamina	Basal lamina

Table 1: Major components of the interstitium [121].

tracellular interstitial space within the tissue in the form of a hydrated gel and have a wide variety of functions (see Figure 4) [51].

Collagen Collagen is the most abundant fibrous protein within the interstitial ECM and constitutes up to 30% of the total protein mass of a multicellular animal. Collagens, which constitute the main structural element of the ECM, provide tensile strength, regulate cell adhesion, support chemotaxis and migration, and direct tissue development [51].

Hyaluronan The most common glycosaminoglycan in connective and epithelial tissues is hyaluronic acid (also called hyaluronan) [29]. Hyaluronan is a megadalton molecule consisting of repeating disaccharide units that allows the extracellular matrix to resist compressive forces. It creates a barrier to bulk fluid flow through the interstitial collagenous matrix by way of its viscosity and water of hydration [22].

Interstitial fluid It is estimated that up to 20% of the body's mass is made up of interstitial fluid, and much of this fluid is in constant slow motion [121]. Drugs

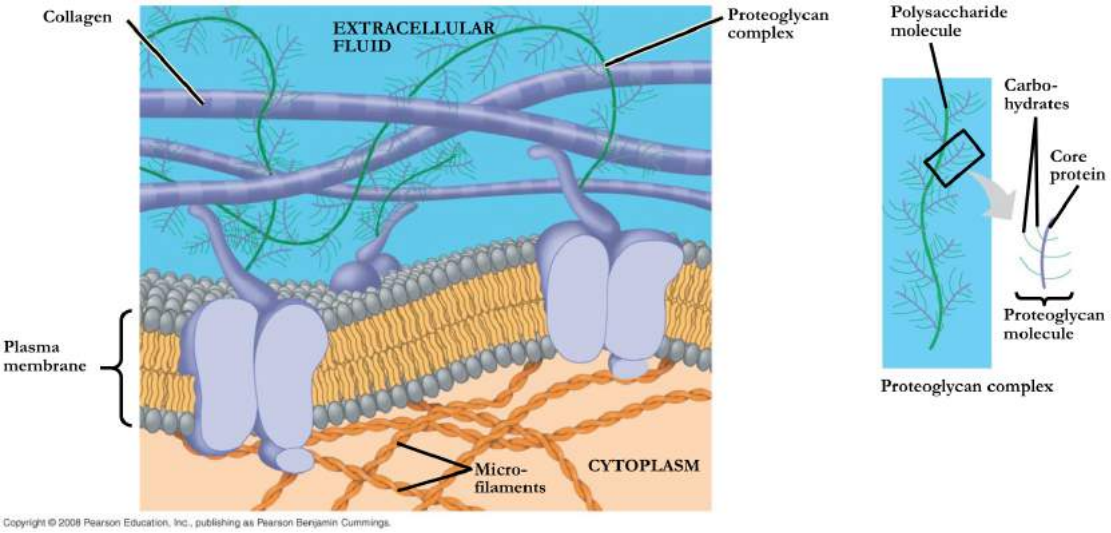

Figure 4: Schematic representation of the extracellular matrix which surrounds the cells.

penetrate normal tissues by both diffusion and convection, with a net flow of fluid from blood vessels balanced by resorption into lymphatics. Thus, the interstitial fluid flow is driven by the interstitial fluid pressure gradients and also influenced by the hydraulic conductivity of the tissue [12]. The physicochemical properties of drugs (for example, molecular weight, shape...) determine the rate of diffusion through tissue. Figure 5 presents the main mechanisms of drug distribution in tissue.

The particular case of solid tumors

Methods for studying drug penetration

In vitro and in vivo approaches have been used to examine how anticancer drugs penetrate and distribute within tumors. A non exhaustive review of these methods can be found in [83].

Multicellular spheroids. Multicellular spheroids are spherical aggregates of tumour cells which reflect many of the properties of solid tumours, including the

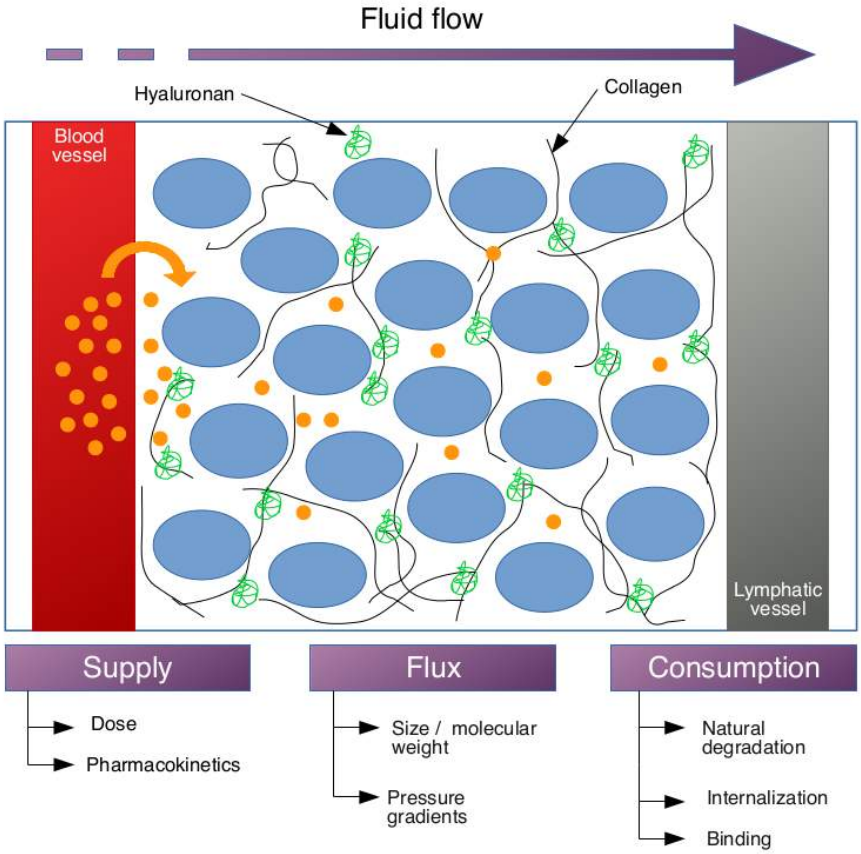

Figure 5: Schematic representation of how a drug penatrates a tissue from capillaries.

development of an ECM, gradients of nutrient concentration and cell proliferation from the exterior to the centre (Figure 6 **a**) [83]. Fluorescence microscopy of sections of spheroids is used to observe the drug penetration into the spheroid [119].

Multilayered cell cultures. Multilayered cell cultures (MCC) are made of tumour cells grown on a permeable plastic membrane. Like spheroids, MCCs have been shown to reflect many of the properties of solid tumours, including the generation of an ECM, gradients of nutrient concentration and cell proliferation, and regions of hypoxia and necrosis in thicker layers [83]. MCC can also be sectioned and the distribution of fluorescent drugs can be visualized directly [59].

Although in vitro techniques offer the advantage of being able to qualitatively

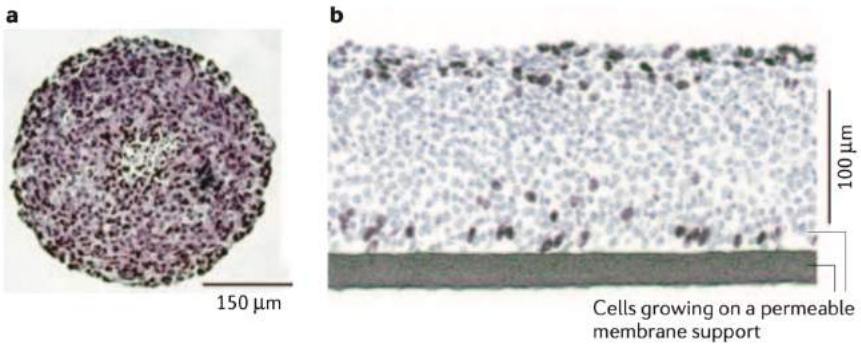

Figure 6: In vitro models used to study the penetration of anticancer drugs through tumor tissue. **a**. Multicellular spheroid. **b**. Multilayered cell culture (MCC) on a permeable membrane support. After [83].

and quantitatively assess drug penetration, they do not take some important features of solid cancers into account, such as variable interstitial fluid pressure or the influence of convection (which commonly occurs in the periphery of tumors and plays an important part in the transport of large molecular weight drugs) [83], [114].

In vivo methods. Several methods exist to study drug distribution in tumors grown in experimental animals. For example, window chambers can be used to study the distribution of naturally fluorescent or colored drugs in tumors of living animals. An alternative in vivo method is to quantify the concentration of fluorescent drugs in tissue sections [122].

Distribution of anticancer drugs in tissue

Transport through interstitial space within a tumor is determined by the physicochemical properties of the drug (e.g., molecular or particle size, diffusivity...) and the specific biologic properties of a tumor [e.g., tumor vasculature, extracellular matrix components, interstitial fluid pressure (IFP), tumor cell density, tissue structure and composition] that are unique to tumors and are not found in normal tissues. As a consequence of these factors, many anticancer drugs have limited distribution in solid tumors, which limits their effectiveness.

In spheroids and tumor histocultures (Figures 7a and 7b) high levels of doxorubicin accumulation in the cells at the tissue surface are observed [80], [11]. The degree of accumulation is considerably reduced deeper than the first few cell layers, to the point of observing no doxuribicin at all at the center of the spheroid or the histocultutre. In vivo, the doxuribicin is distributed around tumor blood vessels (Figure 7c).

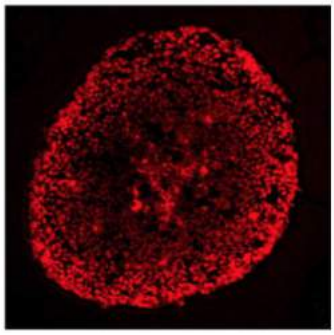

(a) Doxorubicin uptake in spheroid model [80]

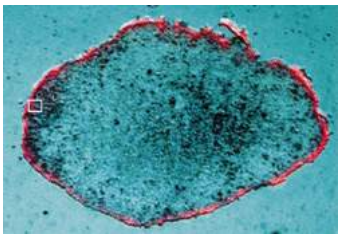

(b) Doxorubicin uptake in tumor histocultures [11]

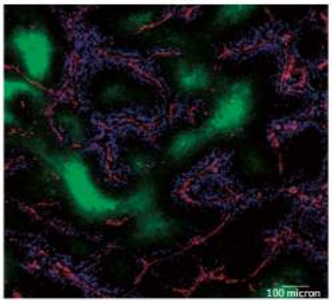

(c) Doxorubicin uptake in vivo [83]

Figure 7: Distribution of doxorubicin. **(a)** High level of doxorubicin accumulation in the cells at the spheroid surface. **(b)** Great periphery-to-center concentration gradients in tumor histocultures. **(c)** *In vivo*. A Section from a mouse mammary tumour showing the distribution of doxorubicin (blue) in relation to tumour blood vessels (red) and regions of hypoxia (green). Note that doxorubicin is distributed around tumour blood vessels.

Key factors to understand the limited drug distribution within tumors

High cellular density. In [11], it was determined that tumor cell density is a determinant of the drug penetration rate into a solid tumor. Indeed, a more rapid distribution to the areas with a low cell density compared to areas with higher cell density was observed. In [101], a computational model of interstitial transport that incorporates the biophysical properties of the tumor tissue reproduced the fact that the tissue cellular porosity and density influence the depth of penetration in a nonlinear way, with sparsely packed tissues being traveled through more

slowly than the denser tissues.

ECM Composition. Abnormal ECM composition and structure in solid tumors are major obstacles to penetration of anticancer drugs [68]. The matrix of tumor tissue shows characteristic changes compared to normal connective tissue [51]. Excessive ECM production is observed in tumor tissues, leading to deregulated accumulation of various types of collagen networks [92], as well as hyaluronan concentrations usually higher in tumors than in normal tissues [125], [57]. As a result, tumors are characteristically stiffer than the surrounding normal tissue.

Elevated interstitial fluid pressure. Another consequence of the abnormal structure and composition of tumors, is the high interstitial fluid pressure (IFP) in tumors. Since 1950, it has been known that IFP is significantly higher in tumors compared to normal tissues [129]. IFP restricts the access of therapeutic agents to tumor cells by reducing the driving forces for extravasation of fluid and macromolecules and by generating a convective flux of fluid and solute towards the periphery of tumors [24]. As far as the pressure profile in tumors is concerned, a model developed in [63] suggests that the pressure is elevated throughout the tumor, except for a sharp drop at the tumor-normal tissue interface.

0.2.2 Physical methods to increase drug penetration and uptake

Several strategies exist to improve drug penetration and uptake in biological tissues, and in solid tumors in particular (a review of those different methods in the case of tumors can be found in [122]). We focused on two of these methods. First, the electroporation, method used to overcome the barrier formed by the cell membrane in the case of macromolecules. Second, the enzyme-based therapies, method used to degrade the ECM in order to improve the penetration of therapeutic molecules.

0.2.2.1 Electroporation

The application of pulsed electric field induces transient or irreversible and localized cell membrane permeabilization, as well as an important increase of membrane conductivity. When the applied voltage is high enough, the cell may remain permeable for several minutes, allowing the exchange of molecules between the extracellular medium and the cytoplasm. The basic mechanisms of this phenomenon, called electroporation or electropermeabilization, were mainly studied at the single-cell level, although the situation is more complex in a tissue. The tissue is composed of cells that are in close contact with each other and their proximity affects electroporation. In addition, most tissues are not homogenous structures. They are composed of different cell types that are irregularly shaped and have different electrical properties that affect current density and electric field distribution and consequently also electroporation effectiveness [66]. Several electroporation regimes exist, depending mainly on the amplitude and the duration of application of the electric field (Figure 8). If the electric field magnitude or pulse duration is too small, there will be no effect. As soon as a certain voltage threshold is locally overpassed, the cells membranes are permeabilized, and the permeabilization is reversible if the voltage is not too high. For higher voltages, the electropermeabilization is irreversible, the damages to the cells are too important and they eventually end up dying. If the pulse parameters are much too intense, the Joule effect induced by the electric field leads to the destruction of the cells due to thermal effects. For efficient tissue electroporation in vivo, the electric field distribution, which depends on electrode geometry, position, and electrical properties of the sample, is thus crucial.

Electroporation has many different application. The method is successfully used in medicine in clinical practice as electrochemotherapy. The cells are treated with cytotoxic drugs, such as bleomycin, while exposing them to pulsed electric fields [58]. The main advantage of such a treatment is to avoid some of the secondary effects of classic chemotherapy, since the treatment is localized. Example of treatments with bleomycin, application of electric pulses or electrochemotherapy are shown in Figure 9.

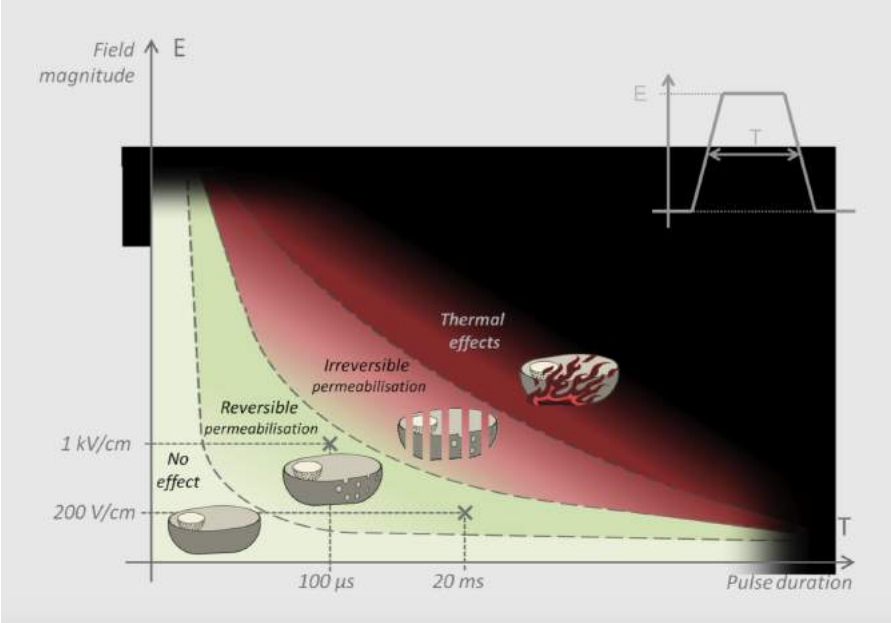

Figure 8: Schematic representation of the different modes of electroporation depending on the duration and amplitude of the electric pulses applied (no scale).

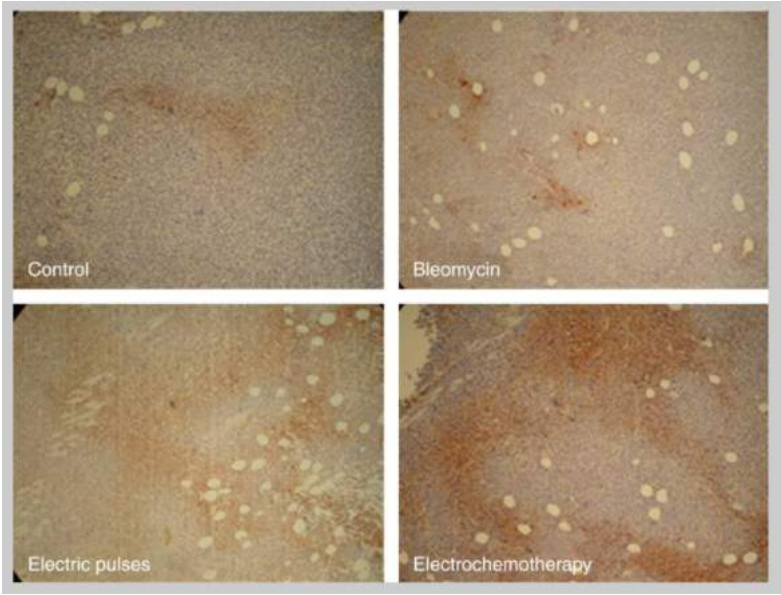

Figure 9: Tumour sections 90 min after treatment with bleomycin, application of electric pulses or electrochemotherapy. Brown regions are the cells stained with a marker of tumour hypoxia [111].

0.2.2.2 Enzyme-based therapies

Spreading agents containing interstitial matrix-degrading enzymes can be used to facilitate the dispersion and absorption of other drugs. Modification of the extracellular matrix removes part of the diffusive hindrance, increasing the dispersion of locally or systemically injected drugs.

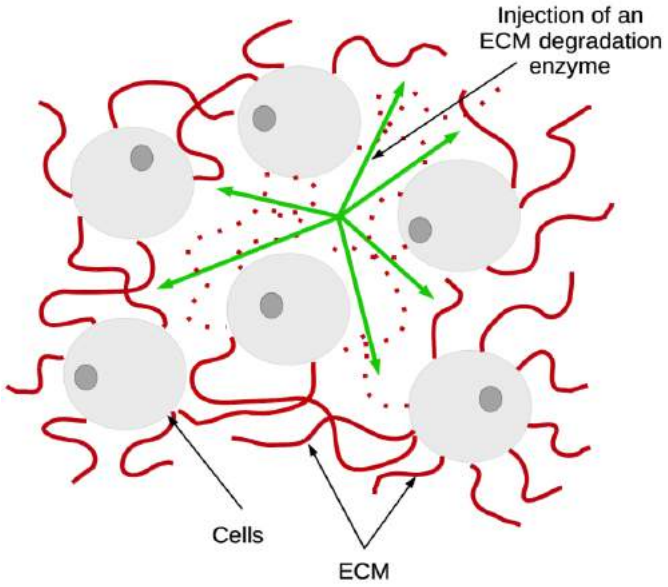

Figure 10: Schematic representation of the effect of a localized injection of matrix degrading enzymes on the extracellular matrix.

Studies have shown that significant transport improvements could be achieved after pretreatment with matrix-degrading enzymes such as collagenase or hyaluronidase [22]. Furthermore, this type of pretreatment is reversible, as the interstitial viscoelastic barriers of the treated tissue are fully restored after some time. In [22], hyaluronidase was shown to increase dispersion of different type of molecules up to 200 nm in diameter (see Figure 11).

Furthermore, in the particular case of tumor therapy, it was proven that an intratumoral injection of matrix degrading enzymes removes diffusive hindrance to the penetration of therapeutic molecules in tumor models [47, 69, 54]. Those enzymes also improve convection, as IFP may be temporarily reduced by degrading the tumor ECM. It has been shown that collagenase and hyaluronidase reduce IFP,

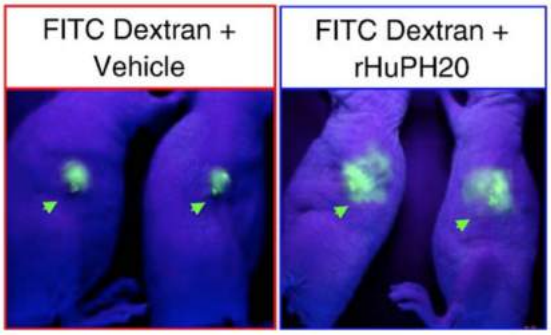

(a) Significantly increased infusion rates for FITC Dextran particles up to 200 nm in diameter

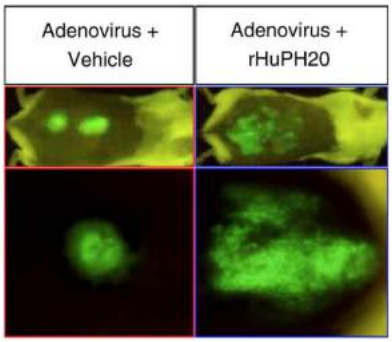

(b) Significant effects of hyaluronidase on viral dispersion

Figure 11: Determination of the gap sizes generated by the use of hyaluronidase rHuPH20 in two different cases [22]. **(a)** FITC Dextran particles. **(b)** Adenoviral particles.

thereby improving the uptake and distribution of molecules within solid tumors [45, 46, 27, 48, 99].

0.2.3 Gene therapy

There are several physical approaches to perform nonviral gene therapy. The simplest is the injection of naked DNA in the skeletal or cardiac muscle which leads to some expression of the injected genes [126]. However, this expression is very low and very variable from sample to sample. The main physical barrier encountered by DNA plasmids, the cell membrane, can be overcome using DNA electrotransfer [9]. But in the case of skeletal muscle, there is another limitation which is the access of the plasmid DNA to the muscle fiber surface. Controlled and partial degradation of ECM with matrix degrading enzymes is used to increase the diffusion and distribution of plasmid DNA into the muscle fiber. It has been shown that a pretreatment of skeletal muscle with hyaluronidase followed by DNA electrotransfer improves gene expression [1, 108, 113] (see Figure 12).

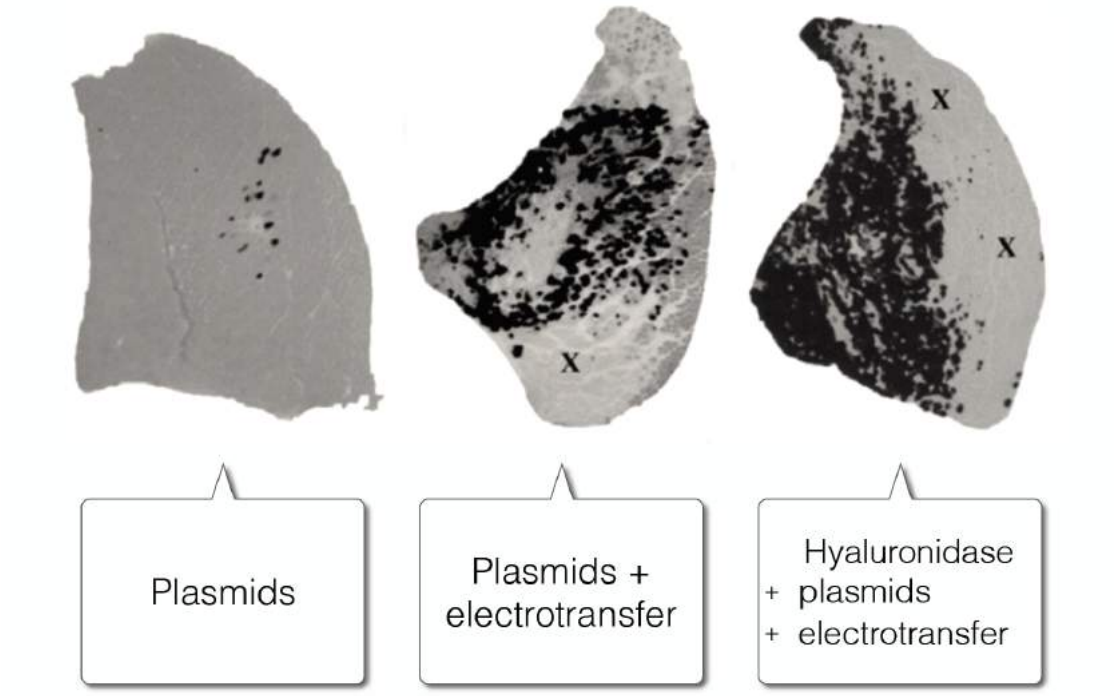

Figure 12: Sections through mouse muscle injected with plasmids and not subjected to electrotransfer (left), subjected to electrotransfer at 200 V/cm (center) or electrotransfer at 200 V/cm with hyaluronidase pretreatment (right) [113].

0.3 Outline of the thesis

This PhD Thesis deals with models of electroporation at the tissue scale on one hand, and the construction of a poroelastic model of enzyme and drug transport in biological tissue on the other hand. It is composed of two parts.

0.3.1 Modeling electroporation: from cell to tissue

Part I deals essentialy with the modeling of the electroporation phenomenon from the cell scale to the tissue scale, starting from partial differential equations to describe the space distribution and time evolution of the electroporation process. It is divided in three parts.

- Chapter 1 presents different models of cell electroporation. We first briefly

present how to model the electric potential of a cell in the linear regime, before electroporation occurs, from the Schwan model to a more generic model in which the thin membrane is accounted for by imposing equivalent transmission conditions accross the interface between the cytoplasm and the outer medium. We then focus on the electroporation phenomenon by presenting a quick review of the existing models of electroporation at the cell scale. Those models consist in introducing an *ad hoc* membrane conductivity law to the equations established in the linear regime. The chapter lays down the foundations of the study of the electroporation process at the tissue scale. It rielaborates some works done before the PhD. A complete study of these models can be found in [72] and [97].

- Chapter 2 is focused on the phenomenological modeling of the electroporation process at the tissue scale. These models are used in the bioengineering community. They consist in describing the biological tissues as conductive media whose conductivity nonlinearly depends on the electric field. The computation for the distribution of the electric field within biological tissues is crucial in the treatment planning of electroporation-based procedures. To perform this kind of simulations, an *ad hoc* law has to be built in order to model the electrical properties of the tissue: it must establish the relation between the electric field and the total current density induced inside the tissue. Up to now, the constitutive laws commonly used in models are based on static hypotheses. Numerous studies use this type of static approximation [110, 28, 106], including for treatment planning [131, 82, 44, 42]. We propose a proof of well-posedness for a boundary value problem involving such a nonlinear static hypothese on the tissue conductivity. Furthermore, even though the dynamic modeling at the cell scale is quite advanced in the literature, the attempts to model dynamically the process of electroporation at the tissue scale are much more recent and sparse [85, 123, 71]. In those studies, the main goal to reproduce the available and reliable data i.e. the current chronograms obtained experimentally when performing electroporation. We present in this chapter three different mathematical models of

tissue electroporation, based on the existing literature. An important part of this chapter is devoted to presenting the numerical methods involved when resolving the equations of these different models with the Finite Element Method. In particular, we propose a volume method to compute the electric current in order to readuce the computational time. The last part of this chapter deals with the numerical results given by the different models, and the varying knowledge they can bring to us about the electroporation process. The comparison between the experimental data, namely the current chronograms, and the results of the different models simulations makes it possible to rationally determine the main features of each phenomenological approach. The goal of this study can be summarized as

Studying numerically and comparing different models of tissue electroporation.

- Chapter 3 consists in creating a link between the modeling at the cell scale and the modeling at the tissue scale, by using an homogenization process. We use homogenization techniques with asymptotic expansions to derive an homogenized problem starting from a static problem at the cell scale, with a nonlinear assumption on the membrane conductivity. We prove a rigorous convergence of the initial problem to the homogenized problem via two-scale convergence. We verified the L^2 numerical convergence of the microscopic model towards the homogenized model. We then present some numerical results involving the bidomain model obtained by homogenization. We investigate first the influence of the cell geometry on the value of the homogenized conductivity tensors. Then we present some simulations of the bidomain model and determine the spatial distribution of the electroporated homogenized tissue. The goal of this study can be summarized as

Establishing a macroscopic model of tissue electroporation from a well-established microscopic model of cell electroporation by using a homogenization process.

0.3.2 Modeling enzyme-based therapies

Part II deals with the construction and use of a new model of tissue degradation based on a poroelastic medium approach. It is divided in two parts.

- Chapter 4 presents a new poroelastic model to account for tissue degradation. From the biological point of view, the effects of matrix degrading enzymes on drug transport are well known. However, the literature suffers from a lack of models describing the active transport of those enzymes in the extracellular medium and the resulting changes on the ECM. The aim of this chapter is to provide a mathematical model that addresses this phenomenon in order to provide a better understanding of the physical involved phenomena. The model consists of a nonlinear system of partial differential equations. It is derived directly from physical conservation laws. Constitutive relations are added to close the system. We adopt a poroelastic approach to model the mechanics of a biological tissue. This choice implies first to derive equations with Eulerian formalism and then reduce them to a fixed reference domain via a suitable change of variables in order to make the numerical processing possible. In addition, equations on the volume fraction of each component of the tissue are included to take the structural changes into account. In the end, the main variables of interest are the three different volume fractions, the interstitial pressure, the displacement and the concentrations of enzyme and therapeutic agent respectively. We then provide a numerical method that allows to simulate the complete model in 1D-, 2D-, and axisymmetric configurations in order to compare the results with the qualitative data available in the literature. The goal of this study can be summarized as

  Establishing a new model to describe the effects of matrix degrading enzymes on tissue porosity and their consequences on drug transport.

  The long-term goal of the project is to provide a first step towards the numerical optimization of drug delivery with enzyme pretreatment, which is the subject of the last chapter.

- Chapter 5 is devoted to the implementation of an optimization algorithm in an attempt to determine an optimal protocol when considering an enzyme based therapy. The goal is to determine a set of chosen parameters for which the area where the drug concentration is sufficiently high is maximal. In the framework of gene therapy, both physical strategies (enzyme pretreatment and electroporation) can be combined. Determining the optimal time at which electroporation should be performed is then crucial. Thus, we also retrieve the time at which this maximum area is reached. We use a strategy based on Kriging interpolation. After some generalities about Kriging interpolation, we present the results obtained using this interpolation method on a test case, using a simple 2D geometry and fixed parameters that were not calibrated on biological data. The goal of this study can be summarized as

Numerical strategies to optimize the distribution of drugs in the tissue after an injection of matrix degrading enzymes.

0.4 Main results

This goal of this section is to provide a substantial summary of the main results obtained during this PhD. All the results are detailed in the different chapters of this document.

0.4.1 Phenomenological models of tissue electroporation

Let us consider a bounded domain Ω, representing the tissue and let us assume that an electric field is applied between two electrodes E^+ and E^-. All models of tissue electroporation existing in the literature feature the same equation on the electric current $\overrightarrow{j}$ flowing through the tissue:

$$-\nabla \cdot \overrightarrow{j} = 0, \text{ in } \Omega. \tag{1}$$

The differences come from how the total current is computed.

0.4.1.1 Monophasic models

The standard monophasic approach consists in describing the tissue as a conductive material of conductivity σ. The current $\overrightarrow{j}$ is computed as the product of the tissue conductivity σ and the gradient of the electric potential φ

$$\overrightarrow{j} = \sigma \cdot \nabla\varphi,$$

where φ verifies the following set of boundary conditions:

$$\begin{cases} \varphi = U(t) \text{ on } E^+, & \text{(2a)} \\ \varphi = 0 \text{ on } E^-, & \text{(2b)} \\ \partial_n\varphi = 0 \text{ on } \partial\Omega, & \text{(2c)} \end{cases}$$

where $\partial\Omega$ stands for the outer surfaces of the domain Ω.

Static monophasic models. Assuming a static hypothesis, the conductivity σ is chosen as a nonlinear function of $\nabla\varphi$:

$$\sigma = \sigma(|\nabla\varphi|).$$

Different kinds of models have been considered in the literature but the most suitable ones rely on sigmoid functions [28, 110]. Although appearing quite simple, it is not trivial to show that the boundary value problem (1)-(2) is well-posed (Theorem 1). The difficulty comes from the fact that the nonlinearity is given as a function of the gradient of φ.

Theorem 1. *Assume the following assumptions on the function* $\sigma : \mathbb{R} \to \mathbb{R}$*:*

$$\left.\begin{array}{l} \sigma \text{ is continuous on } \mathbb{R}, \\ s \mapsto \sigma(s) \text{ is even on } \mathbb{R}, \\ 0 < \sigma_{min} \leq \sigma(s) \leq \sigma_{max}, \\ \sigma \text{ is increasing on } \mathbb{R}^+, \\ \lim\limits_{s \to +\infty} \sigma(s) = \sigma_{max}, \end{array}\right\}$$

and take $f \in L^2(\Omega)$*. Then, the boundary value problem*

$$\begin{cases} \nabla \cdot (\sigma(|\nabla\varphi|)\nabla\varphi) = f, & \text{in } \Omega \\ \varphi_{|\partial\Omega} = 0, & \text{on } \partial\Omega. \end{cases}$$

is well-posed.

Dynaminal monophasic model. In a first attempt to take dynamical effects into account, the conductivity σ can be chosen as a nonlinear function of the time t and of $\nabla\varphi$ [67]:

$$\sigma = \sigma(t, |\nabla\varphi|) = \sigma_0 + \sigma_1 X_1(t, \nabla\varphi) + \sigma_2 X_2(t, X_1),$$

where σ_1 and σ_2 are the equivalent conductivities related respectively to an unpulsed tissue and a deeply electroporated tissue once the dynamics are complete. X_1 and X_2 are functions whose values are between 0 and 1 given by:

$$\begin{cases} \dfrac{dX_1}{dt} = \dfrac{1}{\tau_1}(\beta(\nabla\varphi) - X_1), \text{ with } \beta(\nabla\varphi) = \dfrac{1 + \tanh(k(|\nabla\varphi| - E_{th}))}{2}, \\ \dfrac{dX_2}{dt} = \dfrac{1}{\tau_2}(X_1 - X_2). \end{cases}$$

Parameters τ_1 and τ_2 are the characteristic times of the two different dynamic processes.

0.4.1.2 New biphasic model

The **biphasic** approach consists in computing $\overrightarrow{j}$ as the product of the sum of two current densities:

$$\overrightarrow{j} = \sigma_e \cdot \nabla\varphi + \overrightarrow{\mathbf{J}}_{cells}(t, \nabla\varphi),$$

where the current density $\overrightarrow{\mathbf{J}}_{cells}(t, \nabla\varphi)$ flows through the cells and the current density $\sigma_e \cdot \nabla\varphi$ flows through the extracellular medium. $\overrightarrow{\mathbf{J}}_{cells}$ is governed by the a first order differential equation

$$\left(1 + \frac{\sigma_m(t, v_m)}{\sigma_c}\right) \overrightarrow{\mathbf{J}}_{cells} + \frac{\varepsilon_m}{\sigma_c} \frac{d\overrightarrow{\mathbf{J}}_{cells}}{dt} = \sigma_m(t, v_m)\nabla\varphi + \varepsilon_m \frac{d\nabla\varphi}{dt},$$

where σ_m is the equivalent conductivity at the tissue scale for the membrane, whose value is affected by the amplitude of the transmembrane voltage at the tissue scale, denoted v_m and defined as

$$v_m(t, x) = d_{cell} \left\| \frac{1}{2} \left(\nabla\varphi(t, x) - \frac{\overrightarrow{\mathbf{J}}_{cells}(t, x)}{\sigma_c} \right) \right\| \text{ in } [0, T] \times \Omega.$$

$\sigma_m(t, v_m)$ is obtained as:

$$\sigma_m(t, v_m) = \sigma_{m0} + \sigma_{m1} X_1(t, v_m) + \sigma_{m2} X_2(t, X_1),$$

where σ_{m0}, σ_{m1} and σ_{m2} are the equivalent membrane conductivities related respectively to an unpulsed tissue and a deeply electroporated tissue once the dynamics are complete. X_1 and X_2 are functions whose values are between 0 and 1 given by:

$$\frac{dX_1}{dt} = \begin{cases} \frac{\beta_1(v_m) - X_1}{\tau_1}, & \text{if } \beta_1(v_m) \geq X_1, \\ 0, & \text{else,} \end{cases}, \text{ with } \beta_1(v_m) = \frac{1 + \tanh(k_1(v_m - V_{th}))}{2},$$

$$\frac{dX_2}{dt} = \begin{cases} \frac{\beta_2(X_1) - X_2}{\tau_2}, & \text{if } \beta_2(X_1) \geq X_2, \\ 0, & \text{else,} \end{cases} \text{ with } \beta_2(X_1) = \frac{1 + \tanh(k_2(X_1 - X_{th}))}{2}.$$

Parameters τ_1 and τ_2 are the characteristic times of the two different dynamic processes. In a steady-state approximation, the equivalent tissue conductivity σ is obtained as:

$$\sigma = \sigma_e + \frac{\sigma_c \sigma_m}{\sigma_c + \sigma_m}.$$

This makes it possible to compare the monophasic and biphasic approaches. The interesting features lies in the fact that even though the cell membrane conductivity increases a lot, at the tissue scale σ stays between σ_e and $\sigma_e + \sigma_c$. Thus, to compare numerically the three models of tissue electroporation, we observe the **tissue conductivity** σ, whose spatial distribution is a good indicator to determine the electroporated area, and the **electric current**, which can be easily compared to experimental current chronograms.

We propose adapted numerical tools to study the three models, each solved using the Finite Element Method in 2D and 3D. Using the symmetry of the problem, a simplified 2D computational domain (see Figure 13) is derived with boundary conditions on the symmetric planes $\mathcal{B}_1$ and $\mathcal{B}_2$ (3) added to the original set of boundary conditions (2).

$$\begin{cases} \varphi = 0 \text{ on } \mathcal{B}_1, & \text{(3a)} \\ \partial_n \varphi = 0 \text{ on } \mathcal{B}_2. & \text{(3b)} \end{cases}$$

First, we show that, in the static case, the stiff nonlinear problem, which may cause numeric instabilities, can be solved using a modified fixed point iteration [28]. Then, we show that the choice of method when computing the simulated current I is crucial. While the simulated current is usely computed as a **surface integral** on one of the electrodes, namely

$$I_{surf} = \int_{E^+} \overrightarrow{j}_{|_{E^+}} \cdot \overrightarrow{n}_{|_{E^+}} dS,$$

we propose instead a **volume method** to calculate the current (see Figure 14 in the linear case $\overrightarrow{j} = \sigma \nabla \varphi$ with $\sigma = 1$):

$$I_{vol} = \int_{\Omega} \overrightarrow{j} \cdot \nabla w \, dx,$$

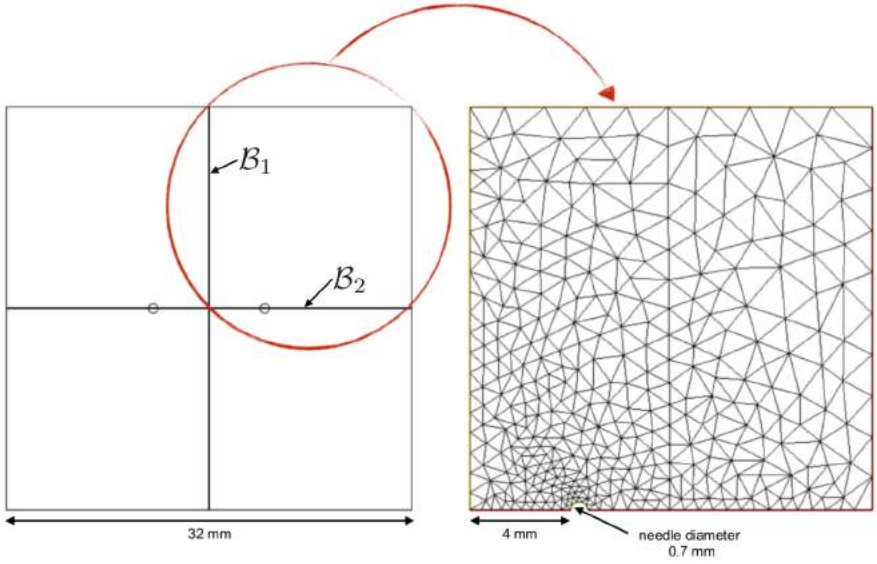

Figure 13: 2D computational domain.

where w is the unique solution of the following Laplace problem

$$\begin{aligned} \Delta w &= 0, && \text{in } \Omega, \\ w &= 1, && \text{on } E^+, \\ \partial_n w &= 0, && \text{on } \partial\Omega, \\ w &= 0, && \text{on } \mathcal{B}_1, \\ \partial_n w &= 0, && \text{on } \mathcal{B}_2. \end{aligned}$$

The long-term goal of this study is to calibrate each model with biological data. A **comparison between the experimental data** available, namely the current chronograms, **and the simulated current** I obtained using the different models permits to rationally determine the main features of each phenomenological approach (see Figure 15).

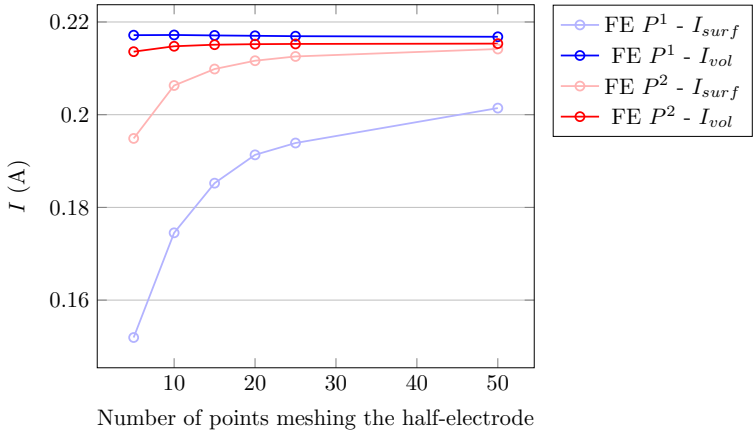

Figure 14: Value of I_{surf} and I_{vol} in the linear case ($j = \sigma\nabla\varphi$ with $\sigma = 1$) for different 2D mesh precisions from 5 points meshing the electrode surface E^+ to 50 points using both P^1 and P^2 elements and both surface and volume methods.

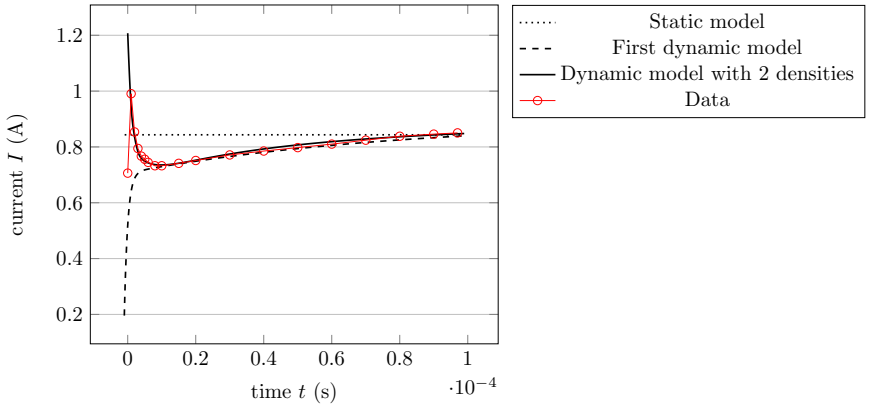

Figure 15: Comparison between experimental current and the computed currents (P^2 elements, volume method) with three different phenomenological models for an applied voltage of 875 V/cm.

0.4.2 A model of tissue electroporation obtained with a homogenization process

Even though the *ad hoc* biphasic tissue model seems to be validated with the experiments, its physical meaning is poorly justified. To fill the gap between cell scale and tissue, we propose here a rigorous **homogenization process**. To use a

homogenization procedure, it is convenient to assume that biological tissues have a periodic microstructure. Let $\varepsilon > 0$ be a small parameter. The domain Ω, representing the tissue, contains a periodic array of cells whose size is controlled by ε (see Figure 0.4.2). Let us denote $[u^\varepsilon] = u_e^\varepsilon - u_i^\varepsilon$, where u_e^ε (resp. u_i^ε) is the

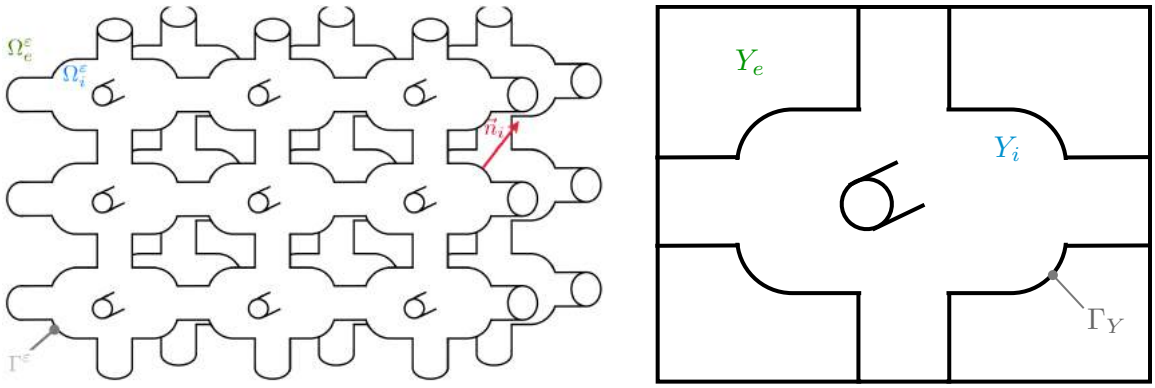

(a) Domain Ω (b) Periodic cell Y

Figure 16: Schematic illustration of the periodic medium Ω and of a unit period Y.

induced electric potential of the extracellular (resp. intracellular) medium in this whole macroscopic domain Ω. $(u_e^\varepsilon, u_i^\varepsilon)$ are proven to be solutions to the following microscopic problem:

$$
\begin{cases}
\nabla_x \cdot (\sigma_i \nabla_x u_i^\varepsilon) = 0, & \text{in } \Omega_i^\varepsilon, \quad (4a)\\
\nabla_x \cdot (\sigma_e \nabla_x u_e^\varepsilon) = f, & \text{in } \Omega_e^\varepsilon, \quad (4b)\\
\sigma_i \nabla_x u_i^\varepsilon \cdot \vec{\mathbf{n}}_i = \sigma_e \nabla_x u_e^\varepsilon \cdot \vec{\mathbf{n}}_i, & \text{on } \Gamma^\varepsilon, \quad (4c)\\
\varepsilon S_m([u^\varepsilon])[u^\varepsilon] = \sigma_i \nabla_x u_i^\varepsilon \cdot \vec{\mathbf{n}}_i, & \text{on } \Gamma^\varepsilon, \quad (4d)\\
\sigma_i \nabla_x u_i^\varepsilon \cdot \vec{\mathbf{n}}_i = \sigma_e \nabla_x u_e^\varepsilon \cdot \vec{\mathbf{n}}_i = 0, & \text{on } \partial\Omega, \quad (4e)\\
u_{e|_{E_+}}^\varepsilon = 0, & \text{on } E_+, \quad (4f)\\
u_{e|_{E_-}}^\varepsilon = 0, & \text{on } E_-, \quad (4g)
\end{cases}
$$

where σ_i (resp. σ_e) is the conductivity of the intracellular (resp. extracellular) medium and where S_m is a sigmoid function that accounts for the membrane

conductivity, assumed to be a function of the transmembrane potential voltage $[u^\varepsilon]$ [67, 72]. This system is obtained once a proper scaling procedure has been applied, the consequence being the appearance of the parameter ε in equation (4d). We prove a **rigorous convergence** of the microscopic problem (4) to an homogenized problem via two-scale convergence (see Theorem 2).

Theorem 2. *The sequence of solutions $(u_e^\varepsilon, u_i^\varepsilon)$ of problem (4) verify the following two-scale convergences:*

- $u_e^\varepsilon(x)$ *two-scale converges to* $\chi_{Y_e}(y)u_e^0(x)$,
- $u_i^\varepsilon(x)$ *two-scale converges to* $\chi_{Y_i}(y)u_i^0(x)$,
- $\nabla u_e^\varepsilon(x)$ *two-scale converges to* $\chi_{Y_e}(y)(\nabla_x u_e^0(x) + \nabla_y u_e^1(x,y))$,
- $\nabla u_i^\varepsilon(x)$ *two-scale converges to* $\chi_{Y_i}(y)(\nabla_x u_i^0(x) + \nabla_y u_i^1(x,y))$,
- $v^\varepsilon(x) = u_e^\varepsilon(x)_{|\Gamma^\varepsilon} - u_i^\varepsilon(x)_{|\Gamma^\varepsilon}$ *two-scale converges to* $v^0(x) = u_e^0(x) - u_i^0(x)$,

where

$$
\begin{aligned}
u_i^1(x,y) &= -\psi_i(y)\nabla_x u_i^0(x),\\
u_e^1(x,y) &= -\psi_e(y)\nabla_x u_e^0(x),
\end{aligned}
$$

with ψ the solution to the following cell problem

$$
\begin{cases}
\nabla_y \cdot (\sigma_i \nabla_y \psi_i) = 0, & \text{in } Y_i,\\
\nabla_y \cdot (\sigma_e \nabla_y \psi_e) = 0, & \text{in } Y_e,\\
\sigma_i(\nabla_y \psi_i^{1,2,3} - e^{1,2,3}) \cdot \vec{\boldsymbol{n}}_i = \sigma_e(\nabla_y \psi_e^{1,2,3} - e^{1,2,3}) \cdot \vec{\boldsymbol{n}}_i = 0, & \text{on } \Gamma_Y,\\
\psi_{e,i}^{1,2,3} \text{ is } Y\text{-periodic.}
\end{cases}
$$

The limit (u_e^0, u_i^0) is the unique solution of the following two-scale homogenized system given in $\Omega \times Y$

$$
\begin{aligned}
-\nabla_x \cdot \left(\widetilde{\sigma_i}\nabla_x u_i^0 + \widetilde{\sigma_e}\nabla_x u_e^0\right) &= \frac{|Y_e|}{|Y|} f,\\
\frac{|\Gamma_Y|}{|Y|}\left(S_m(u_e^0 - u_i^0)(u_e^0 - u_i^0)\right) &= \nabla_x \cdot \left(\widetilde{\sigma_e}\nabla_x u_e^0\right).
\end{aligned}
$$

with

$$\widetilde{\sigma_{i,e}} = \sigma_{i,e}\frac{|Y_{i,e}|}{|Y|}I_2 - \sigma_{i,e}\frac{1}{|Y|}\int_{Y_{i,e}} \nabla_y \psi(y)dy.$$

The convergence in L^2 of the microscopic model (4) towards the homogenized model is verified numerically.

In order to compare this model, obtained mathematically, to the phenomenological models of tissue electroporation previously presented, one must determine the **tissue conductivity** σ, whose spatial distribution permits to determine the electroporated area. The equivalent tissue conductivity of this model is obtained using the following formula:

$$\sigma = \widetilde{\sigma_e} + \frac{\widetilde{\sigma_i} l_0^2 \frac{|\Gamma_Y|}{|Y|} S_m}{\widetilde{\sigma_i} + l_0^2 \frac{|\Gamma_Y|}{|Y|} S_m},$$

where $\widetilde{\sigma_e}$ and $\widetilde{\sigma_i}$ are assumed to be scalar tensors. l_0 is the characteristic length of the tissue. One can see that this formula is very similar to the one obtained in the case of the phenomenological model using two current densities. Nevertheless, despite the similarities between the model using two current densities and the homogenized model, they give very different results. At the cell scale, the membrane conductivity S_m is assumed to depend on the transmembrane potential voltage $[u^\varepsilon]$. As a result, the tissue conductivity σ **also depends on the homogenized transmembrane potential voltage** $u_e^0 - u_i^0$. But the spatial distribution of this physical quantity does not cope with the electroporated area observed in the experiments (see Figure 17).

We believe that this indicates that we should go further in the formal expansion of $v^\varepsilon(x) = u_e^\varepsilon(x)_{|\Gamma^\varepsilon} - u_i^\varepsilon(x)_{|\Gamma^\varepsilon}$. Formally, the first term of the expansion is the limit $v^0 = u_e^0 - u_i^0$. But the next term reveals a dependence on $\nabla_x u_e^0$ (and $\nabla_x u_i^0$), whose spatial distribution is closer to the experimental electroporated area (see Figure 18).

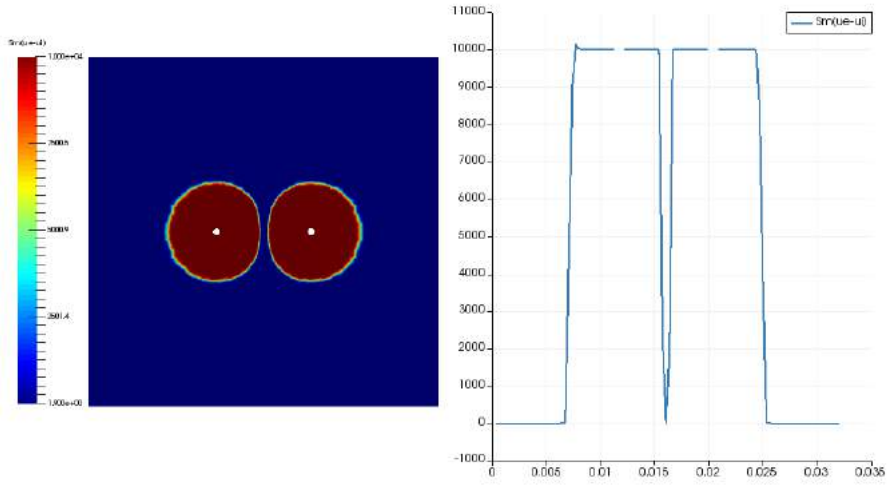

Figure 17: Spatial distribution of the homogenized tissue conductivity $\sigma(u_e^0 - u_i^0)$ computed with the static bidomain model.

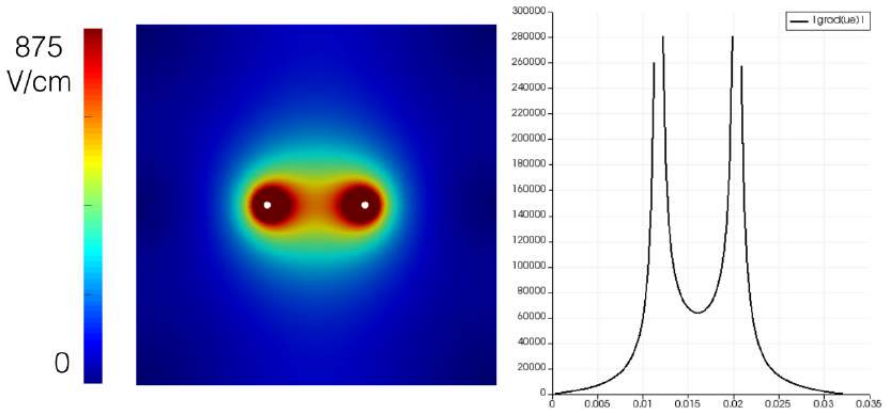

Figure 18: Spatial distribution of the homogenized electric field ∇u_e^0 computed with the static bidomain model.

0.4.3 A new poroelastic model of tissue degradation

We first present briefly the model established in Chapter 4 and we refer to Chapter 4 for the significance of all constants. Biological tissue can be modeled as a **saturated poroelastic mixture** made of three different constituants: the interstitial fluid, the ECM and the cells. The medium is assumed to be saturated:

$$g_{\mathcal{E}} + g_{\mathcal{C}} + f = 1,$$

where f is the volume fraction of fluid, $g_{\mathcal{E}}$ is the volume fraction of extracellular matrix and $g_{\mathscr{C}}$ is the volume fraction occupied by cells. The mechanics of the mixture are described by the following poroelastic system:

$$\begin{cases} \boldsymbol{\nabla} \cdot \left((g_{\mathcal{E}} + g_{\mathscr{C}}) \left(\lambda (\nabla \cdot \mathbf{u}) I + \mu (\nabla \mathbf{u} + \nabla \mathbf{u}^T) \right) \right) = \nabla P, \\ (g_{\mathcal{E}} + g_{\mathscr{C}}) s_0 \dfrac{\partial P}{\partial t} - \nabla \cdot (\boldsymbol{\kappa} \nabla P) = Q_{\text{inj}}^{\text{tot}} + \gamma (P_v - P) \\ \qquad\qquad + \left(\dfrac{\rho_s^{R,0}}{\rho_f^R} - 1 \right) g_{\mathcal{E}} (Kh + a_r (f(0, \mathbf{x}) - f)) - \nabla \cdot \left(\dfrac{\partial \mathbf{u}}{\partial t} \right), \end{cases}$$

where $\mathbf{u}$ is the displacement of the solid phase and P the interstitial fluid pressure. The volume fractions of ECM and of cells are given as the solutions of the following ODEs:

$$\begin{cases} \dfrac{\partial g_{\mathscr{C}}}{\partial t} + \left(s_0 \dfrac{\partial P}{\partial t} + \nabla \cdot \left(\dfrac{\partial \mathbf{u}}{\partial t} \right) \right) g_{\mathscr{C}} = 0, \\ \dfrac{\partial g_{\mathcal{E}}}{\partial t} + \left(Kh + a_r (f(0, \mathbf{x}) - f) + s_0 \dfrac{\partial P}{\partial t} + \nabla \cdot \left(\dfrac{\partial \mathbf{u}}{\partial t} \right) \right) g_{\mathcal{E}} = 0. \end{cases}$$

The volume fraction of fluid f is obtained using the saturation condition. The concentration of matrix-degrading enzyme is described by the following convection-diffusion reaction equation:

$$\frac{\partial h}{\partial t} = \nabla \cdot (f \mathbf{D}_{\text{enz}}^0 \nabla h + h J_{\text{enz}}) + h \left(-\frac{k_{\text{enz}}^d}{f} - \nabla \cdot \left(\frac{\partial \mathbf{u}}{\partial t} \right) \right) + \mathcal{S}_{\text{enz}},$$

where $J_{\text{enz}} = \frac{1}{f} \boldsymbol{\kappa} \nabla P - \mathbf{D}_{\text{enz}}^0 \nabla f$. The concentration of therapeutic agent, injected after the matrix-degrading enzyme, is described by the following convection-diffusion reaction equation:

$$\frac{\partial c}{\partial t} = \nabla \cdot (f \mathbf{D}_{\text{drug}}^0 \nabla c + c J_{\text{drug}}) + c \left(-\frac{k_{\text{drug}}^d}{f} - \nabla \cdot \left(\frac{\partial \mathbf{u}}{\partial t} \right) \right) + \mathcal{S}_{\text{drug}},$$

where $J_{\text{drug}} = \frac{1}{f} \boldsymbol{\kappa} \nabla P - \mathbf{D}_{\text{drug}}^0 \nabla f$. The complete model is coupled with a set of boundary conditions that can vary with the different test cases that may be considered. Namely, on the boundary, one can impose either

- the displacement $\mathbf{u}$ or the stress $\mathbf{S}_s^E\,\mathbf{n}$,
- the pressure P or the pressure flux $\nabla P \cdot \mathbf{n}$,
- the enzyme's concentration h or flux $\left(f\mathbf{D}^0_{\text{enz}}\nabla h + hJ_{\text{enz}}\right)\cdot\mathbf{n}$,
- the drug's concentration c or flux $\left(f\mathbf{D}^0_{\text{drug}}\nabla c + hJ_{\text{drug}}\right)\cdot\mathbf{n}$.

The results given by the simulations are **qualitatively compared to the following experimental data** for validation:

- Distribution of anticancer fluorescent agent (to be compared with the distribution of the simulated drug's concentration c),
- Experimental interstitial fluid pressure (IFP) (to be compared with the simulated normalized pressure P).

We use the model to describe two situations: the incubation of a spheroid into an ECM degradation enzyme and the intratumoral injection of enzyme in vivo.

Incubation of a spheroid. We observe that a pretreatment with ECM degradation enzyme **affects the distribution** of therapeutic agents, thereby improving the diffusion process. Where without pretreatment, the macromolecules stay mainly at the periphery of the spheroid, a pretreatment with hyaluronidase permit to obtain a wider distribution (Figure 19).

Intratumoral injection of enzyme in vivo. Given the dependency of the pressure on the porosity variable, an intratumoral injection of enzyme results in a **reduction of the IFP**. This reduction depends on the enzyme's concentration and reaches a maximum value, a further increase of the dose resulting in a smaller reduction, which is in accordance with the experiments (Figure 20).

It also appears that a pretreatment with ECM degradation enzyme **affects the distribution** of therapeutic agents, thereby increasing its area of action by improving both the diffusion and the convection processes. This is once more in accordance with the experiments (data from [46]). Indeed, without pretreatment,

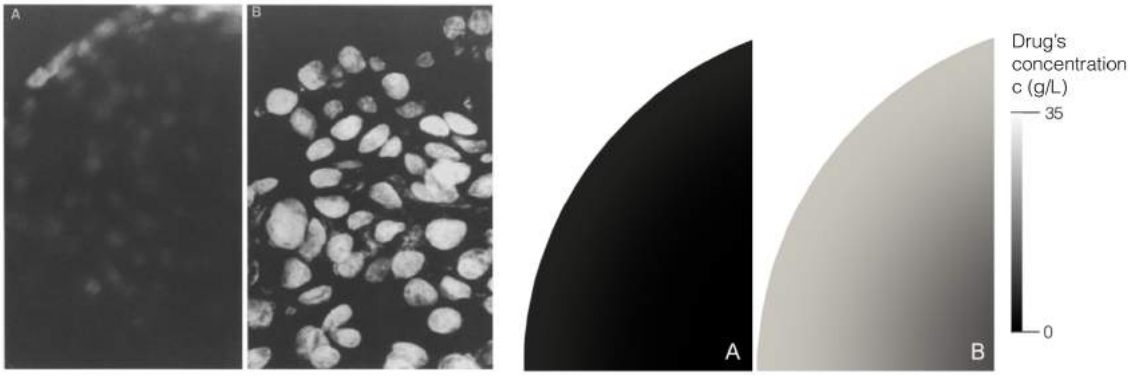

Figure 19: Comparison between experimental doxuribicin fluorescence (left, data from [69]) and numerically simulated concentration of anticancer agent c in a spheroid previously incubated with hyaluronidase (B) or not (A).

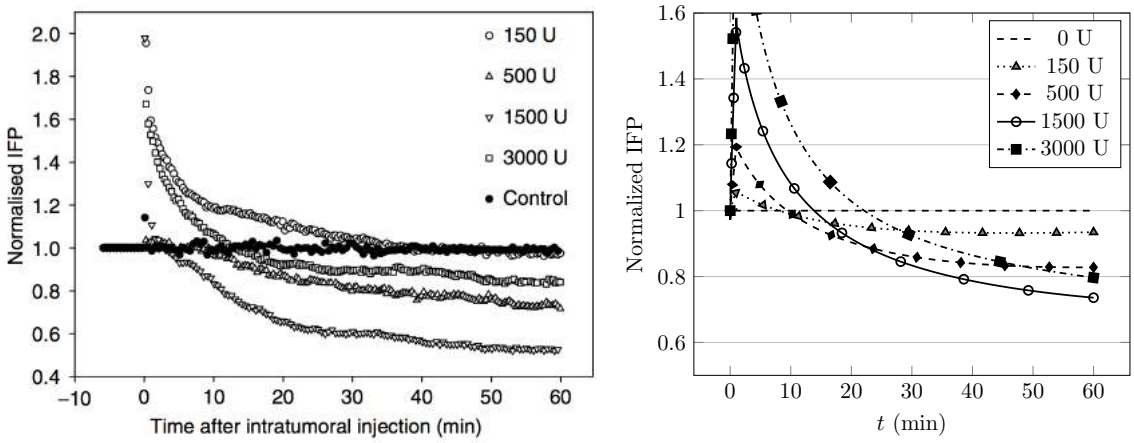

Figure 20: Comparison between experimental IFP (left, data from [46]) and numerically simulated IFP. Normalized interstitial fluid pressure is represented in both cases as a function of time after intratumoral injection of 150 U, 500 U, 1500 U and 3000 U hyaluronidase in tumors compared to no pretreatment (intratumoral injection of saline solution).

the macromolecules stay only at the periphery of the tumor, the transcapillary transport being greatly reduced by the high IFP inside the tumor. A pretreatment with hyaluronidase permit to obtain a wider distribution. The molecules are thus distributed all over the tumor (Figure 21).

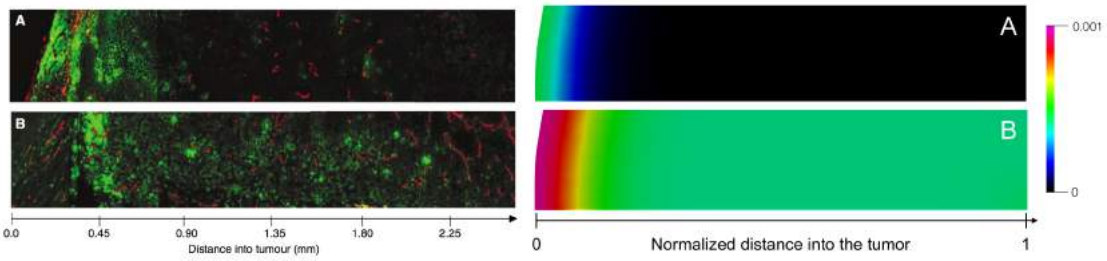

Figure 21: Comparison between experimental distribution of anticancer fluorescent agent (left, data from [46]) and numerically simulated concentration of agent. In case A, no pretreatment was previously performed on the tissue whereas in case B, the tissue was pretreated with 1500 U hyaluronidase.

0.4.4 An optimization algorithm for enzyme based therapies

The last contribution of this PhD thesis lies within the nonlinear numerical optimization framework. It consists in using mathematical modeling as a tool to **optimize drug delivery in enzyme-based therapies**. We use the model developed in Chapter 4 and presented in the previous section to model the processes that govern drug distribution in tissue after an injection of matrix-degrading enzyme. All the other parameters being fixed, three independent control variables are at our disposal to optimize the protocol:

- T the time lag between the injection of enzyme and the injection of therapeutic agent,
- y_0 the position of the injection point,
- $c_{\text{drug}}^{\text{inj}}$ the concentration of therapeutic agent in the fluid injected.

The goal of our optimization strategy is simple: find a set of parameters $(T, y_0, c_{\text{drug}}^{\text{inj}})$ for which the area where the concentration of drug c is above a minimum concentration $c_{\min}$ is the widest possible. The quantity of interest is thus

$$F_{max} = \max_{t\in[T,T+T_{obs}]} \frac{1}{|\Omega|} \times \int_{\Omega} \frac{[c(t,x) - c_{\min}]^+}{c(t,x) - c_{\min}}\, dx,$$

where T is the time at which the injection of drugs begins and T_{obs} is the time of observation. Using an optimization strategy based on **Kriging interpolation**, we can derive an optimized protocol in order to obtain the maximal area where the drug concentration is sufficiently high. The results of this interpolation are obtained on a test case, using a simple 2D geometry and fixed parameters that were not calibrated on biological data. As the optimized protocol is obtained for the maximal value of $c_{\text{drug}}^{\text{inj}}$ tested, visualization in the two-dimensional parameter space (T, y_0) gives some insights on the variations of F_{max} (see Figure 22).

All the main results presented in this summary are now detailed in the different chapters of this document, starting with the modeling of the electroporation phenomenon.

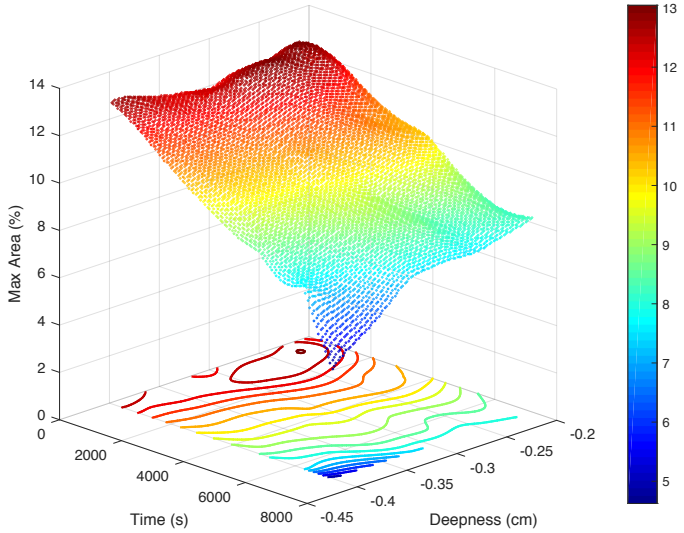

(a)

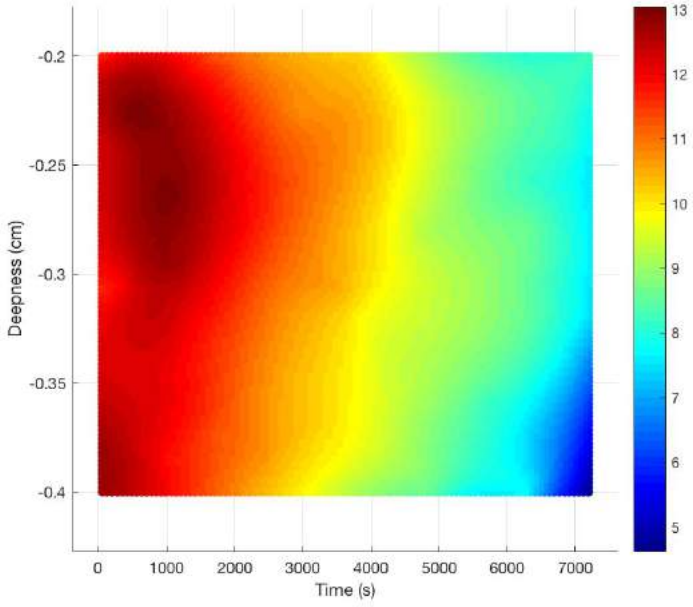

(b)

Figure 22: Visualization in the 2D parameter space of F_{max} obtained using Kriging interpolation.

Part I

Modeling electroporation: from cell to tissue

Chapter 1

Models of electroporation at the cell scale

Cell electroporation is a complex phenomenon in which cell membrane permeability is increased by exposing the cell to short high electric pulses. Since the end of the 90's, biophysical models have been developed to explain and predict the conditions of cell electroporation. In this chapter, we present a quick overview of different models of cell electroporation. The idea is to lay down the foundations for the study of the electroporation process at the tissue scale developed in Chapters 2 and 3. What is presented here does not fall within the actual work done during the PhD.

1.1 Electric model for a biological cell in the linear regime

1.1.1 The Schwan model

Analytical description of steady-state transmembrane voltage induced on spherical cells was derived six decades ago by H. P. Schwan [109]. To simplify the derivation, Schwan assumed the membrane to be nonconductive, which led to the

well-known relation, often referred to as the (steady-state) Schwan's equation

$$\Delta V = \frac{3}{2} ER\cos(\varphi), \tag{1.1}$$

where ΔV is the induced transmembrane voltage, E is the amplitude of the external electric field, R is the cell radius, and φ is the polar angle measured from the center of the cell with respect to the direction of the field. This model exhibits an interesting linear dependency of the transmembrane voltage on the radius, but it cannot describe the influence of the cell shape.

1.1.2 PDE model derived from Maxwell equations

To take the cell shape into account, one can derive a PDE model using Maxwell equations on a simplified geometry: the biological cell is considered as an homogeneous medium protected by a thin membrane and embedded in an homogeneous extracellular medium. Nevertheless, to perform computations on realistic cell shapes without meshing the cell membrane, it is possible to replace the membrane by an equivalent condition on the boundary of the cytoplasm, see Figure 1.1.

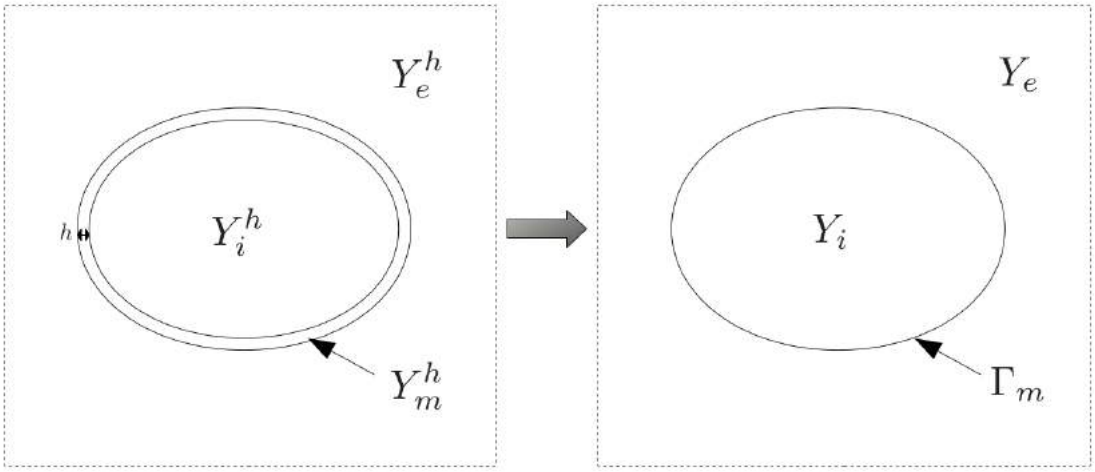

Figure 1.1: Cell geometry from real membrane representation to equivalent simple interface problem.

Denoting by S_0 the surface conductivity and by C_m the capacitance of the membrane, the electric potential V is approached by u the solution of:

$$\begin{cases} \nabla \cdot (\sigma_i \nabla u) = 0, & \text{in } Y_i, \quad (1.2a) \\ \nabla \cdot (\sigma_e \nabla u) = 0, & \text{in } Y_e, \quad (1.2b) \\ \sigma_i \nabla u \cdot \vec{\mathbf{n}}_i = \sigma_e \nabla u \cdot \vec{\mathbf{n}}_i, & \text{on } \Gamma_m, \quad (1.2c) \\ C_m \dfrac{\partial [u]}{\partial t} + S_m[u] = \sigma_i \nabla u \cdot \vec{\mathbf{n}}_i, \text{ where } [u] = u_{|_{\Gamma_m^+}} - u_{|_{\Gamma_m^-}}, & \text{on } \Gamma_m, \quad (1.2d) \\ u_{|_{\partial\Omega}} = g, u_{|_{t=0}} = V_0. & (1.2e) \end{cases}$$

The approximate potential u is discontinuous across the interface: this is the effect of the high resistivity and the small thickness of the membrane. System (1.2) takes the cell geometry and the electric field orientation into account thanks to the fact that the Neumann derivative is linked to the Dirichlet jump of the potential. When considering a spherical geometry, system (1.2) can be solved and (1.1) is recovered. The mathematical proof of this approximation has been presented in [96].

1.2 Model of Neu Krassowska

One of the most cited model in the literature was proposed by Neu and Krassowska [93]. The main idea of this model is to add an electroporation current I_{ep} to the condition on the jump of the transmembrane voltage (1.2d):

$$C_m \frac{\partial [u]}{\partial t} + S_m[u] + I_{ep} = \sigma_i \nabla u \cdot \vec{\mathbf{n}}_i \text{ on } \Gamma_m. \quad (1.3)$$

To define this current, Neu and Krassowska [93] use a description of the membrane permeabilization based on the creation of pores. This current is then described as the product between the pore density N_{ep} and the current through a single pore i_{ep}:

$$I_{ep} = i_{ep} \cdot N_{ep}.$$

Debruin and Krassowska [38] proposed the following formula for i_{ep}:

$$i_{ep}(\nu_m) = \frac{\pi r_m^2 \sigma \nu_m RT}{Fh} \frac{e^{\nu_m} - 1}{\frac{w_0 e^{w_0 - n\nu_m} - n\nu_m}{w_0 - n\nu_m} e^{\nu_m} - \frac{w_0 e^{w_0 + n\nu_m} + n\nu_m}{w_0 + n\nu_m}}, \tag{1.4}$$

where

- ν_m is the non dimensionalized transmembrane potential: $\nu_m = \frac{[u]F}{RT}$, F is the Faraday constant, R the universal gas constant and T the temperature in Kelvin,
- r_m the radius of the pore,
- σ the pore conductivity,
- w_0 the membrane barrier energy inside a pore,
- n the relative entrance length of the pore
- h is the membrane thickness.

The pore density N_{ep} follows the following first order differential equation:

$$\frac{dN_{ep}}{dt} = \alpha e^{([u]/[u]_{ep})^2} \left(1 - \frac{N_{ep}}{N_0} e^{-q([u]/[u]_{ep})^2}\right), \tag{1.5}$$

where

- N_0 the pore density at rest,
- $[u]_{ep}$ the threshold membrane voltage above which electroporation occurs,
- α and q are *ad hoc* parameters.

The main drawback of this kind of approach lies in the number of non-measurable parameters and the sensitivity of the results to the parameters which makes the model calibration hardly obtainable [97]. In order to simplify this problem, one can notice that linearizing i_{ep} around small values of the transmembrane potential gives

$$i_{ep} \sim K[u] \implies I_{ep} \sim N_{ep} K[u],$$

where $K = K(r_m, \sigma, \delta, n, w_0)$ is a constant. $N_{ep}K$ is found to be homogeneous to a surface conductivity. The idea behind the models of cell electroporation presented next is to determine a phenomenological law on this surface conductivity, and explain how the transmembrane potential affects it.

1.3 Static model

In [62], the authors proposed a static model of conductivity, described as a sigmoid function around the electroporation threshold value. When no voltage is applied, the membrane conductivity S_m value is the one of a cell at rest, S_0. When the applied voltage is above the electroporation threshold V_{th}, the conductivity tends toward its maximum value S_1:

$$S_m([u]) = S_0 + (S_1 - S_0)\frac{1 + \tanh(k_{ep}(|[u]| - V_{th}))}{2}, \tag{1.6}$$

where k_{ep} accounts for the speed of transition between the two states. A comparative study of this model with the ones of Neu and Krassowska [93] and of Ivorra [62] has been caried out in Leguèbe's PhD thesis [72].

Remark 1. Other choices of sigmoid function are possible. For instance, one can use

$$S_m([u]) = S_0 + (S_1 - S_0)e^{-V_{th}^2/|[u]|^2}. \tag{1.7}$$

1.4 Dynamic model

The phenomenological model of membrane permeabilization proposed in [67] is based on the following assumptions, which come from experimental experiments [97]:

- Permeabilization results from a long-term effect of defects in the membrane.
- The dynamics of alteration and reconstruction of the membrane are quite long.

- Lipids diffuse along the membrane quite rapidly, so surface diffusion has to be accounted for.

In [67, 72], a two-step model for membrane electroporation is proposed. The membrane surface conductivity is given by

$$S_m(t,\cdot) = S_0 + S_1 X_1(t,\cdot) + S_2 X_2(t,\cdot), \tag{1.8}$$

where S_0 is the membrane conductivity at rest, S_1 is the conductivity of the fully porated membrane, S_2 is the membrane conductivity due to the long term effect of electroporation. The dimensionless variables X_1 and X_2 refer to as the degree of poration during the pulse, and the degree of long term changes in the membrane respectively. They satisfy the following equations:

$$\frac{\partial X_1}{\partial t} = \frac{\beta(V_m(t,\cdot)) - X_1(t, V_m(t,\cdot))}{\tau_1}, t > 0 \tag{1.9a}$$

$$\frac{\partial X_2}{\partial t} - d_\Gamma \Delta_\Gamma X_2 = \left[\frac{(X_1 - X_2)}{\tau_2}\right]^+, t > 0 \tag{1.9b}$$

$$X_{1|_{t=0}} = X_1^0, X_{2|_{t=0}} = X_2^0. \tag{1.9c}$$

where $[\cdot]^+$ denotes the positive part, τ_1 and τ_2 are the characteric times of pore creation and changes in the membrane. The β is a sigmoidal function, for instance

$$\beta(\lambda) = \frac{1 + \tanh(k_1(|\lambda| - V_{th}))}{2}.$$

1.5 Conclusion

In this first chapter, we presented some models of cell electroporation found in the literature. From the general model of electric potential of a cell in the linear regime, models of electroporation can be derived by either adding an electroporation current or assuming an *ad hoc* on the membrane conductivity. In the second case, the phenomenological law can be chosen based on a static hypothesis or can take the dynamical effects of the phenomenon into account. Now, the idea is to

generalize this second approach and derive an accurate model of tissue electroporation. This can be done either by deriving phenomenological models directly at the tissue scale (see Chapter 2) or by obtaning a macroscopic model starting from a well-established model at the cell scale (see Chapter 3).

Chapter 2

Numerical study of existing phenomenological models of tissue electroporation

This chapter is the result of a collaboration with the bioelectromagnetism lab Ampère (Lyon, France).

Although a single-cell model is a valuable tool to study the basic mechanisms of electroporation, it cannot describe tissue electroporation. For efficient *in vivo* tissue electroporation, the electric field distribution, which depends on electrode geometry, position, and electrical properties of the sample, is crucial [66]. The electrical properties of biological tissue (conductivity and permitivity) change once the tissue is permeabilized and the electric field distribution is changed. The largest part of these changes is attributed to increased membrane conductivity due to electroporation. In a medical framework, it is important to generate minimal damage to the healthy tissue surrounding a tumor tissue, so it is desirable the use of mathematical models and computational tools that allow the simulation of the distribution of electric field applied to create an appropriate treatment strategy. We present here a non exhaustive review of models of tissue electroporation in order to compare their features.

2.1 Experimental framework

2.1.1 Experimental set-up

We first present a typical experimental set up of tissue electroporation [110]: 100 μs pulses are delivered using needles inserted perpendicularly to the tissue surface. Different applied pulse amplitudes are considered.

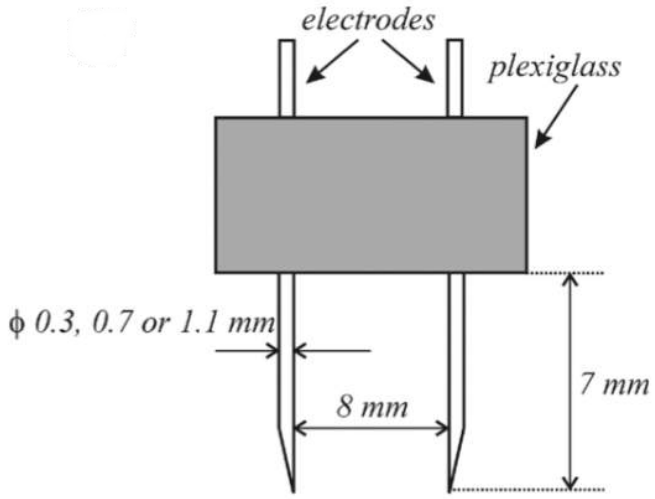

Figure 2.1: Needle electrodes used in experiments of [110].

2.1.2 Data available

The area of reversibly permeabilized tissue can be determined by means of the bleomycin method. Experiment description and details of the method can be found in [81]. When irreversible electroporation is performed on cell cultures, the electroporated zone (ablation zone) can be imaged using green fluorescent protein for living cells and red fluorescent protein for dead cells (see Figure 2.2) [107]. Nevertheless, this type of data is not the most reliable to perform model calibration, especially when *in vivo* experiments are considered.

The applied voltage and resulting current can be acquired much more easily using high voltage and current probes respectively with an oscilloscope. The

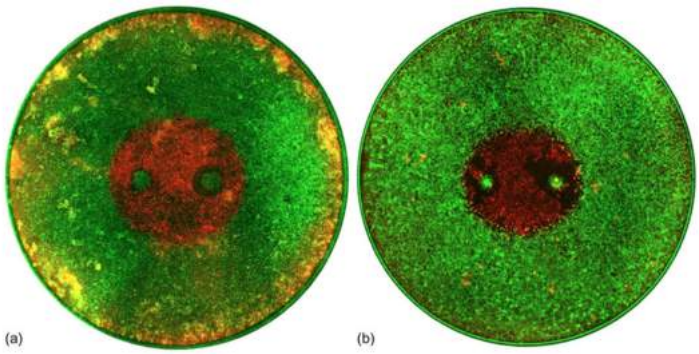

Figure 2.2: Visualization of the area of tissue irreversibly electroporated. Cells grown in **(a)** 3D Matrigel or **(b)** 2D media-only culture conditions [107].

chronograms of current thus obtained give valuable information on the dynamics of the electroporation process. Indeed, in Figure 2.3 a typical behavior of the current signal when a rectangular electroporating pulse is applied to a living tissue is presented. This example does not correspond to an actual experiment but it shows the main features that can be noticed in experimental measurements in tissues [37]: after an initial peak due to cell membrane charging, current increases exponentially and afterwards it seems to increase much slower in a linear fashion or it stops increasing. The initial abrupt change in conductance is probably the manifestation of the immediate and reversible membrane permeabilization. The later exponential rise shows that membrane conductance increases slowly and moderately during the pulse. The gray line in Figure 2.3 shows what would be the behavior of the tissue in case the electroporation phenomenon did not exist [106]. Thus, observations made of a typical recording of current during the application of a pulse underline the necessity to develop a time-dependent model in order to provide accurate prediction of the electric current in the treated tissue throughout the whole duration of applied electric pulses.

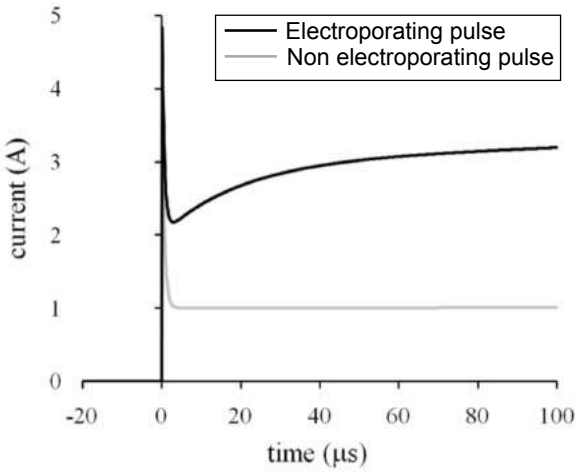

Figure 2.3: Typical recording (black line) of current during the application of a 100 μs pulse. The gray line indicates what would be the response if electroporation did not occur [106].

2.2 Different approaches to model electroporation at the tissue scale

2.2.1 Statement of the problem

Given the geometry presented in Figure 2.1, all models of tissue electroporation presented next will be stated in a closed domain Ω, corresponding to the piece of tissue on which electroporation is applied. Those models always feature an equation on the electric potential φ. To close the problem, boundary conditions must be stated on φ. On the outer surfaces of the domain $\partial\Omega$, a Neumann homogeneous boundary condition is applied whereas a Dirichlet boundary condition is applied on each electrode E^+ and E^-.

$$\begin{cases} \varphi = U(t) \text{ on } E^+, & \text{(2.1a)} \\ \varphi = 0 \text{ on } E^-, & \text{(2.1b)} \\ \partial_n \varphi = 0 \text{ on } \partial\Omega. & \text{(2.1c)} \end{cases}$$

We now present two different approaches to model tissue electroporation. The

first one is based on the assumption that the tissue is made of a single phase through which a single conductive current density is assumed to flow (see section 2.2.2). The second approach assumes that two kinds of current densities coexist in the tissue: one flows through the cells and the other one flows through the extracellular medium. This assumption is made in an attempt to take into account the biphasic biological composition of the tissue (see section 2.2.3).

The purpose of this chapter is to carry out a numerical comparison of different models of tissue electroporation in the same configuration.

2.2.2 Monophasic models

2.2.2.1 Static model

Steady-state model of electroporation. In most cases, the model used to simulate the electric field distribution at the tissue scale is based on a static hypothesis, where the tissue is described as a conductive medium [110] :

$$\nabla \cdot (\sigma \nabla \varphi) = 0 \quad \text{in } \Omega, \tag{2.2}$$

where σ and φ are the tissue conductivity and the electric potential, respectively. This type of model describes only the steady-state that appears once the process of electroporation is completed. First, a simple Laplace equation is considered, together with two types of boundary conditions (Dirichlet on the electrodes and Neumann on the outer boundaries), to describe the electric field inside the tissue [78, 81]. It corresponds to taking the tissue conductivity σ as a constant. The spatial distribution of the electric field is then correlated with the tissue necrosis observed when irreversible electroporation is performed [81]. However, as electroporation leads to an increase of cell membrane permeability when the transmembrane potential (TMP) exceeds a certain threshold, and therefore an increase of the membrane conductivity, a nonlinear model of the tissue conductivity $\sigma(\nabla\varphi)$ with respect to the local electric field $\nabla\varphi$ is later introduced. Different kinds of models have been considered but the most suitable ones rely on sigmoid functions

[28, 110]. For instance [28]

$$\sigma(\nabla\varphi) = \sigma_{min} + (\sigma_{max} - \sigma_{min}) \left(\frac{1 + \tanh(k(|\nabla\varphi| - E_{th}))}{2} \right) \tag{2.3}$$

σ_{min} and σ_{max} are respectively, the conductivities for safe and electropermeabilized tissues, E_{th} is the electric field threshold and k is a fitting coefficient that modulates the transition to the electroporation.

Equation (2.2) is based on a static hypothese. In the literature, numerous studies use this static approximation [110, 28, 106], includind for treatment planning [131, 82, 44, 42].

Well-posedness. Let Ω be an open closed set of $\mathbb{R}^n$. Let f belong to $L^2(\Omega)$ and $\sigma : \mathbb{R} \to \mathbb{R}$ be such that

$$\left.\begin{array}{l} \sigma \text{ is continuous on } \mathbb{R}, \\ s \mapsto \sigma(s) \text{ is even on } \mathbb{R}, \\ 0 < \sigma_{min} \leq \sigma(s) \leq \sigma_{max}, \\ \sigma \text{ is increasing on } \mathbb{R}^+, \\ \lim\limits_{s \to +\infty} \sigma(s) = \sigma_{max}. \end{array}\right\} \tag{2.4}$$

The goal of this paragraph is to show that the boundary value problem (2.5) is well-posed.

$$\begin{cases} \nabla \cdot (\sigma(|\nabla\varphi|)\nabla\varphi) = f, & \text{in } \Omega \quad (2.5a) \\ \varphi_{|\partial\Omega} = 0, & \text{on } \partial\Omega. \quad (2.5b) \end{cases}$$

Remark 2. In order to use classical results in the proof and to avoid some technicalities, boundary value problem (2.5) features a volumic source term f and homogeneous Dirichlet conditions. Let us remark that solving (2.5) does not exactly correspond to solving equation (2.2) associated with non homogeneous Dirichlet boundary conditions on the electrodes (such as (2.1)).

Definition 3. *We define the functional J as the operator from $H_0^1(\Omega)$ to $\mathbb{R}$ such*

that

$$\forall u \in H_0^1(\Omega),\ J(u) := \int_\Omega \int_0^{|\nabla u|(x)} s\sigma(s)\, ds dx - \int_\Omega f u\, dx. \tag{2.6}$$

- J is well defined: Let $u \in H_0^1(\Omega)$.

$$|J(u)| \leq \frac{1+\sigma_{max}}{2} \|\nabla u\|^2_{L^2(\Omega)} + \|f\|_{L^2(\Omega)} \|u\|_{L^2(\Omega)} < +\infty,$$

  so J is well defined.

- J is differentiable: Let us take $(u,h) \in (H_0^1(\Omega))^2$.

$$\begin{aligned} J(u+h) - J(u) &= \int_\Omega \int_{|\nabla u|(x)}^{|\nabla (u+h)|(x)} s\sigma(s)\, ds dx - \int_\Omega fh\, dx \\ &= \int_\Omega \sigma(|\nabla u|)\nabla u \cdot \nabla h\, dx - \int_\Omega fh\, dx + o(h). \end{aligned}$$

  This guarantees that J is differentiable and that

$$J'(u)\cdot h = \int_\Omega \sigma(|\nabla u|)\nabla u \cdot \nabla h\, dx - \int_\Omega fh\, dx. \tag{2.7}$$

- J is strictly convex: we show that J' is monotonous, meaning

$$(J'(u) - J'(v), u - v) \geq 0,\ \ \forall (u,v) \in (H_0^1(\Omega))^2. \tag{2.8}$$

  First remark that

$$\begin{aligned} (J'(u) - J'(v), u - v) &= \int_\Omega \sigma(|\nabla u|)|\nabla u|^2\, dx - \int_\Omega \sigma(|\nabla u|)\nabla u \cdot \nabla v\, dx \\ &\quad - \int_\Omega \sigma(|\nabla v|)\nabla u \cdot \nabla v\, dx + \int_\Omega \sigma(|\nabla v|)|\nabla v|^2\, dx, \\ &= \int_\Omega \Big(\sigma(|\nabla u|)\nabla u - \sigma(|\nabla v|)\nabla v\Big) \cdot \nabla (u-v)\, dx. \end{aligned}$$

Denoting $U = \nabla u$ and $V = \nabla v$, we can write

$$
\begin{aligned}
(\sigma(|U|)U - \sigma(V)V) \cdot (U - V) &= \sum_{i=1}^{n} (\sigma(|U|)U_i - \sigma(V)V_i) \times (U_i - V_i) \\
&= \sum_{i=1}^{n} \sigma(|U|)U_i^2 + \sigma(V)V_i^2 - (\sigma(|U|) + \sigma(|V|))U_iV_i, \\
&\geq \sum_{i=1}^{n} \sigma(|U|)U_i^2 + \sigma(V)V_i^2 - \frac{\sigma(|U|) + \sigma(|V|)}{2}(U_i^2 + V_i^2), \\
&= \sum_{i=1}^{n} \frac{\sigma(|U|) - \sigma(|V|)}{2}(U_i^2 - V_i^2), \\
&= \frac{\sigma(|U|) - \sigma(|V|)}{2}(|U|^2 - |V|^2), \\
&= \frac{|U| + |V|}{2}(\sigma(|U|) - \sigma(|V|))(|U| - |V|) \geq 0,
\end{aligned}
$$

as σ is an increasing function. Thus (2.8) is satisfied, and J is convex.

- $\lim J(u) = +\infty$ when $\|u\|_{H_0^1(\Omega)} \to +\infty$: Let $u \in H_0^1(\Omega)$ and $\alpha > 0$ be a positive constant.

$$
\begin{aligned}
J(u) &\geq \frac{1 + \sigma_{min}}{2} \|\nabla u\|_{L^2(\Omega)}^2 - \int_\Omega f u \, dx, \\
&\geq \frac{1 + \sigma_{min}}{2} \|\nabla u\|_{L^2(\Omega)}^2 - \frac{\alpha}{2} \|u\|_{L^2(\Omega)}^2 - \frac{1}{2\alpha} \|f\|_{L^2(\Omega)}^2, \text{ using Young's inequality,} \\
&\geq \left(\frac{1 + \sigma_{min}}{2} C - \frac{\alpha}{2} \right) \|u\|_{L^2(\Omega)}^2 - \frac{1}{2\alpha} \|f\|_{L^2(\Omega)}^2, \text{ using Poincaré's inequality.}
\end{aligned}
$$

Choosing α such that $C(1 + \sigma_{min}) - \alpha > 0$, we obtain that $\lim J(u) = +\infty$ when $\|u\|_{H_0^1(\Omega)} \to +\infty$.

J is a differentiable convex functional verifying $\lim J(u) = +\infty$ when $\|u\|_{H_0^1(\Omega)} \to +\infty$, which guarantees that there exists an unique $\varphi \in H_0^1(\Omega)$ that minimizes J, i.e. such that

$$
J'(\varphi) \cdot h = \int_\Omega \sigma(|\nabla \varphi|) \nabla \varphi \cdot \nabla h \, dx - \int_\Omega f h \, dx = 0 \quad \forall h \in H_0^1(\Omega). \tag{2.9}
$$

As (2.9) is exactly the variational formulation associated with the boundary value problem (2.5), we have shown that problem (2.5) have an unique solution $\varphi \in H_0^1(\Omega)$.

Toward dynamic models. The static approach presents critical limitations since electroporation is a complex dynamic phenomenon during which the physiology of the membrane as well as the composition of the intra and extracellular media change during and after pulse delivery [85]. A static model cannot describe the dynamical behavior of the current signal measured during a pulse either. In the literature, a very few attempts exist to take the time dependent effects of tissue electroporation into account. In sections 2.2.2.2 and 2.2.3, we present two different phenomenological approaches which claim to reproduce some of these time effects. It is worth noticing that an other dynamic model of tissue electroporation, constructed using inverse analysis, is presented in [71]. We did not include the numerical study of this model in the comparison presented in this chapter. From now on, we do not investigate the well-posedness of the different boundary value problems stated. Each would necessit a full mathematical analysis, which is not the goal of the following study.

2.2.2.2 A first dynamic model of tissue conductivity

As previously stated in section 1.4, a phenomenological model was proposed in [67] in order to describe the dynamic related to the membrane alteration during cell electroporation. To this end, undimensional functions are introduced to model the degree of poration or permeabilization of the cell. Inspired by this approach, but reducing the study to the dynamic response of the tissue during the application of the pulse voltage, one can introduce two functions X_1 and X_2, which vary between 0 and 1 and are ruled by different dynamics: X_1 is related to the process for the pore creation while X_2 reports the growing of the electroporation once it has been initialized. In those conditions, the distribution of electric field is given by:

$$\nabla \cdot (\sigma(t, \nabla\varphi) \cdot \nabla\varphi) = 0 \quad \text{in } \Omega. \tag{2.10}$$

The membrane conductivity is given by:

$$\sigma(t, \nabla\varphi) = \sigma_0 + \sigma_1 X_1(t, \nabla\varphi) + \sigma_2 X_2(t, X_1), \tag{2.11}$$

where σ_0, σ_1 and σ_2 are the equivalent conductivities related respectively to an unpulsed tissue and a deeply electroporated tissue once the dynamics are complete. Concerning the pore creation, the dynamic for X_1 satisfies the following equation:

$$\frac{dX_1}{dt} = \frac{1}{\tau_1}(\beta(\nabla\varphi) - X_1), \text{ with } \beta(\nabla\varphi) = \frac{1 + \tanh(k(|\nabla\varphi| - E_{th}))}{2}, \tag{2.12}$$

where the characteristic time τ_1 is introduced to account for the increase of the poration creation. The threshold effect is modeled by the sigmoid function β in a similar way as equation (2.3). The appearance of pores in the membrane induces an alteration of the membrane that goes on growing during the application of the pulse voltage. The dynamic of this second phenomenum is governed by the following equation:

$$\frac{dX_2}{dt} = \frac{1}{\tau_2}(X_1 - X_2), \tag{2.13}$$

where the characteristic time τ_2 is introduced to account for the increase of the membrane alteration.

2.2.3 Biphasic model

The idea of introducing a phenomenological model of dynamic conductivity based on [67, 72] was actually introduced in [85, 123] with an important addition compared to what we just presented in section 2.2.2.2. Whereas a single conductive current density is assumed in equation (2.10), two kinds of current densities are considered in the dynamic modeling: one flows through the cells and the other one flows through the extracellular medium. Namely, a dynamic equation on the current flowing through one cell is introduced considering equivalent circuit laws at the cell level and this equation is translated in terms of electric field and macroscopic current density introducing the dimensions of the sample. This addition is made in a attempt to reproduce the capacitive current peak observed

in the experiments (see Figure 2.3). In those conditions, the distribution of electric field is now given by:

$$\nabla \cdot \left(\sigma_e \cdot \nabla\varphi + \overrightarrow{\mathbf{J}}_{cells}(t, \nabla\varphi) \right) = 0 \quad \text{in } \Omega, \tag{2.14}$$

where σ_e is the equivalent conductivity at the tissue scale for the extracellular medium and $\overrightarrow{\mathbf{J}}_{cells}$ is the current density flowing through the cells, governed by the following first order differential equation

$$\left(1 + \frac{\sigma_m(t, v_m)}{\sigma_c} \right) \overrightarrow{\mathbf{J}}_{cells} + \frac{\varepsilon_m}{\sigma_c} \frac{d\overrightarrow{\mathbf{J}}_{cells}}{dt} = \sigma_m(t, v_m)\nabla\varphi + \varepsilon_m \frac{d\nabla\varphi}{dt}, \tag{2.15}$$

where σ_c and σ_m are the equivalent conductivity at the tissue scale for the intracellular medium and the membrane, respectively and ε_m is the equivalent permittivity of the membrane at the tissue scale. The equivalent membrane conductivity σ_m is affected by the amplitude of the homogenised electric field around the membrane. The homogenised electric field $\mathbf{E}_m$ can be computed using the local electric field defined at the tissue scale as

$$\mathbf{E}_m(t, x) = \frac{1}{2} \left(\nabla\varphi(t, x) - \frac{\overrightarrow{\mathbf{J}}_{cells}(t, x)}{\sigma_c} \right) \quad \text{at any time } t \text{ and at any point } x \in \Omega. \tag{2.16}$$

The amplitude of the transmembrane voltage at the tissue scale, denoted v_m, is then defined as

$$v_m(t, x) = d_{cell} |\mathbf{E}_m(t, x)| \quad \text{at any time } t \text{ and at any point } x \in \Omega. \tag{2.17}$$

$\sigma_m(t, v_m)$ is obtained using phenomenological laws substantially similar to those introduced in section 2.2.2.2:

$$\sigma_m(t, v_m) = \sigma_{m0} + \sigma_{m1} X_1(t, v_m) + \sigma_{m2} X_2(t, X_1), \tag{2.18}$$

where σ_{m0}, σ_{m1} and σ_{m2} are the equivalent membrane conductivities related respectively to an unpulsed tissue and a deeply electroporated tissue once the dynamics

are complete. Concerning the pore creation, the dynamic for the function X_1, which varies between 0 and 1, satisfies the following equation:

$$\frac{dX_1}{dt} = \begin{cases} \frac{\beta_1(v_m)-X_1}{\tau_1}, & \text{if } \beta_1(\nabla\varphi) \geq X_1, \\ 0, & \text{else.} \end{cases} \tag{2.19}$$

where τ_1 is the the characteristic time for the increase of the pores creation. The threshold effect is modeled by the sigmoid function β_1 in a similar way as in equations (2.3) and (2.12):

$$\beta_1(v_m) = \frac{1+\tanh(k_1(v_m - V_{th}))}{2}, \tag{2.20}$$

except that the argument in the hyperbolic tangent is expressed in terms of amplitude of the transmembrane voltage v_m. Concerning the second dynamic, the function X_2 verifies a dynamic similar to the one introduced in (2.13)

$$\frac{dX_2}{dt} = \begin{cases} \frac{\beta_2(X_1)-X_2}{\tau_2}, & \text{if } \beta_2(X_1) \geq X_2, \\ 0, & \text{else.} \end{cases} \tag{2.21}$$

except here a sigmoid function β_2 is introduced, with a threshold effect controlled by parameter X_{th}, which is not especially sought:

$$\beta_2(X_1) = \frac{1+\tanh(k_2(X_1 - X_{th}))}{2}. \tag{2.22}$$

Equivalent tissue conductivity. Let us remark that σ_m does not represent the tissue conductivity. A steady-state approximation of equation (2.15) leads to solving the following equivalent form of equation (2.14):

$$\nabla \cdot \left(\left(\sigma_e + \frac{\sigma_c \sigma_m}{\sigma_c + \sigma_m} \right) \cdot \nabla\varphi \right) = 0 \quad \text{in } \Omega, \tag{2.23}$$

An equivalent tissue conductivity can thus be defined as

$$\sigma_{eq} = \sigma_e + \frac{\sigma_c \sigma_m}{\sigma_c + \sigma_m}. \tag{2.24}$$

Remark 3. Formula (2.24) implies that at any time t and at any point $x \in \Omega$,

$$\sigma_e \leq \sigma_{eq}(t,x) \leq \sigma_e + \sigma_c.$$

The tissue conductivity stays bounded, and cannot take high values (as it cannot overpass $\sigma_e + \sigma_c$) whereas when the membrane of one cell is permeabilized, its conductivity can take very high values (10^6 S/m). This difference between permeabilized membrane conductivity values and electroporated tissue conductivity values has been observed experimentally.

Let us finish this section by noting that in the three modeling approaches presented, none takes the Joule effect into consideration. Indeed, the application of high-voltage pulses to biological tissue causes not only electroporation but also significant heating and can result in thermal damage to the tissues. The presented models do not take heating into account as electroporation, even when it is irreversible, is not necessarily accompanied by thermal damage in the treated region [40]. Nevertheless, thermal damage can appear in specific regions where the electric field is too large, for instance, at the edges of the electrodes.

2.3 Numerical methods

2.3.0.1 Computational model.

2D configuration. To proceed to a valid comparison between models, the first step is to choose a computational domain which must be the same for each simulation and each model considered, to be related to a single set of experiments. We chose to use the computational domain presented in [85, 123], in order to use both the experimental data and the parameters of [85, 123] in our simulations. This 2D domain is in relation with the experimental set up presented in Figure 2.1. As the length of the needles is very large compared to the diameter of the needles, the numerical problem can be reduced to a 2D problem. To model a piece of tissue, a square with dimensions 32 mm $\times$ 32 mm is defined. As previously stated, Neumann homogeneous boundary conditions are set on the outer bound-

ary of this domain, and the potential is forced on the boundary of the electrodes, which are positioned in the middle of the domain. Because of the symmetries, the computational domain can be reduced to a quarter of the initial geometry with the proper boundary conditions set (2.25) on the symmetric planes $\mathcal{B}_1$ and $\mathcal{B}_2$.

$$\begin{cases} \varphi = 0 \text{ on } \mathcal{B}_1, & \text{(2.25a)} \\ \partial_n \varphi = 0 \text{ on } \mathcal{B}_2. & \text{(2.25b)} \end{cases}$$

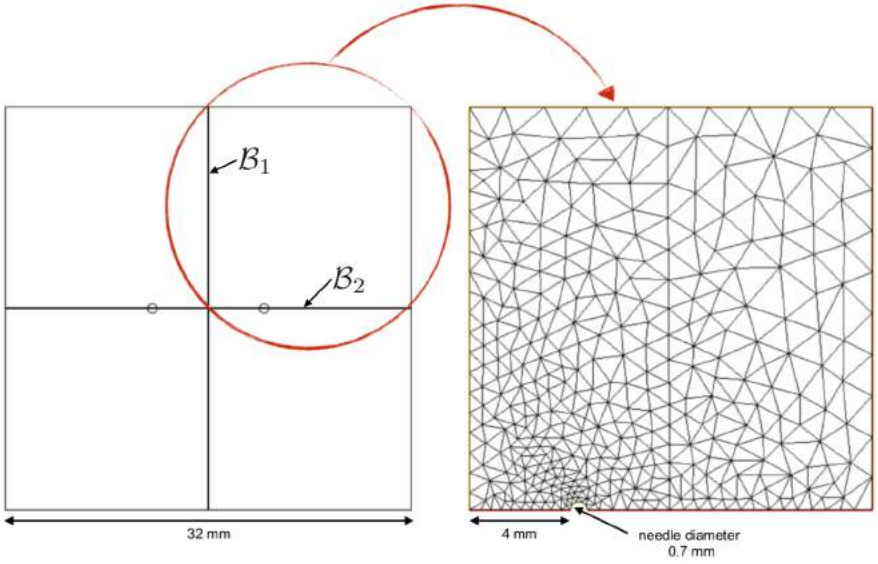

Figure 2.4: 2D full domain and final computational mesh obtained considering the symmetry of the problem.

A discretization of the variables in the spatial domain is made using the finite element method. Problem geometry was meshed (see Figure 2.4) and simulations of electroporation are performed using Freefem++ [61]. To solve the elliptic equations (2.2), (2.10) and (2.14), a discretization of the variables in the spatial domain is made using the finite element method with Freefem++ [61]. For the static model, the nonlinear model is solved using a modified fixed point method (see section 2.3.0.2). The discretization in time, when needed, is performed using a Runge Kutta scheme of order 4 to solve equations (2.12), (2.13), (2.15), (2.19) and (2.21).

3D configuration. Another possibility is to use a 3D domain for the simulations, to account for the complete geometry of the experiment. To this end, we considered to use the computational domain presented in [71]. To model a piece of tissue, a box with dimensions 30 mm × 20 mm × 20 mm is defined. As always, Neumann homogeneous boundary conditions are set on the outer boundary of this domain, and the potential is forced on the boundary of the electrodes, which are positioned in the middle of the domain, the tip 5 mm above the box boundary.

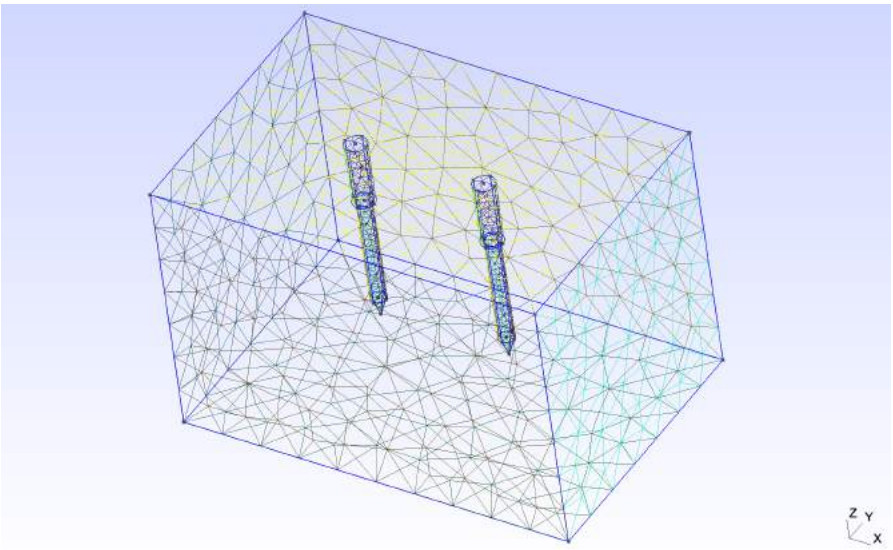

Figure 2.5: Numerical set-up of the 3D experiment.

Again, a discretization of the variables in the spatial domain is made using the finite element method. Problem geometry is meshed with the GMSH mesher [31] (see Figure 2.5) and the resulting mesh is imported to Freefem++ [61] in order to perform simulations of electroporation.

Choice of elements. P^2 elements are the natural choice of function space to apply the finite element method to our problems since the nonlinearity involves the gradient of φ. Nevertheless, we also did simuations with P^1 elements for the sake of comparison with standard numerical studies in the literature.

2.3.0.2 Resolution of the nonlinear problem.

To solve the nonlinear problem (2.2) with σ as in (2.3), the most straightforward approach is to use a fixed point algorithm:

- Initialization:

- Solve $\nabla \cdot (\sigma_{min} \nabla \varphi^0) = 0$ in Ω + boundary conditions.

- Loop: while $n < N_{max}$ do

- Compute $\sigma(\nabla \varphi^n) = \sigma_{min} + (\sigma_{max} - \sigma_{min}) \left(\frac{1+\tanh(k(|\nabla \varphi^n| - E_{th}))}{2} \right)$,

- Solve $\nabla \cdot (\sigma(\nabla \varphi^n) \nabla \varphi^{n+1}) = 0$ in Ω + boundary conditions.

Nevertheless, this scheme leads to a solution oscillating between two potential values, when the sigmoid function σ is too stiff: indeed, the conductivity can go directly from its initial value σ_{min} to its maximum value σ_{max} without stabilizing at an intermediate value (see Figure 2.6). This issue was addressed in [28], where a modified fixed point method is suggested to overcome this convergence problem. We reproduce here this method in a variational from, adapted for the use of the software FreeFem++ [61].

- The problem is: solve $\nabla \cdot (\sigma(\nabla \varphi) \nabla \varphi) = 0$ + Dirichlet boundary conditions on the electrodes and Neumann boundary condition on the outer boundaries. In matricial form, this is equivalent to solving the nonlinear system $A(\varphi)\varphi = b$.

- Initialization:

- Solve $\nabla \cdot (\sigma_{min} \nabla \varphi^0) = 0$ in Ω + Dirichlet boundary conditions on the electrodes and Neumann boundary condition on the outer boundaries.

- $K = 1$, $\|r_{old}\| = +\infty$.

- Loop: while $\|r_{old}\| > \|r\|$

- Compute $\sigma(\nabla \varphi^n) = \sigma_{min} + (\sigma_{max} - \sigma_{min}) \left(\frac{1+\tanh(k(|\nabla \varphi^n| - E_{th}))}{2} \right)$,

- Get the FE matrix A and compute $r = b - A(\varphi^n)\varphi^n$.

- If $\|r\| > \|r_{old}\|$, take $K = K/2$.

- Solve $\nabla \cdot (\sigma(\nabla\varphi^n)\nabla(\varphi^{n+1} + (1-K)\varphi^n)) = 0$ in Ω + Dirichlet boundary conditions on the electrodes and Neumann boundary condition on the outer boundaries.

For the two dynamic models, the choice of a sufficiently small time step can free us from applying a fixed point algorithm (see [72]).

2.3.0.3 How to compute the numerical electric current?

The numerical current I is obtained when summing the total current density $\overrightarrow{j}$ over the surface of one electrode. Naming this electrode E^+, we can state that

$$I = \int_{E^+} \overrightarrow{j}_{|_{E^+}} \cdot \overrightarrow{n}_{|_{E^+}} dS \tag{2.26}$$

Compute I directly with the surface integral. With $Freefem++$, it is possible to compute I using directly formula (2.26) and surface integrals (1D integral in 2D, with a correction to relate to the 3D experiments, and 2D integral in 3D).

```
I = int1d(Sh,E+)( (N.x*J_x + N.y*J_y)*lenghtE ) in 2D
or
I = int2d(Sh,E+)( N.x*J_x + N.y*J_y + N.z*J_z ) in 3D
```

The drawback of such a calculus is the importance of the mesh precision around the electrodes that greatly influences the output. This is already the case with a simple Laplace equation:

$$\begin{aligned} \Delta\varphi &= 0, && \text{in } \Omega, \\ \varphi &= U^+, && \text{on } E^+, \\ \partial_n\varphi &= 0, && \text{on } \partial\Omega. \end{aligned}$$

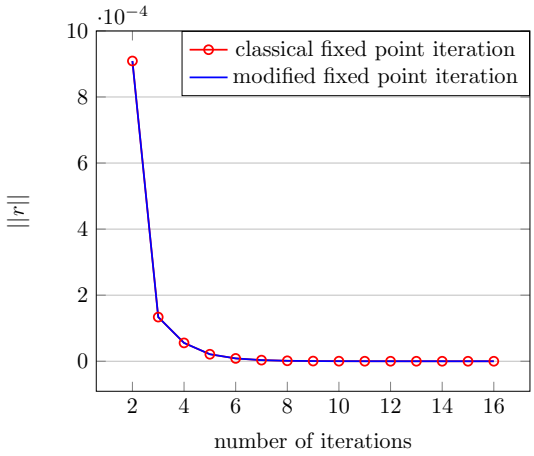

(a) Voltage applied = 375 V, $k = 10^{-5}$

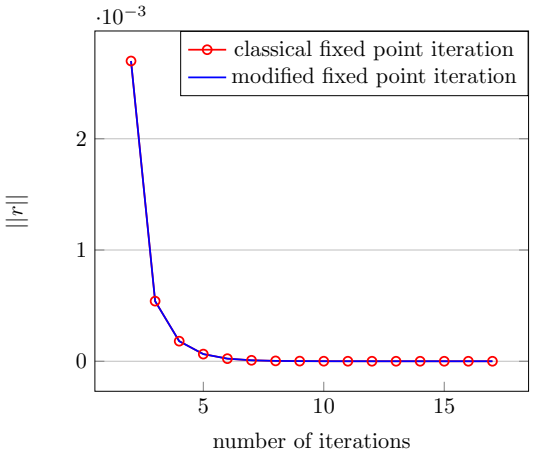

(b) Voltage applied = 875 V, $k = 10^{-5}$

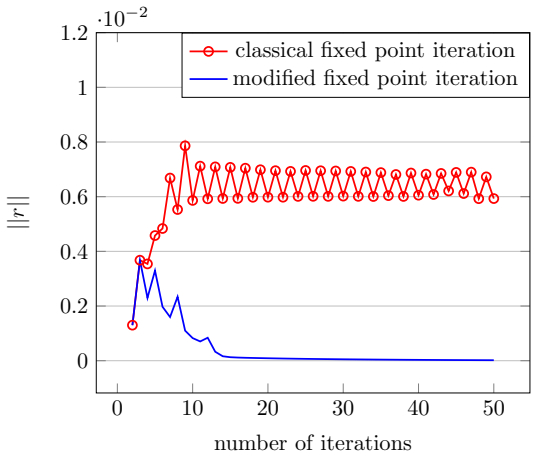

(c) Voltage applied = 375 V, $k = 0.0006$

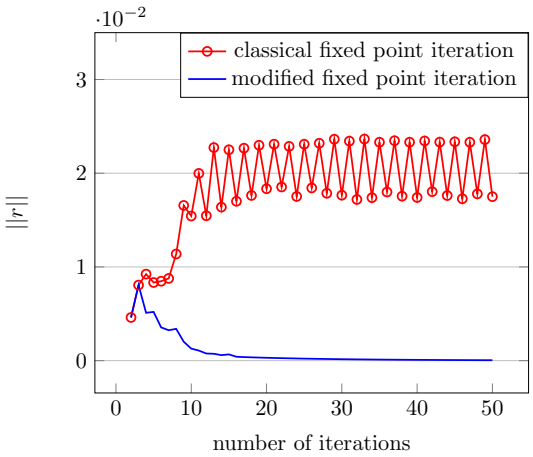

(d) Voltage applied = 875 V, $k = 0.0006$

Figure 2.6: Convergence study using the classical fixed point iterations and the modified one to solve the nonlinear problem (2.2) for two different voltages: **(a), (c)** 375 V, below E_{th} and **(b), (d)** 875 V, above E_{th}, and for two different values of k: **(a), (b)** $k = 10^{-5}$ and **(c), (d)** $k = 0.0006$.

In 2D, the following boundary conditions are added on the symmetric planes $\mathcal{B}_1$ and $\mathcal{B}_2$:

$$\begin{aligned} \varphi &= 0, && \text{on } \mathcal{B}_1, \\ \partial_n \varphi &= 0, && \text{on } \mathcal{B}_2, \end{aligned}$$

while in 3D a Dirichlet boundary condition is added on E^-:

$$\varphi = 0, \text{ on } E^-.$$

This corresponds to solving equation (2.2) in the linear case ($\overrightarrow{j} = \sigma\nabla\varphi$ with $\sigma = 1$). Let us consider the quantity

$$I = \int_{E^+} \partial_n\varphi \, dS.$$

In Figure 2.7, I is displayed for different 2D mesh precisions from 5 points meshing the half-electrode surface to 50 points. A preoccupying feature is that it seems that a very high precision around the electrode is needed to achieve convergence.

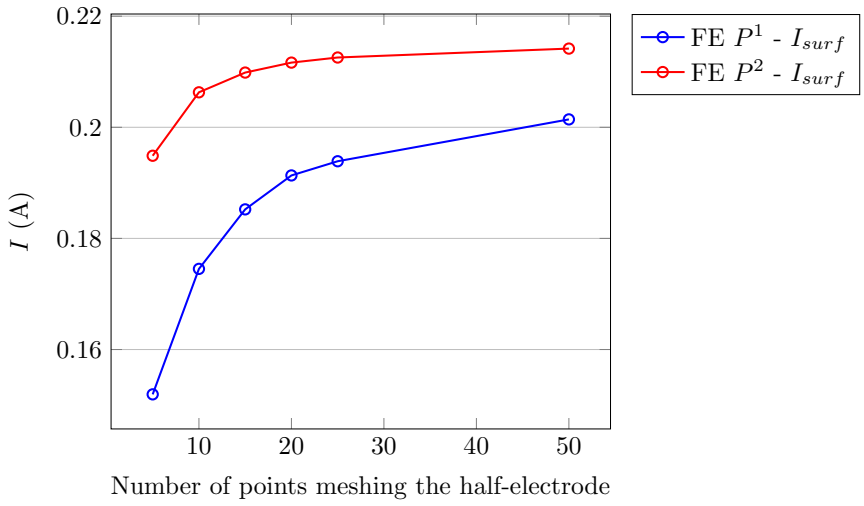

Figure 2.7: Value of quantity I for different 2D mesh precisions from 5 points meshing the (half-)electrode surface to 50 using both P_1 and P_2 elements.

In 3D, the exact same type of behavior can be observed when solving a simple Laplace equation. When solving the nonlinear static model presented in section 2.2.2.1, one can compute the numerical current for different meshes. Figure 2.8 represents the four different surface meshes that we used to investigate the convergence in space of the numerical scheme. Figure 2.9 presents the simulated currents for all four meshes, computed with both P_1 and P_2 elements.

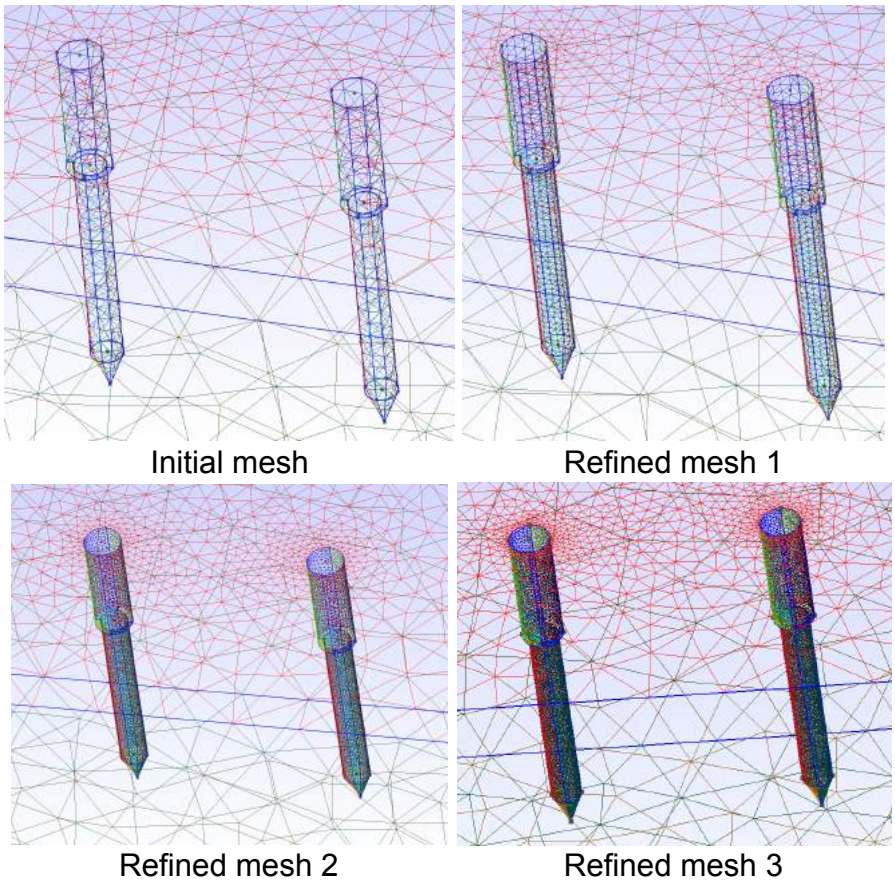

Figure 2.8: Four different meshes are used to investigate the convergence in space of the numerical scheme. The initial mesh (top left) is the one used in [71], provided by the authors.

In Figure 2.9, we can see that the simulated current amplitude increases when refining the mesh, which is the sign that the convergence in space was not completed with the initial mesh. Our machine could not handle a finer mesh than the refined mesh 3 presented in Figure 2.8, so we cannot even be sure that convergence was achieved with P^2 elements and the finer mesh.

Compute I with a volume integral. All models presented in section 2.2 are based on solving, at one point, the following PDE:

$$-\nabla \cdot \overrightarrow{j} = 0 \quad \text{in } \Omega. \tag{2.27}$$

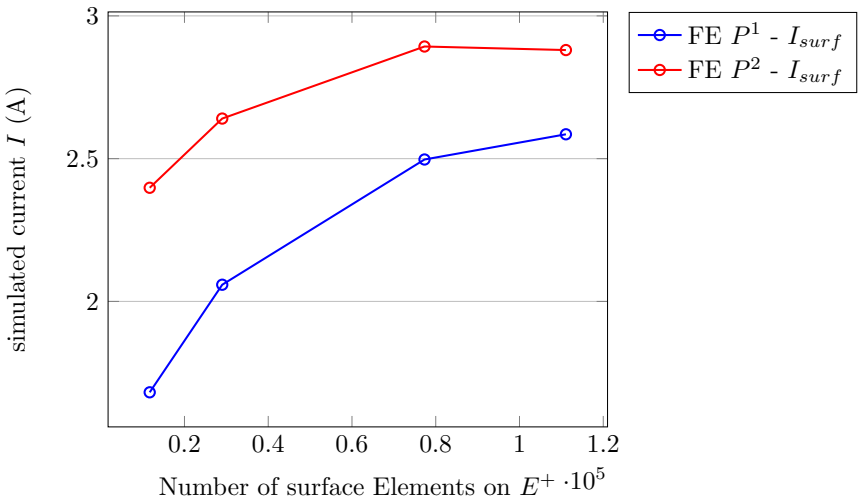

Figure 2.9: Simulated current I computed using a surface integral. I is obtained from the static model of section 2.2.2.1 for the four different meshes presented in Figure 2.8. Both P_1 and P_2 elements are used for comparison.

Multiplying (2.27) by a test function w, integrating on Ω and using Green's formula yields:

$$\int_\Omega \overrightarrow{j} \cdot \nabla w \, dx = \int_{\partial\Omega} \overrightarrow{j} \cdot \overrightarrow{n}_{|\partial\Omega} w \, dS. \tag{2.28}$$

Let us consider the following test function: w is the unique solution of the following Laplace problem

$$\begin{aligned} \Delta w &= 0, && \text{in } \Omega, \\ w &= 1, && \text{on } E^+, \\ \partial_n w &= 0, && \text{on } \partial\Omega. \end{aligned}$$

In 2D, the following boundary conditions are added on the symmetric planes $\mathcal{B}_1$ and $\mathcal{B}_2$:

$$\begin{aligned} w &= 0, && \text{on } \mathcal{B}_1, \\ \partial_n w &= 0, && \text{on } \mathcal{B}_2, \end{aligned}$$

while in 3D a Dirichlet boundary condition is added on E^-:

$$w = 0, \text{ on } E^-.$$

Putting w in (2.28) yields

$$\int_\Omega \overrightarrow{j} \cdot \nabla w \, dx = \int_{E^+} \overrightarrow{j} \cdot \overrightarrow{n}_{|_{E^+}} w \, dS = I. \tag{2.29}$$

Equality (2.29) gives a method to compute the simulated current I using a volume integral instead of a surface integral. The main advantage of this approach is to free oneself from the mesh precision issue precedently raised. In Figure 2.10 are displayed the same quantities I_{surf} displayed in Figure 2.7, with addition of the quantities I_{vol} obtained using a volume integral to compute I in the linear case ($\overrightarrow{j} = \sigma \nabla \varphi$ with $\sigma = 1$):

$$I = \int_\Omega \nabla \varphi \cdot \nabla w \, dx.$$

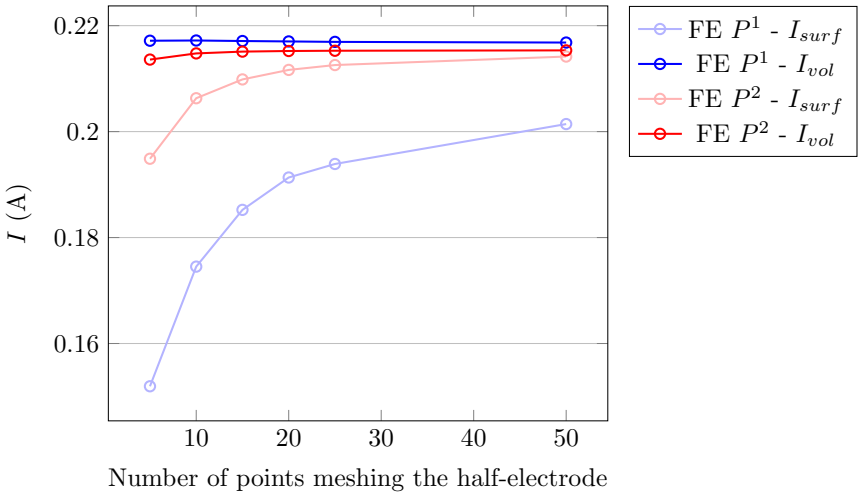

Figure 2.10: Value of quantity I in the linear case ($j = \sigma \nabla \varphi$ with $\sigma = 1$) for different 2D mesh precisions from 5 points meshing the half-electrode surface to 50 using both P_1 and P_2 elements and both surface and volume methods to compute I.

In Figure 2.11 are displayed the simulated currents computed using the nonlin-

ear static model of section 2.2.2.1 for the four 3D meshes of Figure 2.8, with both P_1 and P_2 elements, and with I calculated via a surface integral or a volumic one.

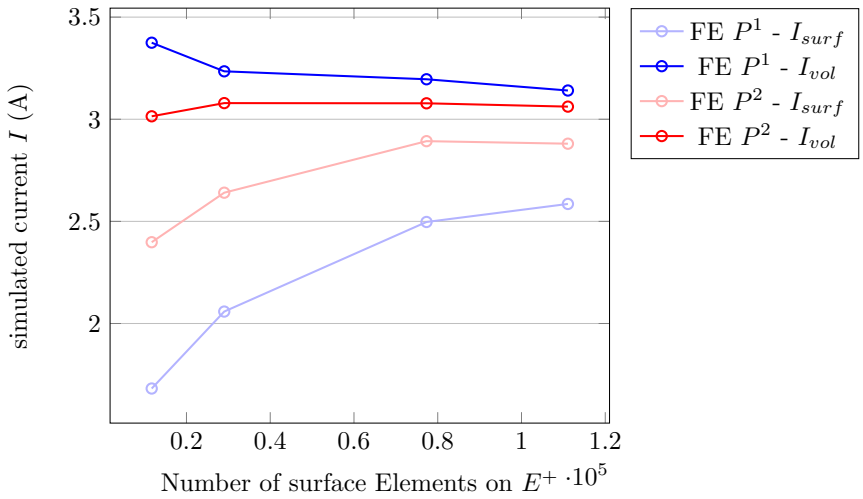

Figure 2.11: Simulated current computed using the static model of section 2.2.2.1 for the four different meshes presented in Figure 2.8. Both P_1 and P_2 elements are used. The current is computed with either the surface or volume method for comparison.

It appears that the volume method, used with P^2 elements, gives right away the limit value of the surfacic method even for a looser mesh, which results in a very important gain when considering the computational cost of the simulation, especially in 3D. We believe this is the right configuration to use in order to compute the simulated current, and used it to compute the different currents of each model presented in section 2.2.

2.4 Numerical comparison of 3 models of tissue electroporation with experimental data

2.4.0.1 Numerical results obtained in 2D for the static model.

As presented in section 2.3.0.2, the nonlinear equation (2.2) is solved using a modified fixed point iteration. Numerical simulations were done using the Finite

Element software FreeFem++ [61] on the 2D-mesh featured in Figure 2.4. The parameters used for the simulations are those presented in Table 2.1. The simulated currents are calculated with the volumic method (see section 2.3.0.3). Figure 2.12 shows the simulated currents flowing through the needles when a 100 μs pulse is applied between the needles, with different nominal electric fields (375 V/cm, 625 V/cm, 875 V/cm, 1125 V/cm, 1375 V/cm), for electrodes of diameter 0.7 mm. As we are working on a steady-state hypothesis, the current is logically constant throughout the pulse.

Table 2.1: Parameters of the simulations for the static model of tissue electroporation.

Parameter	Symbol	Value	Unit
Initial conductivity	σ_{min}	0.065	S/m
Final conductivity	σ_{max}	0.39	S/m
Electric field threshold	E_{th}	472	V/cm
Parameter in the sigmoid	k	0.0006	

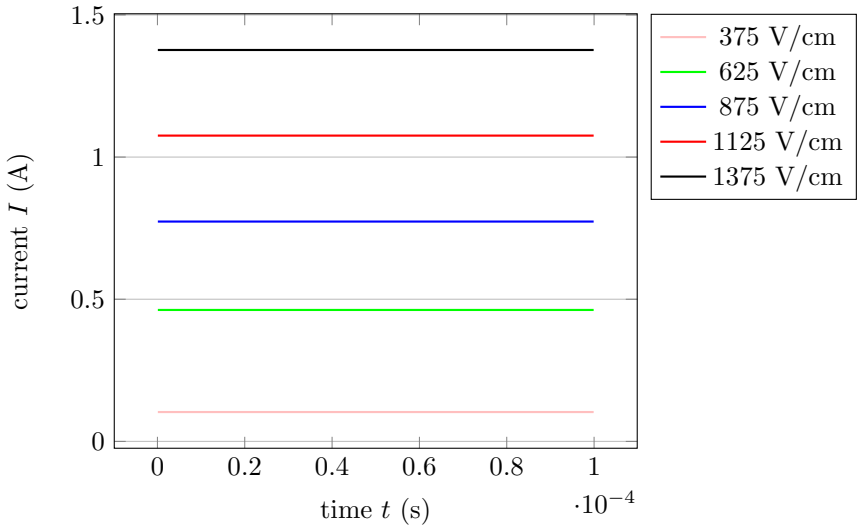

Figure 2.12: Simulated current of the static model for five different voltage applied.

The tissue conductivity shows where the tissue is electroporated. Figure 2.21 shows the spatial distribution of the simulated tissue conductivity σ for all different

voltages applied.

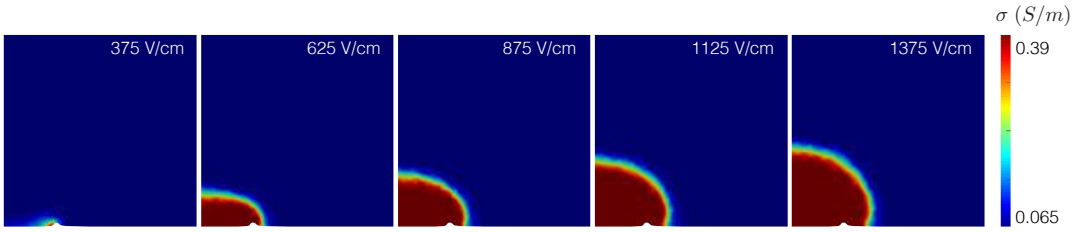

Figure 2.13: Spatial distribution of the conductivity σ with the static model.

In Figure 2.14 is displayed the value of σ locally in the middle point between the two electrodes for all different fields applied. Two behaviors are observed: below the electroporation threshold, the conductivity is constant (equal to σ_{min}) whereas above the electroporation threshold, the conductivity is constant (equal to σ_{max}). There is no distinction in the conductivity value between the four electric fields which are above the electroporation threshold.

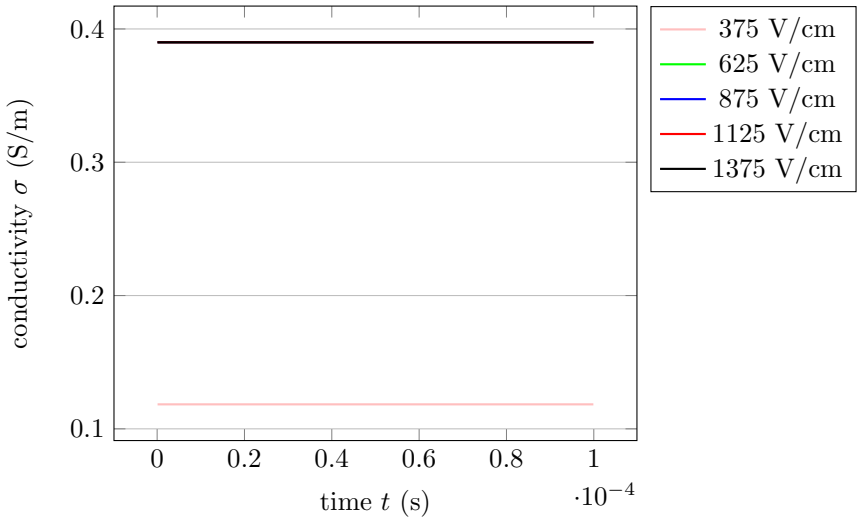

Figure 2.14: Value of the conductivity σ computed with the static model in the middle point between the two electrodes.

2.4.0.2 Numerical results obtained in 2D for the first dynamic model.

Equations (2.12) and (2.13) are solved using a Runge Kutta scheme of order 4. Choosing a sufficiently small time step ensures convergence without using a fixed point method to solve (2.10). Numerical simulations were done using the Finite Element software FreeFem++ [61] on the 2D-mesh featured in Figure 2.4. The parameters used for the simulations are those presented in Table 2.2.

Table 2.2: Parameters of the simulations for the first dynamic model of tissue electroporation.

Parameter	Symbol	Value	Unit
Initial conductivity	σ_0	0.065	S/m
Conductivity for the 1^{st} process	σ_1	0.257	S/m
Time constant for the 1^{st} process	τ_1	1	μs
Conductivity for the 2^{nd} process	σ_2	0.093	S/m
Time constant for the 2^{nd} process	τ_2	80	μs
Electric field threshold	E_{th}	472	V/cm
Parameter in the sigmoid	k	0.0006	

Figure 2.15 shows the simulated currents flowing through the needles when a 100 μs pulse is applied between the needles, with different nominal electric fields (375 V/cm, 625 V/cm, 875 V/cm, 1125 V/cm, 1375 V/cm), for electrodes of diameter 0.7 mm.

The spatial distribution of the different quantities involved in the model can be analyzed. The tissue conductivity shows where the tissue is electroporated. Figure 2.21 shows the spatial distribution of the simulated tissue conductivity σ for a voltage of 875 V.

In Figure 2.17 is displayed the value of σ locally in the middle point between the two electrodes for all different fields applied. Two behaviors are observed: below the electroporation threshold, the conductivity stays more or less constant whereas above the electroporation threshold, the conductivity rises rapidly and then slowly during the pulse. There is almost no distinction in the conductivity behavior between the four electric fields which are above the electroporation threshold.

The spatial distribution of both electroporation processes X_1 and X_2 is dis-

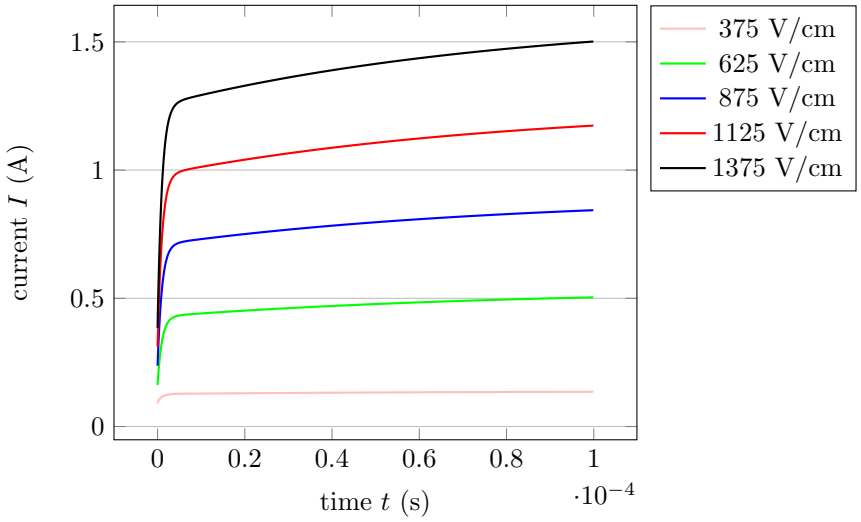

Figure 2.15: Simulated current of the first dynamic model for five different voltage applied.

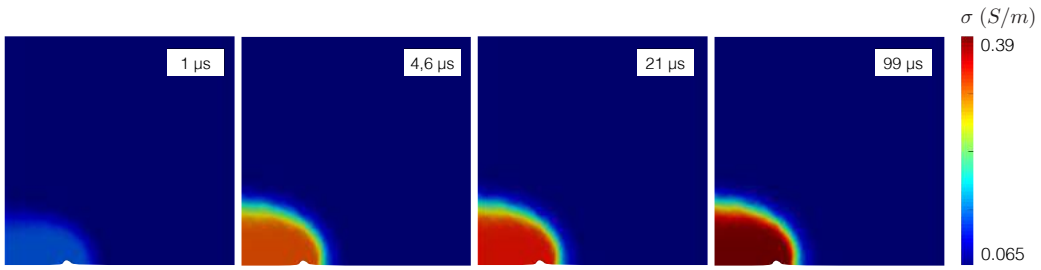

Figure 2.16: Spatial distribution over time of the conductivity σ computed with the first dynamic model for an applied voltage of 875 V/cm.

played in Figure 2.18 for an applied voltage of 875 V, and locally at the central point between the electrodes for all different applied voltage in Figure 2.19. X_1 quickly reaches a stationary regime in the whole tissue, with two different amplitudes only, for electric fields below or above the electroporation threshold. Concerning X_2, the time evolution is slower than the one of X_1: the stationary regime is not reached at the end of the pulse. As for X_1, only two different amplitudes are observed.

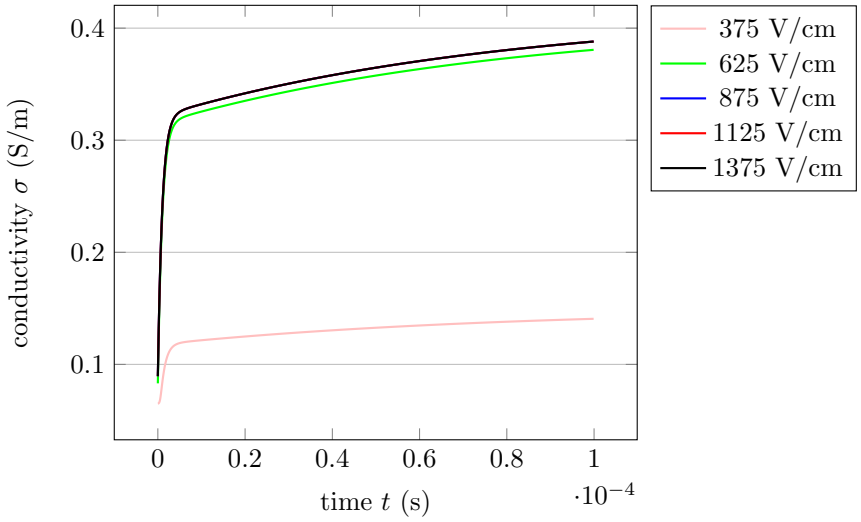

Figure 2.17: Value of the conductivity σ computed with the first dynamic model in the middle point between the two electrodes for an applied voltage of 875 V/cm.

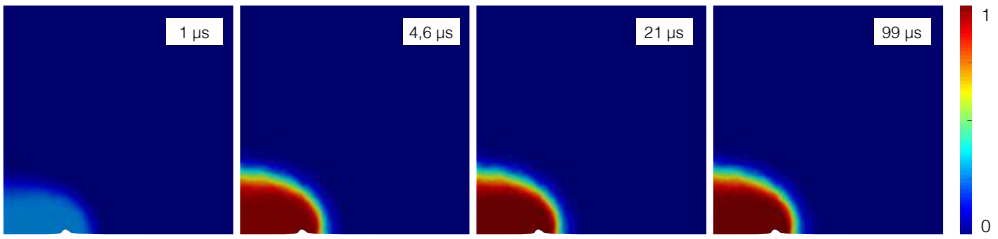

(a) X_1

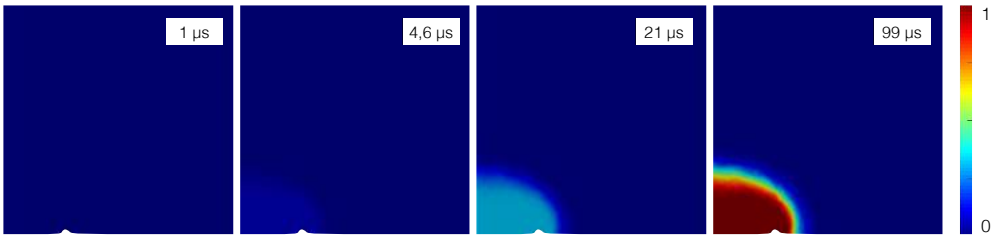

(b) X_2

Figure 2.18: Spatial distribution over time of both electroporation processes X_1 and X_2 computed with the first dynamic model for an applied voltage of 875 V/cm.

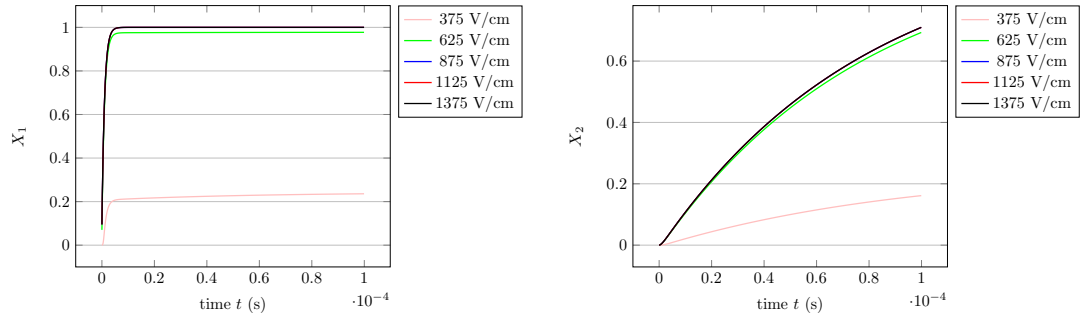

(a) X_1 (b) X_2

Figure 2.19: Evolution over time of the functions X_1 and X_2 computed with the first dynamic model in the middle point between the two electrodes for an applied voltage of 875 V/cm.

2.4.0.3 Numerical results obtained in 2D for the dynamic model with two current densities.

Equations (2.15), (2.19) and (2.21) are solved using a Runge Kutta scheme of order 4. To avoid the approximation of the time derivative of $\nabla\varphi$ in equation (2.15), we solve equation (2.30) instead.

$$\frac{\varepsilon_m}{\sigma_c}\frac{d\overrightarrow{\mathbf{J}}_{cells}}{dt} + \frac{\sigma_m(t,\nabla\varphi)}{\sigma_c}\overrightarrow{\mathbf{J}}_{cells} + \overrightarrow{\mathbf{J}}_{cells} = 0, \tag{2.30}$$

where $\overrightarrow{\mathbf{J}}_{cells} = \overrightarrow{\mathbf{J}}_{cells} - \sigma_c\nabla\varphi$. As precedently, choosing a sufficiently small time step ensures convergence without using a fixed point method to solve (2.14). Numerical simulations were done using the Finite Element software FreeFem++ [61] on the 2D-mesh featured in Figure 2.4. The parameters used for the simulations are those presented in Table 2.3. Figure 2.20 shows the simulated currents flowing through the needles when a 100 μs pulse is applied between the needles, with different nominal electric fields (375 V/cm, 625 V/cm, 875 V/cm, 1125 V/cm, 1375 V/cm), for electrodes of diameter 0.7 mm. We noticed first that the curves of current that we obtained does not fit the experimental data as well as the simulations presented in [85] (data not shown). We assume this difference is due to the way the simulated current is calculated (surface integral versus volume integral,

Table 2.3: Parameters of the simulations for the dynamic model of tissue electroporation using two current densities.

Parameter	Symbol	Value	Unit
Extracellular medium conductivity	σ_e	0.08	S/m
Intracellular medium conductivity	σ_c	0.35	S/m
Membrane relative permittivity	ε_m	60000	F/m
Vacuum permittivity	ε_0	$8.85 \cdot 10^{-12}$	F/m
Typical size of a cell	d_{cells}	22	μm
Initial membrane conductivity	σ_0	0.01	S/m
Membrane conductivity for the 1^{st} process	σ_1	3	S/m
Time constant for the 1^{st} process	τ_1	1	μs
Membrane conductivity for the 2^{nd} process	σ_2	7	S/m
Time constant for the 2^{nd} process	τ_2	80	μs
Transmembrane voltage threshold	V_{th}	0.52	V
Parameter in the sigmoid β_1	k_1	40	V^{-1}
Threshold X_{th} in the sigmoid β_2	X_{th}	0.33	
Parameter in the sigmoid β_2	k_2	10	

see section 2.3.0.3). Nevertheless, varying some parameters leads to obtaining a better fit, at least for the first three voltages (see Figure 2.25, where parameter X_{th} was changed from 0.33 to 0.25). However, it seems very unlikely to recover the rightful current curves for the two highest voltages. This is probably due to the fact that electrode/tissue reactivity is not taken into account by this model. The impact of this phenomenon could induce nonlinear effects, especially for higher electric fields.

This dynamic model brings some insights on the dynamics of electroporation at the tissue scale. We propose to study the time evolution of the electroporation process. The spatial distribution of the different quantities involved in the model can be analyzed. We also consider the different quantities values localy at two different points of the computational domain: on the boundary of one needle (point P_E) and in the middle point between the two electrodes (point P_M).

The distribution of the equivalent tissue conductivity (2.24) is a good indicator of where the tissue is electroporated. Figure 2.21 shows the spatial distribution of

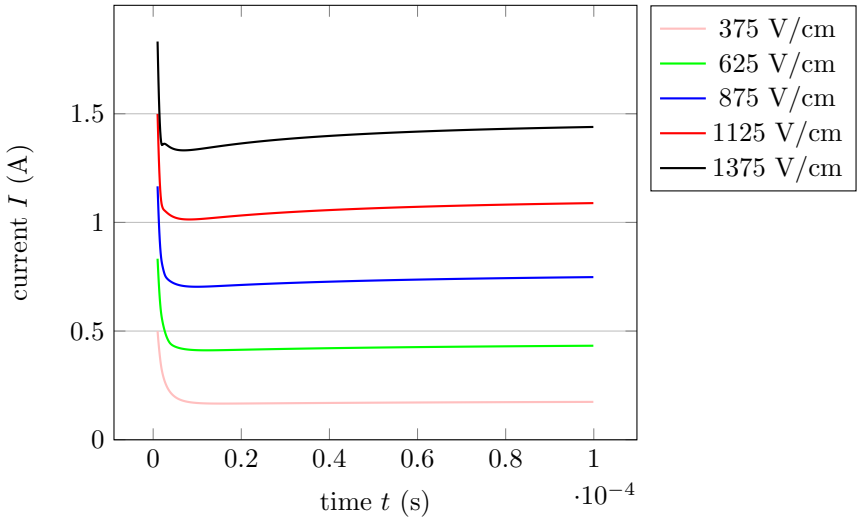

Figure 2.20: Numerical chronograms of current for ⊘ 0.7 mm electrodes. The simulations were done using the dynamic model using two current densities with parameters reported in Table 2.3

the simulated tissue conductivity σ_{eq} for a voltage of 875 V/cm.

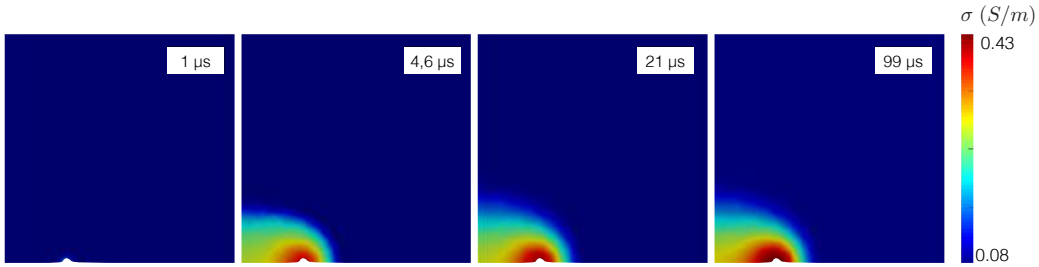

Figure 2.21: Spatial distribution over time of the conductivity σ_{eq} computed with the dynamic model using two current densities for an applied voltage of 875 V.

In Figure 2.22 is displayed the value of σ_{eq} locally at point P_M for all different fields.

Figure 2.23 shows the spatial distribution of the transmembrane potential v_m at the tissue scale, and both electroporation processes X_1 and X_2.

The amplitude of the transmembrane potential v_m and both electroporation processes X_1 and X_2 at points P_M and P_E are displayed in Figure 2.24. It appears

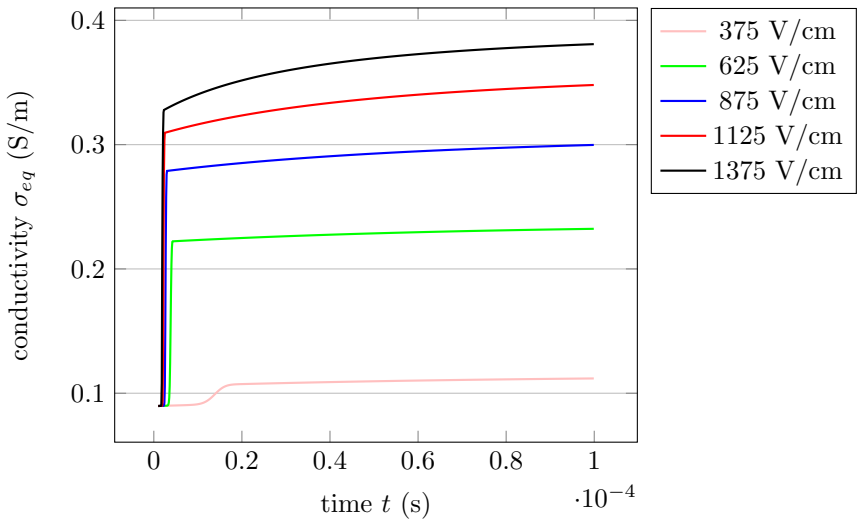

Figure 2.22: Value of the conductivity σ_{eq} computed with the dynamic model using two current densities in the middle point between the two electrodes for all applied voltages.

that for the transmembrane potential, different behaviors coexist in the tissue, in particular because of the heterogeneous distribution of the electric field between the needles, the amplitude of the electric field being higher in the neighborhood of the needles. The time evolution of X_1 and X_2 at the points P_M and P_E have expected behaviors. X_1 quickly reaches a stationary regime at both points, as it is the case in the whole tissue, with different amplitudes due to the electric field distribution. Concerning X_2, the time evolution is slower than the one of X_1: the stationary regime is not reached at the end of the pulse. Let us also denote that this process is much more important (in amplitude) at the vicinity of the electrode.

2.4.0.4 Comparison between the three 2D models and experimental data.

Let us compare the different addings of the 3 models presented. In Figure 2.25 are presented the different simulated currents along with the experimental current when a 875 V/cm is applied with electrodes of 0.7 mm of diameter (data from [110]). It appears that the second dynamic model, with two different current

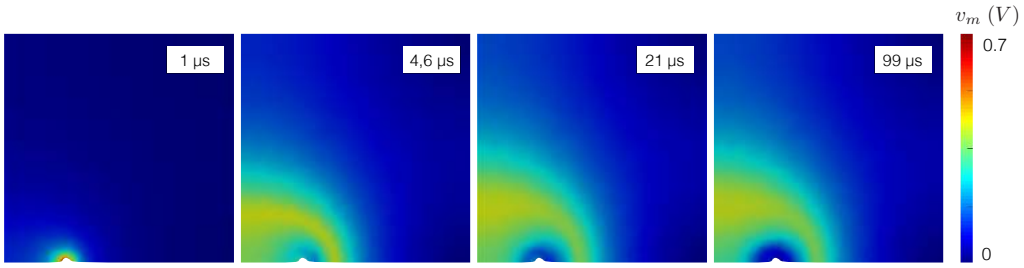

(a) V_m

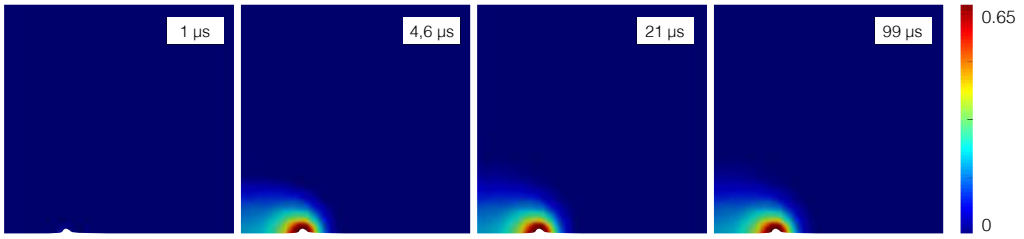

(b) X_1

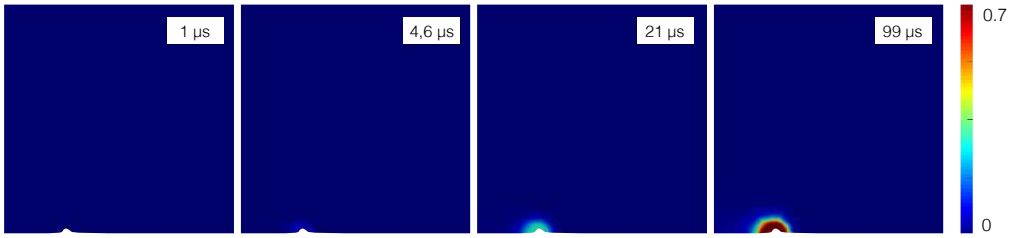

(c) X_2

Figure 2.23: Spatial distribution over time of the magnitude of the mean transmembrane potential v_m and for both electroporation processes X_1 and X_2 computed with the dynamic model using two current densities for an applied voltage of 875 V/cm.

densities, is the one that permits to reproduce best the different features observed on the current chronograms. Indeed, the capacitive peak is well captured, except for the first value computed (peak amplitude) and both dynamics needed are well captured. After an initial peak, current increases exponentially and afterwards it seems to increase much slower or it stops increasing. The other dynamic model, derived naively from [67], only capture well the second dynamic of slow increase during the pulse.

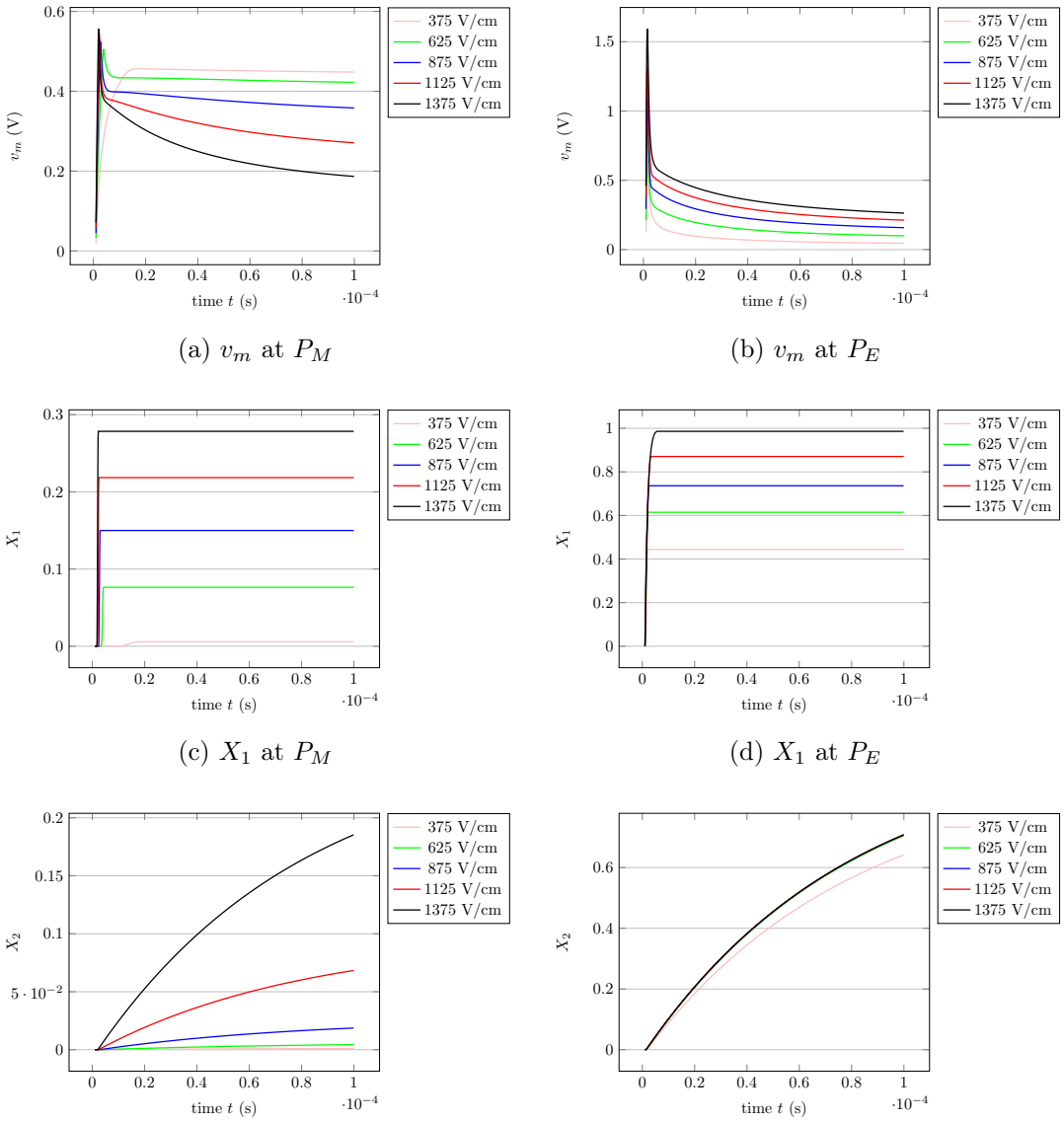

(a) v_m at P_M

(b) v_m at P_E

(c) X_1 at P_M

(d) X_1 at P_E

(e) X_2 at P_M

(f) X_2 at P_E

Figure 2.24: Evolution over time of the functions v_m, X_1 and X_2 computed with the dynamic model using two current densities at points P_M (left) and P_E (right) for all applied voltages.

In Figure 2.25, parameters were found for all three models in order to fit the experimental current in the case of an applied voltage of 875 V. A future work would be to carry out calibration procedures for all three models in order to find

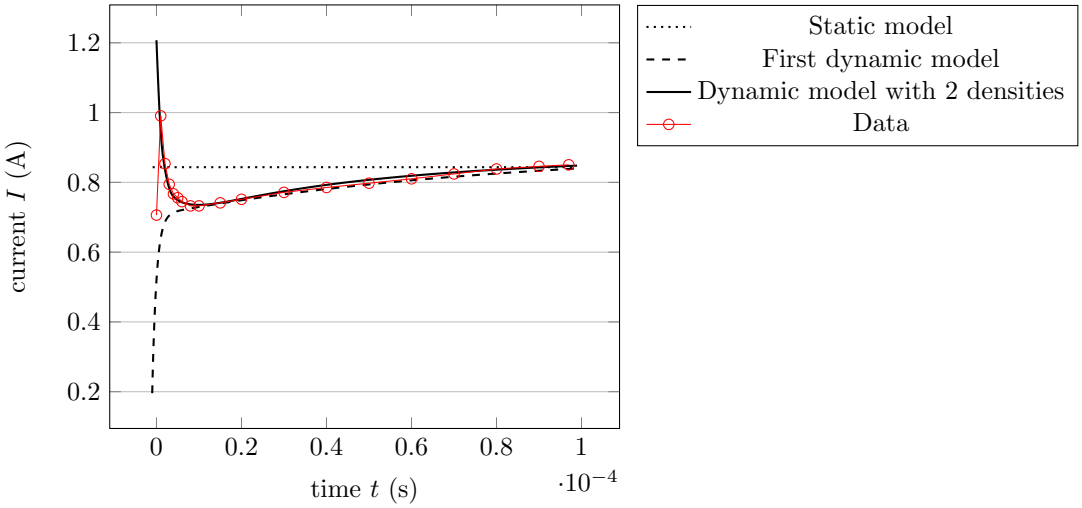

Figure 2.25: Comparison between experimental current and the computed currents with the three different phenomenological models for an applied voltage of 875 V/cm.

a set of parameters valid for all different voltages applied and for different sizes of electrodes.

2.5 Conclusion

In this second chapter, three different phenomenological models of tissue electroporation have been presented. These models, existing in (or inspired by) the literature, are constructed based on two different hypothesis. The first one assumes that the current density flowing through the homogeneous tissue can be expressed as the product of the tissue conductivity and the electric field. The tissue conductivity is assumed to verify an *ad hoc* law to fit the observations made during the experiments. When this law is based on a static hypothesis, it is possible to show that the associated boundary value problem admits an unique solution. On the surface, this approach is a generalization of the approach adopted at the cell scale (see Chapter 1). The second approach assumes that the total current density of the tissue can be expressed as the sum of two current densities: one

flowing through the extracellular medium and the other one flowing through the cells. The equation on the current density flowing through the cells is derived by considering an equivalent electrical circuit. The consideration, in this last model, of the microscopic underlying structure of the tissue raises the question of whether a macroscopic model of tissue electroporation could be derived mathematically from a microscopic well-established model of cell electroporation (see Chapter 3). The numerical part associated with this study also gave interesting results. We established the importance in the choice of numerical tools when running simulations on this type of problems, in 2D and in 3D. When using the Finite Element Method, one should wisely choose the type of elements used, the way the nonlinear problems are treated and the method applied to compute the simulated electric current. The volume method for the current computation is proved to be more precise that the surface method usely presented in the literature, while requiring less mesh precision. Simulations of all models on the same test configuration and using the same numerical tools to solve the equations permits to compare the main features obtained with each model. A first comparison of all three models with experimental data established that the biphasic dynamic model, with two different current densities, is the one that permits to reproduce best the different features observed on the current chronograms. Nevertheless, a further effort has to be done to calibrate the models parameters with experimental data. Despite the fact that the *ad hoc* biphasic tissue model seems to be validated with the experiments, its physical meaning is poorly justified. To fill the gap between cell scale and tissue, we propose in the next chapter a rigorous homogenization procedure (see Chapter 3).

Chapter 3

Rigorous derivation of a static model of tissue electroporation using homogenization

This chapter is the result of a collaboration with A. Collin (Inria Bordeaux) and S. Impériale (LMS, Inria Saclay).

In a biological tissue, there are at least two length scales that must be considered : a microscopic scale (for instance, the size of a single cell) and a macroscopic scale (the size of a typical sample of tissue). As we have seen in chapter 1, at the microscopic level, the partial differential equations based on first principles or the phenomenological equations describing the phenomenon of electroporation are well established and in good agreement with *in vitro* cell experiment. But at the tissue scale, only macroscopic quantities can be computed by the biologist or the engineer. Therefore, a homogenization procedure – see [3] for more details – can be used to link the microscopic and macroscopic behaviors and leads to the equations of the so called bidomain model presented hereunder. This model involves two macroscopic electric potentials, corresponding to the electric potential in the extracellular medium and the intracellular medium respectively. We recall that in chapter 2, we studied a phenomenological model which takes into account

the two different phases that exist at the cell scale, namely the intracellular and the extracellular phases, by considering two different current densities, and this phenomenological model was shown to give results that are in good agreement with the experiments. The idea of this chapter is to recover a similar model, in the static case, using a rigorous homogenization procedure.

3.1 Statement of the problem

3.1.1 Periodic domain.

To use a homogenization procedure, it is convenient to assume that biological tissues have a periodic microstructure. Let $\varepsilon > 0$ be a small parameter. We consider the domain Ω to be a bounded open set of $\mathbb{R}^3$. The domain contains a periodic array of cells whose size is controlled by ε. Let the reference cell be contained in the unit cube $Y = [0,1]^3$, see Figure 3.1b. We divide the domain Ω periodically in each direction in identical squares (Y_n^ε) of size ε, where

$$Y_n^\varepsilon = \varepsilon n + \varepsilon Y.$$

Here $n \in N^\varepsilon = \{k \in \mathbb{Z}^3 | Y_k^\varepsilon \cap \Omega \neq \emptyset\}$. We consider that a cell $Y_{i,n}^\varepsilon$ lives in each small square Y_n^ε. As shown in Figure 3.1a, all cells are identical, up to a translation and scaling of size ε, to the reference cell Y_i. So are their boundaries Γ_n^ε to the boundary Γ^Y of Y_i and so are the extracellular medium $Y_{e,n}^\varepsilon$ to the reference extracellular medium Y_e:

$$\begin{aligned}
&\forall n \in N^\varepsilon, Y_{i,n}^\varepsilon = \varepsilon n + \varepsilon Y_i, \\
&\forall n \in N^\varepsilon, Y_{e,n}^\varepsilon = \varepsilon n + \varepsilon Y_e, \\
&\forall n \in N^\varepsilon, \Gamma_n^\varepsilon = \varepsilon n + \varepsilon \Gamma^Y.
\end{aligned}$$

Let us also assume that all the cells are strictly contained in Ω, that is for every $n \in N^\varepsilon$, the boundary Γ_n^ε of the cell $Y_{i,n}$ does not intersect the boundary $\partial\Omega$:

$$\partial\Omega \cap (\cup_n \Gamma_n^\varepsilon) = \emptyset.$$

The domain Ω is thus composed of two ε-dependent connected subdomains Ω_i^ε and Ω_e^ε, see Figure 3.1a:

$$\cup_n \Omega_{e,n}^\varepsilon = \Omega_e^\varepsilon, \quad \cup_n \Omega_{i,n}^\varepsilon = \Omega_i^\varepsilon, \quad \cup_n \Gamma_n^\varepsilon = \Gamma^\varepsilon.$$

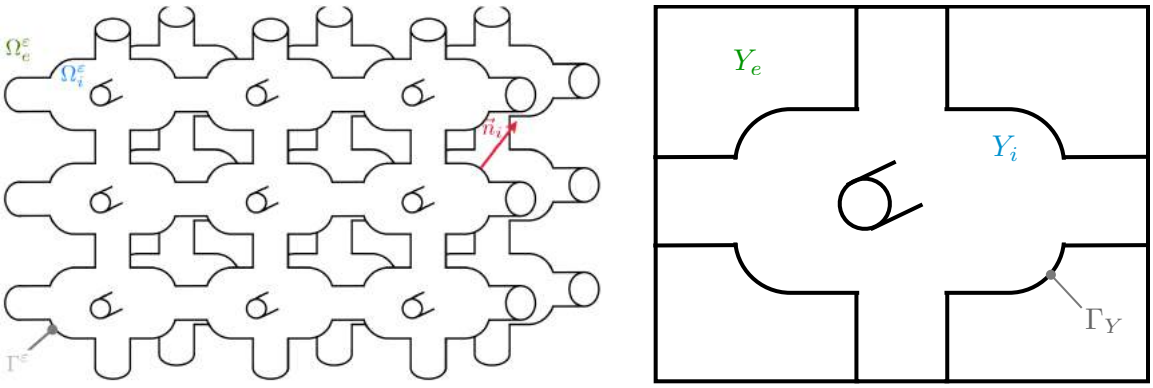

(a) Domain Ω (b) Periodic cell Y

Figure 3.1: Schematic illustration of the periodic medium Ω and of a unit period Y.

3.1.2 Microscopic model.

In section 1.1.2, we stated the electric model at the cell scale. We recall it here and assume a static hypothesis. Let us denote $[u] = u_e - u_i$, where u_e (resp. u_i) is the electric potential of the extracellular (resp. intracellular) medium $\mathcal{O}_e$ (resp. $\mathcal{O}_i$). Both media are separated by an interface γ, standing for the cell membrane. We chose to consider the static nonlinear model previously presented in section 1.3 for the sake of simplicity of the future analysis. We recall that the complete

static microscopic model is given by

$$\begin{cases} \nabla_x \cdot (\sigma_i \nabla_x u_i) = 0, & \text{in } \mathcal{O}_i, \quad (3.1a) \\ \nabla_x \cdot (\sigma_e \nabla_x u_e) = 0, & \text{in } \mathcal{O}_e, \quad (3.1b) \\ \sigma_i \nabla_x u_i \cdot \vec{\mathbf{n}}_i = \sigma_e \nabla_x u_e \cdot \vec{\mathbf{n}}_i, & \text{on } \gamma, \quad (3.1c) \\ S_m([u])[u] = \sigma_i \nabla_x u_i \cdot \vec{\mathbf{n}}_i, & \text{on } \gamma. \quad (3.1d) \end{cases}$$

In this section, we will assume that S_m is a sigmoid function, as (1.6) was. We will work with a general form of S_m:

$$S_m(\lambda) = S_m^s + \frac{1}{\eta}\beta(\lambda), \tag{3.2}$$

where S_m^s is a positive constant, η is a given positive constant which can be small, and β is a regularized Heaviside function such that:

$$\left.\begin{array}{l} \beta \in W^{1,\infty}(\mathbb{R}),\ \lambda \mapsto \beta(\lambda) \text{ is even on } \mathbb{R}, \\ \lambda \mapsto \lambda\beta'(\lambda) \quad \text{belongs to } L^\infty(\mathbb{R}), \\ 0 \le \beta(\lambda) \le 1, \quad \beta \text{ is non decreasing on } (0, +\infty), \\ \lim\limits_{\lambda \to +\infty} \beta(\lambda) = 1. \end{array}\right\} \tag{3.3}$$

We add a Lipschitz hypothesis on the function β:

$$\forall (\lambda_1, \lambda_2), \exists L > 0 \text{ such that } |\beta(\lambda_1) - \beta(\lambda_2)| \le L|\lambda_1 - \lambda_2|. \tag{3.4}$$

3.1.3 Normalization.

A normalization of the system is necessary in order to understand the relative amplitudes of the different terms involved. Let l_0 be a characteristic length of the tissue, σ_0 a characteristic conductivity, $C_{m,0}$ a characteristic membrane capacitance and u_0 a characteristic potential. We set

$$x = l_0\,\overline{x}, \quad u_e = u_0\overline{u_e}(\overline{x}), \quad u_i = u_0\overline{u_i}(\overline{x}), \quad \sigma_i = \sigma_0\overline{\sigma_i}, \quad \sigma_e = \sigma_0\overline{\sigma_e},$$

where the bars denote the dimensionless variables. We also assume that $S_m([u])$ can be written as

$$S_m([u]) = S_{m,0}\overline{S_m}([\overline{u}]).$$

We obtain from (3.1) the dimensionless system

$$\begin{cases} \nabla_{\overline{x}} \cdot (\overline{\sigma_i}\nabla_{\overline{x}}\overline{u_i}) = 0, & \text{in } \mathcal{O}_i^{l_0}, \quad (3.5a) \\ \nabla_{\overline{x}} \cdot (\overline{\sigma_e}\nabla_{\overline{x}}\overline{u_e}) = 0, & \text{in } \mathcal{O}_e^{l_0}, \quad (3.5b) \\ \overline{\sigma_i}\nabla_{\overline{x}}\overline{u_i} \cdot \vec{\mathbf{n}}_i = \overline{\sigma_e}\nabla_{\overline{x}}\overline{u_e} \cdot \vec{\mathbf{n}}_i, & \text{on } \gamma^{l_0}, \quad (3.5c) \\ \dfrac{l_0 S_{m,0}}{\sigma_0}\overline{S_m}([\overline{u}])[\overline{u}] = \overline{\sigma_i}\nabla_{\overline{x}}\overline{u_i} \cdot \vec{\mathbf{n}}_i, & \text{on } \gamma^{l_0}, \quad (3.5d) \end{cases}$$

where $\mathcal{O}_{e,i}^{l_0}$ and γ^{l_0} are rescaled by l_0. We define the $\varepsilon-$parameter which tends to zero in the homogenization process as the ration between the length of a cell denoted by $d_c = 10^{-5}$m and $l_0 = 10^{-2}$m. This implies that ε is of the order of 10^{-3}. We assume that the term $S_{m,0}$ allows us to have the dimensionless quantity

$$\frac{l_0 S_{m,0}}{\sigma_0} \sim \varepsilon$$

of the order of ε, so we set this quantity to be equal to ε. For the sake of clarity, from now on, we do not keep the bar notation, but we write the dependence in ε. In the whole macroscopic domain Ω, the induced potential u^ε is given by

$$\begin{cases} \nabla_x \cdot (\sigma_i \nabla_x u_i^\varepsilon) = 0, & \text{in } \Omega_i^\varepsilon, \quad (3.6a) \\ \nabla_x \cdot (\sigma_e \nabla_x u_e^\varepsilon) = 0, & \text{in } \Omega_e^\varepsilon, \quad (3.6b) \\ \sigma_i \nabla_x u_i^\varepsilon \cdot \vec{\mathbf{n}}_i = \sigma_e \nabla_x u_e^\varepsilon \cdot \vec{\mathbf{n}}_i, & \text{on } \Gamma^\varepsilon, \quad (3.6c) \\ \varepsilon S_m([u^\varepsilon])[u^\varepsilon] = \sigma_i \nabla_x u_i^\varepsilon \cdot \vec{\mathbf{n}}_i, & \text{on } \Gamma^\varepsilon. \quad (3.6d) \end{cases}$$

On the outer boundaries, homogeneous Neumann conditions are imposed, except on the surface of the electrodes, where non homogeneous Dirichlet conditions are

imposed on u_e^ε

$$\sigma_i \nabla_x u_i^\varepsilon \cdot \vec{\mathbf{n}}_i = \sigma_e \nabla_x u_e^\varepsilon \cdot \vec{\mathbf{n}}_i = 0, \qquad \text{on } \partial\Omega, \tag{3.7a}$$

$$u_{e|_{E_+}}^\varepsilon = u^+, \qquad \text{on } E_+, \tag{3.7b}$$

$$u_{e|_{E_-}}^\varepsilon = u^-, \qquad \text{on } E_-. \tag{3.7c}$$

In order to use classical results of the homogenization theory, we will study for the sake of simplicity problem (3.8) instead. A volumic source term f is added to the Laplace equation on u_e^ε and homogeneous Dirichlet conditions are imposed. Considering problem (3.6) with non homogeneous Dirichlet boundary conditions (3.7) introduces technical difficulties but do not fundamentally change the reasoning.

$$\begin{cases} \nabla_x \cdot (\sigma_i \nabla_x u_i^\varepsilon) = 0, & \text{in } \Omega_i^\varepsilon, \quad (3.8a) \\ \nabla_x \cdot (\sigma_e \nabla_x u_e^\varepsilon) = f, & \text{in } \Omega_e^\varepsilon, \quad (3.8b) \\ \sigma_i \nabla_x u_i^\varepsilon \cdot \vec{\mathbf{n}}_i = \sigma_e \nabla_x u_e^\varepsilon \cdot \vec{\mathbf{n}}_i, & \text{on } \Gamma^\varepsilon, \quad (3.8c) \\ \varepsilon S_m([u^\varepsilon])[u^\varepsilon] = \sigma_i \nabla_x u_i^\varepsilon \cdot \vec{\mathbf{n}}_i, & \text{on } \Gamma^\varepsilon, \quad (3.8d) \\ \sigma_i \nabla_x u_i^\varepsilon \cdot \vec{\mathbf{n}}_i = \sigma_e \nabla_x u_e^\varepsilon \cdot \vec{\mathbf{n}}_i = 0, & \text{on } \partial\Omega, \quad (3.8e) \\ u_{e|_{E_+}}^\varepsilon = 0, & \text{on } E_+, \quad (3.8f) \\ u_{e|_{E_-}}^\varepsilon = 0, & \text{on } E_-. \quad (3.8g) \end{cases}$$

The well-posedness of problem (3.8) was investigated and proved in [67]. Thus, problem (3.8) has an unique solution $(u_e^\varepsilon, u_i^\varepsilon)$ with

$$u_e^\varepsilon \in H^1(\Omega_e^\varepsilon) \text{ and } u_i^\varepsilon \in H^1(\Omega_i^\varepsilon).$$

3.2 Formal derivation of the macroscopic model.

We introduce the microscopic variable $y = x/\varepsilon$ and we assume that u_e^ε and u_i^ε can be written as

$$u_{e,i}^\varepsilon = u_{e,i}^0(x,y) + \varepsilon u_{e,i}^1(x,y) + \varepsilon^2 u_{e,i}^2(x,y) + \dots$$

with $u^k_{e,i}(x,y)$ Y-periodic functions. Plugging this ansatz into the system of equations (3.6) leads to a cascade of equations with respect to the power of ε. We are interested in the first three terms (order 0, 1 and 2) that allow us to obtain the macroscopic problem. The following expressions of the Laplacian operator and of the gradient operator are used:

$$\begin{aligned}\Delta u^\varepsilon &= \frac{1}{\varepsilon^2}\Delta_y u^0 + \frac{1}{\varepsilon}(\Delta_y u^1 + (\nabla_y \cdot \nabla_x + \nabla_x \cdot \nabla_y)u^0) \\ &\quad + \Delta_y u^2 + (\nabla_y \cdot \nabla_x + \nabla_x \cdot \nabla_y)u^1 + \Delta_x u^0 + \dots \\ \nabla u^\varepsilon &= \frac{1}{\varepsilon}\nabla_y u^0 + (\nabla_y u^1 + \nabla_x u^0) + \varepsilon(\nabla_y u^2 + \nabla_x u^1) + \dots\end{aligned}$$

where ∇_x and ∇_y denote the partial derivatives with respect to the first and the second variable of $u^k_{e,i}(x,y)$. We can then obtain equations on $u^0, u^1, u^2, \dots$ identifying the rightful powers of ε.

Power ε^{-2}: u^0 is solution of

$$\begin{cases} \nabla_y \cdot (\sigma_i \nabla_y u_i^0) = 0, & \text{in } \Omega_i^\varepsilon \times Y_i, \quad (3.9a) \\ \nabla_y \cdot (\sigma_e \nabla_y u_e^0) = 0, & \text{in } \Omega_e^\varepsilon \times Y_e, \quad (3.9b) \\ \sigma_i \nabla_y u_i^0 \cdot \vec{\mathbf{n}}_i = \sigma_e \nabla_x u_e^0 \cdot \vec{\mathbf{n}}_i = 0, & \text{on } \Gamma^\varepsilon \times \Gamma_Y, \quad (3.9c) \\ + \text{ periodic boundary conditions} & \text{on } \partial Y. \quad (3.9d) \end{cases}$$

It guarantees that $u^0_{e,i}$ are independent of y i.e.

$$u^0_{e,i}(x,y) = u^0_{e,i}(x).$$

Power ε^{-1}: u^1 is solution of

$$\begin{cases} \nabla_y \cdot (\sigma_i \nabla_y u_i^1) = 0, & \text{in } \Omega_i^\varepsilon \times Y_i, \quad (3.10a) \\ \nabla_y \cdot (\sigma_e \nabla_y u_e^1) = 0, & \text{in } \Omega_e^\varepsilon \times Y_e, \quad (3.10b) \\ \sigma_i \nabla_y u_i^1 \cdot \vec{\mathbf{n}}_i + \sigma_i \nabla_x u_i^0 \cdot \vec{\mathbf{n}}_i = 0, & \text{on } \Gamma^\varepsilon \times \Gamma_Y, \quad (3.10c) \\ \sigma_e \nabla_y u_e^1 \cdot \vec{\mathbf{n}}_i + \sigma_e \nabla_x u_e^0 \cdot \vec{\mathbf{n}}_i = 0, & \text{on } \Gamma^\varepsilon \times \Gamma_Y, \quad (3.10d) \\ + \text{ periodic boundary conditions} & \text{on } \partial Y. \quad (3.10e) \end{cases}$$

From (3.10), we see that the terms $u^1_{e,i}$ can be expressed as functions of $u^0_{e,i}$ in a standard way [7] as

$$\begin{cases} u^1(x,y) = -\psi(y)\nabla_x u^0_i(x) + \widetilde{u_i}^1(x), & \text{in } \Omega^\varepsilon_i \times Y_i, \\ \qquad\quad = -\psi(y)\nabla_x u^0_e(x) + \widetilde{u_e}^1(x), & \text{in } \Omega^\varepsilon_e \times Y_e. \end{cases} \tag{3.11}$$

where ψ is solution to the following cell problem

$$\begin{cases} \nabla_y \cdot (\sigma_i \nabla_y \psi_i) = 0, & \text{in } Y_i, \quad (3.12a) \\ \nabla_y \cdot (\sigma_e \nabla_y \psi_e) = 0, & \text{in } Y_e, \quad (3.12b) \\ \sigma_i(\nabla_y \psi_i^{1,2,3} - e^{1,2,3}) \cdot \vec{\mathbf{n}}_i = \sigma_e(\nabla_y \psi_e^{1,2,3} - e^{1,2,3}) \cdot \vec{\mathbf{n}}_i = 0, & \text{on } \Gamma_Y, \quad (3.12c) \\ \psi^{1,2,3}_{e,i} \text{ is } Y\text{-periodic.} & (3.12d) \end{cases}$$

Power ε^0: u^2 is solution to

$$\begin{cases} \nabla_y \cdot (\sigma_i \nabla_y u^2_i) = -\nabla_x \cdot (\sigma_i \nabla_x u^0_i) - \nabla_y \cdot (\sigma_i \nabla_x u^1_i) \\ \qquad\qquad - \nabla_x \cdot (\sigma_i \nabla_y u^1_i), & \text{in } Y_i, \quad (3.13a) \\ \nabla_y \cdot (\sigma_e \nabla_y u^2_e) = -\nabla_x \cdot (\sigma_e \nabla_x u^0_e) - \nabla_y \cdot (\sigma_e \nabla_x u^1_e) \\ \qquad\qquad - \nabla_x \cdot (\sigma_e \nabla_y u^1_e), & \text{in } Y_e, \quad (3.13b) \\ (\sigma_i \nabla_y u^2_i + \sigma_i \nabla_x u^1_i) \cdot \vec{\mathbf{n}}_i = (\sigma_e \nabla_y u^2_e + \sigma_e \nabla_x u^1_e) \cdot \vec{\mathbf{n}}_i \\ \qquad\qquad = S_m([u^0])[u^0], & \text{on } \Gamma_Y. \quad (3.13c) \end{cases}$$

Note that the convergence of the nonlinear term $S_m([u^\varepsilon])[u^\varepsilon]$ towards $S_m([u^0])[u^0]$ was assumed here to write the formal expansion. This convergence will be rightfully justified in the next section. Integrating equation (3.13a) on Y_i and (3.13b) on Y_e and summing, we obtain

$$\left(\int_{Y_i} + \int_{Y_e}\right) \left(\nabla_y \cdot (\sigma \nabla_y u^2 + \sigma \nabla_x u^1)\right) dy = -\left(\int_{Y_i} + \int_{Y_e}\right) \left(\nabla_x \cdot (\sigma \nabla_x u^0 + \sigma \nabla_y u^1)\right) dy.$$

Integrating by part, the left-hand term is equal to zero as $\sigma_i \nabla_y u_i^2 \cdot \vec{\mathbf{n}}_i + \sigma_i \nabla_x u_i^1 \cdot \vec{\mathbf{n}}_i = \sigma_e \nabla_y u_e^2 \cdot \vec{\mathbf{n}}_i + \sigma_e \nabla_x u_e^1 \cdot \vec{\mathbf{n}}_i$. Let's focus on the right-hand term. As

$$
\begin{aligned}
&- \int_{Y_i} \left(\nabla_x \cdot (\sigma_i \nabla_x u_i^0 + \sigma_i \nabla_y u_i^1) \right) dy = -\nabla_x \cdot \left(\sigma_i \frac{|Y_{i,e}|}{|Y|} \nabla_x u_i^0 + \sigma_i \frac{1}{|Y|} \int_{Y_i} \nabla_y u_i^1 dy \right) \\
&= -\nabla_x \cdot \left(\left(\sigma_i \frac{|Y_{i,e}|}{|Y|} I - \sigma_i \frac{1}{|Y|} \int_{Y_i} \nabla_y \psi(y) dy \right) \nabla_x u_i^0 \right) \text{ (after (3.11))}, \\
&= -\nabla_x \cdot \left(\widetilde{\sigma_i} \nabla_x u_i^0 \right).
\end{aligned}
$$

where

$$
\widetilde{\sigma_{i,e}} = \sigma_{i,e} \frac{|Y_{i,e}|}{|Y|} I - \sigma_{i,e} \frac{1}{|Y|} \int_{Y_{i,e}} \nabla_y \psi(y) dy. \tag{3.14}
$$

Likewise, $- \int_{Y_e} \left(\nabla_x \cdot (\sigma_e \nabla_x u_e^0 + \sigma_e \nabla_y u_e^1) \right) dy = -\nabla_x \cdot (\widetilde{\sigma_e} \nabla_x u_e^0)$. Thus, we obtain the first compatibily condition

$$
-\nabla_x \cdot \left(\widetilde{\sigma_i} \nabla_x u_i^0 + \widetilde{\sigma_e} \nabla_x u_e^0 \right) = 0. \tag{3.15}
$$

Next, integrating (3.13c) on Γ_Y reads

$$
\begin{aligned}
\int_{\Gamma_Y} S_m([u^0])[u^0] ds &= \int_{\Gamma_Y} \left(\sigma_i \nabla_y u_i^2 \cdot \vec{\mathbf{n}}_i + \sigma_i \nabla_x u_i^1 \cdot \vec{\mathbf{n}}_i \right) ds \\
&= \int_{Y_i} \left(\nabla_y \cdot \left(\sigma_i \nabla_y u_i^2 + \sigma_i \nabla_x u_i^1 \right) \right) dy \\
&= - \int_{Y_i} \left(\nabla_x \cdot (\sigma_i \nabla_x u_i^0 + \sigma_i \nabla_y u_i^1) \right) dy \text{ (after (3.13a))} \\
&= -\nabla_x \cdot \left(\widetilde{\sigma_i} \nabla_x u_i^0 \right) = \nabla_x \cdot \left(\widetilde{\sigma_e} \nabla_x u_e^0 \right).
\end{aligned}
$$

Finally, as u^0 does not depend on y, $\int_{\Gamma_Y} S_m([u^0])[u^0] ds = \frac{|\Gamma_Y|}{|Y|} \left(S_m([u^0])[u^0] \right)$ and we obtain the second compatibility condition

$$
\frac{|\Gamma_Y|}{|Y|} \left(S_m([u^0])[u^0] \right) = \nabla_x \cdot \left(\widetilde{\sigma_e} \nabla_x u_e^0 \right). \tag{3.16}
$$

Homogenized problem. Equations (3.15) and (3.16) represent the homogenized macroscopic problem, whose solution (u_e^0, u_i^0) is the formal limit of $(u_e^\varepsilon, u_i^\varepsilon)$ when

$\varepsilon \to 0$, and does not depend on the small scale y. The small scale effects are taken into account through the conductivity tensors $\widetilde{\sigma_{i,e}}$ and parameter $A_m = \frac{|\Gamma_Y|}{|Y|}$ - the ratio of membrane area by unit volume - that do not depend on the choice of Ω but on the shape and size of the reference cell chosen. This dependance is investigated in part 3.4.1.

This method of formal expansion leads to the homogenized system of equations but as it is based on an ansatz, it is not in any case a proof of the convergence of $(u_e^\varepsilon, u_i^\varepsilon)$ to (u_e^0, u_i^0). Moreover the convergence of the nonlinear term $S_m([u^\varepsilon])[u^\varepsilon]$ to $S_m([u^0])[u^0]$ has yet to be justifed. The rigorous proof of this convergence is presented in the next section.

Bidomain model: existence and uniqueness. We can add boundary conditions to equations (3.15) and (3.16) to obtain the so-called bidomain model:

$$\begin{cases} -\nabla_x \cdot \left(\widetilde{\sigma_i}\nabla_x u_i^0 + \widetilde{\sigma_e}\nabla_x u_e^0\right) = 0, & \text{in } \Omega, \quad (3.17)\\ A_m\left(S_m([u^0])[u^0]\right) = \nabla_x \cdot \left(\widetilde{\sigma_e}\nabla_x u_e^0\right), & \text{in } \Omega, \quad (3.18)\\ (\widetilde{\sigma_e}\nabla_x u_e^0)\cdot \overrightarrow{n}_{\partial\Omega} = 0, & \text{on } \partial\Omega, \quad (3.19)\\ (\widetilde{\sigma_i}\nabla_x u_i^0)\cdot \overrightarrow{n}_{\partial\Omega} = 0, & \text{on } \partial\Omega, \quad (3.20)\\ u_e^0 = V^{+,-}, & \text{on } E_{+,-}, \quad (3.21)\\ (\widetilde{\sigma_i}\nabla_x u_i^0)\cdot \overrightarrow{n}_{E_{+,-}} = 0, & \text{on } E_{+,-}. \quad (3.22) \end{cases}$$

where

$$\widetilde{\sigma_{i,e}} = \sigma_{i,e}\frac{|Y_{i,e}|}{|Y|}I_2 - \sigma_{i,e}\frac{1}{|Y|}\int_{Y_{i,e}} \nabla_y \psi(y)dy. \quad (3.23)$$

The existence and uniqueness of the bidomain model has been studied for different type of nonlinearity, mostly ionic models in the framework of electrocardiology [25]. It is shown that - under assumptions on the nonlinear term - a unique solution (u_e^0, u_i^0) of problem (3.17) exists. Nevertheless, most of the bidomain models usually present a time evolution. In our case, as we considered the steady-state equations from the start, we can show that problem (3.17) is well-posed by

using the same method presented in section 2.2.2.1. In this case, the functional J should be chosen as

$$\begin{aligned} J(u_e^0, u_i^0) :=& \frac{1}{2}\int_\Omega \widetilde{\sigma_i}\nabla u_i^0 \cdot \nabla u_i^0 \, dx + \frac{1}{2}\int_\Omega \widetilde{\sigma_e}\nabla u_e^0 \cdot \nabla u_e^0 \, dx \\ &+ A_m \int_\Omega \int_0^{|u_e^0 - u_i^0|(x)} s S_m(s) \, ds dx. \end{aligned} \tag{3.24}$$

It can be shown that this functional is well defined, that its differential is exactly the variational formulation associated with problem (3.17) and is monotone and that J goes to $+\infty$ when $\|(u_e^0, u_i^0)\|$ goes to $+\infty$. This guarantees that problem (3.17) has a unique solution $(u_e^0, u_i^0) \in H^1(\Omega)^2$.

3.3 Two-scale convergence towards the macroscopic model

In this section, η is fixed as a constant independent of ε.

3.3.1 Uniform bounds

In order to apply the process of two-scale convergence, we must first determine uniform bounds on the unknowns. The derivation of estimates on the unknowns is based on previous works, in particular on articles by Allaire, Damlamian, Hornung and Murat [3, 4, 5] and on Giovangigli's PhD thesis [55, 56]. In order to use those previous results, we must introduce hypothesis on the geometry of the domain Ω: let the macroscopic domain Ω be a bounded open set of class $\mathcal{C}^2$ with Lipschitz boundary $\partial\Omega$, Ω being locally located on one side of its boundary. At the microscopic scale, we must assume that Y_e is a connected open set of class $\mathcal{C}^2$ with Lipschitz boundary, and is locally located on one side of its boundary. Furthermore, the material volume fraction $|Y_e|/|Y|$ must be strictly positive [5, 55].

We begin with citing three lemmas that are used to establish estimates (3.25).

Lemma 4 (Poincaré inequality in Ω_e^ε, Lemma A.4 p.93 [5])**.** *There exists a constant*

C, which does not depend on ε*, such that, for any* $g^\varepsilon \in H^1(\Omega_e^\varepsilon)$ *satisfying* $g^\varepsilon = 0$ *on* $\partial\Omega_e^\varepsilon \cap \partial\Omega$*, we have*

$$||g^\varepsilon||_{L^2(\Omega_e^\varepsilon)} \leq C||\nabla g^\varepsilon||_{L^2(\Omega_e^\varepsilon)}.$$

Lemma 5 (Lemma Appendix C.1. p.657 [55])**.** *There exists a constant* C *independent of* ε *such that, for any* $g_e^\varepsilon \in H^1(\Omega_e^\varepsilon)$ *and* $g_i^\varepsilon \in H^1(\Omega_i^\varepsilon)$*,*

$$\left\|g_{e,i}^\varepsilon\right\|_{L^2(\Gamma^\varepsilon)}^2 \leq C\left(\varepsilon^{-1}\left\|g_{e,i}^\varepsilon\right\|_{L^2(\Omega_{e,i}^\varepsilon)}^2 + \varepsilon\left\|\nabla g_{e,i}^\varepsilon\right\|_{L^2(\Omega_{e,i}^\varepsilon)}^2\right).$$

Lemma 6 (Lemma Appendix C.2. p.658 [55])**.** *There exists a constant* C *independent of* ε *such that, for any* $g_i^\varepsilon \in H^1(\Omega_i^\varepsilon)$*,*

$$\|g_i^\varepsilon\|_{L^2(\Omega_i^\varepsilon)} \leq C\left(\sqrt{\varepsilon}\,\|g_i^\varepsilon\|_{L^2(\Gamma^\varepsilon)} + \varepsilon\,\|\nabla g_i^\varepsilon\|_{L^2(\Omega_i^\varepsilon)}\right).$$

Now, we can state uniform bounds on the unknowns of problem (3.8).

Proposition 7. *Denote* $v^\varepsilon = u_e^\varepsilon - u_i^\varepsilon$ *and denote with* $\widetilde{\cdot}$ *the extension by zero of functions on* Ω_e^ε *and* Ω_i^ε *in the respective domains* Ω_i^ε *and* Ω_e^ε*. If* f *is uniformly bounded in* $L^2(\Omega_e^\varepsilon)$*, then there exists a constant* C *independent of* ε *such that the following uniform bounds hold*

$$\begin{aligned}
&\int_{L^2(\Omega)} |\widetilde{\nabla u_e^\varepsilon}|^2 \leq C, \quad \int_{L^2(\Omega)} |\widetilde{\nabla u_i^\varepsilon}|^2 \leq C,\\
&\varepsilon\int_{L^2(\Gamma^\varepsilon)} |v^\varepsilon|^2 \leq C, \quad \varepsilon\int_{L^2(\Gamma^\varepsilon)} |S_m(v^\varepsilon)v^\varepsilon|^2 \leq C,\\
&\int_{L^2(\Omega)} |\widetilde{u_e^\varepsilon}|^2 \leq C, \quad \int_{L^2(\Omega)} |\widetilde{u_i^\varepsilon}|^2 \leq C.
\end{aligned} \tag{3.25}$$

Proof. The variational problem associated to (3.8) is find $(u_i^\varepsilon, u_e^\varepsilon) \in H^1(\Omega_i^\varepsilon) \times H^1(\Omega_e^\varepsilon)$ such that $\forall (v_i^\varepsilon, v_e^\varepsilon) \in H^1(\Omega_i^\varepsilon) \times H^1(\Omega_e^\varepsilon)$,

$$\begin{aligned}
(\sigma_i \nabla_x u_i^\varepsilon, \nabla_x v_i^\varepsilon)_{\Omega_i^\varepsilon} + (\sigma_e \nabla_x u_e^\varepsilon, \nabla_x v_e^\varepsilon)_{\Omega_e^\varepsilon}&\\
+ \varepsilon\langle S_m(u_e^\varepsilon - u_i^\varepsilon)(u_e^\varepsilon - u_i^\varepsilon), v_e^\varepsilon - v_i^\varepsilon\rangle_{\Gamma^\varepsilon} = (f, v_e^\varepsilon)_{\Omega_e^\varepsilon}&.
\end{aligned} \tag{3.26}$$

We take $v_{i,e}^\varepsilon = u_{i,e}^\varepsilon$ in (3.26) in order to derive an a priori estimate and we obtain

$$(\sigma_i \nabla_x u_i^\varepsilon, \nabla_x u_i^\varepsilon)_{\Omega_i^\varepsilon} + (\sigma_e \nabla_x u_e^\varepsilon, \nabla_x u_e^\varepsilon)_{\Omega_e^\varepsilon} + \varepsilon S_m^s \langle u_e^\varepsilon - u_i^\varepsilon, u_e^\varepsilon - u_i^\varepsilon \rangle_{\Gamma^\varepsilon} + \frac{\varepsilon}{\eta} \langle \beta(u_e^\varepsilon - u_i^\varepsilon)(u_e^\varepsilon - u_i^\varepsilon), u_e^\varepsilon - u_i^\varepsilon \rangle_{\Gamma^\varepsilon} = (f, u_e^\varepsilon)_{\Omega_e^\varepsilon}.$$

We define

$$\mathcal{E}^\varepsilon = (\sigma_i \nabla_x u_i^\varepsilon, \nabla_x u_i^\varepsilon)_{\Omega_i^\varepsilon} + (\sigma_e \nabla_x u_e^\varepsilon, \nabla_x u_e^\varepsilon)_{\Omega_e^\varepsilon} + \varepsilon S_m^s \|u_e^\varepsilon - u_i^\varepsilon\|_{\Gamma^\varepsilon}^2. \tag{3.27}$$

As $0 \leq \beta(u_e^\varepsilon - u_i^\varepsilon) \leq 1$, we have that

$$\begin{aligned} &\mathcal{E}^\varepsilon \leq \mathcal{E}^\varepsilon + \frac{\varepsilon}{\eta} \langle \beta(u_e^\varepsilon - u_i^\varepsilon)(u_e^\varepsilon - u_i^\varepsilon), u_e^\varepsilon - u_i^\varepsilon \rangle_{\Gamma^\varepsilon} \leq \mathcal{E}^\varepsilon + \frac{\varepsilon}{\eta} \|u_e^\varepsilon - u_i^\varepsilon\|_{\Gamma^\varepsilon}^2, \\ &\text{hence } \mathcal{E}^\varepsilon \leq (f, u_e^\varepsilon)_{\Omega_e^\varepsilon} \leq \mathcal{E}^\varepsilon + \frac{\varepsilon}{\eta} \|u_e^\varepsilon - u_i^\varepsilon\|_{\Gamma^\varepsilon}^2. \end{aligned} \tag{3.28}$$

Let us apply Cauchy-Schwarz inequality on one hand and Poincaré inequality (Lemma 4) on the other hand on $u_e^\varepsilon \in H^1(\Omega_e^\varepsilon)$ on the left hand side of inequality (3.28). Thus there exists a constant α independent of ε such that

$$\alpha \|u_e^\varepsilon\|_{L^2(\Omega_e^\varepsilon)}^2 + (\sigma_i \nabla_x u_i^\varepsilon, \nabla_x u_i^\varepsilon)_{\Omega_i^\varepsilon} + \varepsilon S_m^s \|u_e^\varepsilon - u_i^\varepsilon\|_{\Gamma^\varepsilon}^2 \leq \mathcal{E}^\varepsilon \leq \|f\|_{L^2(\Omega_e^\varepsilon)} \|u_e^\varepsilon\|_{L^2(\Omega_e^\varepsilon)}.$$

As f is uniformly bounded in $L^2(\Omega_e^\varepsilon)$, we obtain than u_e^ε is uniformly bounded in $L^2(\Omega_e^\varepsilon)$. Thus, there exists a constant C independent of ε such that $\mathcal{E}^\varepsilon \leq C$. As $\mathcal{E}^\varepsilon$ is the sum of three positive terms, each of them is also bounded by C. Thus we obtain that

$$\|\nabla u_e^\varepsilon\|_{L^2(\Omega_e^\varepsilon)} \leq C, \quad \|\nabla u_i^\varepsilon\|_{L^2(\Omega_i^\varepsilon)} \leq C, \quad \varepsilon \|u_e^\varepsilon - u_i^\varepsilon\|_{L^2(\Gamma^\varepsilon)}^2 \leq C.$$

Finally, using the Lipschitz condition on β (3.4), we also have that

$$\varepsilon \|\beta(u_e^\varepsilon - u_i^\varepsilon)(u_e^\varepsilon - u_i^\varepsilon)\|_{L^2(\Gamma^\varepsilon)}^2 \leq C.$$

It remains to show that u_i^ε is uniformly bounded in $L^2(\Omega_i^\varepsilon)$ which is a direct consequence of Lemmas 5 and 6. Indeed, as u_e^ε and ∇u_e^ε are uniformly bounded in

$L^2(\Omega_e^\varepsilon)$, using Lemma 5 yields

$$\varepsilon \left\| u_e^\varepsilon \right\|^2_{L^2(\Gamma^\varepsilon)} \leq C \left(\left\| u_e^\varepsilon \right\|^2_{L^2(\Omega_e^\varepsilon)} + \varepsilon^2 \left\| \nabla u_e^\varepsilon \right\|^2_{L^2(\Omega_e^\varepsilon)} \right),$$

which guarantees that $\sqrt{\varepsilon} \left\| u_e^\varepsilon \right\|_{L^2(\Gamma^\varepsilon)}$ is controlled uniformly in ε. Then, we apply Lemma 6 and the triangle inequality

$$\left\| u_i^\varepsilon \right\|_{L^2(\Omega_i^\varepsilon)} \leq C \left(\sqrt{\varepsilon} \left\| u_e^\varepsilon - u_i^\varepsilon \right\|_{L^2(\Gamma^\varepsilon)} + \sqrt{\varepsilon} \left\| u_e^\varepsilon \right\|_{L^2(\Gamma^\varepsilon)} + \varepsilon \left\| \nabla u_i^\varepsilon \right\|_{L^2(\Omega_i^\varepsilon)} \right).$$

We have previously shown that all three terms on the right-hand side of this last inequality are bounded uniformly in ε so we obtain that u_i^ε is uniformly bounded in $L^2(\Omega_i^\varepsilon)$ which completes the proof.

□

3.3.2 Two-scale limits

The a priori estimates (3.25) allow to apply the 2-scale convergence. We first recall the definition of two-scale convergence and a few results of this theory [3, 4]. The notion of two-scale convergence makes sense because of the next compactness theorem.

Theorem 8 (Theorem 0.1 p.1483 [3]). *Let $f^\varepsilon(x)$ be a bounded sequence in $L^2(\Omega)$. Then, there exists a subsequence (still denoted by ε) and a function $f^0(x,y) \in L^2(\Omega \times Y)$ such that f^ε two-scale converges to $f^0(x,y)$ in the sense that, for any function $g \in C(\Omega \times C_\#(Y))$*

$$\lim_{\varepsilon \to 0} \int_\Omega f^\varepsilon(x) g(x, \frac{x}{\varepsilon})\, dx = \int_\Omega \int_Y f^0(x,y) g(x,y)\, dy dx.$$

Two-scale convergence can be extended to sequences defined on periodic surfaces.

Theorem 9 (Theorem 2.1 p.2 [4]). *Let f^ε be a sequence in $L^2(\Gamma^\varepsilon)$ such that*

$$\varepsilon \int_{\Gamma^\varepsilon} |f^\varepsilon(x)|^2 \, d\Gamma^\varepsilon \leq C,$$

where C is a positive constant independent of ε. Then, there exists a subsequence (still denoted by ε) and a two-scale limit $f^0(x,y) \in L^2(\Omega \times L^2(\Gamma^Y))$ such that f^ε two-scale converges to $f^0(x,y)$ in the sense that, for any function $g \in C(\Omega \times C_\#(Y))$

$$\lim_{\varepsilon \to 0} \varepsilon \int_{\Gamma^\varepsilon} f^\varepsilon(x) g(x, \frac{x}{\varepsilon}) \, d\Gamma^\varepsilon = \int_\Omega \int_{\Gamma^Y} f^0(x,y) g(x,y) \, d\Gamma^Y dx.$$

In the case where f^ε is the trace on Γ^ε of some function in $H^1(\Omega)$, a link can be established between its usual and surface two-scale limits.

Proposition 10 (Proposition 2.6 p.3 [4]). *Let f^ε be a sequence in $H^1(\Omega)$ such that $\|f^\varepsilon\|_{L^2(\Omega)} + \varepsilon \|\nabla f^\varepsilon\|_{L^2(\Omega)} \leq C$, where C is a positive constant independent of ε. Then the trace of f^ε on Γ^ε satisfies the estimate*

$$\varepsilon \int_{\Gamma^\varepsilon} |f^\varepsilon(x)|^2 d\Gamma^\varepsilon \leq C,$$

and up to a subsequence, it two-scale converges to a limit $f^0(x,s)$ which is the trace on Γ of the usual two-scale limit, also denoted $f^0(x,y)$, a function in $L^2(\Omega, H^1_\#(Y))$. More precisely, for any function $g \in C(\Omega \times C_\#(Y))$,

$$\lim_{\varepsilon \to 0} \int_\Omega f^\varepsilon(x) g(x, \frac{x}{\varepsilon}) \, dx = \int_\Omega \int_Y f^0(x,y) g(x,y) dy dx,$$
$$\lim_{\varepsilon \to 0} \varepsilon \int_{\Gamma^\varepsilon} f^\varepsilon(x) g(x, \frac{x}{\varepsilon}) \, d\Gamma^\varepsilon = \int_\Omega \int_{\Gamma^Y} f^0(x,s) g(x,s) \, ds dx.$$

From the uniform bounds we obtained, by direct application of the theory developed in [3, 4], we can state the following two-scale convergences:

Proposition 11. *For all $g \in C(\Omega \times C_\#(Y))$ and $\varphi \in C(\Omega \times C_\#(Y))^2$*

- $\lim_{\varepsilon\to 0}\int_\Omega \widetilde{u_e^\varepsilon}(x)g(x,\frac{x}{\varepsilon})\,dx = \int_\Omega\int_Y \chi_{Y_e}(y)u_e^0(x)g(x,y)\,dydx,$
- $\lim_{\varepsilon\to 0}\int_\Omega \widetilde{u_i^\varepsilon}(x)g(x,\frac{x}{\varepsilon})\,dx = \int_\Omega\int_Y \chi_{Y_i}(y)u_i^0(x)g(x,y)\,dydx,$
- $\lim_{\varepsilon\to 0}\int_\Omega \widetilde{\nabla u_e^\varepsilon}\cdot\varphi(x,\frac{x}{\varepsilon})\,dx = \int_\Omega\int_Y \chi_{Y_e}(y)(\nabla_x u_e^0(x)+\nabla_y u_e^1(x,y))\cdot\varphi(x,y)\,dydx,$
- $\lim_{\varepsilon\to 0}\int_\Omega \widetilde{\nabla u_i^\varepsilon}\cdot\varphi(x,\frac{x}{\varepsilon})\,dx = \int_\Omega\int_Y \chi_{Y_i}(y)(\nabla_x u_i^0(x)+\nabla_y u_i^1(x,y))\cdot\varphi(x,y)\,dydx,$
- $\lim_{\varepsilon\to 0}\varepsilon\int_{\Gamma^\varepsilon} v^\varepsilon(x)g(x,\frac{x}{\varepsilon})\,d\Gamma^\varepsilon = \int_\Omega v^0(x)\int_{\Gamma^Y} g(x,y)\,d\Gamma^Y dx,$
  where $v^0(x)=u_e^0(x)-u_i^0(x)$ *and* $v^\varepsilon(x)=u_e^\varepsilon(x)-u_i^\varepsilon(x)$,
- $\lim_{\varepsilon\to 0}\varepsilon\int_{\Gamma^\varepsilon} S_m(v^\varepsilon(x))v^\varepsilon(x)g(x,\frac{x}{\varepsilon})\,d\Gamma^\varepsilon = \int_\Omega\int_{\Gamma^Y} I_\#(x,y)g(x,y)\,d\Gamma^Y dx,$

for some functions $u_{e,i}^0\in H^1(\Omega)$, $u_{e,i}^1\in L^2(\Omega,H^1_\#(Y))$ *and* $I_\#\in L^2(\Omega,L^2_\#(Y))$.

Proof. From the estimates (3.25), $\widetilde{u_{e,i}^\varepsilon}$ and $\widetilde{\nabla u_{e,i}^\varepsilon}$ are bounded sequences in $L^2(\Omega)$. Theorem 8 states that, up to a subsequence, they two-scale converge to $\tau_{e,i}(x,y)$ and $\xi_{e,i}(x,y)$. Since $\widetilde{u_{e,i}^\varepsilon}$ and $\widetilde{\nabla u_{e,i}^\varepsilon}$ vanish in $\Omega_{e,i}^\varepsilon$, so do $\tau_{e,i}$ and $\xi_{e,i}$. Consider $\varphi\in C(\Omega\times C_\#(Y))^2$ such that $\varphi=0$ for $y\in\overline{Y_i}$. By integrating by parts, it follows that

$$\varepsilon\int_{\Omega_e^\varepsilon}\nabla u_e^\varepsilon(x)\cdot\varphi(x,\frac{x}{\varepsilon})\,dx = \int_{\Omega_e^\varepsilon} u_e^\varepsilon(x)\left(\mathrm{div}_y\varphi(x,\frac{x}{\varepsilon})+\varepsilon\mathrm{div}_x\varphi(x,\frac{x}{\varepsilon})\right)\,dx.$$

We take the limit of this equality as ε goes to zero:

$$\int_\Omega\int_{Y_e}\tau_e(x,y)\mathrm{div}_y\varphi(x,\frac{x}{\varepsilon})\,dydx=0,$$

therefore, τ_e does not depend on y in Y_e which means that there exists a function $u_e^0\in L^2(\Omega)$ such that $\tau_e(x,y)=\chi_e(y)u_e^0(x)$ for all $(x,y)\in\Omega\times Y$. Take now $\varphi\in C(\Omega\times C_\#(Y))^2$ such that $\varphi=0$ for $y\in\overline{Y_i}$ and $\mathrm{div}_y\varphi=0$. Integrating by parts and taking the limit as ε goes to zero yields

$$\int_\Omega\int_{Y_e}\xi_e(x,y)\cdot\varphi(x,\frac{x}{\varepsilon})\,dydx = -\int_\Omega\int_{Y_e}u_e^0(x)\mathrm{div}_x\varphi(x,\frac{x}{\varepsilon})\,dydx.$$

For φ independent of y, this implies that $u_e^0 \in H^1(\Omega)$. Furthermore, integrating by parts the right-hand side of this last inequality, we get

$$\int_\Omega \int_{Y_e} \xi_e(x,y) \cdot \varphi(x, \frac{x}{\varepsilon})\, dydx = \int_\Omega \int_{Y_e} \nabla u_e^0(x) \cdot \varphi(x, \frac{x}{\varepsilon})\, dydx,$$

for all $\varphi \in C(\Omega \times C_\#(Y))^2$ such that $\mathrm{div}_y \varphi = 0$ and $\varphi(x,y) \cdot \vec{\mathbf{n}}_i = 0$ for y on Γ. Since the orthogonal of the divergence-free functions are exactly the gradients, there exists a function $u_e^1 \in L^2(\Omega, H^1_\#(Y))$ such that

$$\xi_e(x,y) = \chi_e(y) \left(\nabla u_e^0(x) + \nabla_y u_e^1(x,y) \right),$$

for all $(x,y) \in \Omega \times Y$. Likewise, there exists functions $u_i^0 \in L^2(\Omega)$ and $u_i^1 \in L^2(\Omega, H^1_\#(Y))$ such that

$$\tau_i(x,y) = \chi_i(y) u_i^0(x) \text{ and } \xi_i(x,y) = \chi_i(y) \left(\nabla u_i^0(x) + \nabla_y u_i^1(x,y) \right),$$

for all $(x,y) \in \Omega \times Y$. As estimates (3.25) hold, Theorem 9 states that there exist two-scale limits $v^0(x,y) \in L^2(\Omega \times L^2(\Gamma^Y))$ and $I_\#(x,y) \in L^2(\Omega \times L^2(\Gamma^Y))$ such that v^ε two-scale converges to v^0 and $S_m(v^\varepsilon)v^\varepsilon$ two-scale converges to $I_\#$. It remains to show that $v^0(x,y) = v^0(x) = u_e^0(x) - u_i^0(x)$ for all $(x,y) \in \Omega \times Y$, which is a direct consequence of Proposition 10. □

3.3.3 Two-scale limit of the nonlinear problem

Proposition 12. *For any (u_e, u_i), let us define the energy functional*

$$\mathcal{W}(u_e, u_i) = \int_{\Omega_e^\varepsilon} \sigma_e |\nabla u_e|^2\, dx + \int_{\Omega_i^\varepsilon} \sigma_i |\nabla u_i|^2\, dx.$$

Let $(u_e^\varepsilon, u_i^\varepsilon)$ be the solution of problem (3.6). The energy functional $\mathcal{W}$ satisfies

$$\mathcal{W}(u_e^\varepsilon, u_i^\varepsilon) + \varepsilon \int_{\Gamma^\varepsilon} S_m(u_e^\varepsilon - u_i^\varepsilon)(u_e^\varepsilon - u_i^\varepsilon)^2\, d\Gamma^\varepsilon = \int_{\Omega_e^\varepsilon} f u_e^\varepsilon\, dx. \tag{3.29}$$

Let us take $(z_e^\varepsilon, z_i^\varepsilon)$ *and denote* $v_z^\varepsilon = z_e^\varepsilon - z_i^\varepsilon$. *The following inequality holds*

$$\mathcal{W}(u_e^\varepsilon - z_e^\varepsilon, u_i^\varepsilon - z_i^\varepsilon) + \varepsilon \int_{\Gamma^\varepsilon} (S_m(v^\varepsilon)v^\varepsilon - S_m(v_z^\varepsilon)v_z^\varepsilon) \cdot (v^\varepsilon - v_z^\varepsilon)\, d\Gamma^\varepsilon \geq 0. \tag{3.30}$$

Proof.

- $\forall (u_e, u_i)$, $\mathcal{W}(u_e, u_i) \geq 0$ as sum of two positive terms.

- Let us show that $\forall (v_1, v_2)$, $(S_m(v_1)v_1 - S_m(v_2)v_2) \cdot (v_1 - v_2) \geq 0$.

$$\begin{aligned} B(v_1, v_2) &= (S_m(v_1)v_1 - S_m(v_2)v_2) \cdot (v_1 - v_2) \\ &= S_m(v_1)(v_1)^2 \cdot \left(1 - \frac{v_2}{v_1}\right)\left(1 - \frac{S_m(v_2)v_2}{S_m(v_1)v_1}\right). \end{aligned}$$

  Let us assume that $v_1 \geq v_2$. The properties (3.3) guarantee that $S_m(v_1)(v_1)^2 \geq 0$ and that $S_m(v_1)v_1 \geq S_m(v_2)v_2$.

  - If $v_1 \geq v_2 \geq 0$, then $\left(1 - \frac{v_2}{v_1}\right) \leq 0$ and $\left(1 - \frac{S_m(v_2)v_2}{S_m(v_1)v_1}\right) \leq 0$ so $B(v_1, v_2) \geq 0$.
  - If $0 \geq v_1 \geq v_2$, then $\left(1 - \frac{v_2}{v_1}\right) \geq 0$ and $\left(1 - \frac{S_m(v_2)v_2}{S_m(v_1)v_1}\right) \geq 0$ so $B(v_1, v_2) \geq 0$.
  - If $v_1 \geq 0 \geq v_2$, then $\frac{v_2}{v_1} \leq 0$ so $B(v_1, v_2) \geq 0$.

□

Now we want to show the following result:

Proposition 13. *For all* $g \in C(\Omega \times C_\#(Y))$,

$$\lim_{\varepsilon \to 0} \varepsilon \int_{\Gamma^\varepsilon} S_m(v^\varepsilon(x))v^\varepsilon(x) g(x, \frac{x}{\varepsilon})\, d\Gamma^\varepsilon = \int_\Omega \int_{\Gamma^Y} S_m(v^0(x))v^0(x) g(x, y)\, d\Gamma^Y dx,$$

where $v^0(x) = u_e^0(x) - u_i^0(x)$ *for all* $x \in \Omega$.

Proof. We develop expression (3.30) as follows

$$\begin{aligned}
&\int_{\Omega_e^\varepsilon} \sigma_e |\nabla(u_e^\varepsilon - z_e^\varepsilon)|^2 \, dx + \int_{\Omega_i^\varepsilon} \sigma_i |\nabla(u_i^\varepsilon - z_i^\varepsilon)|^2 \, dx \\
&+ \varepsilon \int_{\Gamma^\varepsilon} (S_m(v^\varepsilon)(v^\varepsilon)^2 - S_m(v^\varepsilon) v^\varepsilon v_z^\varepsilon - S_m(v) v_z^\varepsilon v^\varepsilon + S_m(v_z^\varepsilon)(v_z^\varepsilon)^2) \, d\Gamma^\varepsilon \geq 0, \\
\text{hence } &\mathcal{W}(u_e^\varepsilon, u_i^\varepsilon) + \varepsilon \int_{\Gamma^\varepsilon} S_m(v^\varepsilon)(v^\varepsilon)^2 \, d\Gamma^\varepsilon \\
&+ \int_{\Omega_e^\varepsilon} \sigma_e \nabla z_e^\varepsilon \cdot (\nabla z_e^\varepsilon - 2u_e^\varepsilon) \, dx + \int_{\Omega_i^\varepsilon} \sigma_i \nabla z_i^\varepsilon \cdot (\nabla z_i^\varepsilon - 2u_i^\varepsilon) \, dx \\
&+ \varepsilon \int_{\Gamma^\varepsilon} (-S_m(v^\varepsilon) v^\varepsilon v_z^\varepsilon - S_m(v) v_z^\varepsilon v^\varepsilon + S_m(v_z^\varepsilon)(v_z^\varepsilon)^2) \, d\Gamma^\varepsilon \geq 0.
\end{aligned}$$

Now we use the fact that $(u_e^\varepsilon, u_i^\varepsilon)$ is the solution of problem (3.6), so equality (3.29) holds. Hence, we can write

$$\begin{aligned}
&\int_{\Omega_e^\varepsilon} \sigma_e \nabla z_e^\varepsilon \cdot (\nabla z_e^\varepsilon - 2\nabla u_e^\varepsilon) \, dx + \int_{\Omega_i^\varepsilon} \sigma_i \nabla z_i^\varepsilon \cdot (\nabla z_i^\varepsilon - 2\nabla u_i^\varepsilon) \, dx \\
&+ \varepsilon \int_{\Gamma^\varepsilon} (-S_m(v^\varepsilon) v^\varepsilon v_z^\varepsilon - S_m(v_z^\varepsilon) v_z^\varepsilon v^\varepsilon + S_m(v_z^\varepsilon)(v_z^\varepsilon)^2) \, d\Gamma^\varepsilon + \int_{\Omega_e^\varepsilon} f u_e^\varepsilon \, dx \geq 0.
\end{aligned} \tag{3.31}$$

Now let us choose z_e^ε and z_i^ε as follows

$$\begin{aligned}
z_e^\varepsilon(x) &= u_e^0(x) + \alpha\varphi_e(x) + \varepsilon\varphi_e^1\left(x, \frac{x}{\varepsilon}\right), \\
z_i^\varepsilon(x) &= u_i^0(x) + \alpha\varphi_i(x) + \varepsilon\varphi_i^1\left(x, \frac{x}{\varepsilon}\right), \\
v_z^\varepsilon(x) &= z_e^\varepsilon(x) - z_i^\varepsilon(x) = v^0(x) + \alpha\Phi(x) + \varepsilon\left(\varphi_e^1\left(x, \frac{x}{\varepsilon}\right) - \varphi_i^1\left(x, \frac{x}{\varepsilon}\right)\right),
\end{aligned}$$

where $\varphi_{e,i}^1\left(x, \frac{x}{\varepsilon}\right)$ are smooth functions that two-scale converge towards $u_{e,i}^1(x, y)$ and where $\Phi(x) = \varphi_e(x) - \varphi_i(x)$. From the construction, we have the following strong convergences in $L^2(\Omega \times Y)$:

$$\begin{aligned}
&z_{e,i}^\varepsilon \text{ strongly converges to } u_{e,i}^0 + \alpha\varphi_{e,i}, \\
&\nabla z_{e,i}^\varepsilon \text{ strongly converges to } \nabla u_{e,i}^0 + \alpha\nabla\varphi_{e,i} + \nabla_y u_{e,i}^1, \\
&v_z^\varepsilon \text{ strongly converges to } v^0 + \alpha\Phi.
\end{aligned}$$

Thus, using Proposition 11 and classical results to pass to the limit in some product of two-scale convergence (Theorem 1.8 p.1488 [3]), we obtain the following two-scale convergences:

$$\begin{aligned}
&\lim_{\varepsilon\to 0}\int_{\Omega^\varepsilon_{e,i}} \sigma_{e,i}\nabla z^\varepsilon_{e,i}\cdot(\nabla z^\varepsilon_{e,i}-2\nabla u^\varepsilon_{e,i})\\
&\quad=\int_\Omega\int_Y \sigma_{e,i}\chi_{e,i}(y)(\nabla u^0_{e,i}+\alpha\nabla\varphi_{e,i}+\nabla_y u^1_{e,i})\cdot(-\nabla u^0_{e,i}+\alpha\nabla\varphi_{e,i}-\nabla_y u^1_{e,i}),\\
&\lim_{\varepsilon\to 0}\varepsilon\int_{\Gamma^\varepsilon} S_m(v^\varepsilon)v^\varepsilon v^\varepsilon_z\,d\Gamma^\varepsilon=\int_\Omega\int_{\Gamma^Y} I^\#(x,s)(v^0(x)+\alpha\Phi(x))\,dsdx,\\
&\lim_{\varepsilon\to 0}\varepsilon\int_{\Gamma^\varepsilon} S_m(v^\varepsilon_z)v^\varepsilon_z v^\varepsilon\,d\Gamma^\varepsilon=\int_\Omega\int_{\Gamma^Y} S_m(v^0(x)+\alpha\Phi(x))(v^0(x)+\alpha\Phi(x))v^0(x)\,dsdx,\\
&\lim_{\varepsilon\to 0}\varepsilon\int_{\Gamma^\varepsilon} S_m(v^\varepsilon_z)(v^\varepsilon_z)^2\,d\Gamma^\varepsilon=\int_\Omega\int_{\Gamma^Y} S_m(v^0(x)+\alpha\Phi(x))(v^0(x)+\alpha\Phi(x))^2\,dsdx.
\end{aligned}$$

Thus, passing to the two-scale limit in inequality (3.31), we have

$$\begin{aligned}
&\int_\Omega\int_Y f\chi_e(y)u^0_e(x)\,dydx-\int_\Omega\int_{\Gamma^Y} I^\#(x,s)v^0(x)\,dsdx\\
&+\int_\Omega\int_Y \sigma_e\chi_e(y)\left((\alpha\nabla\varphi_e(x))^2-(\nabla u^0_e(x)+\nabla_y u^1_e(x,y))^2\right)dydx\\
&+\int_\Omega\int_Y \sigma_i\chi_i(y)\left((\alpha\nabla\varphi_i(x))^2-(\nabla u^0_i(x)+\nabla_y u^1_i(x,y))^2\right)dydx\\
&+\int_\Omega\int_{\Gamma^Y}\alpha^2 S_m(v^0(x)+\alpha\Phi(x))\Phi(x)^2\,dsdx\\
&+\int_\Omega\int_{\Gamma^Y}-\alpha I^\#(x,s)\Phi(x)+\alpha S_m(v^0(x)+\alpha\Phi(x))v^0(x)\Phi(x)\,dsdx\geq 0.
\end{aligned}\tag{3.32}$$

Moreover, passing to the two-scale limit in equality (3.26) using test functions $\varphi_{e,i}(x)=u^0_{e,i}(x)+\varepsilon\varphi^1_{e,i}\left(x,\frac{x}{\varepsilon}\right)$ with $\varphi^1_{e,i}\left(x,\frac{x}{\varepsilon}\right)$ the previously introduced smooth functions that two-scale converge towards $u^1_{e,i}(x,y)$ gives

$$\begin{aligned}
&\int_\Omega\int_Y \sigma_e\chi_e(y)(\nabla u^0_e(x)+\nabla_y u^1_e(x,y))^2+\sigma_i\chi_i(y)(\nabla u^0_i(x)+\nabla_y u^1_i(x,y))^2\,dydx\\
&+\int_\Omega\int_{\Gamma^Y} I^\#(x,s)v^0(x)\,dsdx=\int_\Omega\int_Y f\chi_e(y)u^0_e(x)\,dydx.
\end{aligned}\tag{3.33}$$

Using this equality, and dividing every remaining term by $\alpha > 0$, we obtain from (3.32)

$$\begin{aligned}
&\alpha \int_\Omega \int_Y \sigma_e \chi_e(y)(\nabla \varphi_e(x))^2 + \alpha \sigma_i \chi_i(y)(\nabla \varphi_i(x))^2 \, dydx \\
&+ \alpha \int_\Omega \int_{\Gamma^Y} S_m(v^0(x) + \alpha\Phi(x))\Phi(x)^2 \, dsdx \\
&+ \int_\Omega \int_{\Gamma^Y} -I^\#(x,s)\Phi(x) + S_m(v^0(x) + \alpha\Phi(x))v^0(x)\Phi(x) \, dsdx \geq 0.
\end{aligned}$$

Then letting α go to zero, we obtain that for any functions $\Phi \in C(\Omega \times C_\#(Y))$

$$\int_\Omega \int_{\Gamma^Y} \left(-I^\#(x,s) + S_m(v^0(x))v^0(x)\right) \Phi(x) \, dsdx \geq 0.$$

Thus we conclude that the two-scale limit of $S_m(v^\varepsilon)v^\varepsilon$ is $S_m(v^0)v^0$. □

3.3.4 Main convergence result

Theorem 14. *Denote the sequence of solutions $(u_e^\varepsilon, u_i^\varepsilon)$ of the problem (3.6). Having the two-scale convergences previously stated, then $(u_e^0, u_i^0, u_e^1, u_i^1)$ is the unique solution of the following two-scale homogenized system given in $\Omega \times Y$*

$$\begin{aligned}
&-\nabla_x \cdot \left[\int_Y \sigma_i \chi_i(y)(\nabla_x u_i^0 + \nabla_y u_i^1(x,y)) \right] \\
&\quad - \nabla_x \cdot \left[\int_Y \sigma_e \chi_e(y)(\nabla_x u_e^0 + \nabla_y u_e^1(x,y)) dy \right] = \frac{|Y_e|}{|Y|} f
\end{aligned} \tag{3.34a}$$

$$A_m \left(S_m(u_e^0 - u_i^0)(u_e^0 - u_i^0) \right) = \nabla_x \cdot \left[\int_Y \sigma_e \chi_e(y)(\nabla_x u_e^0 + \nabla_y u_e^1(x,y)) dy \right] \tag{3.34b}$$

Furthermore, we can recover the classical homogenized and cell equations by unicity if we use the relations

$$\begin{aligned}
u_i^1(x,y) &= -\psi_i(y)\nabla_x u_i^0(x), \\
u_e^1(x,y) &= -\psi_e(y)\nabla_x u_e^0(x).
\end{aligned}$$

Proof. To find the homogenized equations we choose the test funtion

$$\begin{aligned}\varphi(x) =&\varphi_e(x) + \varepsilon\varphi_e^1\left(x, \frac{x}{\varepsilon}\right)\\ &\varphi_i(x) + \varepsilon\varphi_i^1\left(x, \frac{x}{\varepsilon}\right)\end{aligned}$$

with $\varphi_{e,i}(x) \in \mathcal{D}(\Omega)$ and $\varphi_{e,i}^1(x,y) \in \mathcal{D}(\Omega; C_\#(Y))$. Then by the partial integration and passing to the two-scale limit, using the assumptions previously shown on the nonlinear term, we derive the homogenized system of equations. □

Remark 4. Note that, when cells in suspension are considered, the intracellular medium is not connected. We can see then that the solution $\psi_i(y)$ of problem (3.12) is y. As a consequence, we have

$$\widetilde{\sigma_i} = \sigma_i \frac{|Y_i|}{|Y|} I + \sigma_i \frac{1}{|Y|}\int_{Y_i} -\nabla_y \psi_i(y)\, dy = \sigma_i \frac{|Y_i|}{|Y|} I + \sigma_i \frac{1}{|Y|}\int_{Y_i} -\nabla_y (y)\, dy = 0.$$

Thus, problem (3.34) in $\Omega \times Y$ becomes

$$\begin{aligned}&-\nabla_x \cdot \left(\widetilde{\sigma_e}\nabla_x u_e^0\right) = 0,\\ &A_m\left(S_m(u_e^0 - u_i^0)(u_e^0 - u_i^0)\right) = \nabla_x \cdot \left(\widetilde{\sigma_e}\nabla_x u_e^0\right) = 0,\\ &+ \text{ boundary conditions},\end{aligned} \tag{3.35}$$

which implies that $v^0 = u_e^0 - u_i^0 = 0$. Thus, u_e^0 can only be influenced by u_i^0 if the cells are assumed to be connected.

Equivalent tissue conductivity. Let us remark that S_m, the homogenized membrane conductivity, does not represent the tissue conductivity. Nevertheless, one can obtain an equivalent tissue conductivity from S_m using the following formula:

$$\sigma_m^{eq} = \widetilde{\sigma_e} + \frac{\widetilde{\sigma_i} l_\Omega^2 A_m S_m}{\widetilde{\sigma_i} + l_\Omega^2 A_m S_m}, \tag{3.36}$$

where we assume that $\widetilde{\sigma_e}$ and $\widetilde{\sigma_i}$ are scalar and where l_Ω is the characteristic length of the domain Ω. Note that the right-hand term of (3.36) is homogeneous to a conductivity (S/m).

Remark 5. This formula is obtained from equations (3.34a)-(3.34b). Assume for the sake of simplicity that S_m is a constant and assume that $\widetilde{\sigma_e}$ and $\widetilde{\sigma_i}$ are scalar. The homogenized problem can then be written as

$$\begin{aligned} &-\nabla\cdot\left(\widetilde{\sigma_e}\nabla u_e^0+\widetilde{\sigma_i}\nabla u_i^0\right)=0,\\ &\left(id-\frac{\widetilde{\sigma_i}}{A_mS_m}\Delta\right)u_i^0=u_e^0,\\ &+\ \text{boundary conditions.} \end{aligned} \tag{3.37}$$

Denoting by $\mathcal{L}$ the linear inversible operator

$$\mathcal{L}=id-\frac{\widetilde{\sigma_i}}{A_mS_m}\Delta,$$

problem (3.37) is equivalent to

$$\begin{aligned} &-\nabla\cdot\left((\widetilde{\sigma_e}+\widetilde{\sigma_i}\mathcal{L}^{-1})\nabla u_e^0+\widetilde{\sigma_i}[\nabla,\mathcal{L}^{-1}]u_e^0\right)=0,\\ &\left(id-\frac{\widetilde{\sigma_i}}{A_mS_m}\Delta\right)u_i^0=u_e^0,\\ &+\ \text{boundary conditions.} \end{aligned} \tag{3.38}$$

Let us look at the symbol of the operator $\mathcal{L}$ in the domain Ω of length l_Ω:

$$\Sigma(k)=1+\frac{\widetilde{\sigma_i}}{A_mS_ml_\Omega^2}|k|^2.$$

In a first approximation, one can consider only the first mode ($|k|=1$). Assuming that the commutator $[\nabla,\mathcal{L}^{-1}]$ is negligible, problem (3.38) is reduced to

$$\begin{aligned} &-\nabla\cdot\left(\left(\widetilde{\sigma_e}+\widetilde{\sigma_i}\left(1+\frac{\widetilde{\sigma_i}}{A_mS_ml_\Omega^2}\right)^{-1}\right)\nabla u_e^0\right)=0,\\ &+\ \text{boundary conditions,} \end{aligned} \tag{3.39}$$

where $\widetilde{\sigma_e}+\widetilde{\sigma_i}\left(1+\frac{\widetilde{\sigma_i}}{A_mS_ml_\Omega^2}\right)^{-1}=\sigma_m^{eq}$.

Remark 6. Equation (3.39) can be related to the steady-state equation (2.23) ob-

tained for the phenomenological model using two current densities presented in Chapter 2. One can observe the formula of the equivalent tissue conductivity obtained using a homogenization procedure is similar to the formula of the equivalent tissue conductivity obtained for the phenomenological model using two current densities.

3.3.5 Numerical convergence in the linear case

In this section, we assume that $S_m = S_m^s$. We want to observe numerically the convergence of problem (3.6) to the derived homogenized problem (3.34), and to find the rate of convergence. In order to do this, we run simulations for problem (3.6) for several values of ε and one simulation for the homogenized problem (3.34). All simulations should be carried out on the same test case: we choose a two-dimensional domain in the shape of a square of size 1. An electric field is applied between two plate electrodes positionned along the left and right borders of the domain. We assume the cells to be circular of radius $0.3\times\varepsilon$. We run the simulations for several sizes of periodic cell:

$$\varepsilon \in \left(\frac{1}{5}, \frac{1}{10}, \frac{1}{15}, \frac{1}{20}, \frac{1}{25}\right).$$

In Figure 3.2, we display the quantity $u^\varepsilon - u^0$ for several sizes of periodic cell to observe how the error is spatially distributed.

Remark 7. We notice that the error is mainly localized next to the two borders where Dirichlet boundary conditions are applied. It is possible to avoid this issue by using a corrector.

To find the rate of convergence, we compute the relative L^2 errors on u_e^ε and u_i^ε, defined as

$$e_{e,L^2}^\varepsilon = \frac{\|u_e^\varepsilon - u_e^0\|_{L^2(\Omega_e^\varepsilon)}}{\|u_e^\varepsilon\|_{L^2(\Omega_e^\varepsilon)}} \text{ and } e_{i,L^2}^\varepsilon = \frac{\|u_i^\varepsilon - u_i^0\|_{L^2(\Omega_i^\varepsilon)}}{\|u_i^\varepsilon\|_{L^2(\Omega_i^\varepsilon)}}.$$

We use the log-log scale to obtain approximatively the convergence rate, which is

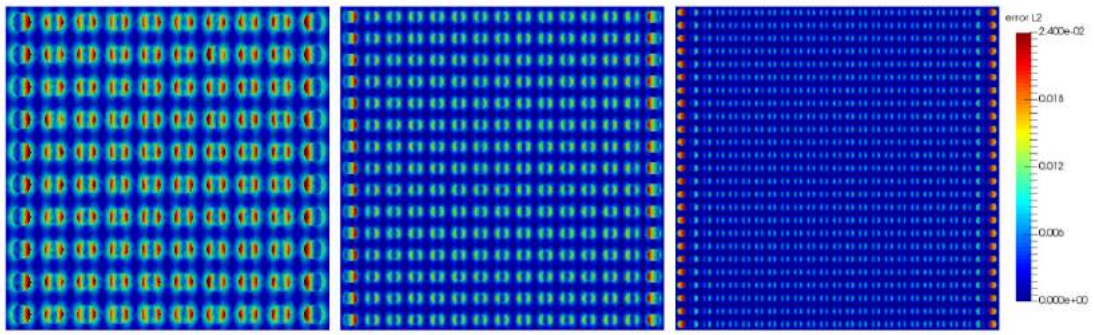

Figure 3.2: Error between the microscopic model and the bidomain model ($|u_e^0 - u_e^\varepsilon|$ outside the cells and $|u_i^0 - u_i^\varepsilon|$ inside the cells) for three different sizes of cells $\varepsilon \in \left(\frac{1}{10}, \frac{1}{15}, \frac{1}{25}\right)$.

1 for both quantities (see Figure 3.3b).

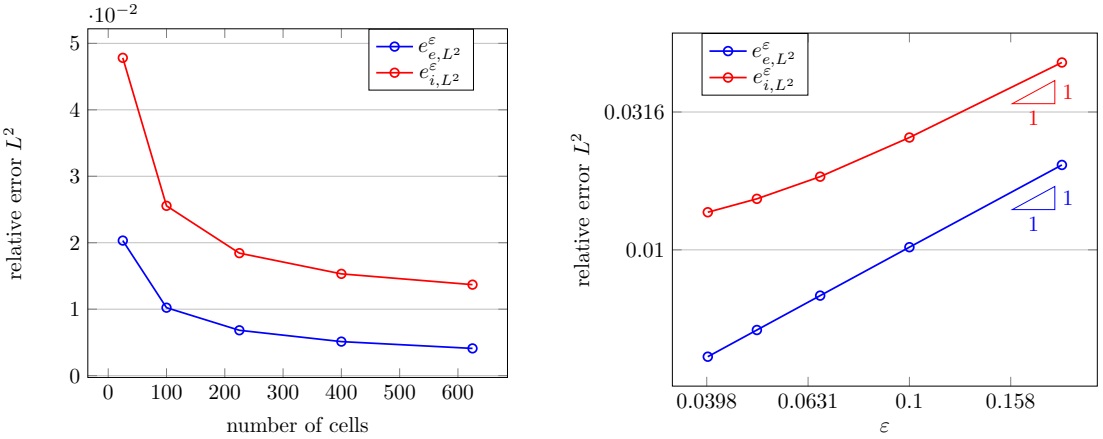

Figure 3.3: Relative error in L^2 norm between the microscopic model and the bidomain model (e^ε_{e,L^2} outside the cells and e^ε_{i,L^2} inside the cells).

3.4 Numerical results on the bidomain model

To solve numerically the macroscopic problem (3.34), one must first compute the homogenized conductivities $\widetilde{\sigma_e}$ and $\widetilde{\sigma_i}$, that depend on the cell problem (3.12),

that must then be solved first. In particular, it implies to choose a specific geometry for one cell. In this section, we investigate first the influence of the choice of the 3D cell geometry on the value of the homogenized conductivities. Then, we present some 2D numerical results of the bidomain nonlinear static model.

3.4.1 Influence of the cell geometry on the homogenized conductivities

The macroscopic model (3.34) obtained via the homogenization process presents the advantage of containing some knowledge of the microscopic problem at the cell scale. This knowledge manifests itself in particular when are computed the homogenized conductivities

$$\begin{aligned} \widetilde{\sigma_e} &= \sigma_e \tfrac{|Y_e|}{|Y|} I_3 + \sigma_e \tfrac{1}{|Y|} \textstyle\int_{Y_e} -\nabla_y \psi(y) dy, \\ \widetilde{\sigma_i} &= \sigma_i \tfrac{|Y_i|}{|Y|} I_3 + \sigma_i \tfrac{1}{|Y|} \textstyle\int_{Y_i} -\nabla_y \psi(y) dy. \end{aligned}$$

They depend on ψ, which is the solution of the following cell problem:

$$\begin{cases} -\sigma \Delta_y \psi = 0, & \text{in } Y_e \cup Y_i, \\ \sigma_i (\nabla_y \psi_i^{1,2,3} - e^{1,2,3}) \cdot \vec{\mathbf{n}}_i = \sigma_e (\nabla_y \psi_e^{1,2,3} - e^{1,2,3}) \cdot \vec{\mathbf{n}}_i, & \text{on } \Gamma_Y, \\ \sigma_e (\nabla_y \psi_e^{1,2,3} - e^{1,2,3}) \cdot \vec{\mathbf{n}}_i = 0, & \text{on } \Gamma_Y. \end{cases} \tag{3.40}$$

We want to investigate the effect of the chosen cell geometry on the value of the homogenized conductivitie tensors $\widetilde{\sigma_e}$ and $\widetilde{\sigma_i}$. In particular, we want to investigate the difference between cells in suspension and connective tissues. We use the software FreeFem++ to solve (3.40) and to compute $\widetilde{\sigma_e}$ and $\widetilde{\sigma_i}$ in four different reference cases presented in Figure 3.4. We used the values of $\sigma_{e,i}$ presented in Table 3.2.

The computed value of the homogenized conductivitie tensors $\widetilde{\sigma_e}$ and $\widetilde{\sigma_i}$ are presented in Table 3.4.1.

Let us remark first that in all chosen configurations, we never have that $\widetilde{\sigma_i} = \sigma_i \times I_3$ and/or $\widetilde{\sigma_e} = \sigma_e \times I_3$. When cells in suspension are considered (Figure 3.4a), it appears that $\widetilde{\sigma_i} = 0$ and $\widetilde{\sigma_e} = \frac{|Y_e|}{|Y|}\sigma_e \times I_3$, which is in accordance with what

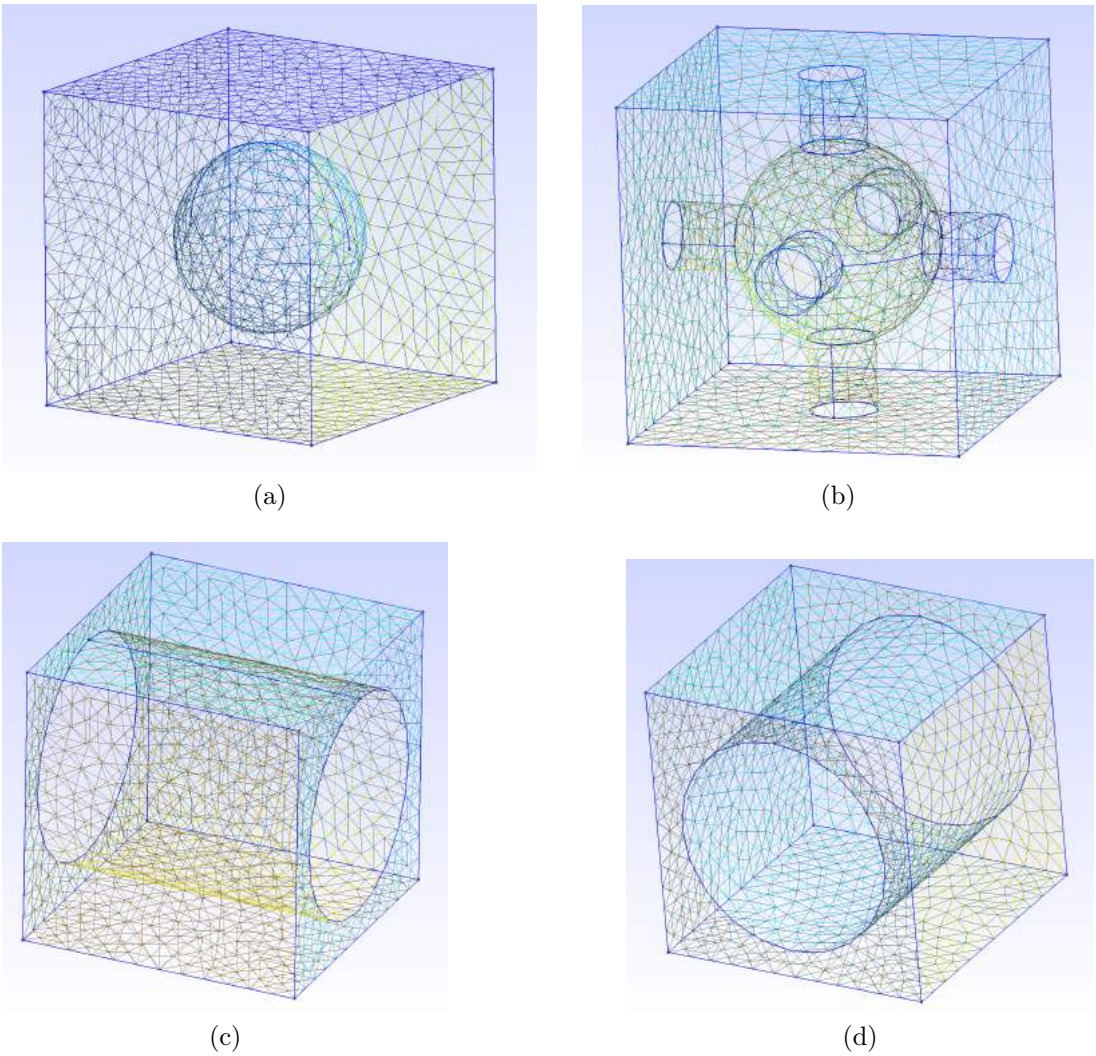

(a) (b)

(c) (d)

Figure 3.4: Meshes of the two different cell geometries. External domain - $[0,1] \times [0,1] \times [0,1]$. Cell - **(a)** Centered sphere of radius 0.3. **(b)** Centered sphere of radius 0.3 with cylindrical junctions of radius 0.1. **(c)** Centered cylinder of radius 0.1 and of axis (Ox). **(d)** Centered cylinder of radius 0.1 and of axis (Oy).

was stated in Remark 4. When cells are connected in all three directions (Figure 3.4b), $\widetilde{\sigma_i}$ is no longer 0 but both tensors have diagonal forms, namely $\widetilde{\sigma_i} = a \times I_3$ and $\widetilde{\sigma_e} = b \times I_3$. This is a consequence of the symmetry in all three directions of the domain. When cylindrical cells are considered (Figures 3.4c and 3.4d), the cell domain is no longer symmetric in all three direction. The consequence is that the

Geometry	$\widetilde{\sigma_i}(1,1)$	$\widetilde{\sigma_i}(1,2)$	$\widetilde{\sigma_i}(1,3)$	$\widetilde{\sigma_i}(2,1)$	$\widetilde{\sigma_i}(2,2)$	$\widetilde{\sigma_i}(2,3)$	$\widetilde{\sigma_i}(3,1)$	$\widetilde{\sigma_i}(3,2)$	$\widetilde{\sigma_i}(3,3)$
Fig. 3.4a	6.18e-17	-2.79e-17	-4.64e-17	-1.09e-16	2.49e-16	-9.11e-19	-5.19e-17	-9.62e-18	-5.38e-17
Fig. 3.4b	**0.022**	3.55e-7	7.34e-7	3.55e-7	**0.022**	1.33e-07	7.34e-7	1.33e-07	**0.022**
Fig. 3.4c	**0.228**	-2.92e-19	1.03e-19	-9.17e-18	1.17e-15	1.59e-16	3.73e-19	-1.99e-17	-3.66e-17
Fig. 3.4d	1.74e-16	-1.49e-18	8.73e-17	1.81e-20	**0.228**	2.41e-20	1.06e-16	-9.95e-19	1.30e-16
Geometry	$\widetilde{\sigma_e}(1,1)$	$\widetilde{\sigma_e}(1,2)$	$\widetilde{\sigma_e}(1,3)$	$\widetilde{\sigma_e}(2,1)$	$\widetilde{\sigma_e}(2,2)$	$\widetilde{\sigma_e}(2,3)$	$\widetilde{\sigma_e}(3,1)$	$\widetilde{\sigma_e}(3,2)$	$\widetilde{\sigma_e}(3,3)$
Fig. 3.4a	**4.22**	2.84e-4	-2.48e-4	2.84e-4	**4.22**	4.61e-05	-2.48e-4	4.61e-05	**4.22**
Fig. 3.4b	**3.87**	-2.64e-4	-1.67e-4	-2.09e-4	**3.87**	-9.48e-6	-1.13e-4	-9.48e-6	**3.87**
Fig. 3.4c	**2.50**	-5.21e-08	-9.61e-08	-5.21e-08	**1.62**	-8.03e-05	-9.61e-08	-8.03e-05	**1.62**
Fig. 3.4d	**1.62**	4.30e-08	7.36e-05	4.30e-08	**2.50**	2.72e-07	7.36e-05	2.72e-07	**1.62**

Table 3.1: Computed homogenized conductivities $\widetilde{\sigma_i}$ and $\widetilde{\sigma_e}$ in the four reference cases presented in Figure 3.4.

tensors are no longer scalar, but remain diagonal. Should the symmetry be more disrupted, both tensors could no longer be diagonal (data not shown).

3.4.2 Numerical results obtained in 2D with the homogenized model

The nonlinear case. In this section, we used the following formula for the nonlinear conductivity S_m

$$S_m = S_m(u_e - u_i) = S_m^s + \frac{1}{\eta} \times \frac{1 + \tanh(k(|u_e - u_i| - V_{th}))}{2}. \tag{3.41}$$

Problem (3.34) is solved using a classical fixed point iteration. Numerical simulations were done using the Finite Element software FreeFem++ [61] on the 2D-mesh featured in Figure 3.5. This 2D domain is to be related to the experimental set up presented in Figure 2.1. As the length of the needles is very large compared to the diameter of the needles, the numerical problem is reduced to a 2D problem as we did already in Chapter 2.

The parameters used for the simulations are those presented in Table 3.2. The simulated currents are calculated with the volumic method (see section 2.3.0.3). Figure 3.6 shows the simulated currents flowing through the needles when a 100 μs pulse is applied between the needles, with different nominal electric fields (375 V/cm, 625 V/cm, 875 V/cm, 1125 V/cm, 1375 V/cm), for electrodes of diameter 0.7 mm. As we are working on a steady-state hypothesis, the current is logically

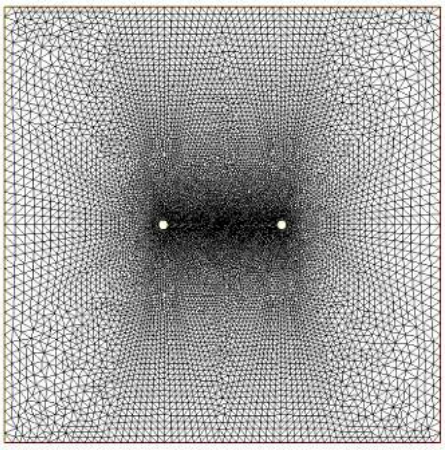

Figure 3.5: Mesh of the computational domain used for the simulations of the bidomain model.

constant throughout the pulse.

Table 3.2: Parameters of the simulations for the bidomain model.

Parameter	Symbol	Value	Unit
Intracellular conductivity	σ_i	0.455	S/m
Extracellular conductivity	σ_e	5	S/m
Membrane conductivity at rest	S_m^s	1.9	S/m^2
Maximal membrane conductivity	$1/\eta$	10^4	S/m^2
Electroporation threshold	V_{th}	1.5	V
Electric field threshold	E_{th}	575	V/cm
Parameter in the sigmoid	k	40	V^{-1}

In Figures 3.7 and 3.8 are displayed the spatial distributions of the homogenized electric field ∇u_e and the homogenized transmembrane potential $v = u_e - u_i$ for an applied nominal electric field of 875 V/cm. Figure 3.7 was obtained while calculating the homogenized conductivities using connected cells (see Figure 3.4b) and Figure 3.8 was obtained while calculating the homogenized conductivities using cells in suspension (see Figure 3.4a).

When cells in suspension are considered, the transmembrane potential v is equal to zero (see Figure 3.8b). This result was expected (see Remark 4), but the consequence is that the homogenized membrane conductivity $S_m(u_e - u_i)$ is always

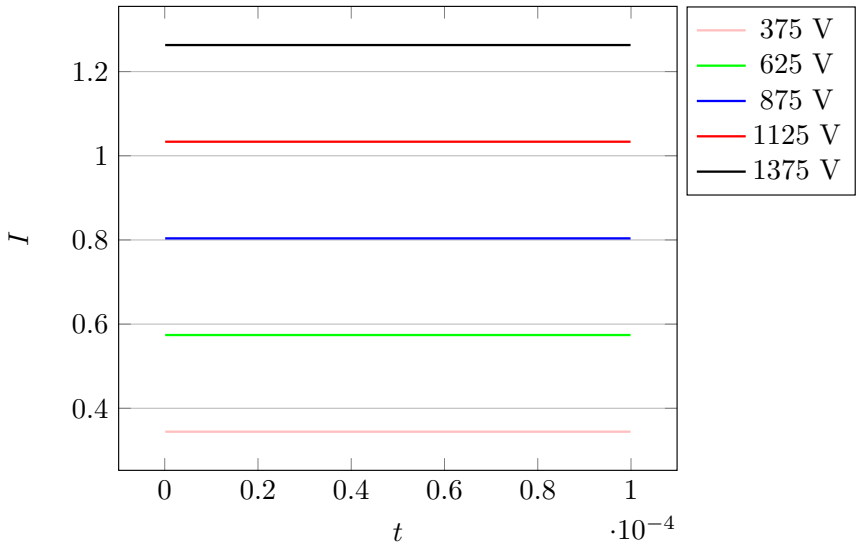

Figure 3.6: Simulated current of the static homogenized model for five different voltage applied.

equal to S_m^s, its value at rest. When the cells are connected, the transmembrane potential v presents a symmetry (see Figure 3.7b). To determine where the tissue is electroporated, it is useful to consider the spatial distribution of the tissue conductivity. The equivalent tissue conductivity σ_m^{eq}, obtained using formula (3.36), is displayed in Figure 3.9 for connected cells and cells in suspension. As $v = 0$ in the case of cells in suspension, the conductivity $\sigma_m^{eq}(u_e - u_i)$ is equal to the conductivity at rest all over the tissue (see Figure 3.4.2). As a consequence of the previously noted symmetry of $v = u_e - u_i$ in the case of connected cells, the conductivity $\sigma_m^{eq}(u_e - u_i)$ is always equal to the conductivity at rest at the point between the two electrodes for all applied voltages (see Figure 3.4.2). These features are not in accordance with the experiments.

Back to the linear case. As the equivalent tissue conductivity obtained using the bidomain model is not satisfying, we assume in this section that $S_m = S_m^s$. We want to observe, for all 4 cases of reference cells presented in Figure 3.4, how the homogenized transmembrane potential v is distributed all over the tissue. We solve system (3.34) taking $S_m = S_m^s$ and we display in Figure 3.10 the quantity $|v|$

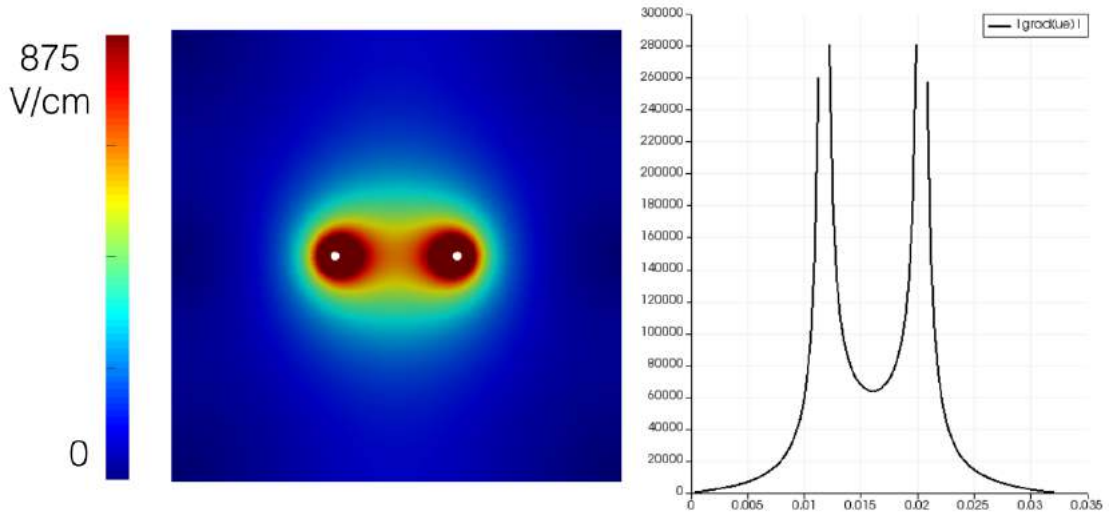

(a)

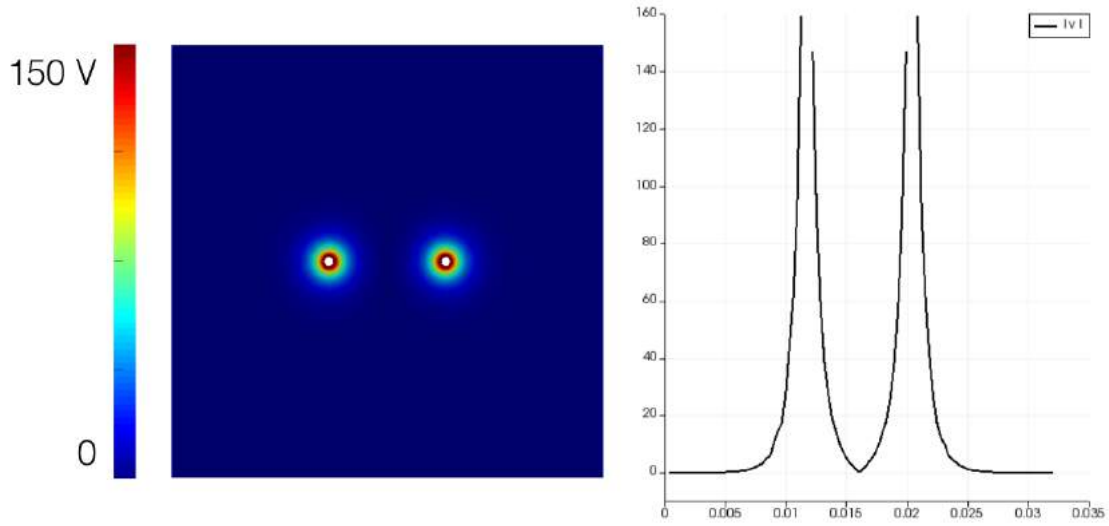

(b)

Figure 3.7: Spatial distribution of **(a)** the homogenized electric field ∇u_e and of **(b)** the homogenized transmembrane potential $v = u_e - u_i$ computed with the static bidomain model for an applied voltage of 875 V for connected cells (see Figure 3.4b).

obtained using all 4 cases of reference cells. For the case of comparison, we also display the quantity $|\nabla u_e|$.

As it was previously noted in the nonlinear case, if the tissue is made of cells

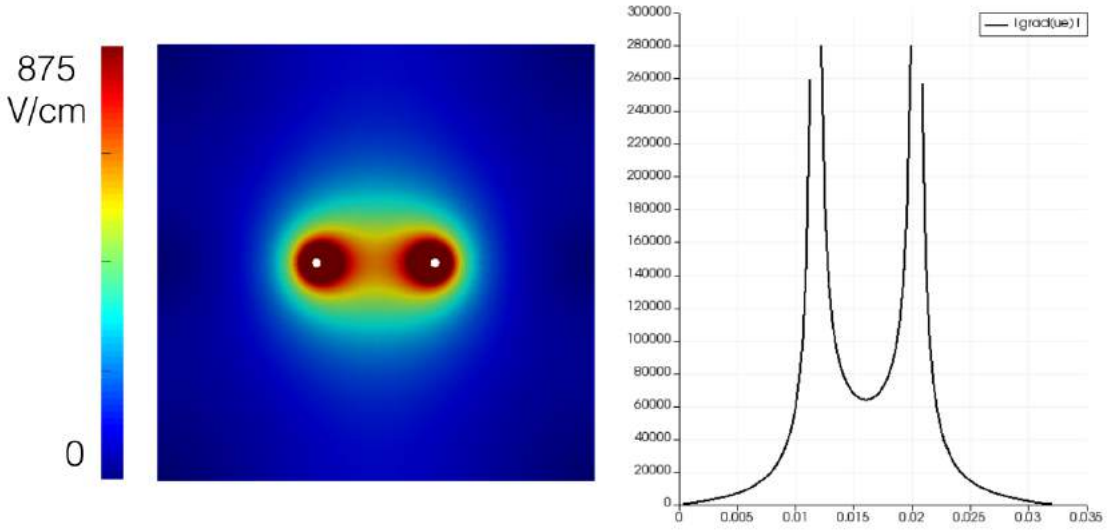

(a)

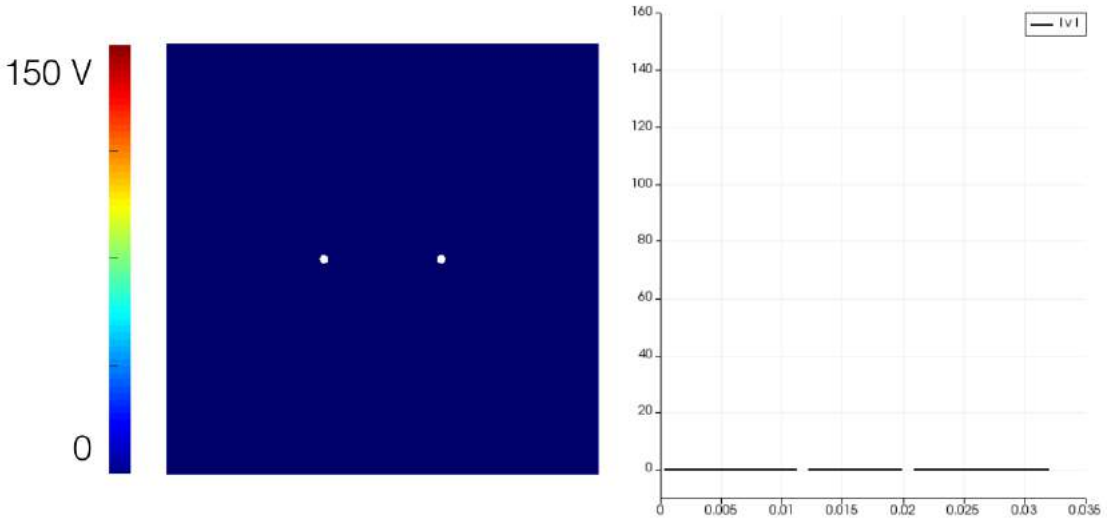

(b)

Figure 3.8: Spatial distribution of **(a)** the homogenized electric field ∇u_e and of **(b)** the homogenized transmembrane potential $v = u_e - u_i$ computed with the static bidomain model for an applied voltage of 875 V for cells in suspension (see Figure 3.4a).

in suspension, v is zero all over the tissue. There is almost no difference between connected cells and cylindrical cells of axis (Ox), as the electric field is applied in the direction given by the axis (Ox). The distribution of v could be in accordance

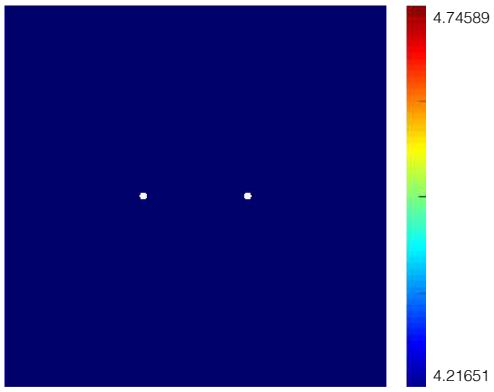

(a) Cells in suspension

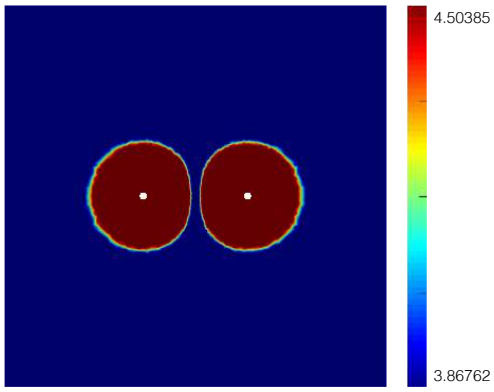

(b) Connective tissue

Figure 3.9: Spatial distribution of the homogenized tissue conductivity $\sigma_m^{eq}(v)$ computed with the static bidomain model.

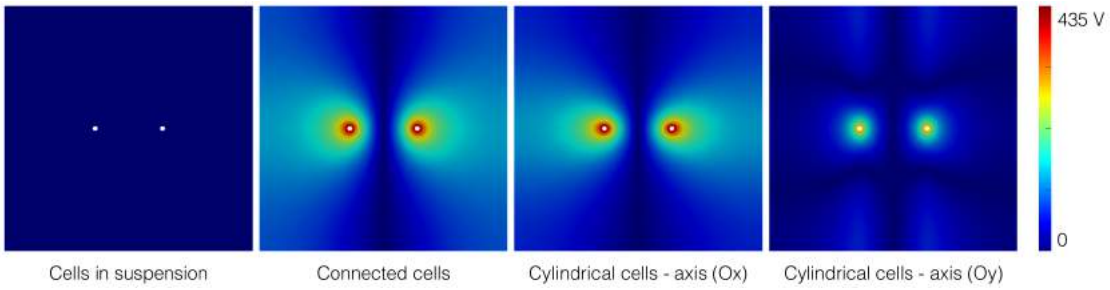

(a) Distribution of the homogenized transmembrane potential $|v|$

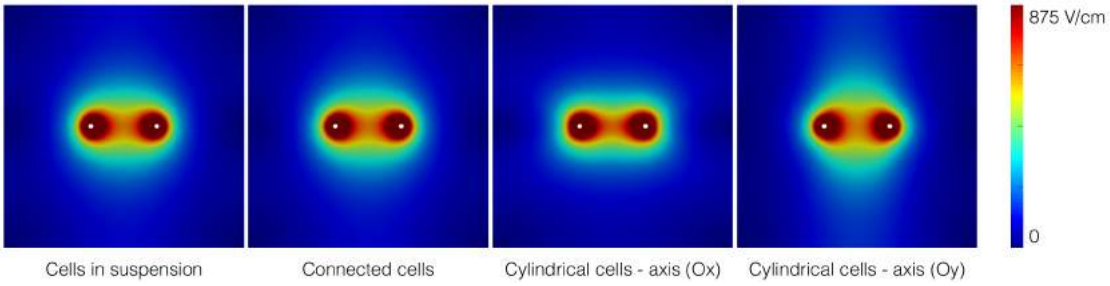

(b) Distribution of the homogenized gradient of the extracellular potential $|\nabla u_e|$

Figure 3.10: Spatial distribution of two homogenized quantities computed in the linear case: **(a)** $|v|$ and **(b)** $|\nabla u_e|$ are obtained in all 4 cases of reference cells presented in Figure 3.4.

with the electroporated area observed in the experiments if v was not zero at the middle point between the electrodes. When the electric field is applied perpendic-

ular to the direction of the cells (cylindrical cells of axis (Oy)), the distribution of v no longer corresponds directly or indirectly to the electroporated area observed in the experiments. On the other hand, the distribution of the gradient of the extracellular potential $|\nabla u_e|$ permits to identify a zone that seems to be in accordance with what is observed during the experiments. For isotropic tissues, may they be made of connected cells or of cells in suspension, the distribution of $|\nabla u_e|$ is located all around the electrodes in the shape of an eight. This zone is similar when anisotropic tissues are considered, nevertheless it appears wider in the case of an electric field applied perpendicular to the direction of the cells (cylindrical cells of axis (Oy)).

What quantity should the membrane conductivity S_m depend on? We have just seen that, already in the linear case, the spatial distribution of $|v|$ does not correspond to the electroporated area expected from the experiments. On the other hand, the spatial distribution of the quantity $|\nabla u_e|$ seems to fit better the electroporated area expected from the experiments. It is then expected that the conductivity should depend on the physical quantity ∇u_e instead of the homogenized transmembrane potential v. We artificially replace the way the nonlinear function S_m is computed in system (3.34). Namely, instead of taking $S_m = S_m(v) = S_m(u_e - u_i)$, we took

$$S_m = S_m(\nabla u_e) = S_m^s + \frac{1}{\eta} \times \frac{1 + \tanh(k(|\nabla u_e| - E_{th}))}{2}. \tag{3.42}$$

Figure 3.11 shows the spatial distribution of the simulated equivalent tissue conductivity $\sigma_m^{eq}(\nabla u_e)$ for both types of tissues: cells in suspension and connected cells.

As Figure 3.11 give more desirable results, we wonder how to obtain a dependence on ∇u_e for the membrane conductivity S_m. We believe we should go further in the formal expansion of the transmembrane potential $v^\varepsilon(x) = u_e^\varepsilon(x)_{|\Gamma^\varepsilon} - u_i^\varepsilon(x)_{|\Gamma^\varepsilon}$. Formally, the first term of the expansion is the limit $v^0 = u_e^0 - u_i^0$. As the spatial distribution of $|v^0|$ does not correspond to the electroporated area expected from the experiments, perhaps we need to take the next term in the expansion into

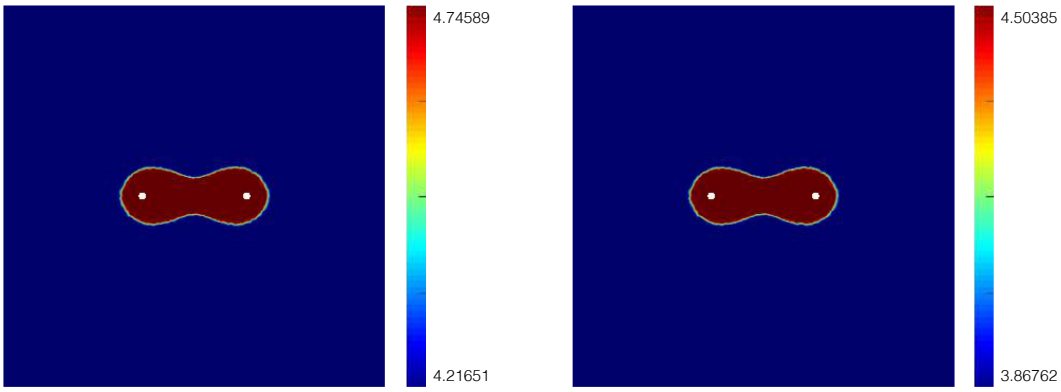

(a) Cells in suspension (b) Connective tissue

Figure 3.11: Spatial distribution of the homogenized tissue conductivity $\sigma_m(\nabla u_e)$ computed with the static bidomain model.

account. The next term reveals a dependence on $\nabla_x u_e^0$ (and $\nabla_x u_i^0$), whose spatial distribution is closer to the experimental electroporated area.

3.5 Conclusion

In this third chapter, we investigated the possibility the derive a model of tissue electroporation starting from a well-established model of cell electroporation. The macroscopic model is obtained using a rigorous homogenization procedure, and the numerical convergence of the microscopic model towards the macroscopic one is verified. One interest of such an approach is that the microscopic structure of the tissue can affect the final macroscopic model through the reference cell problem. Indeed, the cell geometry, that can be significatively different from one type of tissue to another, influences the global result by modifying the value of the homogenized conductivity tensors. Simulations of the bidomain model permit to determine the spatial distribution of the electroporated homogenized tissue in different configurations (cells in suspension and connected cells). The dependance of the microscopic membrane conductivity on the transmembrane voltage, which results in the dependance of the homogenized equivalent tissue conductivity on the difference between the extracellular homogenized potential and the intracellu-

lar homogenized potential, is proven to be not conclusive at the tissue scale. A future work would be to modify the formal expansion in order to obtain, after homogenization, a dependance of the homogenized equivalent tissue conductivity on the gradient of the homogenized extracellular potential.

Part II

Modeling enzyme-based therapies

Chapter 4

A continuum mechanics model of enzyme-based tissue degradation in cancer therapies

This chapter is based on the submitted pre-print [43], which was written in collaboration with R. Natalini (IAC-CNR) and C. Poignard (Inria Bordeaux). Insights on the biological framework of the study and on the experiments were provided by E. Signori (CNR).

4.1 Motivations

Transport through the extracellular matrix (ECM) is a critical step in cell targeted drug delivery. To reach the cell membrane, the therapeutic agent must diffuse through the ECM before being fully degraded by the extracellular nucleases [30]. It is thought that treatment with agents that degrade the ECM components, hyaluronidase for example [29, 57], have the potential to increase the drugs penetration through the tissue and ultimately into cells [125]. They are therefore used in medicine to improve drugs dispersion and delivery [18].

DNA vaccination. There are several physical approaches to perform nonviral gene therapy. The simplest is the injection of naked DNA in the skeletal or cardiac muscle which leads to some expression of the injected genes [126]. However, this expression is very low and very variable from sample to sample. The main physical barrier encountered by DNA plasmids, the cell membrane, can be overcome using DNA electrotransfer [9]. But in the case of skeletal muscle, there is another limitation which is the access of the plasmid DNA to the muscle fiber surface. Controlled and partial degradation of ECM with matrix degrading enzymes is used to increase the diffusion and distribution of plasmid DNA into the muscle fiber. It has been shown that a pretreatment of skeletal muscle with hyaluronidase followed by DNA electrotransfer improves gene expression [113, 1, 108].

Chemotherapy. Delivery of drugs to tumor cells occurs by two independent mechanisms: diffusion and convection. However, the composition and structure of tumor-derived ECM can slow down the movement of therapeutic molecules within the tumor [51, 34, 83]. In addition, the disorganized vascular network and the absence of functional lymphatics cause increased interstitial fluid pressure (IFP), which is a major obstacle to transcapillary transport [13]. As far as diffusion is concerned, it was proven that an intratumoral injection of matrix degrading enzymes removes diffusive hindrance to the penetration of therapeutic molecules in tumor models [47, 54]. As far as convection is concerned, IFP may be temporarily reduced by degrading the tumor ECM. It has been shown that collagenase and hyaluronidase reduce IFP, thereby improving the uptake and distribution of molecules within solid tumors [45, 46, 27].

Need of numerical models. From the biological point of view, the effects of matrix degrading enzymes on drug transport is well known. However, the litterature suffers from a lack of models describing the active transport of those enzymes in the extracellular medium and the resulting changes on the ECM. The aim of this chapter is to provide a mathematical model that addresses this phenomenon in order to offer a better understanding of the physical involved phenomena. The model consists of a nonlinear system of partial differential equation (PDEs). It is

derived directly from physical conservation laws. Constitutive relations are added to close the system. The derivation's steps are presented in Figure 4.4. We adopt a poroelastic approach to model the mechanics of a biological tissue. This choice is made to take into account the swelling of the tissue when fluid is added by injection. It is also in accordance with the studies stating that biological tissue deformations are not negligible in numerical models describing drug delivery [118]. This choice implies to first derive equations with Eulerian formalism and then reduce them to a fixed reference domain via a suitable change of variables in order to make the numerical processing possible. In addition, equations on the volume fractions of each component of the tissue are included to take into account the structural changes. In the end, the main variables of interest of the model are the three different volume fractions, the interstial pressure, the displacement and the concentrations of enzyme and therapeutic agent respectively. The final formulation of the model, system (4.55), is displayed in Section 4.4. To our knowledge, this is the first model describing the alteration of a poroelastic medium produced by chemical species injected directly in the medium. Alteration of a porous media is taken into account in [2, 100] but within a rigid structure. Many mathematical models of passive transport into a poroelastic medium do not take into account exchanges between phases [16, 118]. In [53, 75, 74], models including exchanges between phases are presented on closed poroelastic mixtures (no external sources or sinks). However, the changes are not mediated by external species. In [115, 116], magma is modeled as a poroelastic medium with varying porosity due to temperature changes. However, those changes are assumed to be infinitesimal. In [32, 10], poroelastic models taking into account ECM degradation by matrix degrading enzymes produced by tumor cells are presented within the particular framework of tumor growth. Nevertheless, these models have a very different focus, namely showing the formation of fibrosis. They also make slightly different assumptions: the ECM is rigid, the matrix degrading enzymes are produced by tumor cells and the cells' movement is the one of an elastic fluid. The goal of the chapter is to derive a model that combines the effect of an injection of ECM degradation enzyme with a poroelastic macroscopic model of biological tissue (skeletal muscle

or tumor tissue), and to provide a numerical method that allows to simulate the complete model in 1D-, 2D-, and axisymmetric configurations in order to compare the results with the qualitative data available in the literature. Let us note that the long-term goal of the project is to provide a first step towards the numerical optimization of drug delivery with enzyme pretreatment.

4.2 Main results of the chapter

Numerical simulations illustrating biological phenomena. After testing the model with a set of numerical simulations to investigate the effect of the new parameters added (Figures 4.11 and 4.13), we use the model to describe two situations: the incubation of a spheroid into an ECM degradation enzyme and the intratumoral injection of enzyme in vivo. We observe that, in the first test case, given the dependency of the diffusion tensor on the porosity variable [77], a pretreatment with ECM degradation enzyme affects the distribution of therapeutic agents, thereby improving the diffusion process. Where without pretreatment, the macromolecules stay mainly at the periphery of the spheroid, a pretreatment with hyaluronidase permit to obtain a wider distribution (Figure 4.1).

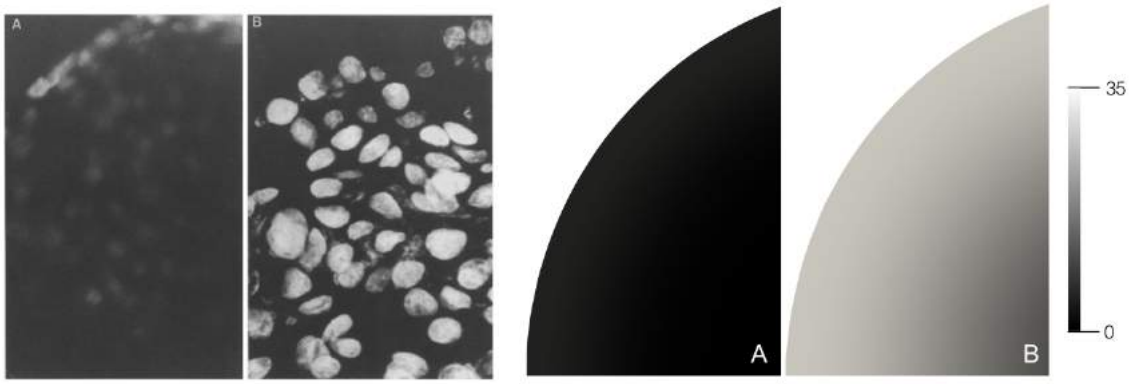

Figure 4.1: Comparison between experimental doxuribicin fluorescence (left, data from [69]) and numerically simulated (see Figure 4.17 in Section 4.6) concentration of anticancer agent in a spheroid previously incubated with hyaluronidase (B) or not (A).

In the second case, given the dependency of the pressure on the porosity variable, an intratumoral injection of enzyme results in a reduction of the IFP. This reduction depends on the enzyme's concentration and reaches a maximum value, a further increase of the dose resulting in a smaller reduction, which is in accordance with the experiments (Figure 4.2).

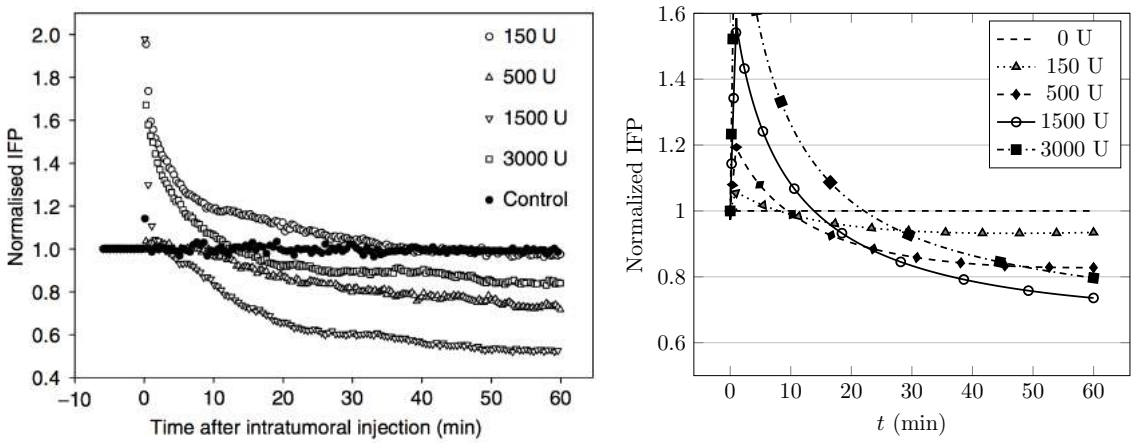

Figure 4.2: Comparison between experimental IFP (left, data from [46]) and numerically simulated IFP (see 4.6.3.4). Normalized interstitial fluid pressure is represented in both cases as a function of time after intratumoral injection of 150 U, 500 U, 1500 U and 3000 U hyaluronidase in tumors compared to no pretreatment (intratumoral injection of saline solution).

It also appears that a pretreatment with ECM degradation enzyme affects the distribution of therapeutic agents, thereby increasing its area of action by improving both the diffusion and the convection processes. This is once more in accordance with the experiments (data from [46]). Indeed, without pretreatment, the macromolecules stay only at the periphery of the tumor, the transcapillary transport being greatly reduced by the high IFP inside the tumor. A pretreatment with hyaluronidase permit to obtain a wider distribution. The molecules are thus distributed all over the tumor (Figure 4.3).

4.2.1 Outline

In this chapter, we construct a nonlinear spatio-temporal model for the active

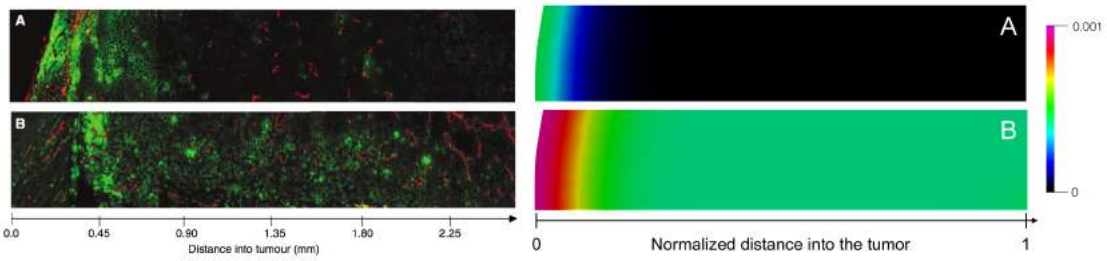

Figure 4.3: Comparison between experimental distribution of anticancer fluorescent agent (left, data from [46]) and numerically simulated concentration of agent. In case A, no pretreatment was previously performed on the tissue whereas in case B, the tissue was pretreated with 1500 U hyaluronidase.

transport of ECM degradation enzyme into a poroelastic biological tissue coupled with the passive transport of therapeutic agents. Section 4.3 is devoted to a precise description of our model following the scheme presented in Figure 4.4. It is divided in two parts: in the first part, we derive some equations from physical conservation laws, while in the second part, we conclude the formulation of our model stating some constitutive relations. Section 4.4 is devoted to the simplification of the model. We formulate the equations of the model in a fixed reference domain and assume a small displacement hypothesis that simplify the numerical processing. Section 4.5 contains the numerical scheme used to solve our PDE simplified model. The main features of the numerical model are then investigated in 1D- and 2D-configurations. We conclude by numerical simulations that corroborate experimental results in the framework of solid tumors in Section 4.6. To the best of our knowledge, it is the first time that a PDE model describes the effect of an injection of ECM degradation enzyme respectively on porosity, interstitial pressure and drug delivery. Calibration of the model with experimental data are planned in forthcoming works.

4.3 Derivation of the model

4.3.1 Framework

Modeling the behavior of porous media in which different continua interact at the microscopic level is not an easy task. In the current literature the mechanics of a porous medium is typically described by two different approaches: the averaging approach and the macroscopic approach [112], also known as mixture theory. The basic premise of the mixture theory is that the space occupied by a mixture is occupied co-jointly by the various constituents of the mixture, each considered as a continuum of its own. Thus, at any point of the space occupied by the mixture, there will be a particle belonging to each constituent [53].

We let $\mathbf{x}$ and t denote the space and time variables, respectively. To simplify notations, we omit the dependence of all variables and model parameters on $\mathbf{x}$ and t, except otherwise stated.

We denote by $\Omega_0 = \Omega(0) \subset \mathbb{R}^d$ $(d = 1, 2, 3)$ the initial spatial configuration, by $\Omega_t = \Omega(t)$ the configuration at time t and by T the final time of the experiment.

The biological tissue is considered as a binary mixture of a solid and an interstitial fluid. The solid phase consists of cells and extracellular matrix (ECM). In what follows, the index ζ refers to one of the three constituents of the tissue: the fluid (f), the ECM $(\mathcal{E})$ or the cells (¢). The index s stands for the solid phase (ECM + cells). The density of the ζ^{th} constituent is denoted by ρ_ζ. It represents the mass of the ζ^{th} constituent per unit volume of the mixture. The density for the ζ^{th} constituent in a homogeneous state is denoted by ρ_ζ^R. It represents the mass of the ζ^{th} constituent per unit volume of the ζ^{th} constituent. The quantity defined by

$$\varphi_\zeta(t, \mathbf{x}) = \frac{\rho_\zeta(t, \mathbf{x})}{\rho_\zeta^R(t, \mathbf{x})}, \tag{4.1}$$

is the volume fraction of the mixture occupied by the ζ^{th} constituent. This definition coincides with the classic definition given by [20]. The following standard assumptions on the mixture are considered.

Assumption 1. (**Saturation**) The mixture is fully saturated, i.e.

$$\varphi_{\mathcal{E}} + \varphi_{\mathscr{C}} + \varphi_f = 1 \quad \forall \mathbf{x} \in \Omega, \ \forall t > 0 \tag{4.2}$$

This saturation condition excludes the possibility of the formation of voids or air bubbles inside the medium.

Assumption 2. (**Incompressibility**) The liquid is incompressible in its pure state i.e. the density of the liquid in a homogeneous state is assumed to be a constant, namely

$$\rho_f^R(t,x) = \rho_f^{R,0}(t,x) \quad \forall \mathbf{x} \in \Omega, \ \forall t > 0. \tag{4.3}$$

Assumption 3. All the solid matrix constituents (cells and ECM) have the same density in a homogeneous state:

$$\rho_{\mathcal{E}}^R(t,\mathbf{x}) = \rho_{\mathscr{C}}^R(t,\mathbf{x}) = \rho_s^R(t,\mathbf{x}). \tag{4.4}$$

Assumption 4. (**Slight compressibility**) The solid phase (ECM + cells) is slightly compressible in its pure state i.e. the density of the solid constituents in a homogeneous state can be written as [33]:

$$\rho_s^R(t,\mathbf{x}) = \rho_s^{R,0}(t,\mathbf{x})(1 + s_0(p(t,\mathbf{x}) - p(0,\mathbf{x}))), \quad \forall \mathbf{x} \in \Omega, \ \forall t > 0, \tag{4.5}$$

where

$$s_0(p(t,\mathbf{x}) - p(0,\mathbf{x})) \ll 1, \quad \forall \mathbf{x} \in \Omega, \ \forall t > 0, \tag{4.6}$$

and where p is the interstitial fluid pressure and where $\rho_s^{R,0}$ is a constant. s_0 can be related to the specific storage coefficient that appears in Biot's constitutive theory of consolidation [21].

Assumption 5. (**Mass exchanges**) We assume that mass exchanges occur only among cells/ECM and fluid, meaning that degrading ECM is detoriated into extracellular fluid, and conversely that the latter is consumed whenever ECM is created.

Assumption 6. (**Fluid source term**) Fluid is exchanged between interstitial space and the blood or lymph vessels: the fluid source term is then assumed to be driven by the average transmural pressure. If fluid is directly injected in the tissue, another external source of fluid is added during the injection.

4.3.2 Model derivation steps

The derivation's steps are presented in Figure 4.4.

4.3.3 Balance laws

In this section we give the set of conservation laws that constitute our proposed mathematical picture of the mechanobiological properties of the tissue using the Eulerian formalism. All the solid matrix constituents (cells and ECM) are experiencing the same motion. Thus $\mathbf{v}_{\mathcal{E}}(t,\mathbf{x}) = \mathbf{v}_{e}(t,\mathbf{x}) = \mathbf{v}_{s}(t,\mathbf{x})$. The motion function refers to the solid phase, so it is useful to use the Eulerian velocity of the fluid with respect to the solid phase defined by

$$\mathbf{w}(t,\mathbf{x}) = \mathbf{v}_f(t,\mathbf{x}) - \mathbf{v}_s(t,\mathbf{x}). \tag{4.7}$$

4.3.3.1 Mass balance for each component of the mixture

The mass of the ζ^{th} constituent can change due to

1. the flux caused by the motion at the velocity $\mathbf{v}_\zeta$ of the constituent,
2. the production that accounts for possible mass conversion between constituents at a certain rate Q_ζ [53],
3. the source term $\mathcal{S}_\zeta$.

One then has

$$\frac{\partial \rho_\zeta}{\partial t} + \nabla \cdot (\rho_\zeta \mathbf{v}_\zeta) - \rho_\zeta Q_\zeta - \mathcal{S}_\zeta = 0, \tag{4.8}$$

where the source term $\mathcal{S}_\zeta$ is given as

$$\mathcal{S}_\zeta = \rho_\zeta^R \Sigma_\zeta. \tag{4.9}$$

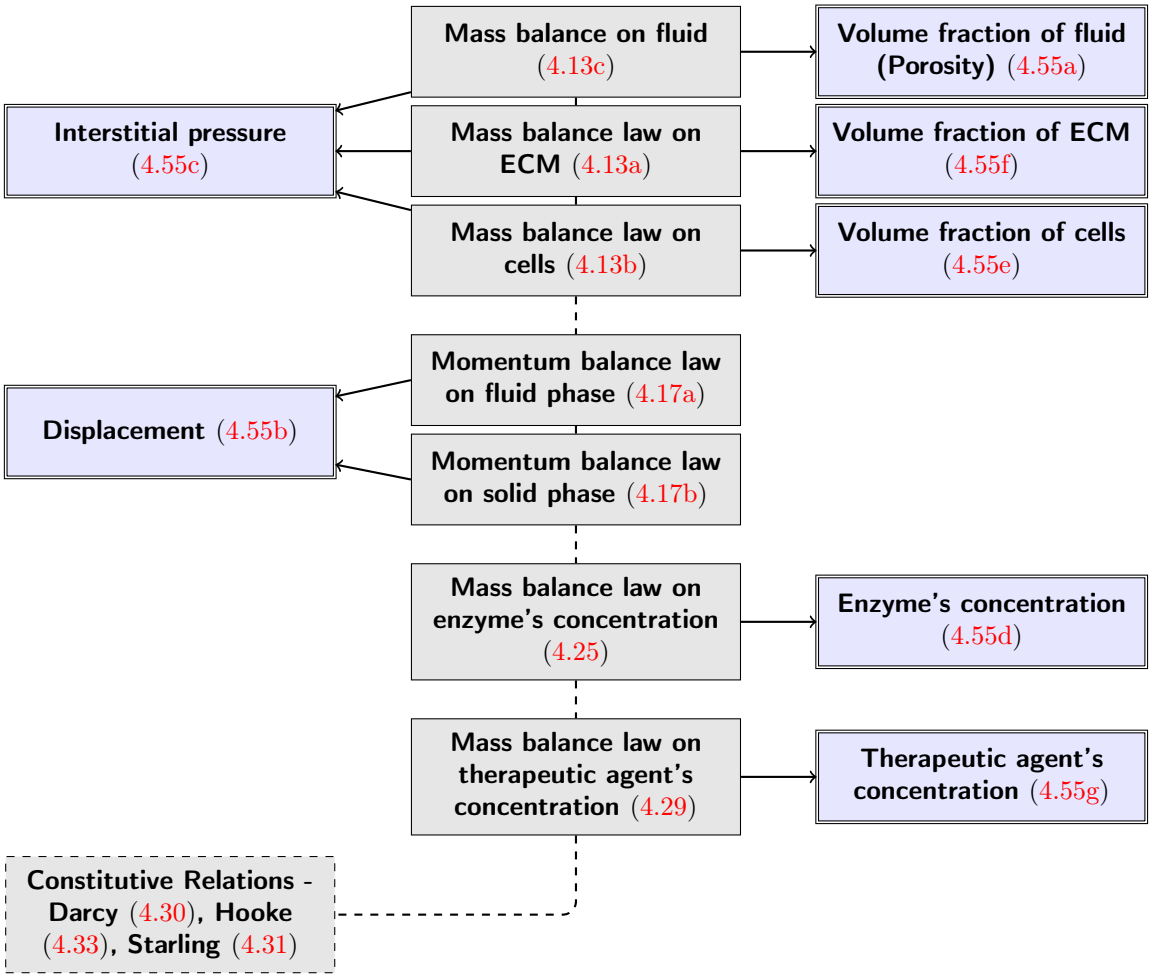

Figure 4.4: Schematic description of the derivation's method of the model. The first set of boxes contain the set of conservation laws and constitutive relations considered while the other boxes contain the final equations on the variables of interest derived from the physical laws. The numbering refers to the corresponding equations in their final form stated further in the article.

Using definition (4.1) we get

$$\frac{\partial(\rho_\zeta^R \varphi_\zeta)}{\partial t} + \nabla \cdot (\rho_\zeta^R \varphi_\zeta \mathbf{v}_\zeta) - \rho_\zeta^R \varphi_\zeta Q_\zeta - \mathcal{S}_\zeta = 0.$$

To translate Assumption 5, we assume the following constraint [53]

$$\rho_s^R \varphi_{\mathcal{E}} Q_{\mathcal{E}} + \rho_f^R \varphi_f Q_f = 0. \tag{4.10}$$

The production terms Q_f and $Q_{\mathcal{E}}$ introduced here describe the mechanisms of addition and/or removal of mass for each species constituting an isolated tissue. We assume that the ECM is degraded proportionally to the enzyme's concentration [6], becoming fluid, and that the tissue recovers towards its initial state.

It is then relevant to choose the production term $Q_{\mathcal{E}}$ as

$$Q_{\mathcal{E}} = -K\varphi_f c_{\text{enz}} + a_r \left(\varphi_f - \varphi_f(0, \mathbf{x})\right). \tag{4.11}$$

where K is the rate of deterioration of the solid phase when in contact with the enzyme, represented by its concentration in the fluid phase $\varphi_f c_{\text{enz}}$. As the ECM is recovered a certain time after the injection of the enzyme [65, 60], the second term in the expression of $Q_{\mathcal{E}}$ represents this reconstitution of the tissue towards its initial state, at a certain rate of natural reconstruction a_r.

To translate Assumption 6, we choose the fluid source term as

$$\Sigma_f = Q_{\text{inj}}^{\text{tot}} + Q_{\text{vas}} - Q_{\text{lym}} \quad \text{where} \quad Q_{\text{inj}}^{\text{tot}} = Q_{\text{inj}}^{\text{enz}} + Q_{\text{inj}}^{\text{drug}}, \tag{4.12}$$

where $Q_{\text{inj}}^{\text{enz}}$ represents the injection term of enzyme, $Q_{\text{inj}}^{\text{drug}}$ represents the injection term of therapeutic agent, Q_{vas} is the transcapillary flow and Q_{lym} is the lymphatic drainage.

The mass balance equations for the tissue's constituents are then expressed by the following coupled system of PDEs in $\Omega_t \times (0, T)$:

$$\begin{cases} \dfrac{\partial}{\partial t}(\rho_s^R \varphi_{\mathcal{E}}) + \nabla \cdot (\rho_s^R \varphi_{\mathcal{E}} \mathbf{v}_s) = \rho_s^R \varphi_{\mathcal{E}} (-K\varphi_f c_{\text{enz}} + a_r \left(\varphi_f - \varphi_f(0, \mathbf{x})\right)), & \text{(4.13a)} \\ \dfrac{\partial}{\partial t}(\rho_s^R \varphi_{\mathscr{C}}) + \nabla \cdot (\rho_s^R \varphi_{\mathscr{C}} \mathbf{v}_s) = 0, & \text{(4.13b)} \\ \dfrac{\partial}{\partial t}(\rho_f^R \varphi_f) + \nabla \cdot (\rho_f^R \varphi_f \mathbf{v}_f) = \rho_s^R \varphi_{\mathcal{E}} \left(K\varphi_f c_{\text{enz}} - a_r \left(\varphi_f - \varphi_f(0, \mathbf{x})\right)\right) \\ \qquad\qquad + \rho_f^R (Q_{\text{inj}}^{\text{tot}} + Q_{\text{vas}} - Q_{\text{lym}}). & \text{(4.13c)} \end{cases}$$

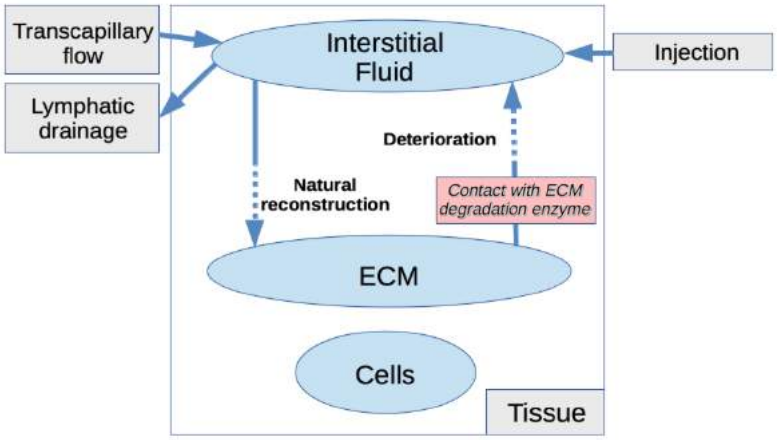

Figure 4.5: Schematic description of exchange pathways and production terms of the different phases.

4.3.3.2 Total mass balance for the mixture

Summing equations $(1/\rho_s^{R,0})\times$ (4.13a), $(1/\rho_s^{R,0})\times$ (4.13b) and $(1/\rho_f^{R})\times$ (4.13c), using Assumptions 1 and 4.3, and conditions (4.6)-(4.10) we get

$$\begin{aligned}\varphi_s s_0 \left(\frac{\partial p}{\partial t} + \nabla p \cdot \mathbf{v}_s\right) + \nabla \cdot (\varphi_s \mathbf{v}_s + \varphi_f \mathbf{v}_f) = Q_{\text{inj}}^{\text{tot}} + Q_{\text{vas}} - Q_{\text{lym}} \\ + \left(1 - \frac{\rho_s^{R,0}}{\rho_f^R}\right) \varphi_{\mathcal{E}}(-K\varphi_f c_{\text{enz}} + a_r\,(\varphi_f - \varphi_f(0,\mathbf{x}))).\end{aligned} \tag{4.14}$$

This equation expresses the conservation of the total mass of the tissue. A simple manipulation allows us to write (4.14) as

$$\begin{aligned}\varphi_s s_0 \left(\frac{\partial p}{\partial t} + \nabla p \cdot \mathbf{v}_s\right) + \nabla \cdot (\mathbf{v}_s + \varphi_f \mathbf{w}) = Q_{\text{inj}}^{\text{tot}} + Q_{\text{vas}} - Q_{\text{lym}} \\ + \left(1 - \frac{\rho_s^{R,0}}{\rho_f^R}\right) \varphi_{\mathcal{E}}(-K\varphi_f c_{\text{enz}} + a_r\,(\varphi_f - \varphi_f(0,\mathbf{x}))).\end{aligned} \tag{4.15}$$

Remark 8. The term $\varphi_s s_0 \left(\frac{\partial p}{\partial t} + \nabla p \cdot \mathbf{v}_s\right)$ in Equation (4.15) comes from Assumptions 4.5 and 4.6. If the density in an homogeneous state of the solid phase were assumed to be a constant, this term would vanish.

4.3.3.3 Momentum balance for each component of the mixture

The momentum of the ζ^{th} constituent can change due to

1. the momentum flux caused by the motion at the velocity $\mathbf{v}_\zeta$ of the constituent,
2. contact forces within the constituent acting through the boundary,
3. contact forces due to the interaction with the other constituents within the domain through the interface separating the constituents,
4. momentum supply related to phase changes,
5. momentum supply related to external sources or sinks of mass,
6. body forces.

One can then write the following local form of the momentum balance in conservative form

$$\frac{\partial}{\partial t}(\rho_\zeta \mathbf{v}_\zeta) + \boldsymbol{\nabla} \cdot (\rho_\zeta \mathbf{v}_\zeta \otimes \mathbf{v}_\zeta) = \boldsymbol{\nabla} \cdot \boldsymbol{\sigma}_\zeta + \rho_\zeta \mathbf{b} + \boldsymbol{\pi}_\zeta + \rho_\zeta Q_\zeta \mathbf{v}_\zeta + \mathcal{S}_\zeta \mathbf{v}_\zeta,$$

where

- $\boldsymbol{\sigma}_\zeta$ is called the partial stress,
- $\boldsymbol{\pi}_\zeta$ is called the interaction force,
- $\mathbf{b}$ is an external force applied to the system e.g., extra pressure due to the injection.

Actually using the mass balance equation (4.8), this equation can be simplified as

$$\rho_\zeta \left(\frac{\partial}{\partial t} \mathbf{v}_\zeta + \mathbf{v}_\zeta \cdot \boldsymbol{\nabla} \mathbf{v}_\zeta \right) = \boldsymbol{\nabla} \cdot \boldsymbol{\sigma}_\zeta + \rho_\zeta \mathbf{b} + \boldsymbol{\pi}_\zeta, \tag{4.16}$$

where the inertial term on the left-hand side can usually be neglected when describing biological tissues [14, 15]. Let's recall that all the solid matrix constituents

(cells and ECM) experience the same overall motion, so we can simplify the momentum balance equations for the tissue's constituents into the a coupled system of PDEs to be solved in $\Omega_t \times (0,T)$:

$$\begin{cases} \boldsymbol{\nabla} \cdot \boldsymbol{\sigma}_f + \rho_f^R \varphi_f \mathbf{b} + \boldsymbol{\pi}_f = 0, & (4.17a) \\ \boldsymbol{\nabla} \cdot \boldsymbol{\sigma}_s + \rho_s^R \varphi_s \mathbf{b} + \boldsymbol{\pi}_s = 0, & (4.17b) \end{cases}$$

where (4.17b) is the equation resulting from the sum of (4.16) for $\zeta = \mathcal{E}$, $\mathcal{c}$, and expresses the total momentum of the solid phase as a whole. In the case of a saturated mixture, it can be proved that [26]

$$\begin{cases} \boldsymbol{\sigma}_s = -\varphi_s p \mathbf{I} + \varphi_s \boldsymbol{\sigma}_s^E & (4.18a) \\ \boldsymbol{\sigma}_f = -\varphi_f p \mathbf{I} & (4.18b) \end{cases}$$

where $\boldsymbol{\sigma}_s^E$ is the effective stress tensor of the solid phase of the tissue, whose form will be discussed in Section 4.3.4, and where $p = p(t, \mathbf{x})$ is the pressure exerted by the fluid phase and $\mathbf{I}$ is the identity tensor. The isotropic stress $-p\mathbf{I}$ accounts for the coupling, typical of poroelasticity, between the low of the fluid and the deformation of the solid matrix, and in particular describes the contribution to the stress due to the fluid pressure within the structure.

The quantities $\boldsymbol{\sigma}_\zeta$, $\zeta = s, f$, are the total stress tensors of the solid and fluid phases. As usual, we neglect the effective stress tensor of the fluid, meaning that we assume that the internal fluid viscosity is negligible compared with the friction between the fluid and the solid matrix [15].

We observe that, for all $t \in (0,T)$ and at all $\mathbf{x} \in \Omega$, it holds [98]

$$\boldsymbol{\pi}_s(t, \mathbf{x}) + \boldsymbol{\pi}_f(t, \mathbf{x}) = 0. \tag{4.19}$$

4.3.3.4 Total momentum balance for the mixture

Summing equations (4.16) for $\zeta = s, f$ and using (4.18), we get

$$\boldsymbol{\nabla} \cdot (\varphi_s \boldsymbol{\sigma}_s^E) + (\rho_f + \rho_s)\mathbf{b} = \nabla p. \tag{4.20}$$

This equation expresses the conservation of total momentum of the tissue. In what follows, we will assume the external body forces to be zero, such that equation (4.20) becomes

$$\boldsymbol{\nabla} \cdot (\varphi_s \boldsymbol{\sigma}_s^E) = \nabla p. \tag{4.21}$$

4.3.3.5 Mass balance for ECM degradation enzyme's concentration

Another fundamental quantity of interest from the modeling point of view is the concentration in ECM degradation enzyme, such as hyaluronidase or collagenase, per unit volume within the fluid phase of the tissue, $c_{\text{enz}} = c_{\text{enz}}(t, \mathbf{x})$. However, the concentration c_{enz} has to be related to the volume ratio occupied by the interstitial fluid. Finally the relevant entity for an overall balance over the whole tissue is the *reduced (or weighted) concentration*, e.g. $C_{\text{enz}} = \varphi_f c_{\text{enz}}$. The mass balance system (4.13) for the solid and fluid phases of the tissue is thus accompanied by a corresponding continuity equation for the hyaluronidase concentration that is transported throughout the tissue by the interstitial fluid. We consider that the reduced concentration can change due to

1. the motion of the fluid at the velocity $\mathbf{v}_f$,
2. the diffusive flux,
3. natural degradation and/or the intake due to the source.

Therefore, the following reaction-convection-diffusion equation reads

$$\frac{\partial}{\partial t}(\varphi_f c_{\text{enz}}) + \nabla \cdot (\varphi_f c_{\text{enz}} \mathbf{v}_f) = -\nabla \cdot (\varphi_f \mathbf{j}_{\text{enz}}^f) - k_{\text{enz}}^{d,\text{eff}} \varphi_f c_{\text{enz}} + \mathcal{S}_{\text{enz}}, \tag{4.22}$$

where

- $\mathbf{j}_{\text{enz}}^f$ is diffusive flux inside the liquid phase,
- $k_{\text{enz}}^{d,\text{eff}}$ is the net natural degradation effective rate of the enzyme in the interstitial fluid,
- $\mathcal{S}_{\text{enz}}$ is the contribution consecutive to the injection (directly into the tissue or intravenously) of enzyme.

Fick's law states that the diffusive flux can be assumed to be proportional to the concentration gradient in the liquid, that is

$$\mathbf{j}^f_{\text{enz}} = -\mathbf{D}^f_{\text{enz}} \nabla c_{\text{enz}}, \tag{4.23}$$

where $\mathbf{D}^f_{\text{enz}}$ is the effective diffusion tensor in the liquid, that we choose to be a tensor linearly dependent on the porosity [77]

$$\mathbf{D}^f_{\text{enz}} = \varphi_f \mathbf{D}^0_{\text{enz}}. \tag{4.24}$$

Hence, equation (4.22) in terms of $C_{\text{enz}} = \varphi_f c_{\text{enz}}$ becomes

$$\frac{\partial C_{\text{enz}}}{\partial t} + \nabla \cdot (C_{\text{enz}} \mathbf{v}_f) = \nabla \cdot \left(\varphi_f^2 \mathbf{D}^0_{\text{enz}} \nabla \left(\frac{C_{\text{enz}}}{\varphi_f} \right) \right) - k^{d,\text{eff}}_{\text{enz}} C_{\text{enz}} + \mathcal{S}_{\text{enz}}. \tag{4.25}$$

4.3.3.6 Mass balance for drug concentration

The main quantity of interest from the modeling point of view is the concentration in therapeutic agent per unit volume within the fluid phase of the tissue, $c_{\text{drug}} = c_{\text{drug}}(t, \mathbf{x})$. As previously, the concentration c_{drug} has to be related to the volume ratio the interstitial fluid. The relevant entity for an overall balance over the whole tissue is the *reduced (or weighted) concentration*, e.g. $C_{\text{drug}} = \varphi_f c_{\text{drug}}$. The continuity equation for the therapeutic agent's concentration that is transported throughout the tissue by the interstitial fluid can be deduced considering that the reduced concentration can change due to

1. the motion of the fluid
2. the diffusive flux
3. natural degradation and/or the intake due to the source.

Therefore, the following reaction-convection-diffusion equation can be deduced

$$\frac{\partial}{\partial t}(\varphi_f c_{\text{drug}}) + \nabla \cdot (\varphi_f c_{\text{drug}} \mathbf{v}_f) = -\nabla \cdot (\varphi_f \mathbf{j}^f_{\text{drug}}) - k^{d,\text{eff}}_{\text{drug}} \varphi_f c_{\text{drug}} + \mathcal{S}_{\text{drug}}, \tag{4.26}$$

where

- $\mathbf{j}^f_{\text{drug}}$ is diffusive flux inside the liquid phase,

- $k^{d,\text{eff}}_{\text{drug}}$ is the net natural degradation effective rate of the drug in the interstitial fluid,

- $\mathcal{S}_{\text{drug}}$ is the contribution consecutive to the injection (directly into the tissue or intravenously) of drug.

As before, Fick's law states that the diffusive flux can be assumed to be proportionnal to the concentration gradient in the liquid, that is

$$\mathbf{j}^f_{\text{drug}} = -\mathbf{D}^f_{\text{drug}} \nabla c_{\text{drug}}, \tag{4.27}$$

where $\mathbf{D}^f_{\text{drug}}$ is the effective diffusion coefficient in the liquid, that we choose to be linearly dependent on the porosity [77]

$$\mathbf{D}^f_{\text{drug}} = \varphi_f \mathbf{D}^0_{\text{drug}}. \tag{4.28}$$

Hence, using (4.13c), equation (4.22) simplifies to

$$\frac{\partial C_{\text{drug}}}{\partial t} + \nabla \cdot (C_{\text{drug}} \mathbf{v}_f) = \nabla \cdot \left(\varphi_f^2 \mathbf{D}^0_{\text{drug}} \nabla \left(\frac{C_{\text{drug}}}{\varphi_f} \right) \right) - k^{d,\text{eff}}_{\text{drug}} C_{\text{drug}} + \mathcal{S}_{\text{drug}}. \tag{4.29}$$

4.3.4 Constitutive equations regarding the mechanical and fluid subsystems

4.3.4.1 Darcy's law

We assume the relative velocity to be expressed by Darcy's law [8, 16, 10, 15]

$$\varphi_f \mathbf{w} = \varphi(\mathbf{v}_f - \mathbf{v}_s) = -\boldsymbol{\kappa} \nabla p \tag{4.30}$$

where $\boldsymbol{\kappa}$ is the permeability tensor.

4.3.4.2 Starling's law

The transcapillary flow and the lymphatic drainage are taken into account in (4.12). Both rates Q_{vas} and Q_{lym} can be evaluated throught Starling's law. A complete description of the formulation of this law can be found in [114]. The final result is

$$Q_{\text{vas}} - Q_{\text{lym}} = \frac{L_p S + L_{PL} S_L}{V}(p_v - p), \tag{4.31}$$

where L_p and L_{PL} are the hydraulic conductivities of the microvascular wall and of the lymphatic wall respectively; S/V and S_L/V are the surface area per unit volume of the vasculature and of the lymphatics respectively; and where p_v is the driving pressure. Equation (4.31) will be written as

$$Q_{\text{vas}} - Q_{\text{lym}} = \gamma(p_v - p), \tag{4.32}$$

where $\gamma = (L_p S + L_{PL} S_L)/V$ will be assumed to be a constant.

4.3.4.3 The linear elasticity framework

To complete our derivations of the equations of motion, we must know (or assume) the relationships (constitutive laws) between effective stress and strain. The classical theory of elasticity deals with the mechanical properties of elastic solids for which the stress is directly proportional to the stress in small deformations. Linear elastic theory can be satisfactorily applied for modeling the mechanical properties of biological media [52, 86, 16, 23]: namely, we assume that biological tissues are nearly linear elastic under small strain and follow a constitutive law based on Hooke's law. Specifically, a Hookean elastic solid is a solid that obeys Hooke's Law, that states that the first Piola-Kirchhoff stress tensor $\mathbf{S}_s^E$ is such that

$$\mathbf{S}_{s;ij}^E = C_{ijkl}\boldsymbol{\varepsilon}_{kl} \tag{4.33}$$

where C_{ijkl} is the stiffness tensor and where $\boldsymbol{\varepsilon}$ is the infinitesimal strain (4.48) defined later in Section 4.4.

Remark 9. For most materials, the linear elasticity framework is only valid for

small displacements [104].

Remark 10. In biomechanics, biological tissues are thought to be better described as viscoelastic solids [52, 41]. However, for the sake of simplicity, we choose here to stay within the framework of the linear elasticity theory.

The first Piola-Kirchhoff stress tensor is then related to the Cauchy stress tensor [17] via the deformation gradient A (4.47) defined in Section 4.4

$$\boldsymbol{\sigma}_s^E = \frac{1}{J} A \mathbf{S}_s^E A^T. \tag{4.34}$$

Isotropic media. In the most simple symmetry case of an isotropic elastic solid, the material has only two independent elastic moduli, called the Lamé constants, λ and μ . In such a medium the elastic properties at any point are independent from direction. The Lamé constants are related to the stiffness tensor C_{ijkl} by

$$C_{ijkl} = \lambda \delta_{ij} \delta_{kl} + \mu \left(\delta_{ik} \delta_{jl} + \delta_{il} \delta_{jk} \right),$$

which gives us the following form for the effective stress $\mathbf{S}_s^E$

$$\mathbf{S}_s^E = 2\mu \boldsymbol{\varepsilon} + \lambda Tr(\boldsymbol{\varepsilon}) I_d. \tag{4.35}$$

As far as the diffusion tensors and the permeability tensor are concerned, in the isotropic case, we take

$$\mathbf{D}^0_{\text{enz}} = D^0_{\text{enz}} I_d, \qquad \mathbf{D}^0_{\text{drug}} = D^0_{\text{drug}} I_d, \qquad \boldsymbol{\kappa} = \kappa I_d. \tag{4.36}$$

Transverse isotropic media. It is now well established that anisotropy plays a major role in the mechanical properties of biological media such as muscles, tendons or bones [105]. The most simple anisotropic model is the transverse isotropy. A transversely isotropic tissue is characterized by the existence of a single plane of isotropy and one single axis of rotational symmetry, the normal to the isotropy

plane. Skeletal muscle, for instance, consists of hundreds to thousands, sometimes millions, of long, multinucleated fibers organized and held together by an ECM thus it is relevant to model it as a transverse isotropic media.

In the case of a transverse isotropic medium in 2D, relation (4.33) reduces to (4.35) in the plane of isotropy (xy). If we consider the plane (xz), (4.33) can be written in the following fashion

$$\begin{pmatrix} \mathbf{S}^E_{s;11} \\ \mathbf{S}^E_{s;33} \\ \mathbf{S}^E_{s;13} \end{pmatrix} = \begin{pmatrix} C_{1111} & C_{1133} & 0 \\ C_{1133} & C_{3333} & 0 \\ 0 & 0 & C_{1313} \end{pmatrix} \begin{pmatrix} \varepsilon_{11} \\ \varepsilon_{33} \\ 2\varepsilon_{13} \end{pmatrix}. \tag{4.37}$$

It has been reported [121] that the permeability $\boldsymbol{\kappa}$ depends on many factors including the geometry. Orientation can affect $\boldsymbol{\kappa}$, with perpendicular fibers providing a larger resistance to flow $\kappa_\perp$ than parallel fibers $\kappa_{/\!/}$. Consequently, in a rightful vector basis, we take $\boldsymbol{\kappa}$ as

$$\boldsymbol{\kappa} = \begin{pmatrix} \kappa_{/\!/} & 0 \\ 0 & \kappa_\perp \end{pmatrix}. \tag{4.38}$$

As far as the diffusion tensors are concerned, it was also reported [35, 39] that the diffusion coefficient parallel to a skeletal muscle fiber's long axis $D^0_{\text{enz},/\!/}$ (resp. $D^0_{\text{drug},/\!/}$) is greater than the diffusion coefficient perpendicular to the fiber's long axis $D^0_{\text{enz},\perp}$ (resp. $D^0_{\text{drug},\perp}$). Consequently, in a rightful vector basis,

$$\mathbf{D}^0_{\text{enz}} = \begin{pmatrix} D^0_{\text{enz},/\!/} & 0 \\ 0 & D^0_{\text{enz},\perp} \end{pmatrix}, \quad \text{resp. } \mathbf{D}^0_{\text{drug}} = \begin{pmatrix} D^0_{\text{drug},/\!/} & 0 \\ 0 & D^0_{\text{drug},\perp} \end{pmatrix}. \tag{4.39}$$

4.3.4.4 Degradation rates

The degree of porosity has a significant impact on the net natural degradation effective rate of the enzyme or the drug in the interstitial fluid $k^{d,\text{eff}}_{\text{enz}}, k^{d,\text{eff}}_{\text{drug}}$. The effects are both attributed to a wall effect and a surface area effect because the media with lower porosities or larger pores possess thicker pore walls and smaller surface area, which depress the diffusion of degradation products [127]. Consequently, we

choose

$$k_{\text{enz}}^{d,\text{eff}} = \frac{k_{\text{enz}}^{d}}{\varphi_f} \text{ and } k_{\text{drug}}^{d,\text{eff}} = \frac{k_{\text{drug}}^{d}}{\varphi_f}, \tag{4.40}$$

where k_{enz}^{d} and k_{drug}^{d} are positive constants.

4.3.4.5 Source terms.

Let the index ω denote either of the chemical species of interest (enzyme and/or drug).

Injection. If the chemical specie is directly injected in the tissue, we can choose to take the source term as

$$\mathcal{S}_\omega = c_{\text{inj}}^{\omega} Q_{\text{inj}}^{\omega}, \tag{4.41}$$

where c_{inj}^{ω} is the value of the specie concentration injected, which is assumed to be a constant. In the numerical simulations of sections 4.5 and 4.6, Q_{inj}^{ω} is a Gaussian function with a very small spread

$$Q_{\text{inj}}^{\omega} = q_{\text{inj}}^{\omega} \exp\left(- \sum_{i=1}^{d} \frac{(x_i - x_i^0)^2}{2\sigma_{x_i}^2} \right), \tag{4.42}$$

where $q_{\text{inj}}^{\omega}, \sigma_{x_i}$ are positive constants and where $(x_1^0, \ldots, x_d^0)$ indicate the coordinates of the injection point.

Incubation. If the tissue is incubated in the chemical specie, the source term $\mathcal{S}_\omega$ is taken as zero and and we choose instead to apply a non homogeneous Dirichlet boundary condition on C_ω (cf section 4.6).

Transcapillary transport. If the chemical specie is injected intravenously, we choose to take the source term accordingly with the pore model for transcapillary exchange via convection stated in [19]

$$\mathcal{S}_\omega = (1 - \gamma_c)(Q_{\text{vas}} - Q_{\text{lym}}) c_v^{\omega}, \tag{4.43}$$

where γ_c represents the coupling between fluid and solute and c_v^ω is the plasma concentration of the chemical specie. In the numerical simulations of section 4.6, for the sake of simplicity,

$$c_v^\omega = c_{v,0}^\omega \, \chi_{|t_1 \leq t \leq t_2}, \tag{4.44}$$

where $c_{v,0}^\omega$ is a constant, and $[t_1, t_2]$ is the time interval of presence in the capillary network. c_v^ω can be chosen to follow any pharmacokinetic model of interest.

4.4 Formulation of the poroelastic model in a fixed domain

4.4.1 Kinematics of the mixture

The motion of the constituents is described by the position occupied at time t by the particle labelled $\mathbf{X}$

$$\mathbf{x} = \Phi(t, \mathbf{X}), \tag{4.45}$$

$\mathbf{X}$ being the position of the particle in the reference configuration Ω_0. The function $\Phi(t, .)$ represents a mapping from initial (undeformed) configuration Ω_0 to the present (deformed) configuration Ω_t.

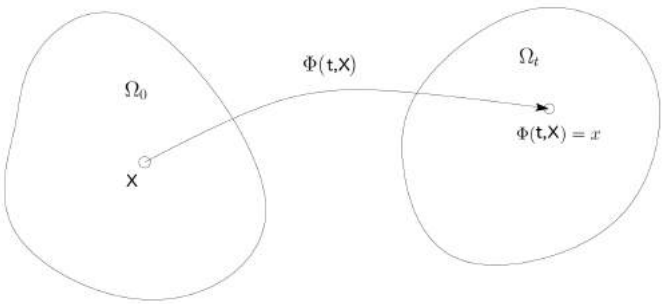

Figure 4.6: Deformation from the fixed domain Ω_0 via the application Φ

The velocity of a particle belonging to the ζ^{th} constituent, often termed the Lagrangian velocity, $\mathbf{V}_\zeta(t, \mathbf{X})$, is the time rate change of the particle position holding $\mathbf{X}$ fixed. As we will use the Eulerian formalism to state conservation

equations, we recall that the Eulerian velocity at time t and position $\mathbf{x}$, $\mathbf{v}_\zeta(t,\mathbf{x})$, is given by

$$\mathbf{v}_\zeta(t,\mathbf{x}) = \mathbf{V}_\zeta(t,\mathbf{X}) \text{ when } \mathbf{x} = \Phi(t,\mathbf{X}). \tag{4.46}$$

The configuration gradient, or deformation gradient, is defined by

$$A := \frac{\partial \mathbf{x}}{\partial \mathbf{X}} = \left(\frac{\partial x_i}{\partial X_j}\right)_{i,j=1..d} \tag{4.47}$$

We also set $B := A^{-1}$ and $J := \det(A)$. We stated that all the solid matrix constituents (cells and ECM) experience the same overall motion [74]. The displacement vector of the solid phase will be denoted $\mathbf{u} = \mathbf{u}(t,\mathbf{X})$. Note that we then have

$$\mathbf{V}_s(t,\mathbf{X}) = \frac{\partial}{\partial t}\mathbf{u}(t,\mathbf{X}).$$

We also define the associated infinitesimal deformation of the volume surrounding the point $\mathbf{X}$ at time t as

$$\boldsymbol{\varepsilon}(t,\mathbf{X}) = \frac{1}{2}\left(\nabla\mathbf{u}(t,\mathbf{X}) + (\nabla\mathbf{u}(t,\mathbf{X})^T\right). \tag{4.48}$$

It is also useful to define the material time derivative following the solid matrix

$$\frac{D(.)}{Dt} = \frac{\partial(.)}{\partial t} + (\mathbf{v}_s.\nabla)(.). \tag{4.49}$$

4.4.2 Change of variables

From now on, the medium is assumed to be isotropic. The formulation in a transverse isotropic medium will be similar as only equation (4.55b) will change. To reduce the governing equations to the reference fixed domain Ω_0, we introduce a suitable change of variable, which is given by the motion function (4.45): $\mathbf{x} = \Phi(t,\mathbf{X})$.

If $\mathbf{u}(t,\mathbf{X}) = \mathbf{x} - \mathbf{X}$ is the displacement vector, Φ is given by

$$\Phi(t,\mathbf{X}) = \mathbf{X} + \mathbf{u}(t,\mathbf{X}). \tag{4.50}$$

Let us set

$$
\begin{aligned}
&f(t,\mathbf{X}) := \varphi_f(t,\Phi(t,\mathbf{X})),\ g_s(t,\mathbf{X}) := \varphi_s(t,\Phi(t,\mathbf{X})),\\
&g_{\mathcal{E}}(t,\mathbf{X}) := \varphi_{\mathcal{E}}(t,\Phi(t,\mathbf{X})),\ g_{\mathscr{C}}(t,\mathbf{X}) := \varphi_{\mathscr{C}}(t,\Phi(t,\mathbf{X})),\\
&P(t,\mathbf{X}) := p(t,\Phi(t,\mathbf{X})),\ P_v(t,\mathbf{X}) := p_v(t,\Phi(t,\mathbf{X})),\\
&h(t,\mathbf{X}) := C_{\text{enz}}(t,\Phi(t,\mathbf{X})),\ c(t,\mathbf{X}) := C_{\text{drug}}(t,\Phi(t,\mathbf{X})),
\end{aligned}
$$

Recall that we have already from Section 4.3.4

$$
\mathbf{v}_s(t,\mathbf{x}) = \mathbf{V}_s(t,\mathbf{X}) = \frac{\partial}{\partial t}\mathbf{u}(t,\mathbf{X}), \tag{4.51}
$$

and

$$
\boldsymbol{\sigma}_s^E = \frac{1}{J}B^{-1}\mathbf{S}_s^E B^{-T} \text{ with } \mathbf{S}_s^E = 2\mu\boldsymbol{\varepsilon} + \lambda Tr(\boldsymbol{\varepsilon})I_d, \tag{4.52}
$$

since we consider the isotropic case. Moreover, every time and space derivative are affected by the change of variables in the following fashion (example on $f = \varphi_f$):

$$
\frac{D\varphi_f}{Dt} = \frac{\partial f}{\partial t},\ \ \nabla_{\mathbf{x}}\,\varphi_f = B\,\nabla_{\mathbf{X}}\,f. \tag{4.53}
$$

4.4.3 Non-dimensionalization

We state that from now ∇ denotes the operator $\nabla_{\mathbf{X}} = (\partial_{X_1},\dots,\partial_{X_d})^T$. Denote by l_0 the typical length of the porous medium. We non-dimensionalize the governing equations by letting

$$
\begin{aligned}
&\mathbf{X} = l_0\overline{\mathbf{X}}, \qquad \mathbf{u} = l_0\overline{\mathbf{u}}, \quad t = \frac{l_0^2}{\kappa(\lambda+2\mu)}\bar{t}, \quad \mathbf{V}_s = \frac{\kappa(\lambda+2\mu)}{l_0}\overline{\mathbf{V}_s},\\
&P = (\lambda+2\mu)\overline{P}, \quad h = c_0\overline{h}, \quad c = c_0\overline{c},
\end{aligned}
$$

where we use bars to denote the dimensionless variables. The dimensionless Piola-Kirchhoff and Cauchy stress tensors are defined as $\overline{\mathbf{S}_s^E} = \mathbf{S}_s^E/(\lambda+2\mu)$ and $\overline{\boldsymbol{\sigma}_s^E} = \boldsymbol{\sigma}_s^E/(\lambda+2\mu)$, respectively, and we define the dimensionless parameters

$$\overline{\mu} = \frac{\mu}{\lambda + 2\mu}, \qquad \overline{\lambda} = \frac{\lambda}{\lambda + 2\mu}, \qquad \overline{s_0} = s_0(\lambda + 2\mu), \quad \overline{\boldsymbol{\kappa}} = \frac{1}{\kappa}\boldsymbol{\kappa},$$

$$\alpha = \frac{l_0^2}{\kappa(\lambda + 2\mu)}, \qquad \overline{K} = \alpha c_0 K, \qquad \overline{a_r} = \alpha a_r, \qquad \overline{\gamma} = \frac{l_0^2}{\kappa}\gamma,$$

$$\overline{\mathbf{D}^0_{\text{enz}}} = \frac{1}{\kappa(\lambda + 2\mu)}\mathbf{D}^0_{\text{enz}}, \qquad \overline{k^d_{\text{enz}}} = \alpha k^d_{\text{enz}}, \qquad \overline{P_v} = \frac{P_v}{\lambda + 2\mu},$$

$$\overline{\mathbf{D}^0_{\text{drug}}} = \frac{1}{\kappa(\lambda + 2\mu)}\mathbf{D}^0_{\text{drug}}, \quad \overline{k^d_{\text{drug}}} = \alpha k^d_{\text{drug}}.$$

We choose the $(\lambda + 2\mu)$ parameter as a natural pressure scale; by this choice the dimensionless elastic parameters $\overline{\lambda}, \overline{\mu}$ are of order 1 [70].

4.4.4 Simplification of the model

The governing equations in Ω_t can be reformulated on the fixed reference domain Ω_0 dimensionless. The first advantage of this process is to obtain a system of equations in a fixed reference domain in order to make the numerical processing possible. Second, the constitutive relation on the stress tensor $\mathbf{S}_s^E$ is given in the lagrangian coordinates $(t, \mathbf{X})$, so it is natural to work within this system of coordinates. The third benefit is to elude the transport equations of the three different volume fractions: in the fixed reference domain, those equations reduce to ordinary differential equations. In particular, we don't have to state boundary conditions on the porosity.

The full derivation calculus in the general case can be found in Appendix A. For the sake of simplicity, we will assume that our system undergo very small perturbations (see Remark 9). One can see then that $B = I_d + \mathcal{M}(\nabla \mathbf{u})$, where in the case of very small deformations, the coefficients of matrix $\mathcal{M}(\nabla \mathbf{u})$ are negligible before 1. Thus we can write the system with $B = I_d$. Let us denote

$$J_{\text{enz}} = \frac{1}{f}\overline{\boldsymbol{\kappa}}\,\nabla P - \overline{\mathbf{D}^0_{\text{enz}}}\nabla f \quad \text{and} \quad J_{\text{drug}} = \frac{1}{f}\overline{\boldsymbol{\kappa}}\,\nabla P - \overline{\mathbf{D}^0_{\text{drug}}}\nabla f. \tag{4.54}$$

The equivalent system in Ω_0 in dimensionless form in this simplified case reads

$$
\begin{cases}
g_{\mathcal{E}} + g_{\mathcal{C}} + f = 1, & \text{(4.55a)}\\
\boldsymbol{\nabla} \cdot \left((g_{\mathcal{E}} + g_{\mathcal{C}}) \left(\overline{\lambda} (\nabla \cdot \mathbf{u}) I + \overline{\mu} (\nabla \mathbf{u} + \nabla \mathbf{u}^T) \right) \right) = \nabla P, & \text{(4.55b)}\\
(g_{\mathcal{E}} + g_{\mathcal{C}}) \overline{s_0} \dfrac{\partial P}{\partial t} - \nabla \cdot (\overline{\boldsymbol{\kappa}} \nabla P) = \alpha \, Q_{\text{inj}}^{\text{tot}} + \overline{\gamma} (\overline{P_v} - P) \\
\qquad + \left(\dfrac{\rho_s^{R,0}}{\rho_f^R} - 1 \right) g_{\mathcal{E}} (\overline{K} h + \overline{a_r} (f(0,\mathbf{x}) - f)) - \nabla \cdot \left(\dfrac{\partial \mathbf{u}}{\partial t} \right), & \text{(4.55c)}\\
\dfrac{\partial h}{\partial t} = \nabla \cdot (f \overline{\mathbf{D}_{\text{enz}}^0} \nabla h + h J_{\text{enz}}) + h \left(- \dfrac{\overline{k_{\text{enz}}^d}}{f} - \nabla \cdot \left(\dfrac{\partial \mathbf{u}}{\partial t} \right) \right) + \dfrac{\alpha \mathcal{S}_{\text{enz}}}{c_0}, & \text{(4.55d)}\\
\dfrac{\partial g_{\mathcal{C}}}{\partial t} + \left(\overline{s_0} \dfrac{\partial P}{\partial t} + \nabla \cdot \left(\dfrac{\partial \mathbf{u}}{\partial t} \right) \right) g_{\mathcal{C}} = 0, & \text{(4.55e)}\\
\dfrac{\partial g_{\mathcal{E}}}{\partial t} + \left(\overline{K} h + \overline{a_r} (f(0,\mathbf{x}) - f) + \overline{s_0} \dfrac{\partial P}{\partial t} + \nabla \cdot \left(\dfrac{\partial \mathbf{u}}{\partial t} \right) \right) g_{\mathcal{E}} = 0, & \text{(4.55f)}\\
\dfrac{\partial c}{\partial t} = \nabla \cdot (f \overline{\mathbf{D}_{\text{drug}}^0} \nabla c + c J_{\text{drug}}) + c \left(- \dfrac{\overline{k_{\text{drug}}^d}}{f} - \nabla \cdot \left(\dfrac{\partial \mathbf{u}}{\partial t} \right) \right) + \dfrac{\alpha \mathcal{S}_{\text{drug}}}{c_0}. & \text{(4.55g)}
\end{cases}
$$

Remark 11 (**Dynamics added on porosity's behavior**). In previous studies, the porosity of the medium (or volume fraction of fluid) is often regarded as a constant [16]. Models that include porosity changes [91] have used the following relation between $\nabla \cdot \mathbf{u}$ and φ_f:

$$f = \frac{f(0,\mathbf{x}) + \nabla \cdot \mathbf{u}}{1 + \nabla \cdot \mathbf{u}},$$

which is obtained traducing an hypothesis of infinitesimal displacement on the variation of volume, or more recently [118]

$$f = 1 - (1 - f(0,\mathbf{x})) e^{-\nabla \cdot \mathbf{u}},$$

which is obtained from Equation (4.55e) in the case of a biphasic system with only incompressible cells and incompressible fluid. However, in our case, since our main hypothesis is that the porosity is not only affected by the deformation of the medium but mostly by the ECM degradation enzyme injected, we must derive

an expression for the effective porosity directly from the mass balance laws of the ECM and cells constituents.

An expression for the effective volume fraction occupied by cells can be derived from the volume balance of the phase occupied by cells assuming the initial conditions $g_{\mathscr{C}}(0,\mathbf{x}) = g^0_{\mathscr{C}}(\mathbf{x})$ and $\nabla\cdot\mathbf{u}(0,\mathbf{x}) = 0$. Integrating Equation (4.55e),

$$g_{\mathscr{C}}(t,\mathbf{x}) = g^0_{\mathscr{C}}(\mathbf{x})e^{-\nabla\cdot\mathbf{u}-\overline{s_0}(P-P^0)}. \tag{4.56}$$

To obtain the effective volume fraction occupied by ECM, consider

$$\widetilde{g}_{\mathcal{E}} = g_{\mathcal{E}}e^{\nabla\cdot\mathbf{u}+\overline{s_0}(P-P^0)}. \tag{4.57}$$

An equation for this quantity assuming the initial conditions $\nabla\cdot\mathbf{u}(0,\mathbf{x}) = 0$, $P(0,\mathbf{x}) = P^0(\mathbf{x})$ and $\widetilde{g}_{\mathcal{E}}(0,\mathbf{x}) = g_{\mathcal{E}}(0,\mathbf{x}) = g^0_{\mathcal{E}}(\mathbf{x})$, is given by

$$\frac{\partial\widetilde{g}_{\mathcal{E}}}{\partial t} + \left(\overline{K}h + \overline{a_r}(f(0,\mathbf{x}) - f)\right)\widetilde{g}_{\mathcal{E}} = 0.$$

This equation reflects the fact that, regardless of the mechanical changes due to the displacement and the compressibility of the tissue, the ECM is deteriorated when in contact with the ECM degradation enzyme, but then reconstruct itself towards its initial state.

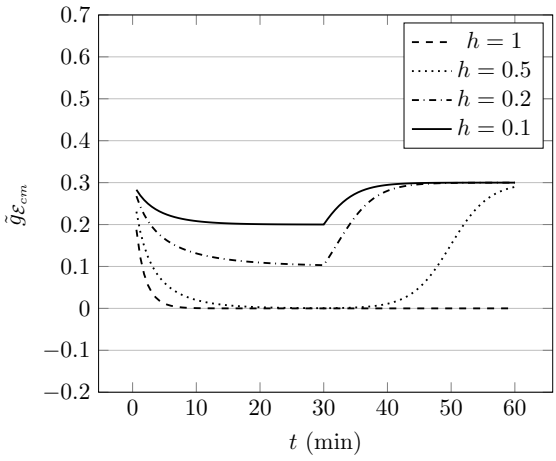

Figure 4.7: $\widetilde{g}_{\mathcal{E}}$ is plotted versus time for an initial volume fraction of ECM of 0.3 and for different concentrations of enzyme applied continuously during 30 minutes, regardless of the space dependency. Both tendencies (degradation during injection - reconstruction) can easily be observed.

4.4.5 Boundary conditions

The primary variables of the problem are the displacement $\mathbf{u}$, the pressure P and the concentrations in ECM degradation enzyme h and in therapeutic agent c. Define the boundary of the domain Ω, denoted Γ. We generically denote by $\mathbf{n}$ the normal to Ω outwardly directed from the inside to the outside of the domain. Next, define the portions of the boundary Γ_u and Γ_t on which displacement and stress are defined, such as $\Gamma_u \cup \Gamma_t = \Gamma$ and

$$\mathbf{u} = \mathbf{u}_{\Gamma_u} \text{ on } \Gamma_u \text{ and } \mathbf{S}_s^E \mathbf{n} = \mathbf{t} \text{ on } \Gamma_t. \tag{4.58}$$

Applying the condition $\mathbf{S}_s^E \mathbf{n} = 0$ to the boundary amounts to considering a free boundary, while setting $\mathbf{u}_{\Gamma_u} = 0$ amounts to considering a fixed boundary.

The portions of the boundary Γ_p and Γ_q are the parts of the boundary on which pressure and pressure flux are specified, such as $\Gamma_p \cup \Gamma_q = \Gamma$ and

$$P = P_{\Gamma_p} \text{ on } \Gamma_p \text{ and } \nabla P \cdot \mathbf{n} = q \text{ on } \Gamma_q. \tag{4.59}$$

Setting a Dirichlet condition on the pressure amounts to considering a permeable boundary in contact with a surrounding medium where the pressure is fixed, while applying the condition $\nabla P \cdot \mathbf{n} = 0$ amounts to considering a wall boundary condition.

The portions of the boundary Γ_h and Γ_β are the parts of the boundary on which the enzyme's concentration and flux are specified, such as $\Gamma_h \cup \Gamma_\beta = \Gamma$ and

$$\begin{cases} h = h_{\Gamma_h} \text{ on } \Gamma_h, & \text{(4.60a)} \\ \left(f\mathbf{D}^0_{\text{enz}} \nabla h + h J_{\text{enz}}\right) \cdot \mathbf{n} = \beta_1 \text{ on } \Gamma_\beta. & \text{(4.60b)} \end{cases}$$

The same type of boundary conditions are applied to the therapeutic agent's concentration and flux

$$\begin{cases} c = c_{\Gamma_h} \text{ on } \Gamma_h, & (4.61a) \\ \left(f\mathbf{D}^0_{\text{drug}}\nabla c + cJ_{\text{drug}}\right)\cdot\mathbf{n} = \beta_2 \text{ on } \Gamma_\beta. & (4.61b) \end{cases}$$

4.5 Numerical simulations

4.5.1 Computational algorithm

We first need to reduce the whole coupled system (4.55) to a sequence of linearized equations of simpler form. We subdivide the time interval $[0,T]$ into $N \geq 1$ uniform subintervals of length $\Delta t = \frac{T}{N}$, in such a way that the discrete time levels $t^n = n\Delta t$, $n = 0,\dots,N$, are obtained. We set

$$\nabla\cdot\mathbf{u}^0 = 0,\ \ g^0_{\mathcal{E}} = g_{\mathcal{E}}(0,\mathbf{x}),\ \ \widetilde{g}^0_{\mathcal{E}} = g_{\mathcal{E}}(0,\mathbf{x}),\ \ g^0_{\mathscr{C}} = g_{\mathscr{C}}(0,\mathbf{x}),\ \ h^0 = 0 \text{ and } c^0 = 0, \tag{4.62}$$

and P^0 is set as the solution of the steady-state pressure equation:

$$-\nabla\cdot(\overline{\boldsymbol{\kappa}}\,\nabla P^0) = \overline{\gamma}(\overline{p_v} - P^0), \tag{4.63}$$

coupled with the boundary conditions (4.59).

For $n = 0,\dots,N-1$, we perform the following iteration:

1. We obtain f^n using (4.55a): $f^n = 1 - g^n_{\mathcal{E}} - g^n_{\mathscr{C}}$, and we set $g^n_s = g^n_{\mathcal{E}} + g^n_{\mathscr{C}}$.

2. We obtain $\mathbf{u}^{n+1}$ and P^{n+1} solving the linear poroelastic system with the finite element solver FreeFem++ [61], choosing P_2 (resp. P_1) elements for $\mathbf{u}^{n+1}$ (resp. P^{n+1}) to guarantee stable Galerkin approximation [50, 87] and discretizing in time with a first order backward Euler scheme [88]. Note that having a parabolic equation on P, which is a consequence of Assumption 4.3,

numerically permits to prevent element locking [64].

$$\begin{cases} \nabla \cdot \left(g_s^n \left(\overline{\lambda} (\nabla \cdot \mathbf{u}^{n+1}) I + 2\overline{\mu} \boldsymbol{\varepsilon}(\mathbf{u}^{n+1}) \right) \right) - \nabla P^{n+1} = 0, & \text{(4.64a)} \\ g_s^n \overline{s_0} \dfrac{P^{n+1}}{\Delta t} - \nabla \cdot (\overline{\boldsymbol{\kappa}} \nabla P^{n+1}) + \overline{\gamma} P^{n+1} + \dfrac{\nabla \cdot \mathbf{u}^{n+1}}{\Delta t} \\ \qquad = g_s^n \overline{s_0} \dfrac{P^n}{\Delta t} + \dfrac{\nabla \cdot \mathbf{u}^n}{\Delta t} + \alpha \, Q_{\text{inj}}^{\text{tot}}(t^{n+1}) & \text{(4.64b)} \\ \qquad\qquad + \overline{\gamma} \, \overline{p_{eq}} + \left(\dfrac{\rho_s^{R,0}}{\rho_f^R} - 1 \right) g_{\mathcal{E}}^n (\overline{K} h^n + \overline{a_r} (f(0, \mathbf{x}) - f^n)), \end{cases}$$

supplied by the approximation of the boundary conditions (4.58) and (4.59)

$$\begin{cases} \mathbf{u}^{n+1} = \mathbf{u}_{\Gamma_u} \text{ on } \Gamma_u \text{ and } \mathbf{S}_s^{E,n+1} \mathbf{n} = \mathbf{t} \text{ on } \Gamma_t, & \text{(4.65a)} \\ P^{n+1} = P_{\Gamma_p} \text{ on } \Gamma_p \text{ and } \nabla P^{n+1} \cdot \mathbf{n} = q \text{ on } \Gamma_q. & \text{(4.65b)} \end{cases}$$

3. Let us denote

$$J_{\text{enz}}^n = \frac{1}{f^n} \overline{\boldsymbol{\kappa}} \nabla P^n - \overline{\mathbf{D}_{\text{enz}}^0} \nabla f^n \quad \text{and} \quad J_{\text{drug}}^n = \frac{1}{f^n} \overline{\boldsymbol{\kappa}} \nabla P^n - \overline{\mathbf{D}_{\text{drug}}^0} \nabla f^n. \tag{4.66}$$

We obtain h^{n+1} and c^{n+1} solving the linear advection-diffusion-reaction equations still using the finite element solver FreeFem++ [61]

$$\begin{aligned} &\frac{h^{n+1}}{\Delta t} - \nabla \cdot (f^n \overline{\mathbf{D}_{\text{enz}}^0} \nabla h^{n+1} + h^{n+1} J_{\text{enz}}^n) \\ &- h^{n+1} \left(- \frac{\overline{k_{\text{enz}}^d}}{f^n} - \left(\frac{\nabla \cdot \mathbf{u}^{n+1} - \nabla \cdot \mathbf{u}^n}{\Delta t} \right) \right) = \frac{h^n}{\Delta t} + \frac{\alpha}{c_0} \mathcal{S}_{\text{enz}}(t^{n+1}), \end{aligned} \tag{4.67}$$

and

$$\begin{aligned} &\frac{c^{n+1}}{\Delta t} - \nabla \cdot (f^n \overline{\mathbf{D}_{\text{drug}}^0} \nabla c^{n+1} + c^{n+1} J_{\text{drug}}^n) \\ &- c^{n+1} \left(- \frac{\overline{k_{\text{drug}}^d}}{f^n} - \left(\frac{\nabla \cdot \mathbf{u}^{n+1} - \nabla \cdot \mathbf{u}^n}{\Delta t} \right) \right) = \frac{c^n}{\Delta t} + \frac{\alpha}{c_0} \mathcal{S}_{\text{drug}}(t^{n+1}), \end{aligned} \tag{4.68}$$

supplied by the following approximation of the boundary conditions (4.60)

and (4.61):

$$\begin{cases} h^{n+1} = h_{\Gamma_h} \text{ on } \Gamma_h, \\ \left(f^n \mathbf{D}^0_{\text{enz}} \nabla h^{n+1} + h^{n+1} J^n_{\text{enz}}\right) \cdot \mathbf{n} = \beta_1 \text{ on } \Gamma_\beta, \end{cases} \tag{4.69a}$$

$$\begin{cases} c^{n+1} = h_{\Gamma_h} \text{ on } \Gamma_h, \\ \left(f^n \mathbf{D}^0_{\text{drug}} \nabla c^{n+1} + c^{n+1} J^n_{\text{drug}}\right) \cdot \mathbf{n} = \beta_2 \text{ on } \Gamma_\beta. \end{cases} \tag{4.69b}$$

4. We obtain $g_{\mathcal{E}}^{n+1}$ by first calculating

$$\widetilde{g}_{\mathcal{E}}^{n+1} = \frac{\widetilde{g}_{\mathcal{E}}^{n}}{1 + \Delta t(\overline{K} h^{n+1} + \overline{a_r}(f(0,\mathbf{x}) - f^n))}.$$

and from (4.57), we deduce

$$g_{\mathcal{E}}^{n+1} = \widetilde{g}_{\mathcal{E}}^{n+1} e^{-\nabla \cdot \mathbf{u}^{n+1} - \overline{s_0}(P^{n+1} - P^0)}.$$

To obtain $g_{\mathcal{C}}^{n+1}$, we use formula (4.56)

$$g_{\mathcal{C}}^{n+1} = g_{\mathcal{C}}^{0}(\mathbf{x}) e^{-\nabla \cdot \mathbf{u}^{n+1} - \overline{s_0}(P^{n+1} - P^0)}.$$

Remark 12 (**Triangulation convergence tests**). We checked numerically that the relative error e_h (resp. e_f, e_P) on the total mass of enzyme (resp. the quantity of fluid, the mean pressure) at $t = 60$ min decreases with order 1 when refining the mesh (Figure 4.8).

Remark 13 (**Conservation of mass**). A test case is performed to check if the total mass of enzyme injected is conserved when its degradation rate is zero. When the degradation rate is nonzero, the enzyme's total mass remains positive, and after reaching a maximum amount at the end of the injection, it decreases gradually till reaching zero as it has been observed in [90] (Figure 4.9).

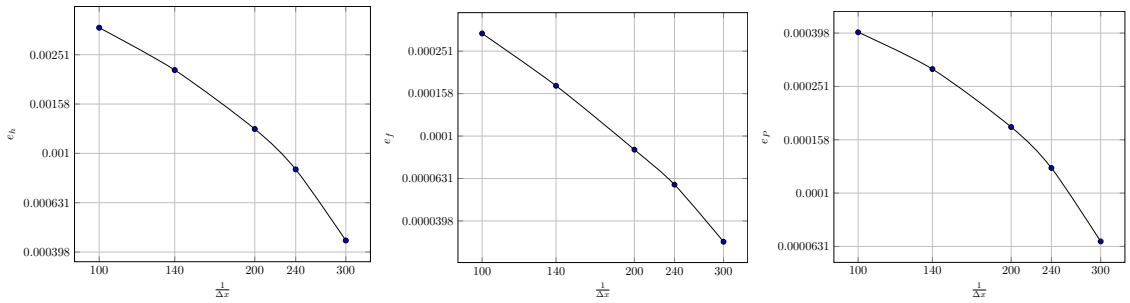

Figure 4.8: Results from the triangulation convergence simulations in 1D at $t = 60$ min (simulations from section 4.5.2). The relative error on $\int_\Omega Z(t = 60 \text{ min})\, dx$ with $Z = h,\ f,\ P$ is plotted using logarithmic scales on both the horizontal and vertical axes.

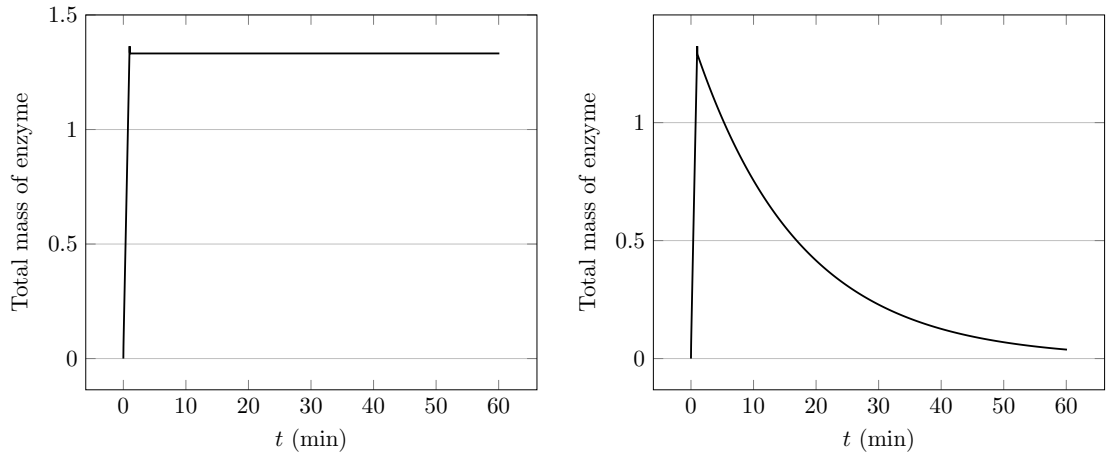

(a) Numerical mass conservation of enzyme.

(b) ECM degradation enzyme's total mass versus time when degradation rate is nonzero.

Figure 4.9: First numerical results on the total mass of enzyme. Numerically, the mass is well conserved when the degradation rate is zero, while the curve has the expected shape when the degradation rate is nonzero.

4.5.2 Numerical tests in 1D

The computational domain. In this section, we formulate the poroelastic transport model in a one-dimensional geometrical configuration (1D). Figure 4.10 shows a schematic representation of the 1D reference domain we considered. Denoting by x the spatial coordinate, the region $x < 0$ represents the tissue far away from the site of injection, the open interval $\Omega = (0, L)$ is the tissue whereas the

region $x > L$ corresponds to the air surrounding the tissue.

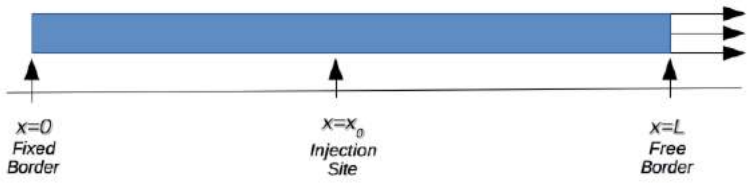

Figure 4.10: Schematic representation of the 1D reference domain.

Simulation Tests. What we want here is to understand the qualitative effect on the porosity of a injection of ECM degradation enzyme. Consequently, we consider in this section system (4.55) without equation (4.55g). In the simulations, $\overline{\gamma}$ is chosen so the initial pressure, derived from equation (4.63), is a constant.

To test the capability of the model, simulations are performed on the homogenous domain represented in Figure 4.10. The border of the domain is divided in two parts: $\Gamma = \Gamma_0 \cup \Gamma_f$. On Γ_0 $(x = 0)$, Dirichlet boundary conditions are imposed, i.e. displacement $\mathbf{u}$ and concentration h are set to zero, and pressure P is set to $\overline{p_v}$. On Γ_f $(x = 1)$, a free boundary condition is imposed on the displacement, i.e. $\mathbf{S}_s^E \mathbf{n} = 0$, while a wall condition is imposed on the pressure and the concentration h, i.e. $\nabla P \cdot \mathbf{n} = 0$ and $\left(\mathbf{D}^0_{\text{enz}} \nabla h + h J_{\text{enz}}\right) \cdot \mathbf{n} = 0$. Visualization with the software FreeFem++ allows us to plot the porosity f and any other quantities of interest directly in a changing domain thanks to the function movemesh [61].

The principal scope of this serie of numerical experiments is to understand the qualitative behavior of the porosity after an injection of ECM degradation enzyme. Four sets of simulation tests are performed to investigate respectively the transport and effect of a passive substance (like water), the sole effect of degradation of the ECM by the enzyme injected, the effect of the enzyme on the ECM with recovery and the effect of the enzyme on the ECM with natural degradation of the enzyme. The fifth set of simulations corresponds to investigating how all the different effects interact together. Table 4.1 sums up these five different sets of simulations.

Simulations are performed first on the computational domain described in Figure 4.10 and the effects on the porosity f are investigated. Figures 4.11 represent

Table 4.1: Investigation of the effects on porosity of the parameters for each simulation test.

	K	a_r	k^d_{enz}	Considered Phenomena
Simulation 1	0	0	0	Passive transport
Simulation 2	0.5	0	0	Effect on ECM
Simulation 3	0.5	0.01	0	Effect on ECM + Recovery
Simulation 4	0.5	0	0.001	Effect on ECM + Natural degradation
Simulation 5	0.5	0.01	0.001	Effect on ECM + Recovery + Natural degradation

the porosity of the medium at four different times for each simulation: after 1 minute, 10 minutes, 30 minutes and 1 hour.

In the case of passive transport of water, the porosity remains equal to its initial value (0.1 in all four simulations). In reality, the porosity varies a little bit because of the volume variation, but when plotted between 0 and 1 it is not obvious and it seems legitimate to assume that the porosity is a constant in this case (4.11a). In the second set of simulations, we want to investigate the sole effect of degradation of the ECM by the enzyme, without recovery of the tissue and without natural degradation of the enzyme. With $K = 0.01$, the effect of the enzyme on the ECM is immediate: after 1 minute, the ECM around the injection site has deteriorated. Then, with the diffusion of the enzyme, the area where the ECM deteriorates expands mostly towards the boundary Γ_f as the enzyme flows out the domain through boundary Γ_0, without ever overcrossing the maximum value possible $f + g_{\mathcal{E}} = 0.5$ (4.11b). When we add a recovery dynamic, we observe that at some point, the area where the ECM has deteriorated stops expanding and the porosity tends to get back to its initial state (4.11c). In the fourth set of simulations, the recovery dynamic is not considered anymore but we take into account the natural degradation of the enzyme. In this case, the area where the ECM deteriorates starts expanding then reaches its equilibrium state (4.11d). In the last set of simulations, all effects are considered together (4.11e).

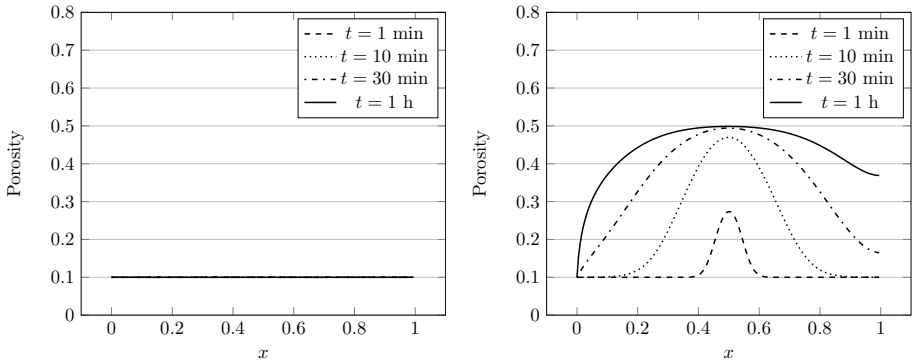

(a) Simulation 1

(b) Simulation 2

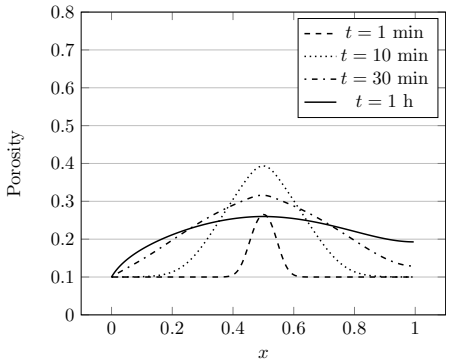

(c) Simulation 3

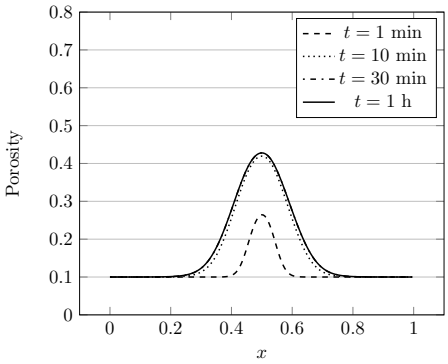

(d) Simulation 4

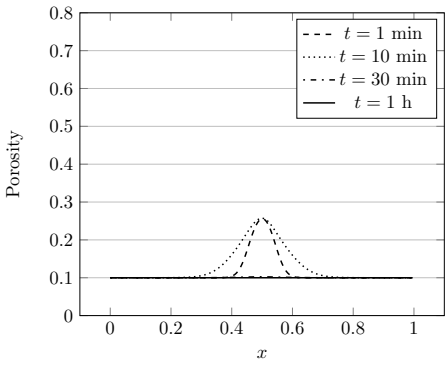

(e) Simulation 5

Figure 4.11: Porosity changes at $t = 1$ min, 10 min, 30 min and 1 hour in the 1D case.

4.5.3 Numerical tests in 2D

The computational domain. Figure 4.12 shows a schematic representation of the 2D reference domain we considered.

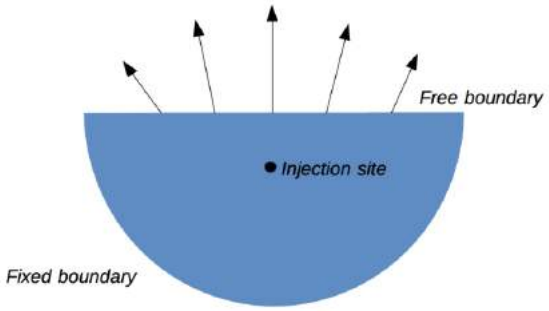

Figure 4.12: Schematic representation of the 2D reference domain. As in the 1D case, the border of the domain was divided in two parts: $\Gamma = \Gamma_0 \cup \Gamma_f$. On Γ_0, Dirichlet boundary conditions were imposed, while on Γ_f, free boundary conditions were imposed.

Simulation tests. As before, we consider in this section system (4.55) without equation (4.55g) and $\overline{\gamma}$ is chosen so the initial pressure, derived from equation (4.63), is a constant. Parameters K, a_r and k^d_{enz} are set in order to mainly observe during the simulation's time the deterioration effect of the enzyme on the ECM. This second set of simulation tests in 2D consists mainly in comparing the isotropic and transverse isotropic cases. As expected the main difference lies in the shape of the area where the ECM has been deteriorated. These 2D simulations emphasize mainly the possibility offered by the mathematical model we developed of considering anisotropic media.

4.6 Comparison with experiments : drug penetration in solid tumors

4.6.1 Experimental framework

To be most effective, anticancer drugs must penetrate tumor tissue efficiently, reaching all cells in a concentration suffcicient to exert a therapeutic effect. Nevertheless, the distribution of many anticancer drugs in tumor tissue is incomplete, as physiological transport barriers can strongly abate their efficiency [83, 122]. In

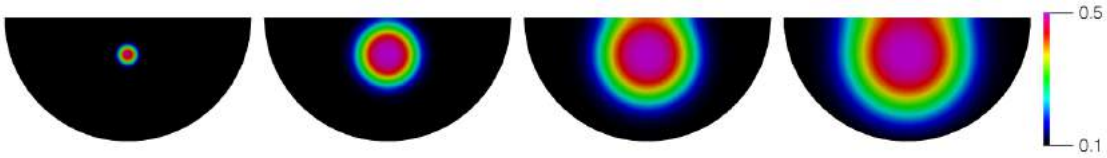

(a) Porosity at $t = 1, 10, 30, 60$ minutes in the 2D isotropic case

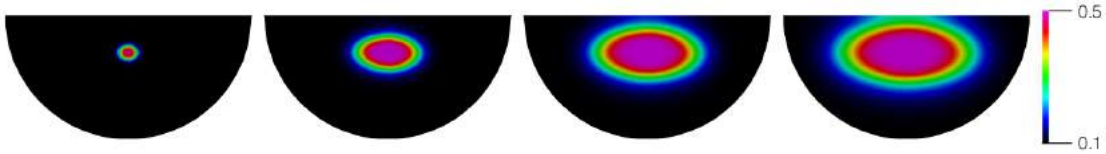

(b) Porosity at $t = 1, 20, 60, 120$ minutes in the 2D anisotropic case

Figure 4.13: Porosity changes at $t = 1$ min, 10 min, 30 min and 1 hour in the 2D case for $K = 50$, $a_r = 0.0005$ and $k^d_{\text{enz}} = 0.0001$.

particular, the composition and structure of the extracellular matrix can slow down the movement of molecules within the tumor [92]. Degradation of the ECM is assumed to improve the penetration of drugs. Delivery of drug to tumor cells occurs by two independent mechanisms: diffusion due to the concentration gradient and convection due to pressure gradient. It has been shown that both those mechanisms are enhanced when the tissue is previously injected or incubated with ECM degradation enzymes such as hyaluronidase and collagenase [46, 47, 45]. Multicellular spheroids are spherical aggregates of tumor cells that reflect many properties of solid tumors, including the development of an ECM, therefore they have been used to study the penetration of anticancer drugs into tumor tissue [83]. Experimental results are consistent in showing limited drug penetration into spheroids [119]. A pretreatment with hyaluronidase or collagenase was shown to increase the diffusion coefficient of larger molecules in spheroids, and the enzymatic treatment also improved the diffusion in the case of smaller molecules in tumor tissue [47], thereby improving the tissue's sensitivity to cytotoxic drugs [117, 69]. Spheroids models allow to evaluate the influence of diffusion on drugs transport, but some features of solid cancer such as variable IFP and the influence of convection (which commonly occurs in the periphery of tumors) are not modeled [83]. In vivo, the disorganized vascular network and the absence of functional lymphatics causes increased interstitial fluid pressure (IFP), which is uniformly elevated throughout

Table 4.2: Values of the model parameters in the simulations of Sections 4.5 and 4.6, except from K, a_r, k^d_{enz} otherwise specified. Parameters indexed with a * have different values in Section 4.6 (see Table 4.3).

Parameter	Symbol	Value	Unit	Reference
Typical length	l_0	10^{-2}	m	
Reference concentration	c_0	10^9	kg/m^3	
Density of fluid phase	ρ_f^R	10^3	kg/m^3	[128]
Density of solid phase	$\rho_s^{R,0}$	1.09×10^3	kg/m^3	[124]
Specific storage coefficient	s_0	10^{-6}	Pa^{-1}	
Injected concentration	$c^{\text{enz}}_{\text{inj}}$	4×10^{-2}	U/μl	[113]
Diffusion coefficient of the enzyme*	D^0_{enz}	10^{-8}	m^2/s	
Permeability	κ	10^{-11}	m^{2}Pa^{-1}s^{-1}	[121]
Lamé first parameter	λ	7.14×10^5	Pa	[130]
Lamé second parameter	μ	1.79×10^5	Pa	[130]
Diffusion coefficient perpendicular to a fiber's axis	$D^0_{\text{enz},\perp}$	10^{-8}	m^2/s	
Diffusion coefficient parallel to a fiber's axis	$D^0_{\text{enz},/\!/}$	$1.5 \times D^0_{\text{enz},\perp}$	-	[35]
Permeability perpendicular to a fiber's axis	$\kappa_\perp$	10^{-11}	m^{2}Pa^{-1}s^{-1}	
Permeability parallel to a fiber's axis	$\kappa_{/\!/}$	$1.5 \times \kappa_\perp$	-	
Elastic constants (TI case)	C_{1111}	2.64×10^6	Pa	[76]
	C_{1133}	3.39×10^6	Pa	[76]
	C_{1313}	10^2	Pa	[76]
	C_{3333}	4.4×10^6	Pa	[76]

Initial values	Symbol	Initial value	Unit
Volume fraction of fluid	$\varphi_f(0,\mathbf{x})$	0.1	-
Volume fraction of ECM	$\varphi_{\mathcal{E}}(0,\mathbf{x})$	0.4	-
Volume fraction of cells	$\varphi_e(0,\mathbf{x})$	0.5	-
Network dilatation	$\nabla.\mathbf{u}(0,\mathbf{x})$	0	-
Concentration in enzyme	$h(0,\mathbf{x})$	0	Um^{-3}
Pressure	$p(0,\mathbf{x})$	0	Pa

a solid tumor and drops precipitously in the tumor periphery [63, 24]. The high IFP is a major obstacle to penetration of therapeutic molecules, as the transcapillary pressure gradient is low, and an outward interstitial flux is generated toward the periphery of the tumor due to the steep pressure gradient in the periphery of the tumor. It has been shown that hyaluronidase and collagenase reduce IFP, thereby improving the tumor uptake and distribution of molecules within solid tumors [46, 27]. The tumor (resp. spheroid) was modeled as a sphere and consequently we chose to perform numerical simulations in axisymmetry. We used the 2D computational domain shown in Figure 4.18 and the computational algorithm

presented in section 4.5.1. The variational formulations used in the algorithm are written in an axisymmetric form (see Appendice B). No calibration of the parameters was done, our objective being to observe the qualitative effects of the incubation with ECM degradation enzyme of a spheroid on diffusion on one hand, and of an intratumoral injection of ECM degradation enzyme on transcapillary transport on the other hand.

4.6.2 Effect of an ECM degradation enzyme on diffusion of therapeutic agent

4.6.2.1 Boundary conditions

Define the portions of the boundary Γ_{ext}, the surface of the spheroid, and Γ_{int} the inner boundaries. To take into account the axisymmetric geometry of the domain, we choose on the internal boundaries Γ_{int} homogeneous Neumann conditions on P, h and c and we impose that the displacement will only be radial. On the surface of a spheroid, there are no contact forces and the pressure at the outer edge is the same as the pressure in the surrounding medium, that we set to be equal to P_{ext}.

$$\begin{cases} \mathbf{S}_s^E \, \mathbf{n} = 0 \text{ on } \Gamma_{\text{ext}}, & \mathbf{u} \cdot \mathbf{n} = 0 \text{ on } \Gamma_{\text{int}}, \quad (4.70a) \\ P = P_{\text{ext}} \text{ on } \Gamma_{\text{ext}}, & \nabla P \cdot \mathbf{n} = 0 \text{ on } \Gamma_{\text{int}}, \quad (4.70b) \end{cases}$$

During the first hour, the spheroid is incubated with the enzyme, so instead of taking a source term in equation (4.55d), we choose a Dirichlet boundary condition on h.

$$\begin{cases} h = \dfrac{\alpha}{c_0} c_{\text{inj}}^{\text{enz}} \text{ on } \Gamma_{\text{ext}}, & \nabla h \cdot \mathbf{n} = 0 \text{ on } \Gamma_{\text{int}}, \end{cases} \quad (4.71)$$

After one hour, the medium containing the enzyme is removed and a fresh medium containing the molecule of interest is added. Consequently, we choose a Dirichlet boundary condition on c and we set the outter flux of enzyme to be zero.

$$\begin{cases} \left(\mathbf{D}^0_{\text{enz}} \nabla h + h J_{\text{enz}}\right) \cdot \mathbf{n} = 0 \text{ on } \Gamma_{\text{ext}}, & \nabla h \cdot \mathbf{n} = 0 \text{ on } \Gamma_{\text{int}}, \quad (4.72a) \\ c = \dfrac{\alpha}{c_0} c^{\text{drug}}_{\text{inj}} \text{ on } \Gamma_{\text{ext}}, & \nabla c \cdot \mathbf{n} = 0 \text{ on } \Gamma_{\text{int}}. \quad (4.72b) \end{cases}$$

After a while, the spheroid can be removed from this second medium. In this third case, we set the outter flux of enzyme and of therapeutic agent to be zero.

$$\begin{cases} \left(\mathbf{D}^0_{\text{enz}} \nabla h + h J_{\text{enz}}\right) \cdot \mathbf{n} = 0 \text{ on } \Gamma_{\text{ext}}, & \nabla h \cdot \mathbf{n} = 0 \text{ on } \Gamma_{\text{int}}, \quad (4.73a) \\ \left(\mathbf{D}^0_{\text{drug}} \nabla c + c J_{\text{drug}}\right) \cdot \mathbf{n} = 0 \text{ on } \Gamma_{\text{ext}}, & \nabla c \cdot \mathbf{n} = 0 \text{ on } \Gamma_{\text{int}}. \quad (4.73b) \end{cases}$$

4.6.2.2 Effect on porosity

As expected, the porosity remains quasi constant and equal to its initial constant value (0.1 in this case) when the spheroid is incubated in a medium with no enzyme. On the contrary, it varies when the tissue is incubated with an ECM degradation enzyme. Thus, at $t = 60$ minutes, the ECM has been degraded substantially all over the spheroid, and although the degradation of the ECM is slightly higher at the boundary, the effect is quite homogeneous (Figure 4.14a). As far as the total mass of fluid within the spheroid is concerned, it increases gradually while the enzyme degrades the ECM (Figure 4.14b).

4.6.2.3 Results

ECM degradation enzymes such as collagenase and hyaluronidase where shown to increase the diffusion of macromolecules in spheroid and in tumor tissue, with a greater impact witnessed in the case of collagenase compared to hyaluronidase [47]. We performed simulations to evaluate the effect of an incubation of a spheroid with enzyme on the distribution of drugs with a low coefficient of diffusion ($D^0_{\text{drug}} = 10^{-9}$ ui), such as the one of a macromolecule. We simulate the incubation during 5 minutes with a therapeutic agent one hour after the incubation with collagenase and we observed the behavior of the drug's concentration for ten minutes, including

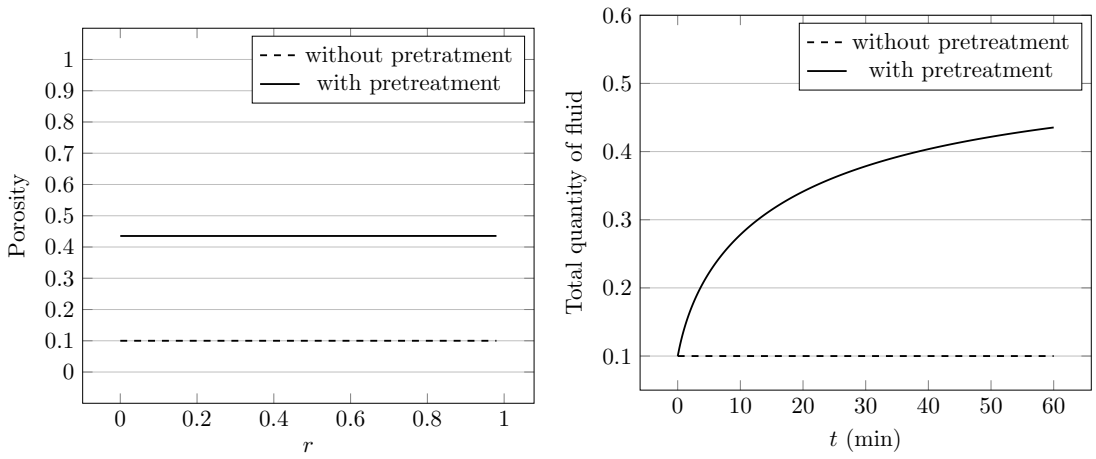

(a) Porosity versus radial position at the end of the incubation phase.

(b) Quantity of fluid in the tissue versus time.

Figure 4.14: Effect on the porosity of a tissue incubated with collagenase (20 U) during 60 minutes compared to incubated with a saline solution (0 U).

the 5 minutes of incubation. It can be observed that the area where the drug is present above a certain minimum concentration is wider when the spheroid was previously incubated with collagenase (Figure 4.15).

We then performed simulations to evaluate the effect of an incubation of a spheroid with enzyme on the distribution of drugs with an higher coefficient of diffusion ($D^0_{\text{drug}} = 10^{-6}$ ui), such as the one of a small molecule. In this case, the whole domain is affected with or without pretreatment, but the degraded ECM has two main effects: the drug reaches the whole domain faster, and naturally degrades slower which results in a higher concentration of drug throughout the tissue after 10 minutes (Figure 4.16).

We finally performed simulations with a quite low coefficient of diffusion ($D^0_{\text{drug}} = 10^{-8}$ ui), but for a tissue incubated longer (15 minutes) and we waited 15 more minutes to look at the drug's distribution. In this case, the result is qualitatively in agreement with the experiments developed by [69] (cf Figure 4.1): with an enzyme pretreatment, the drug distribution after 30 minutes (including 15 minutes of incubation) is way better than if the tissue was not pretreated (Figure 4.17). The drug is not only present all over the tissue, its concentration is also higher,

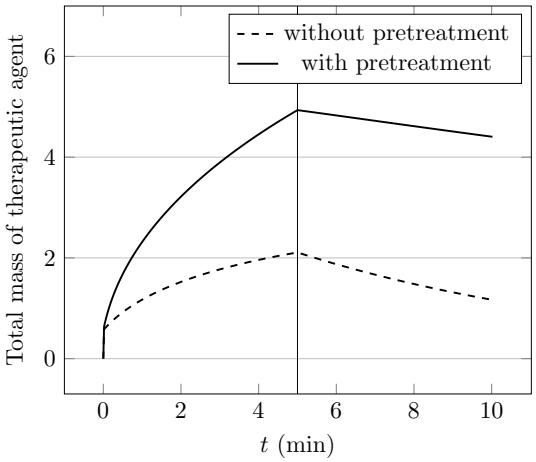

(a) Drug's total mass in the tissue versus time.

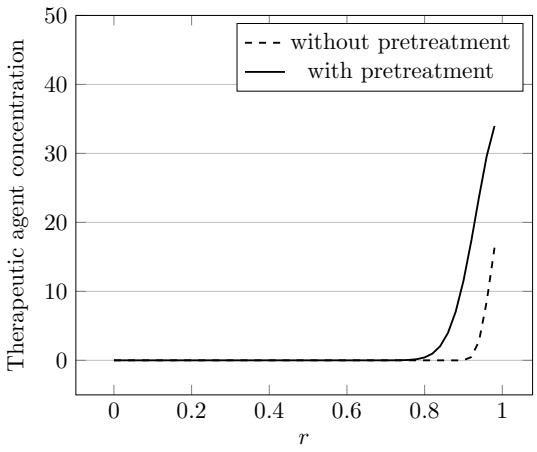

(b) Drug's concentration plotted versus the postion in the tumor at time $t = 10$ minutes.

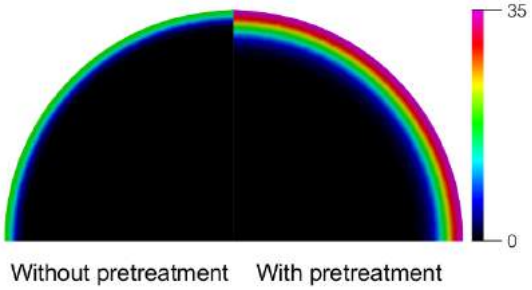

(c) 2D-drug's concentration in the tumor at time $t = 10$ minutes.

Figure 4.15: Numerical results for a therapeutic agent with a low coefficient of diffusion incubated during 5 minutes.

improving thus the chances of uptake by the cells.

In the specific framework of an injection of DNA plasmids, a question of interest would be to determine when to do electrotransfer. If the best moment is when the area where the DNA plasmids concentration is above a certain minimum concentration is the widest, then the model, rightfully calibrated, could allow to calculate this optimized time.

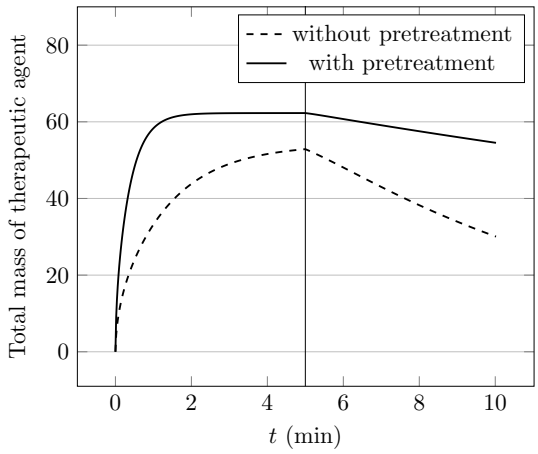

(a) Drug's total mass in the tissue versus time.

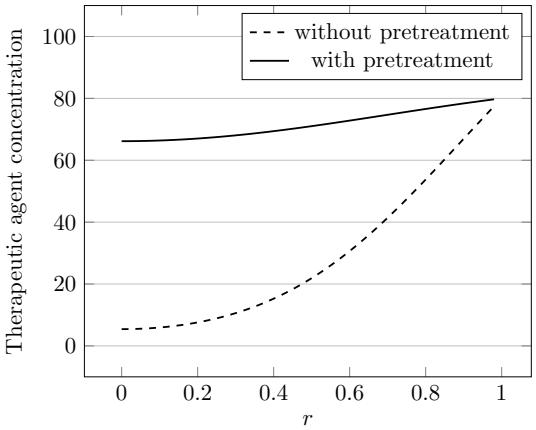

(b) Drug's concentration plotted versus the postion in the tumor at time $t = 1$ minute.

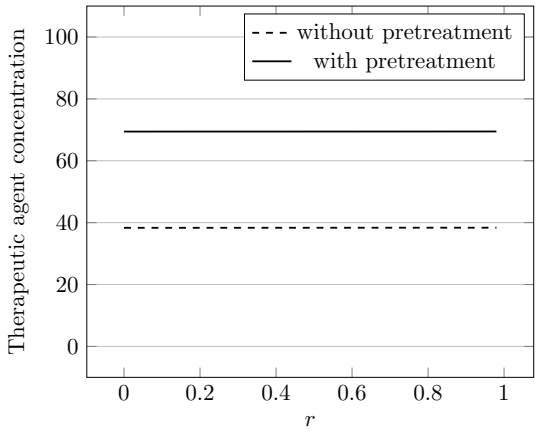

(c) Drug's concentration plotted versus the postion in the tumor at time $t = 10$ minutes.

Figure 4.16: Numerical results for a therapeutic agent with an higher coefficient of diffusion incubated during 5 minutes.

4.6.3 Effect of an ECM degradation enzyme on transcapillary transport of therapeutic agent

4.6.3.1 Boundary conditions

Define the portions of the boundary Γ_{ext}, the surface of the tumor, and Γ_{int} the inner boundaries. On the surface of an isolated tumor, there are no contact forces and the pressure at the outer edge is the same as the pressure in the surrounding

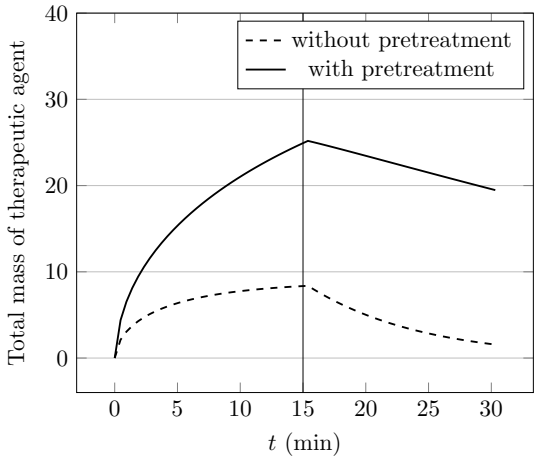

(a) Drug's total mass in the tissue versus time.

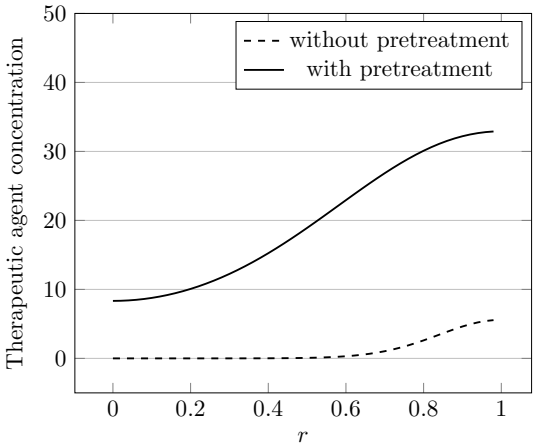

(b) Drug's concentration plotted versus the postion in the tumor at time $t = 30$ minutes.

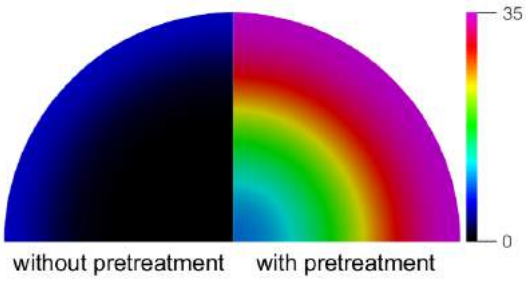

(c) 2D-drug's concentration in the tumor at time $t = 30$ minutes.

Figure 4.17: Numerical results for a therapeutic agent with a quite low coefficient of diffusion incubated during 15 minutes.

tissue, that we set to zero. On the concentration of the injected species, we assume that their flux is zero on Γ_{ext}. To take into account the axisymmetric geometry of the domain, we choose on the internal boundaries Γ_{int} homogeneous Neumann conditions on P, h and c and we impose that the displacement will only be radial.

$$\begin{cases} \mathbf{S}_s^E \mathbf{n} = 0 \text{ on } \Gamma_{\text{ext}}, & \mathbf{u} \cdot \mathbf{n} = 0 \text{ on } \Gamma_{\text{int}}, \quad (4.74a) \\ P = 0 \text{ on } \Gamma_{\text{ext}}, & \nabla P \cdot \mathbf{n} = 0 \text{ on } \Gamma_{\text{int}}, \quad (4.74b) \\ \left(\mathbf{D}^0_{\text{enz}} \nabla h + h J_{\text{enz}}\right) \cdot \mathbf{n} = 0 \text{ on } \Gamma_{\text{ext}}, & \nabla h \cdot \mathbf{n} = 0 \text{ on } \Gamma_{\text{int}}, \quad (4.74c) \\ \left(\mathbf{D}^0_{\text{drug}} \nabla c + c J_{\text{drug}}\right) \cdot \mathbf{n} = 0 \text{ on } \Gamma_{\text{ext}}, & \nabla c \cdot \mathbf{n} = 0 \text{ on } \Gamma_{\text{int}}. \quad (4.74d) \end{cases}$$

Table 4.3: Values of the specific model parameters in the simulations of Section 4.6. All other parameters are taken from Table 4.2.

Parameter	Symbol	Value	Unit	Reference
Diffusion coefficient of the enzyme	D^0_{enz}	10^{-4}	m^2/s	
Diffusion coefficient of the therapeutic agent	D^0_{drug}	10^{-9}, 10^{-6}, 10^{-8}	m^2/s	
Starling's coefficient	γ	5×10^{-5}	$\text{Pa}^{-1}\text{s}^{-1}$	[114]
Fluid/solute coefficient	γ_c	0.9	-	[19]
Measure of treatment efficacity	K	10^{-14}	$\text{m}^3\text{s}^{-1}\text{U}^{-1}$	
Recovery coefficient	a_r	5×10^{-4}	s^{-1}	
Degradation rate of the enzyme	k^d_{enz}	1×10^{-4}	s^{-1}	
Degradation rate of the therapeutic agent	k^d_{drug}	2×10^{-4}	s^{-1}	
Driving pressure	P_v	10^{-1}	Pa	

Initial values	Symbol	Initial value	Unit
Concentration in drug	$c(0, \mathbf{x})$	0	kg m^{-3}
Pressure incubation case	$p(0, \mathbf{x})$	0	Pa

4.6.3.2 Initial pressure profile

In the simulations, $\overline{P_v}$ and $\overline{\gamma}$ are chosen so the initial pressure profile, derived from equation (4.63), fits the type of IFP profile observed in tumors (Figure 4.18).

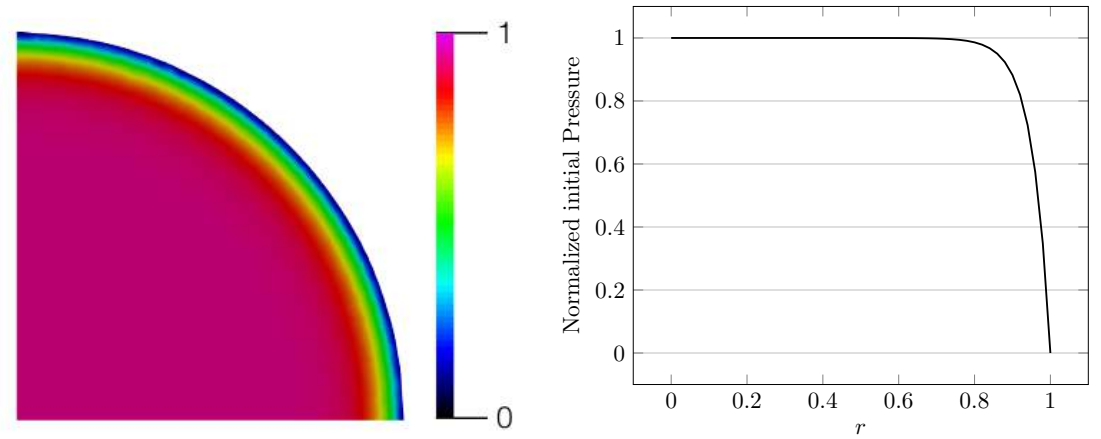

(a) Normalized 2D-pressure in the tumor before the experiment.

(b) Normalized pressure in the tumor before the experiment versus position.

Figure 4.18: Initial normalized pressure profile. This type of steep profile is in agreement with previous studies [19].

4.6.3.3 Effect on porosity

As it was previously observed in Section 4.5.2, the porosity remains quasi constant when only a saline solution is injected. On the contrary, it varies when the tissue is injected with an ECM degradation enzyme. At $t = 60$ minutes, we observe that without enzyme, the porosity is equal to its initial constant value (0.1 in this case) while in presence of enzyme, the ECM has been degraded substantially all over the tissue. Although the degradation of the ECM is the slightly higher in the vicinity of the injection point, the effect is quite homogeneous. As expected, the total mass of fluid within the tissue increases gradually while the enzyme degrades the ECM.

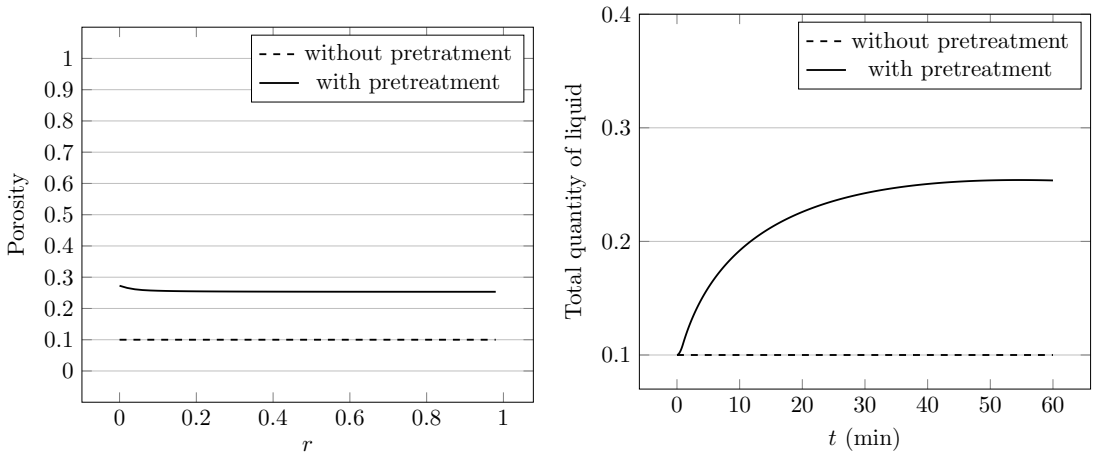

(a) Porosity versus radial position 60 minutes after the injection.

(b) Quantity of fluid in the tissue versus time.

Figure 4.19: Effect on the porosity of a tumor injected with hyaluronidase (1500 U) compared to injected with a saline solution (0 U).

4.6.3.4 Effect on the IFP

The effect of hyaluronidase on IFP was demonstrated experimentally by [46] and [27]. Intratumoral injection of hyaluronidase in tumors reduced IFP in a dose-dependent manner up to a maximum reduction. However, by increasing the dose further, IFP was reduced to a lesser extent. An initial increase in IFP was

observed, explained by the increase in the volume and compression of the tissue at the moment of the intratumoral injection.

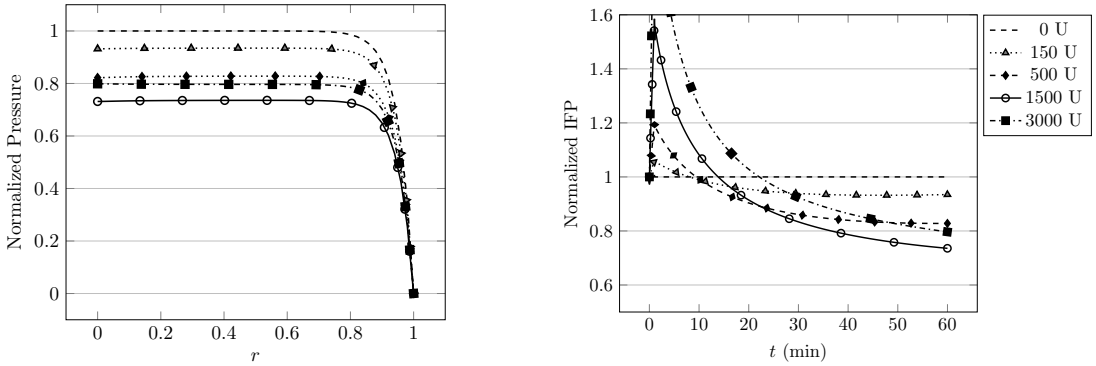

(a) Normalized IFP versus position at time $t = 60$ minutes.

(b) Normalized IFP versus time.

Figure 4.20: Effect on the normalized interstitial fluid pressure of a tumor injected with hyaluronidase (500 U, 1500 U, 3000 U) compared to injected with a saline solution.

The simulation reproduces the three main effects observed in the experiments: an initial increase in IFP due to the intratumoral injection, the fact that IFP reaches a reduced value after some time and finally the nonlinear behavior regarding the concentration.

4.6.3.5 Results

It was shown that both hyaluronidase and collagenase increase convection by inducing transcapillary pressure gradients in human osteosarcoma xenografts [46, 45]. We have seen previously that an injection of enzyme has an effect on the IFP, inducing a transcapillary pressure gradient in a dose-dependent manner up to a maximum reduction. Increasing the dose further, IFP is reduced to a lesser extent. This reduction was shown to improve both the distribution and the uptake of drugs in tumors [46]. In this section, we focus on the distribution of drugs. We simulate an injection during 1 minute of a therapeutic agent one hour after the injection of enzyme and we observed the behavior of the drug's concentration for ten minutes, including during the injection. For all simulatiojns, the same

value of $c_v(t, \mathbf{x}) = \chi_{\{0 \leq t \leq 1\,\mathrm{min}\}}(t)\, c_v$ is taken while different values of $c_{\mathrm{inj}}^{\mathrm{enz}}$ previously injected are considered. For a drug with a low coefficient of diffusion, such as the one of a macromolecule, several features are observed. First, the total mass of therapeutic agent that actually reaches the tumor by transcapillary transport varies with the concentration of enzyme previously injected (Figure 4.21a). Second, while without enzyme the therapeutic agent only penetrates the periphery of the tumor, we observe that with a pretreatment, the therapeutic agent is present all over the tumor (Figure 4.21b). Finally, the same nonlinear behavior regarding the concentration of enzyme previously injected is observed. In particular, if the concentration of enzyme is too high, as the pressure is reduced to a lesser extent, the drug's penetration in the tumor by transcapillary transport is also reduced.

For a drug with an higher coefficient of diffusion, such as the one of a smaller molecule, the transcapillary transport in the tumor is also improved, but the main features of interest are different. In particular, as the drug reaches the whole tumor mainly by diffusion in any case, the contributions of the pretreatment of the tumor with an ECM degradation enzyme are the same as the ones developed in the previous subsection concerning spheroids. In particular, it is when the concentration of enzyme previously injected is the highest that the drug reaches homogeneously the tumor the fastest and that the natural degradation process is slowed the most. Nevertheless, the total mass of therapeutic agent that actually reaches the tumor by transcapillary transport is consistent with the reduction of IFP in the same nonlinear behavior regarding the concentration of enzyme, and consequently, at $t = 10$ minutes, the best configuration is also obtained for the concentration of enzyme that induces the highest reduction in IFP.

The distribution of the drug into the tissue is directly correlated with the transcapillary pressure gradient created by the hyaluronidase injected. In particular, it is for the hyaluronidase's concentration value for which the maximum pressure reduction is obtained that we obtained the best distribution profile. Increasing the dose further, the pressure is reduced to a lesser extent and the consequence on the distribution of drug is that the area where the concentration of therapeutic agent is above a minimum concentration value is smaller. This result is in agreement

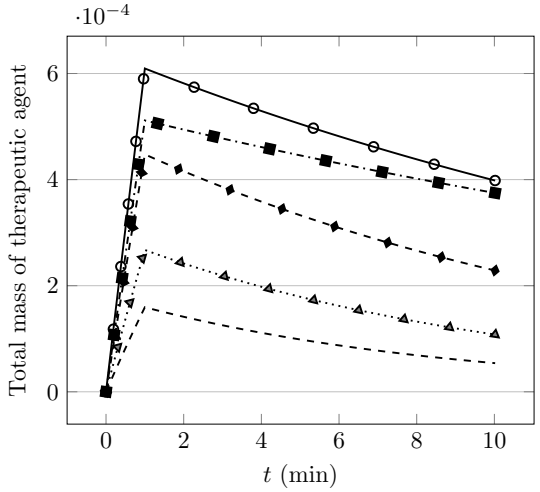

(a) Drug's total mass in the tissue versus time.

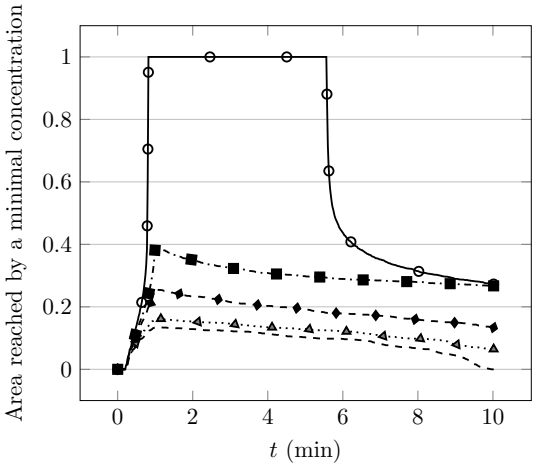

(b) Normalized area reached by a minimal concentration of therapeutic agent versus time.

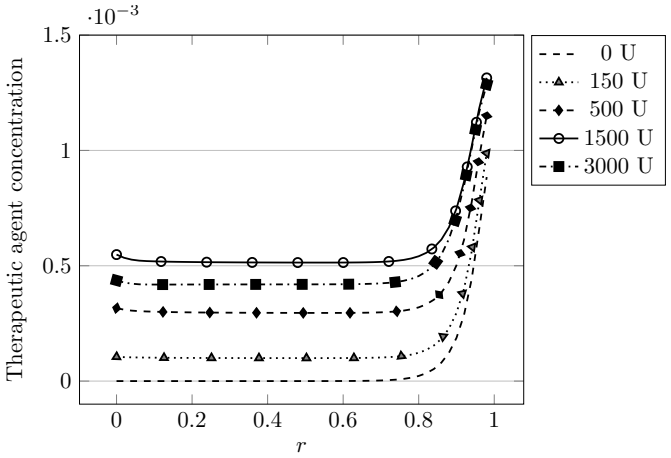

(c) Drug's concentration plotted versus the postion in the tumor at time $t = 5$ minutes.

Figure 4.21: Numerical results for a therapeutic agent with a low coefficient of diffusion injected intravenously.

with the experiments described by [46] where hyaluronidase was shown to improve the distribution of doxorubicin considerably. To go further and consider the possibility of using the model as a strategie to optimize drug delivery, we would need more experimental data to calibrate the model parameters.

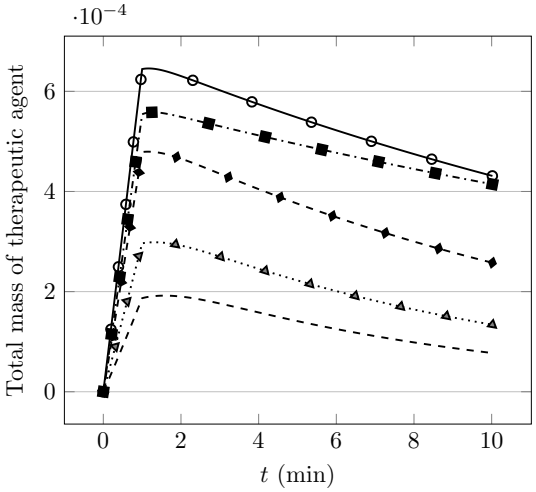

(a) Drug's total mass in the tissue versus time.

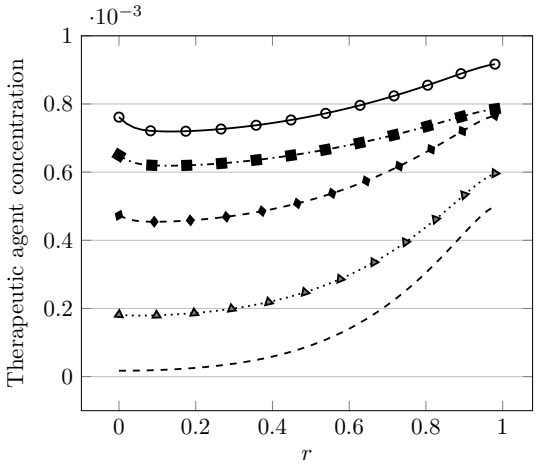

(b) Drug's concentration plotted versus the postion in the tumor at time $t = 1$ minute.

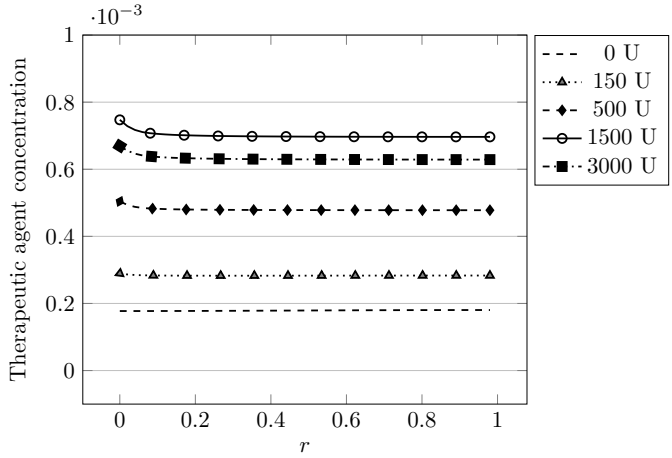

(c) Drug's concentration plotted versus the postion in the tumor at time $t = 5$ minutes.

Figure 4.22: Numerical results for a therapeutic agent with an higher coefficient of diffusion injected intravenously.

4.7 Conclusion

In this chapter we developed a novel mathematical formulation to describe the effect of an ECM degradation enzyme on a soft biological tissue. The principal novelty of our contribution is the development of a model based on the use of Partial Differential Equations (PDEs) that incorporates the effect of an ECM degra-

dation enzyme within the general and well established framework of poroelastic theory of mixtures. Specifically, where usually the fraction volumes of the different phases are assumed to be constants, we derive evolutive equations to describe them. Having defined the possible interactions between phases, our approach consists in deriving a system of conservation laws (mass and linear momentum) for the phases and components of the mixture that includes the enzyme's concentration as main determinant of porosity evolution. The next step was to develop a numerical approximation of the mathematical model introduced in the article. As the medium is assumed to be poroelastic, it can undergo some deformation and potentially change of shape if a boundary condition is applied on stress. It was necessary to formulate our model in a reference fixed domain before developing a computational algorithm to approximate the system's solution. Below we address the more significant outcomes of the conducted simulations.

1. The illustrated numerical tests conducted in 1D indicate the role of each new parameter on the porosity evolution.

2. The illustrated numerical results in 2D can describe a well known principle of prefential flow in the direction of the fiber tracts in the context of a transverse anisotropic media.

3. Model simulations indicate that an intratumoral injection of hyaluronidase results in a reduction of the IFP in a dose-dependent manner up to a maximum reduction, and that once that maximum reduction is achieved, a further increase of the dose results in a smaller reduction. This finding represents a favorable result from the experimentalist point of view, because it is in agreement with several observations previously reported.

4. The injection of an ECM degradation enzyme was also shown to enhance distribution, by improving diffusion and/or convection, of drug throughout the tissue. This outcome reinforces the idea that, used in medicine, these enzymes can improve a treatment by widening its field of action.

Further research effort will be devoted to calibrating the model's parameters with additional experimental data and to considering domains with more complex 3D

geometries. An effort will also be made to rightfully coupled this model with an electrical model in order to explain and quantify the uptake of DNA plasmids observed by [113]. Note that some studies underline the fact that the activity of matrix degrading enzymes can be pro-tumorigenic and pro-metastatic [79]. The use of hyaluronidase (for instance) in order to improve the distribution of anti-cancer drugs is thus controversial. Nevertheless, its interest in the framework of gene therapy, combined with electroporation, has been well established. It is with this application in mind that an optimization procedure is investigated in Chapter 5.

Chapter 5

Optimization of drug delivery with an enzyme pretreatment

This chapter is the result of a collaboration with D. Peri of the Istituto per le applicazioni del calcolo M. Picone (Rome, Italy).

5.1 Motivations

In part I and chapter 4, we presented two differents methods to enhance drug penetration and uptake in tissue: the use of permeabilizing electric pulses and the degradation of the extracellular matrix by injecting specific enzymes. The logic would be, in the case of macromolecules, to combine those two methods to obtain even better penetration and uptake. To our knowledge, this combination has not been tested for anticancer drugs, but has been quite widely studied in the framework of gene therapy [1, 108, 113].

In this chapter, we propose an optimization strategy to determine a set of chosen parameters for which the area where the drug concentration is sufficiently high is maximal. First, a parameters space is chosen to work with. In section 5.2, the mathematical modeling developed in Chapter 4 is used to analyse drug delivery after a pretreatment with a matrix-degrading enzyme. A well-chosen objective

function is found to optimize the protocol. Then, in section 5.3, the numerical methods to construct an analytical approximation of the model based on a limited number of sampling points are presented. The sampling points selection is done by constructing an orthogonal array while the analytical approximation of the model is derived from the sampling points using Kriging interpolation. Finally, we present in section 5.4 the results obtained using this interpolation method on a test case, using a simple 2D geometry and fixed parameters that were not calibrated on biological data, even if the order of magnitude of those parameters was respected.

5.1.1 Optimizing gene therapy

DNA electrotransfer has been used with success since the 90s and is becoming a real alternative to the viral methods for *in vivo* gene transfer [9]. It was shown in 1990 [126] that direct injection of naked DNA in skeletal muscle *in vivo* results in gene expression at low and variable levels. In 1998, different studies consistently showed that good transfection levels could be obtained when combining the injection of DNA and electroporation, in different types of tissues [102], [120], [84]. Numerous efforts have been made to optimize gene expression. In particular the respective influence of the pulse duration, voltage applied, number of pulses and repetition frequency was analysed, showing for example that long pulses act on DNA, provoking its electrophoretic displacement towards, or accross, the cell membrane [9].

Another approach to increase the efficiency of gene electrotransfer is to increase the diffusion and distribution of DNA plasmid into the tissue by controlling and partially degrading the ECM using enzymes such as hyaluronidase and collagenase [49]. This approach is particularly efficient in skeletal muscle [113], [108], for which it was shown that hyaluronidase induces a 10- to 25-fold increase of gene expression in mice and rabbit skeletal muscle after intramuscular injection and electroporation compared to no pretreatment. This is due to an improved distribution of plasmids obtained prior to the electroporation treatment. In [113], it is said that the electroporation procedure is carried out immediately after the

injection of DNA plasmids, in order to avoid the very rapid degradation of the intramuscular injected plasmids [30]. Although it has been determined that electroporation should be carried out rapidly after the DNA injection, no investigation has been made to optimize the exact time of electroporation.

5.1.2 Optimization strategy

Because DNA -or any therapeutic agent- concentration is time and space-dependent, it is crucial to determine a rational drug delivery protocol. In the current work, we used the mathematical modeling developed in Chapter 4 to analyse drug delivery after a pretreatment with a matrix-degrading enzyme. The major goal of the present work is thus the rational design of an optimal drug delivery strategy. Three independent control variables are at our disposal:

- T the time lag between the injection of enzyme and the injection of therapeutic agent,
- y_0 the position of the injection point,
- $c_{\text{drug}}^{\text{inj}}$ the concentration of therapeutic agent in the fluid injected.

The goal of our optimization strategy is simple: the area reached by a minimum concentration of drug should be the widest possible. Another quantity of interest is the time at which this area is the widest (or the first time at which this area is reached), which, in case of electrotransfer or electrochemotherapy, would be the optimal time to perform electroporation.

5.2 The model

We use the model developed in Chapter 4 to model the processes that govern drug distribution in tissue after an injection of matrix-degrading enzyme. We recall here the main features of this model. Let Ω be a bounded domain, and define the boundary of Ω, denoted Γ. Define also the portions of the boundary Γ_1 and Γ_2 on which mixed boundary conditions are defined, such as $\Gamma_1 \cup \Gamma_2 = \Gamma$.

5.2.1 PDE model

The mechanics of biological tissue are taken into account assuming that the tissue can be modeled as a saturated poroelastic mixture made of three different constituants: the interstitial fluid, the ECM and the cells. The medium is assumed to be saturated:

$$g_{\mathcal{E}} + g_{\mathcal{C}} + f = 1, \tag{5.1}$$

where f is the volume fraction of fluid, $g_{\mathcal{E}}$ is the volume fraction of extracellular matrix and $g_{\mathcal{C}}$ is the volume fraction occupied by cells. The mechanics of the mixture are described by the following poroelastic system:

$$\begin{cases} \boldsymbol{\nabla} \cdot \left((g_{\mathcal{E}} + g_{\mathcal{C}}) \left(\lambda (\nabla \cdot \mathbf{u}) I + \mu (\nabla \mathbf{u} + \nabla \mathbf{u}^T) \right) \right) = \nabla P, & \text{(5.2a)} \\ (g_{\mathcal{E}} + g_{\mathcal{C}}) s_0 \dfrac{\partial P}{\partial t} - \nabla \cdot (\boldsymbol{\kappa} \nabla P) = Q_{\text{inj}}^{\text{tot}} + \gamma (P_v - P) \\ \qquad + \left(\dfrac{\rho_s^{R,0}}{\rho_f^R} - 1 \right) g_{\mathcal{E}} (Kh + a_r (f(0, \mathbf{x}) - f)) - \nabla \cdot \left(\dfrac{\partial \mathbf{u}}{\partial t} \right), & \text{(5.2b)} \end{cases}$$

where $\mathbf{u}$ is the displacement of the solid phase and P the interstitial fluid pressure. Equations (5.2) are coupled with the following set of boundary conditions:

$$\begin{cases} \mathbf{u} = 0, & \text{on } \Gamma_1, \quad \text{(5.3a)} \\ \mathbf{S}_s^E \, \mathbf{n} = 0, & \text{on } \Gamma_2, \quad \text{(5.3b)} \\ P = P_v, & \text{on } \Gamma_1, \quad \text{(5.3c)} \\ \nabla P \cdot \mathbf{n} = 0, & \text{on } \Gamma_2. \quad \text{(5.3d)} \end{cases}$$

The volume fractions of ECM and of cells are given as the solutions of the following ODEs:

$$\begin{cases} \dfrac{\partial g_{\mathcal{C}}}{\partial t} + \left(s_0 \dfrac{\partial P}{\partial t} + \nabla \cdot \left(\dfrac{\partial \mathbf{u}}{\partial t} \right) \right) g_{\mathcal{C}} = 0, & \text{(5.4a)} \\ \dfrac{\partial g_{\mathcal{E}}}{\partial t} + \left(Kh + a_r (f(0, \mathbf{x}) - f) + s_0 \dfrac{\partial P}{\partial t} + \nabla \cdot \left(\dfrac{\partial \mathbf{u}}{\partial t} \right) \right) g_{\mathcal{E}} = 0. & \text{(5.4b)} \end{cases}$$

The volume fraction of fluid f is obtained using the saturation condition (5.1). The concentration of matrix-degrading enzyme is described by the following convection-diffusion reaction equation:

$$\frac{\partial h}{\partial t} = \nabla \cdot (f\mathbf{D}^0_{\text{enz}} \nabla h + hJ_{\text{enz}}) + h\left(-\frac{k^d_{\text{enz}}}{f} - \nabla \cdot \left(\frac{\partial \mathbf{u}}{\partial t}\right)\right) + \mathcal{S}_{\text{enz}}, \tag{5.5}$$

where $J_{\text{enz}} = \frac{1}{f}\boldsymbol{\kappa}\nabla P - \mathbf{D}^0_{\text{enz}}\nabla f$. Equation (5.5) is coupled with the following set of boundary conditions:

$$\begin{cases} h = 0, & \text{on } \Gamma_1, \quad (5.6a) \\ \left(f\mathbf{D}^0_{\text{enz}} \nabla h + hJ_{\text{enz}}\right) \cdot \mathbf{n} = 0, & \text{on } \Gamma_2. \quad (5.6b) \end{cases}$$

The concentration of therapeutic agent, injected after the matrix-degrading enzyme, is described by the following convection-diffusion reaction equation:

$$\frac{\partial c}{\partial t} = \nabla \cdot (f\mathbf{D}^0_{\text{drug}} \nabla c + cJ_{\text{drug}}) + c\left(-\frac{k^d_{\text{drug}}}{f} - \nabla \cdot \left(\frac{\partial \mathbf{u}}{\partial t}\right)\right) + \mathcal{S}_{\text{drug}}, \tag{5.7}$$

where $J_{\text{drug}} = \frac{1}{f}\boldsymbol{\kappa}\nabla P - \mathbf{D}^0_{\text{drug}}\nabla f$. Equation (5.5) is coupled with the following set of boundary conditions:

$$\begin{cases} c = 0, & \text{on } \Gamma_1, \quad (5.8a) \\ \left(f\mathbf{D}^0_{\text{drug}} \nabla c + cJ_{\text{drug}}\right) \cdot \mathbf{n} = 0, & \text{on } \Gamma_2. \quad (5.8b) \end{cases}$$

We refer to Chapter 4 for the significance of all constants.

5.2.2 Computational domain and timeline

We chose the same computational domain as in the numerical tests in 2D in Chapter 4 section 4.5.3 (see Figure 4.12). The computational domain is meshed with additional precision in the vicinity of the injection point ($dx = 0.01$). In Figure 5.1 are presented two different meshes of the computational domain: the mesh presented in Figure 5.1b, being finer, will give a better approximation than

the mesh presented in Figure 5.1a.

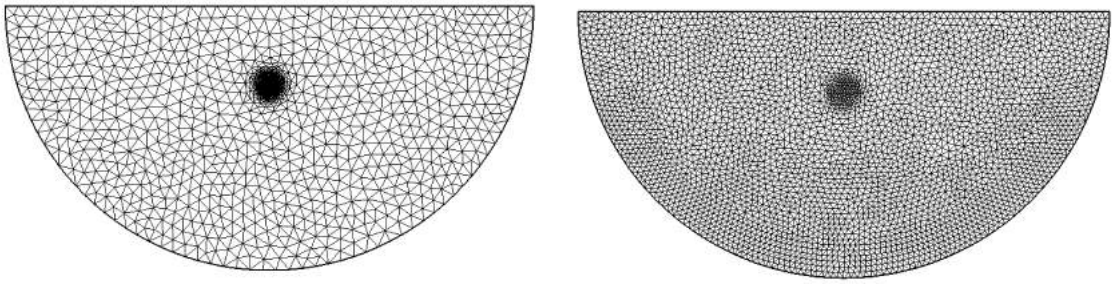

(a) $dx_{max} = 0.05$ (b) $dx_{max} = 0.025$

Figure 5.1: Two different meshes of the computational domain. Both are ajusted around the injection point.

Scheme 5.2.1 shows the timeline of one experiment we considered. The injection of enzyme is performed first ($\mathcal{S}_{\text{enz}} \neq 0$ at point $(0, y_0)$, where y_0 is a parameter to optimize). Then we supposingly wait for the enzyme to be effective during a lapse of time T. This time T varies as it is another parameter to optimize. Finally, the second injection of therapeutic agent is performed ($\mathcal{S}_{\text{drug}} \neq 0$ at point $(0, y_0)$). The drug concentration $c^{\text{inj}}_{\text{drug}}$ in the fluid injected is also a parameter to optimize. We then dispose of a time of observation of 10 minutes to evaluate the spatial distribution of drug in the tissue.

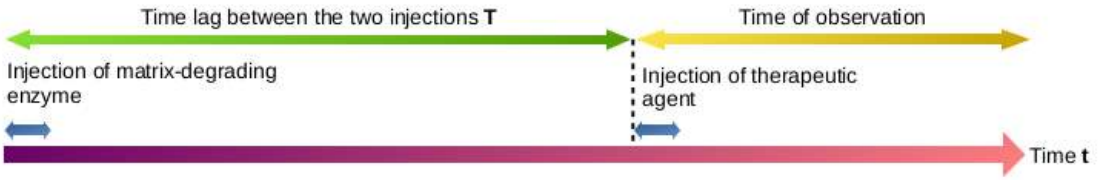

Scheme 5.2.1: Conduct of the test experiment.

5.2.3 Solving one experiment with Freefem++

Using the computational algorithm presented in Chapter 4 section 4.5, the set of PDEs are solved numerically for a given set of parameters using the finite-element

method implemented in the software FreeFem++ [61]. The objective function of interest being the area reached by a minimal concentration $c_{\min}$ of therapeutic drug, we compute the dimensionless function

$$F : t \to \frac{1}{|\Omega|} \times \int_{\Omega} \frac{[c_{\text{drug}}(t,x) - c_{\min}]^+}{c_{\text{drug}}(t,x) - c_{\min}} \, dx$$

for $t \in [T, T + T_{\text{obs}}]$, where T is the time lag between the injection of enzyme and the injection of therapeutic agent (i.e. the time when the injection of therapeutic agent begins) and T_{obs} is the time of observation, here set to 10 minutes.

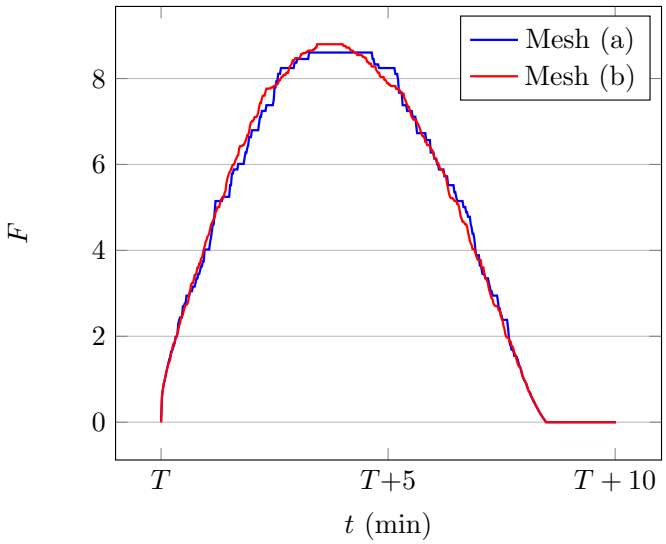

Figure 5.2: Time evolution of the objective function F computed using the two different meshes presented in Figure 5.1.

The time evolution of function F between T and $T + T_{\text{obs}}$ for a given set of parameters is featured in Figure 5.2. F was calculated using the two different meshes presented in Figure 5.1. Both curves are quite irregular, even if the solution calculated on the finer mesh seems smoother. Due to the additional computational cost generated by the use of the finer mesh, we chose instead to apply a binomial filter to the rough solution obtained with the mesh featured in Figure 5.1a.

The time evolution of function F between T and $T + T_{\text{obs}}$ for different sets of parameters is featured in Figure 5.4. F was calculated using the mesh in Figure

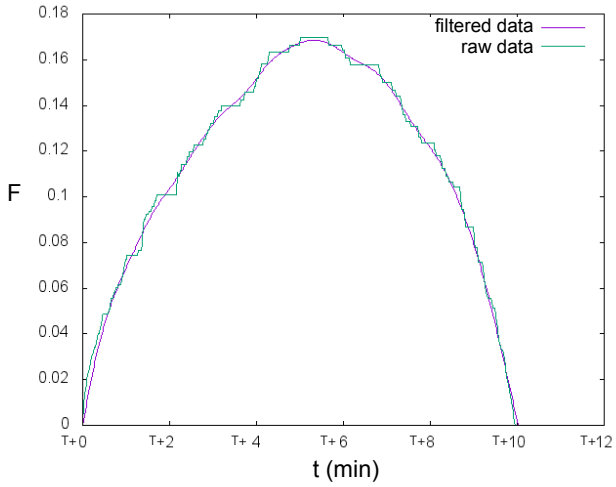

Figure 5.3: Time evolution of the objective function F using mesh 5.1a. Both the raw data obtained with Freefem++ and the data obtained once a binomial filter has been applied are displayed.

5.1a. Different tendencies are observed but it seems that function F has always a parabolic shape. This allows us to define the quantity

$$F_{max} = \max_{t\in[T,T+T_{obs}]} F(t),$$

as the maximum value reached by the objective function F. Another quantity of interest is the first time at which this maximum value is reached, which will be denoted by t_{max} hereafter.

5.3 Numerical methods

To optimize the protocol with respect to the chosen variables, one cannot analyse thousands of different configurations in order to determine the best one due to extremely high computational cost. Different strategies exist to reduce the use of time-consuming solvers, decreasing the total time for the optimization problem solution. The idea is to substitute the time-consuming solver with an analytical approximation based on a limited number of sampling points. The construction of the approximated model requires the high-accuracy evaluation of the objective

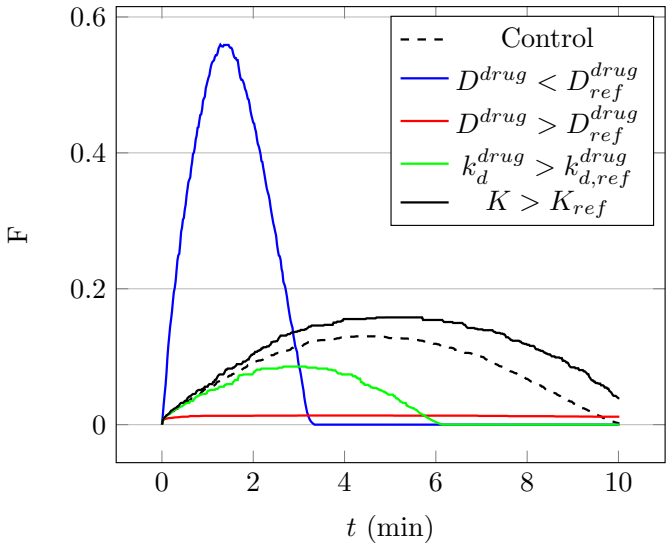

Figure 5.4: Different shapes of the objective function F when changing some fixed parameters. D_{drug} is the diffusion coefficient of the therapeutic agent considered, k_d^{drug} its natural degradation rate. K is the cleavage rate of the hyaluronidase used as a pretreatment.

function of interest on this set of sampling points, usually named training points. In this section, we present the numerical methods that we used to construct the approximated model. We first explain how to select the training points by constructing an orthogonal array. Then we present the interpolation method chosen to construct the approximated model, called Kriging interpolation.

5.3.1 Selecting the training points : orthogonal arrays

Let k be the number of involved variables and L be the number of levels in which each coordinate axis is subdivided. The most straight forward method to explore uniformly the parameter space is the consider the complete L^k factorial design i.e. the cartesian grid obtained by considering all the L possible values of all k variables. But as the number of points to be placed in the training set grows with the number of involved variables k and with the complexity of the objective function itself, the operation of selecting the training points should be done using a limited number of points while still exploring uniformly the parameter space. To

overcome this difficulty, some strategies have been proposed in order to remove some points from the complete L^k factorial design. In our case, orthogonal arrays are used to design the experiments and define the values of the parameters for each experiment. An orthogonal array of L elements, denoted by $OA_N(L^k)$ is an $N \times k$ matrix whose columns have the property that in every pair of columns each of the possible ordered pairs of elements appears the same number of times. The symbols used for the elements of an orthogonal array are arbitrary.

Table 5.1: Example of an Orthogonal Array for $k = 5$ parameters with $L = 4$ levels with $N = 16$ runs (written as its transpose for ease of viewing).

1	1	1	1	2	2	2	2	3	3	3	3	4	4	4	4
1	2	3	4	1	2	3	4	1	2	3	4	1	2	3	4
1	2	3	4	4	3	2	1	2	1	4	3	3	4	1	2
1	2	3	4	2	1	4	3	3	4	1	2	4	3	2	1
1	2	3	4	3	4	1	2	4	3	2	1	2	1	4	3

Orthogonal arrays can be viewed as plans of multifactor experiments where the columns correspond to the factors, the entries in the columns correspond to the test levels of the factors and the rows correspond to the test runs. More specifically, the N rows of an $OA_N(L^k)$ can be viewed as a subset of the possible L^k test runs of a complete cartesian grid of k factors each having L test levels. Thus, an $OA_N(L^k)$ can be viewed as a N/L^k fraction of a complete L^k factorial plan.

5.3.2 Kriging

When an outcome of interest cannot be easily directly measured, a model of the outcome, called surrogate model, can be used instead. Kriging interpolation is one of the most interesting techniques introduced in the field of surrogate modeling. We present here the principles of this spatial interpolation method. The Kriging bears the name of D.G. Krige who developed the approach for the location of mining sites by using geological data. Nevertheless, the theory was formalized by Matheron: looking at the distribution of drilled samples, he observed a susbtantial continuity in the spatial variation of the samples, which may be expressed through

a more or less important deviation between the values of two proximal samples. This approach is based on the availability of the so-called variogram, defined as a curve representing the degree of continuity of the observed quantity.

5.3.2.1 The variogram.

The empirical variogram provides a description of how the data are related (correlated) with distance. The semivariogram function, $\gamma(\delta)$, is calculated from the difference between points separated by a distance δ: given a set of data values z_i corresponding to the locations x_i (i.e. $z_i = F(x_i)$),

$$\gamma(\delta) = \frac{1}{2N(\delta)} \sum_{N(\delta)} (z_i - z_j)^2, \tag{5.9}$$

where $N(\delta)$ is the set of all pairwise Euclidean distances $|\mathbf{x}_i - \mathbf{x}_j| = \delta$, $|N(\delta)|$ is the number of distinct pairs in $N(\delta)$, and z_i and z_j are data values at locations $\mathbf{x}_i$ and $\mathbf{x}_j$, respectively. In general, the semivariogram is an increasing function of the distance. The speed of increase of the semivariogram represents the speed of deterioration of the influence of a given sample over more and more remote regions.

Figure 5.5 shows how the central point is paired with every other surrounding point.

Most of the time, each pair of points defines an unique distance. The empirical semivariogram is first calculated using all pairs available. We denote by X the maximum distance between the measured points. The interval $[0, X]$ is then divided in a certain number of subintervals, to be determine. The mean of the empirical semivariogram is then calculated for each subinterval, and this mean value is to be considered as the mean value of the derived continuous semivariogram, that is obtained by spline interpolation using the available points of the subinterval. An example of continuous semivariogram derived from an empirical semivariogram in our configuration is shown in Figure 5.6.

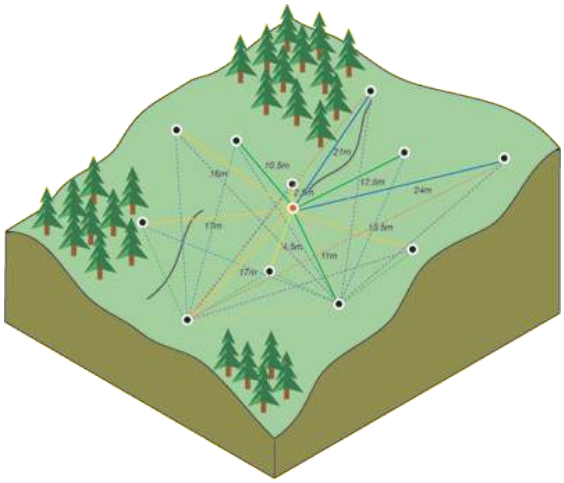

Figure 5.5: Calculus of the squared distance between the possible pairs of points.

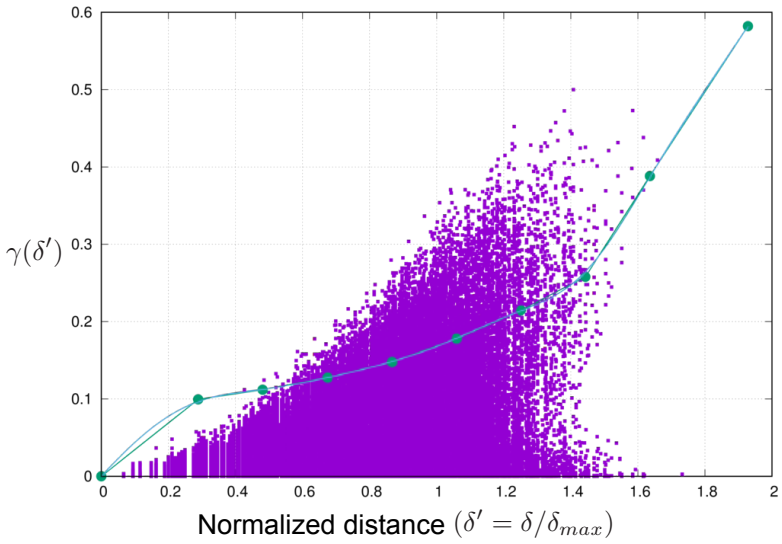

Figure 5.6: An example of variogram obtained with our algorithm. The purple points form the empirical semivariogram while the blue line is the final variogram calculated with a spline interpolation on each subinterval.

5.3.2.2 Spatial interpolation

Once we have defined a shape for the variogram, we have completely defined the spatial relationship between samples: if we have a number of known samples of the interpolating function, we are also able to define the function over the entire space,

theoretically even outside the region included in the known samples. In fact, we can assume that the function is obtained by the sum of the known samples times a proper weight, determined by the variogram, so that

$$f(\mathbf{x}) = \sum_{i=1}^{m} W_i \cdot F(\mathbf{x}_i), \tag{5.10}$$

under the condition that

$$\sum_{i=1}^{m} W_i = 1,$$

where m is the number of available samples. It is then sufficient to build the following system of equations

$$\gamma(h_{11})W_1 + \gamma(h_{21})W_2 + \cdots + \gamma(h_{m1})W_m + \lambda_1 = \gamma(h_{1p}), \tag{5.11}$$
$$\gamma(h_{12})W_1 + \gamma(h_{22})W_2 + \cdots + \gamma(h_{m2})W_m + \lambda_2 = \gamma(h_{2p}), \tag{5.12}$$
$$\cdots \tag{5.13}$$
$$\gamma(h_{1m})W_1 + \gamma(h_{2m})W_2 + \cdots + \gamma(h_{mm})W_m + \lambda_m = \gamma(h_{mp}), \tag{5.14}$$
$$W_1 + W_2 + \cdots + W_m + 0 = 1, \tag{5.15}$$

to determine the values of the weights W_i. $\gamma(h_{ij})$ is the value of the semivariogram corresponding to the distance h_{ij} between the points x_i and x_j. The value $\gamma(h_{ij})$ has already been computed from the sample points thanks to equation (5.9), while $\gamma(h_{ip})$ is obtained using the analytical function that has been ajusted to the sample points of the semivariogram with a spline interpolation (see Figure 5.6). As we need to produce an estimate of the objective function over a large number of different locations, we simply factorize the system matrix once, and only the right-end side has to be recomputed when the computational point is changed. We can observe that the training phase is accomplished by solving a single $m \times m$ system.

5.4 Results of the optimization strategy

We approach the problem considering the following steps:

1. An orthogonal array $OA_{512}(16^3)$ is computed. A full cartesian grid where 3 different factors are to be screened and each is to be observed at 16 different levels would require $16^3 = 4096$ runs. The use of an $OA_{512}(16^3)$ allows us to only perform 512 runs, separated on 8 different processors with a parallel configuration.

2. For each of the 512 training points, the maximal area F_{max} and the first time at which this maximal area is reached t_{max} are computed. In Figure 5.7 are featured the training points derived with fixed parameters in Table 5.2. The three parameters chosen for the optimization strategy take values in the intervals presented in Table 5.3.

3. Kriging is performed to obtain interpolation values on a Cartesian grid $100 \times 100 \times 100$. Two test cases are considered for two different values of D^0_{enz}, the diffusion coefficient of the matrix degrading enzyme. Namely, for $D^0_{enz} = 10^{-8}$ m^2/s, the enzyme concentration is locally sufficiently high for the volume fraction of ECM to become zero after some time. For $D^0_{enz} = 10^{-6}$ m^2/s, the enzyme spreads rapidly, modifying the volume fraction of ECM value rapidly and quite homogeneously. The resulting tendencies of function $F_{max}(T, y_0, c^{\text{inj}}_{\text{drug}})$ are very different.

4. The optimal solution is found with a localized search. It appears that the maximum is reached in both cases for the maximum concentration value of the interval. This is a consequence of the linear dependance of the model to parameter $c^{\text{inj}}_{\text{drug}}$. Thus, we visualize the different computed values of F_{max} in the 2D parameters space (T, y_0) by fixing $c^{\text{inj}}_{\text{drug}}$ at its maximum value. This enables a better visualization of the localization of the optimised configuration. In Figure 5.9a, it appears that the area where the maximum is localized is quite large with little sensitivity to a quite large variation of the parameters. However, in Figure 5.11a, it appears that the maximum is much more localized, which makes our optimization strategy both interesting and valuable. In Figures 5.10a and 5.12a is displayed the way t_{max} varies with the parameters.

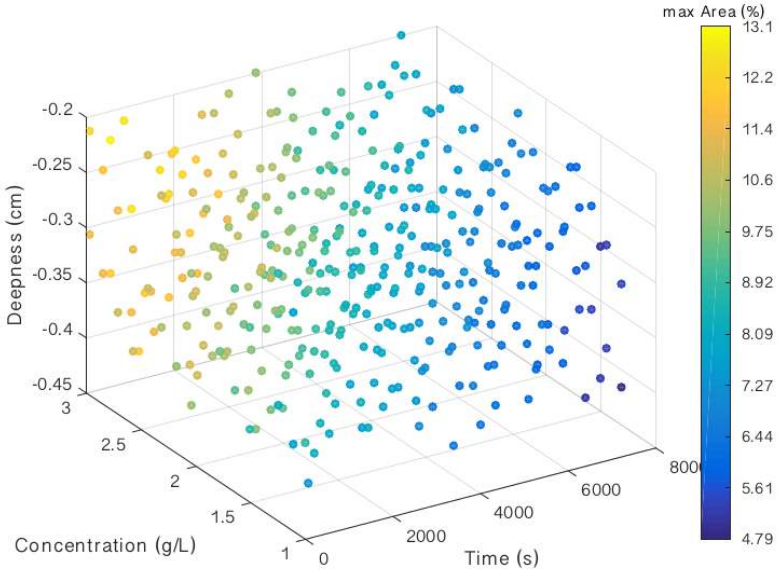

(a) F_{max} values for the training points set

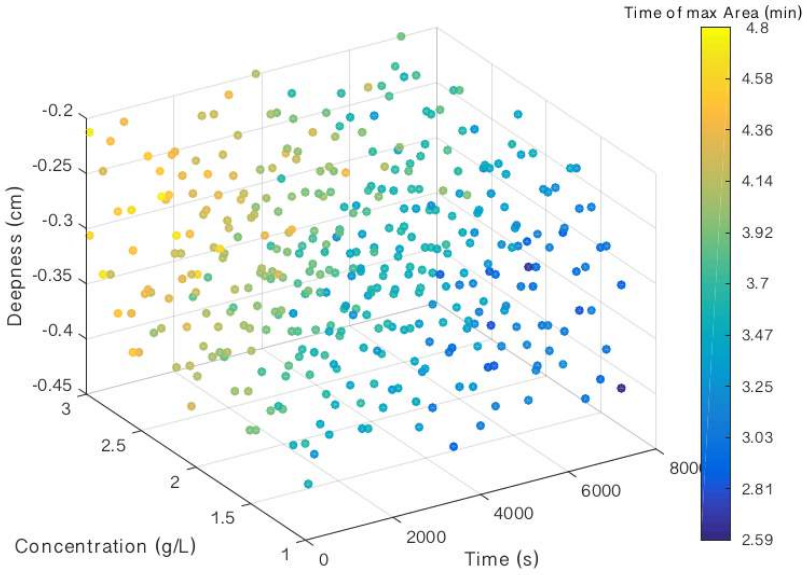

(b) t_{max} values for the training points set

Figure 5.7: Visualization in the parameter space of the training points set computed.

Table 5.2: Values of the fixed parameters in the simulations done with Freefem++ to obtain the training points set.

Parameter	Symbol	Value	Unit
Typical length	l_0	10^{-2}	m
Reference concentration	c_0	10^9	kg/m^3
Density of fluid phase	ρ_f^R	10^3	kg/m^3
Density of solid phase	$\rho_s^{R,0}$	$1.09 \cdot 10^3$	kg/m^3
Permeability	κ	10^{-11}	m^{2}Pa^{-1}s^{-1}
Lamé first parameter	λ	$7.14 \cdot 10^5$	Pa
Lamé second parameter	μ	$1.79 \cdot 10^5$	Pa
Specific storage coefficient	s_0	10^{-6}	Pa^{-1}
Injected concentration of enzyme	$c_{\text{inj}}^{\text{enz}}$	$4 \cdot 10^{-2}$	U/μl
Diffusion coefficient of the enzyme	D_{enz}^0	10^{-8}, 10^{-6}	m^2/s
Degradation rate of the enzyme	k_{enz}^d	$1 \cdot 10^{-4}$	s^{-1}
Minimal effective concentration of the therapeutic agent	$c_{\min}$	10^{-4}	g/L
Diffusion coefficient of the therapeutic agent	D_{drug}^0	10^{-8}	m^2/s
Degradation rate of the therapeutic agent	k_{drug}^d	$1.7 \cdot 10^{-3}$	s^{-1}
Cleavage rate	K	$2.5 \cdot 10^{-7}$	m^{3}s^{-1}U^{-1}
Recovery coefficient	a_r	$5 \cdot 10^{-4}$	s^{-1}
Starling's coefficient	γ	$5 \cdot 10^{-5}$	Pa^{-1}s^{-1}
Fluid/solute coefficient	γ_c	0.9	-
Driving pressure	P_v	10^{-1}	Pa

Initial values	Symbol	Initial value	Unit
Volume fraction of fluid	$\varphi_f(0, \mathbf{x})$	0.1	-
Volume fraction of ECM	$\varphi_{\mathcal{E}}(0, \mathbf{x})$	0.4	-
Volume fraction of cells	$\varphi_e(0, \mathbf{x})$	0.5	-
Network dilatation	$\nabla.\mathbf{u}(0, \mathbf{x})$	0	-
Concentration in enzyme	$h(0, \mathbf{x})$	0	Um^{-3}
Concentration in drug	$c(0, \mathbf{x})$	0	kg m^{-3}
Pressure	$P(0, \mathbf{x})$	P_v	Pa

Table 5.3: Interval values of the control variables in the simulations.

Parameter	Symbol	Interval value	Unit
Time lap between the two injections	T	$[0, 2]$	h
Injection position	y_0	$[2, 4]$	mm
Concentration of therapeutic agent	$c_{\text{drug}}^{\text{inj}}$	$[1, 3]$	g/L

5.5 Comparison between Kriging and the Linear Interpolation Method

In this section, we fix the control variable $c_{\text{drug}}^{\text{inj}}$ at its maximal value: $c_{\text{drug}}^{\text{inj}} = 3$ g/L. Thus we work in the 2D parameters space generated by (T, y_0). This time,

the training set points are computed using a Cartesian grid 25×25 featured in Figure 5.13. It is worth noticing that for several values of y_0, the value of interest F_{max} could not be obtained, mainly because of numerical issues. As y_0 is a spatial data, we believe that refining the mesh would suffice to retrieve the missing points.

We compare the interpolated values obtained using Kriging on a Cartesian grid 100×100 and those obtained using another method of spatial interpolation: the Linear Interpolation Method [95] (see Figure 5.14). The test case considered here corresponds to the test featured in Figure 5.9 ($D^0_{enz} = 10^{-6}$). The general trend of the objective function F is found to be the same in both cases, but the surface obtained using the linear interpolation method, which supposingly is the closest to the raw data, presents some non physical noise.

From this study, we decided that the interpolated values obtained using Kriging form a more stable basis to perform a sensitivity analysis on the 3 control variables of interest.

5.6 Sensitivity analysis

We performed a sensitivity analysis on the test case presented in Figure 5.9 (Kriging interpolation from an orthogonal array). This is the same test case that what considered in Figure 5.14a (Linear interpolation from a cartesian grid): it was then determined that given the intrinsic noise of the raw data, the sensitivity study should be performed on the interpolated values obtained with Kriging (see Section 5.5). In this example, the maximum area is found to be reached at point

$$\mathbf{X}^{max} = (T^{max}, y_0^{max}, c_{\text{drug}}^{\text{inj},max}) = (4842.634\,s, -0.3677757\,cm, 2.999855\,g/L).$$

In particular, as previously noted, $c_{\text{drug}}^{\text{inj},max}$ is the upper bound of the interval of variation considered for the variable $c_{\text{drug}}^{\text{inj}}$ (see Table 5.3). Figure 5.15 shows how the optimal area reached by the drug varies as the three control variables are varied either side of their standard values. The format in Figure 5.15 allows easy comparison of the relative impacts of these parameters when varied up to 3% around the point at which the area is optimal. In this particular example, one can

see that a little variation of the time lag between the two injections (of enzyme and drug) has almost no impact of the optimal value, whereas the position at which is performed the injection has a greater impact. As expected, a greater concentration gives a greater value fot the area reached by the drug but as those values are obtained out of the limits of the interval in which $c_{\text{drug}}^{\text{inj}}$ is allowed to vary, there are not admissible.

In Figure 5.16 is featured the same sensitivity analysis on t_{max}, the time at which F_{max} is reached.

5.7 Conclusion

Optimizing the delivery of therapeutic drugs can remarkably improve their efficacy, especially in cancer treatment. Systemic delivery (e.g., intraveneous injection) or regional delivery (e.g., direct local injection) of drugs are hampered by physiological barriers to drug uptake from the surrounding medium. We considered a protocol with local infusion of therapeutic agents successively to local infusion of matrix targeting enzyme. In this framework, where transcapillary transport is not taken into account, the advantage is the removal of the diffusive hindrance, which has been studied in detail in the literature, and recovered with a PDE model in section 4.6. The present study uses mathematical modeling as a tool for determining the principal mechanisms during localized delivery of drugs and quantitatively simulating drug concentration. Using an optimization strategy based on Kriging interpolation, we can derive an optimized protocol in order to obtain both the maximal area where the drug concentration is sufficiently high and the time at which this maximum is reached. The results we presented are obtained on a test case, using a simple 2D geometry and fixed parameters that were not calibrated on biological data. Nevertheless, the idea behing this study was to construct an optimization algorithm in order to demonstrate its potential utility. With proper biological data, the model could be calibrated and an optimized protocol could be proposed and tested for validation.

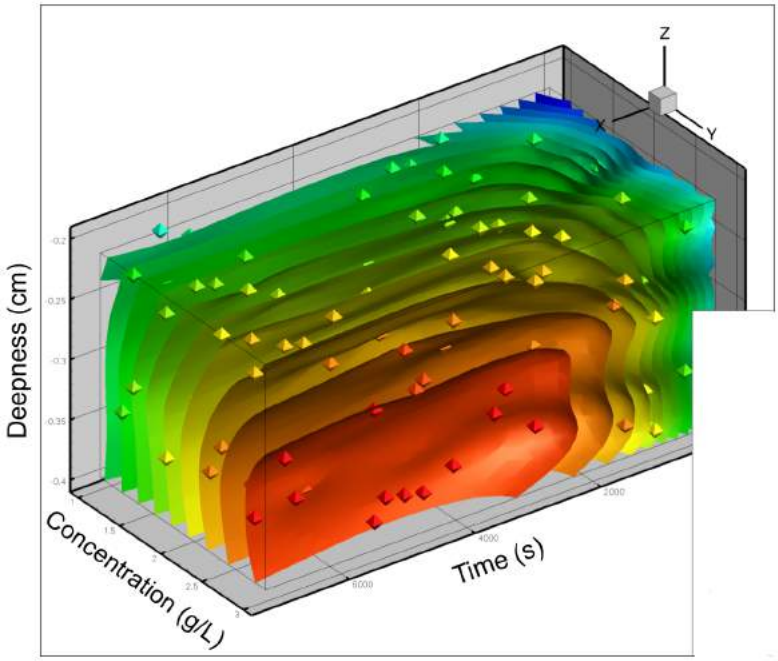

(a) $D^0_{enz} = 10^{-8}$

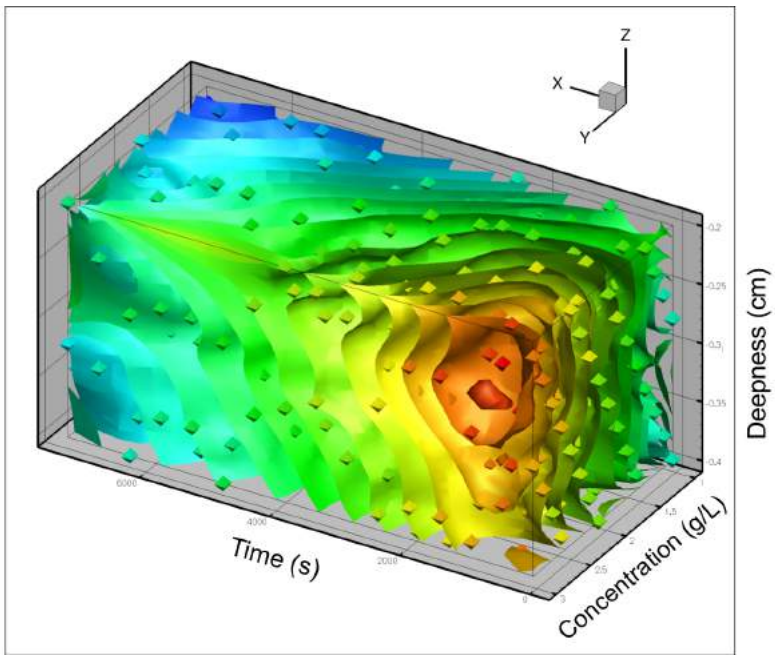

(b) $D^0_{enz} = 10^{-6}$

Figure 5.8: Visualization in the 3D parameter space of F_{max} obtained using Kriging interpolation on the training points set previously computed for two different values of D^0_{enz}.

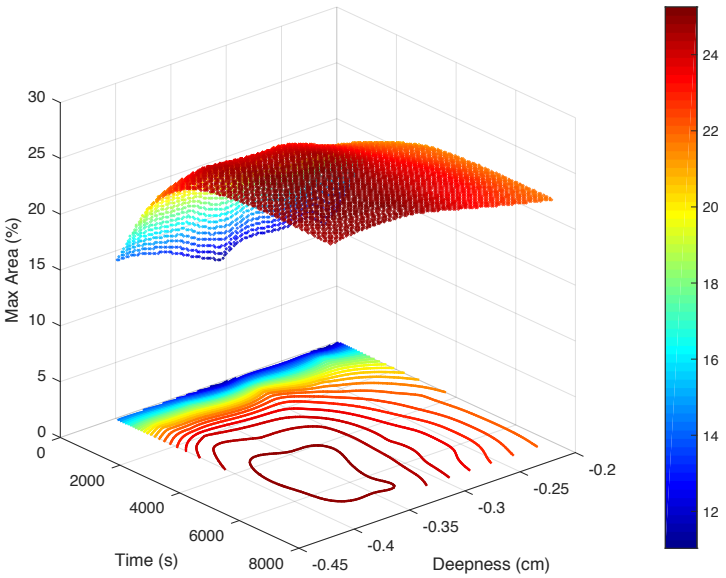

(a)

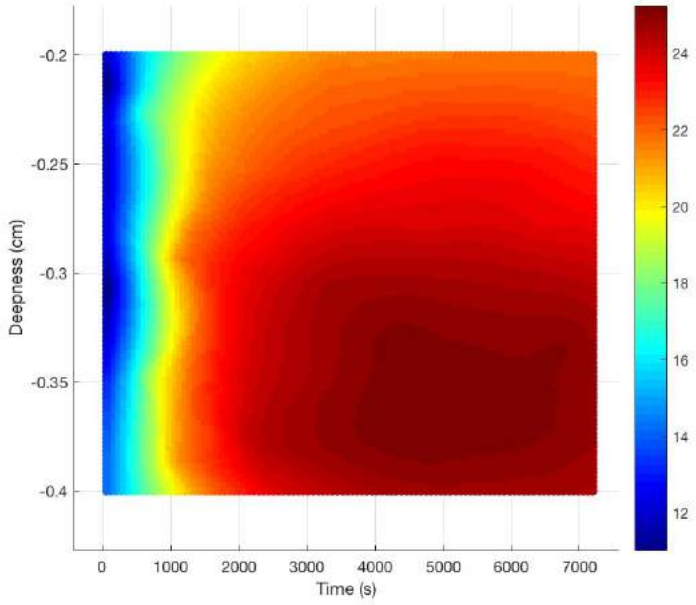

(b)

Figure 5.9: Visualization in the 2D parameter space of F_{max} obtained using Kriging interpolation on the training set previously computed for $D^0_{enz} = 10^{-8}$.

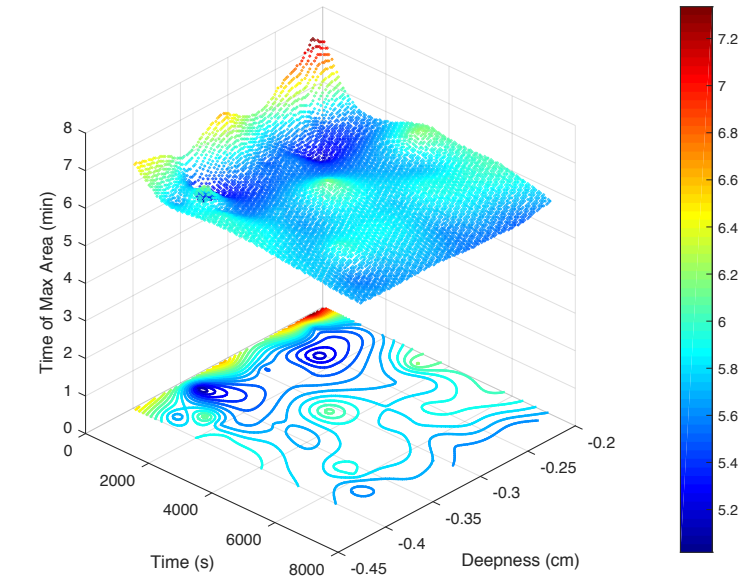

(a)

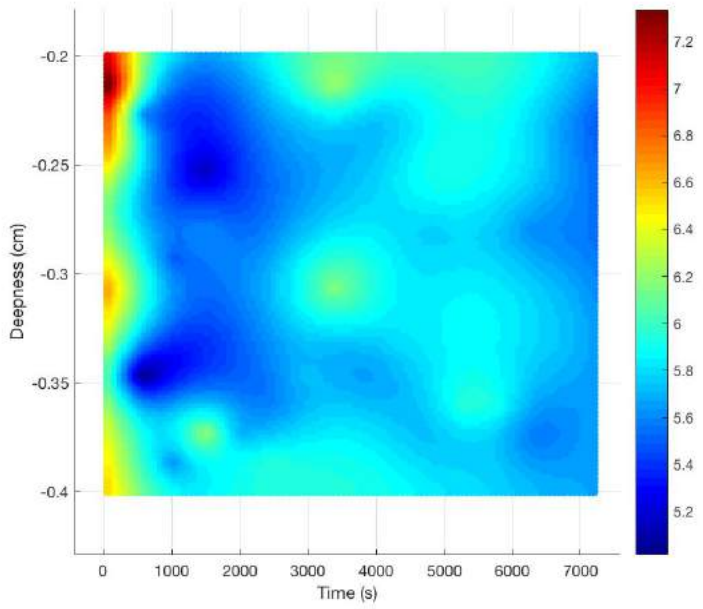

(b)

Figure 5.10: Visualization in the 2D parameter space of t_{max} obtained using Kriging interpolation on the training set previously computed for $D^0_{enz} = 10^{-8}$.

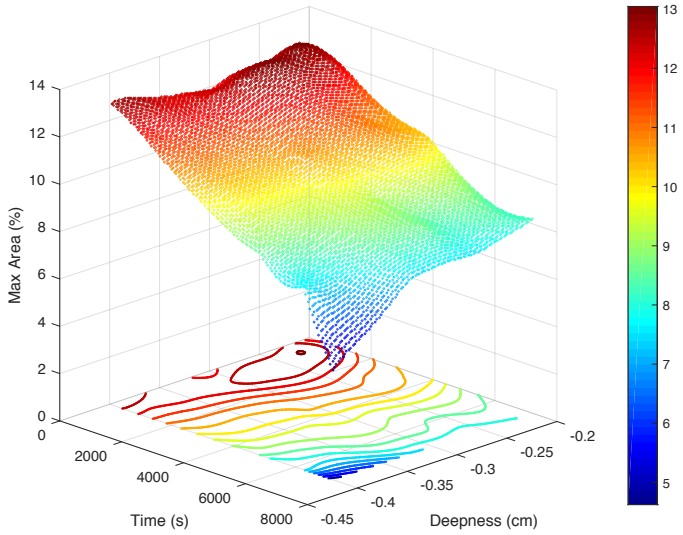

(a)

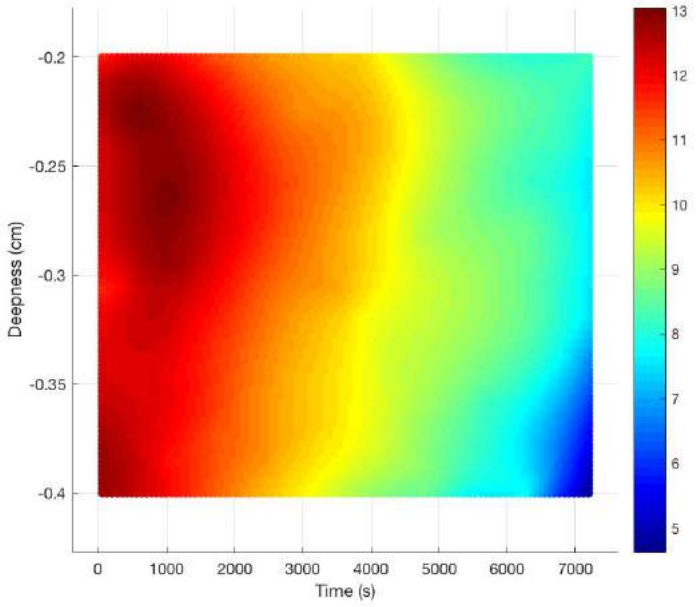

(b)

Figure 5.11: Visualization in the 2D parameter space of F_{max} obtained using Kriging interpolation on the training set previously computed for $D^0_{enz} = 10^{-6}$.

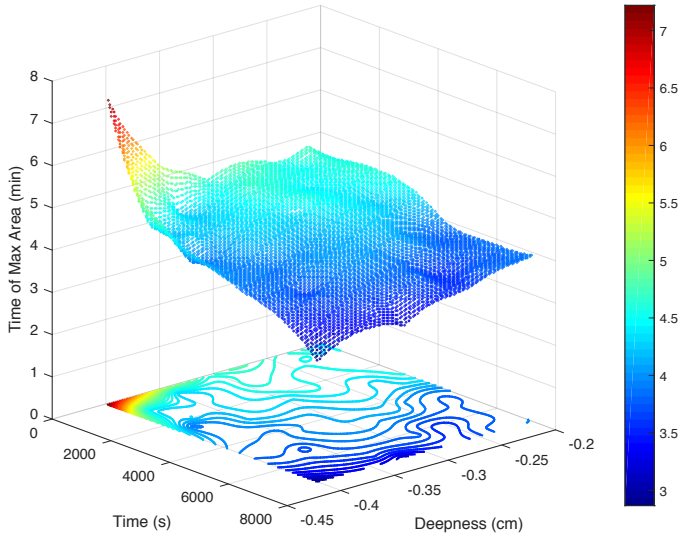

(a)

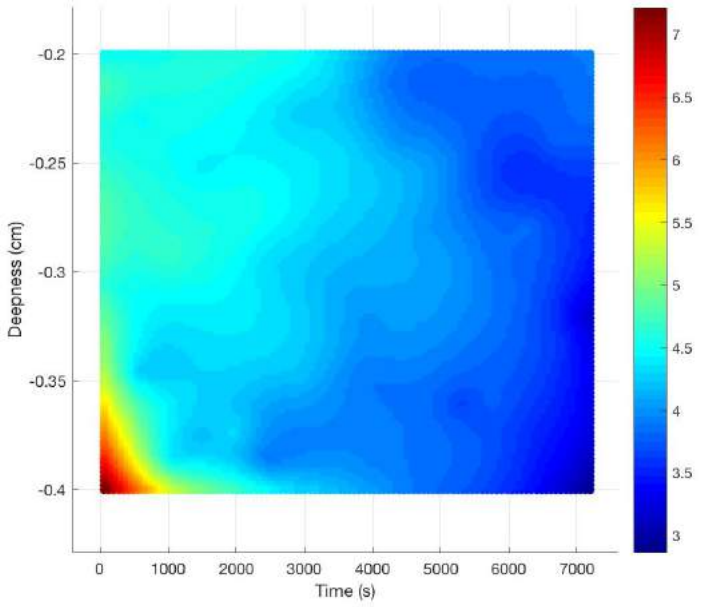

(b)

Figure 5.12: Visualization in the 2D parameter space of t_{max} obtained using Kriging interpolation on the training set previously computed for $D^0_{enz} = 10^{-6}$.

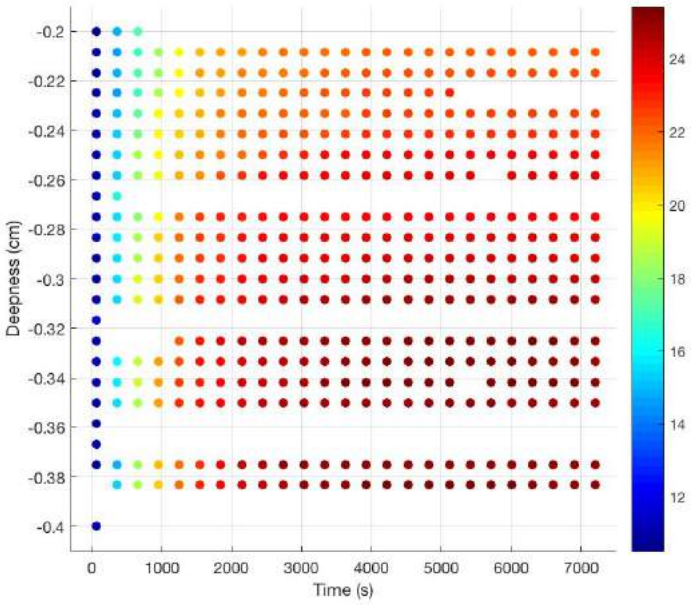

Figure 5.13: Visualization in the 2D parameter space of the cartesian grid of training points computed.

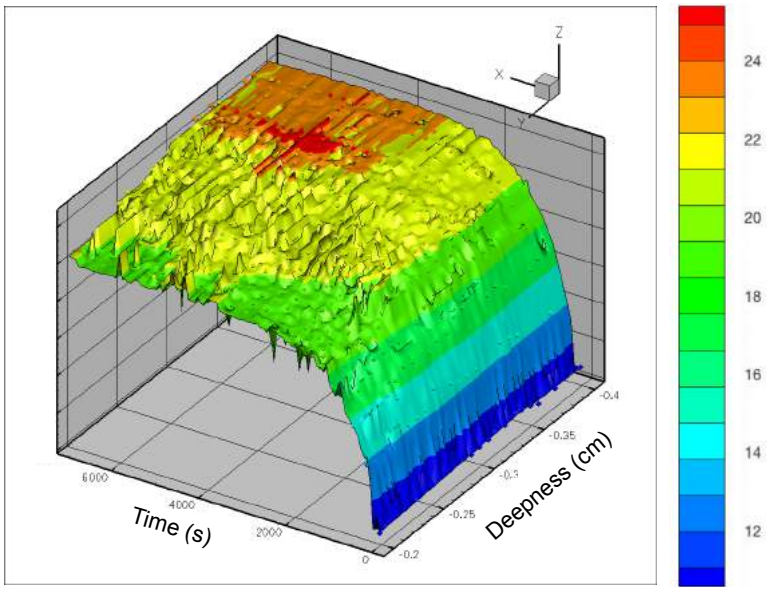

(a)

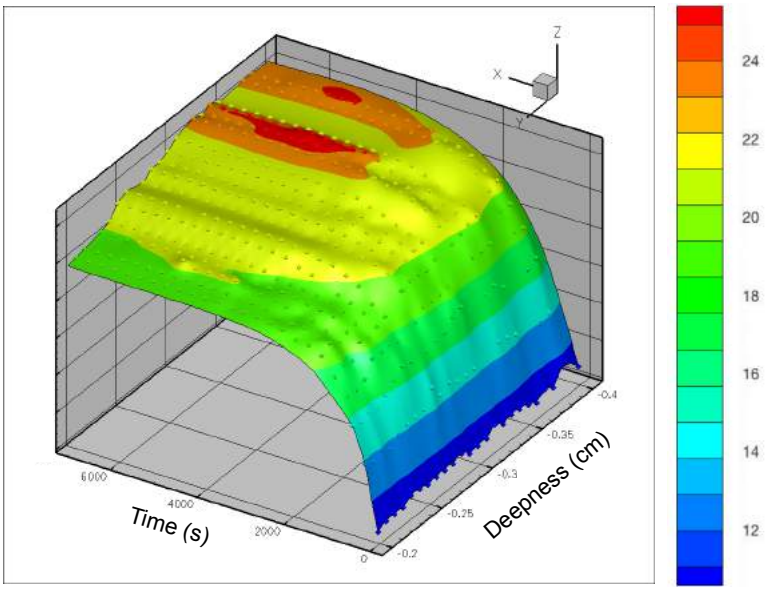

(b)

Figure 5.14: Visualization in the 2D parameter space of F_{max} obtained using two different methods of interpolation on the training set shown in Figure 5.13 for $D^0_{enz} = 10^{-6}$. **(a)** Linear Interpolation Method. **(b)** Kriging.

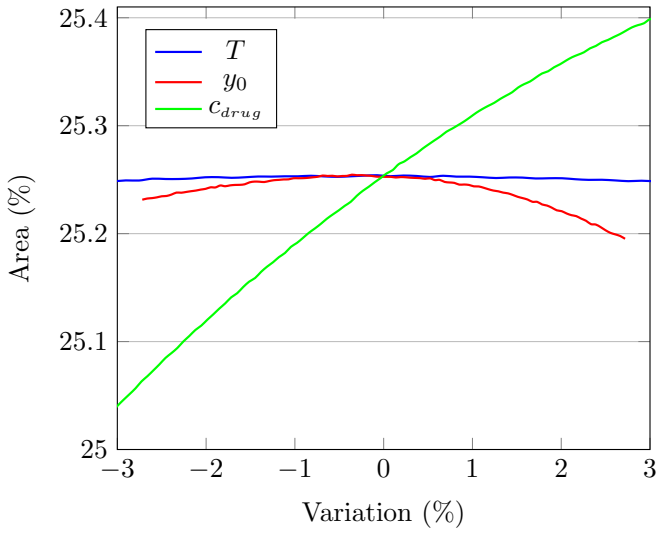

Figure 5.15: Diagram showing the changes in the maximal area reached by the drug F_{max} when varying the three control variables T, y_0 and c_{drug} around the optimal point $\mathbf{X}^{max}$.

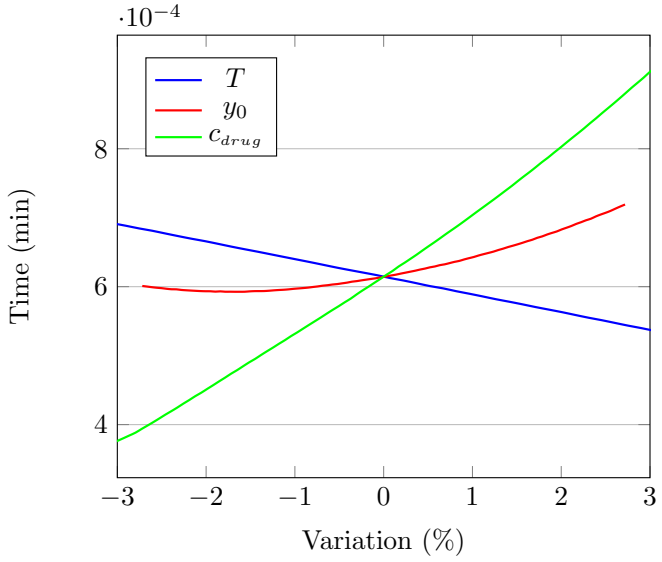

Figure 5.16: Diagram showing the changes in t_{max} when varying the three control variables T, y_0 and $c^{\text{inj}}_{\text{drug}}$ around the optimal point $\mathbf{X}^{max}$.

Conclusion

This work of research is concluded with a summary on the main contributions, the outstanding questions and the new prospects that are opening up through the work done on the modeling of physical methods in order to overcome the biological barriers to drug delivery.

Modeling of tissue electroporation. In the first part of this document, three phenomenological models of tissue electroporation are presented, explored and compared to one another and to experimental data. The three models are based on the description of the biological tissues as conductive media whose conductivity nonlinearly depends on the electric field. We recall that

- The first two models are based on a monophasic approximation while the last model is derived using a biphasic approach with two different current densities. The nonlinear monophasic static problem is shown to have an unique solution.
- An equivalent tissue conductivity can be computed in all three cases. While its value is obvious in the monophasic approach, a steady-state approximation is needed to obtain it in the biphasic approach.
- To calculate the simulated current, a volume method is presented instead of the usual surface method presented in the literature. It enables to solve the problem more accurately without increasing the computational cost.
- A comparison between the current chronograms and the simulated currents obtained using the different models enables to rationally determine that the

biphasic approach is the one that reproduces best the different features observed on the current chronograms.

In attempt to justify the phenomenological biphasic approach at the tissue scale, a homogenization procedure is used to fill the gap between cell scale and tissue. It leads to the equations of the bidomain model.

- The two-scale convergence is established in the static nonlinear case.
- The cell geometry can influence the global result.
- An equivalent homogenized tissue conductivity can be derived from the bidomain model. Its formula is very similar to the equivalent tissue conductivity derived from the phenomenological model using two current densities.
- The dependance of the microscopic membrane conductivity on the transmembrane voltage results in the dependance of the homogenized equivalent tissue conductivity on the difference between the extracellular homogenized potential and the intracellular homogenized potential. The electroporated area identified with the bidomain model is not conclusive.

***

Complete calibration has yet to be done to validate the different modeling approaches (monophasic, biphasic, bidomain). Several biological phenomena could also be added to the phenomenological modeling of tissue electroporation. Long-term permeabilization and heating effects should be taken into account if the effects should be observed on a longer time scale than one pulse of 100 μs. This is not a difficult thing to add in terms of modeling, but it may complicate the calibration procedure. We are confident that the rigorous derivation of the homogenized macroscopic model may be a good start towards the mathematical justification of the phenomenological biphasic approach. The homogenization procedure could also be complexified by considering more accurate phenomenological laws at the cell scale, with dynamical effects and/or surface diffusion taken into account in the definition of the membrane conductivity.

***

Modeling of tissue degradation by mean of enzymatic treatment. A new poroelastic model to account for tissue degradation in the case of enzymatic treatment is presented.

- The model is derived directly from physical conservation laws under the assumption that the tissue is a poroelastic saturated mixture made of cells, extracellular matrix and interstitial fluid.
- This model is written in a fixed reference domain to make the numerical processing possible.
- The results given by the simulations are in accordance with the experimental data: an intratumoral injection of enzyme results in a nonlinear reduction of the interstitial pressure and affects the distribution of therapeutic agents, thereby improving the diffusion and convection process.

The model is then used as a tool to optimize drug delivery in enzyme-based therapies.

- Three independent control variables are chosen to optimize the protocol: the time lag between the injection of enzyme and the injection of therapeutic agent, the position of the injection point and the concentration of therapeutic agent in the fluid injected.
- The optimization strategy is based on Kriging interpolation.
- The results of this interpolation are obtained on a test case, using a simple 2D geometry and fixed parameters that were not calibrated on biological data. An optimal protocol is obtained.

***

Complete calibration with experiments has yet to be done to validate the poroelastic model, even if the qualitative results we obtained are encouraging. Only once the calibration is complete, the optimization algorithm may be used to determine an optimal protocol, to be tested experimentally. Finally, the coupling between

the modeling of tissue degradation by mean of enzymatic treatment and tissue electroporation has yet to be done. In the framework of gene therapy, the use of enzyme was shown to facilitate not only the distribution of plasmids but also their access to the muscle fibers. The variable porosity could then be considered as a parameter in a model of tissue electroporation.

***

Appendices

Appendix A

Formulation of the poroelastic model in a fixed domain: the general case

Let us derive the final equations of the model. The calculus in the general case gives the final system of equations (A.3). Recall that matrix B is defined as the inverse of matrix A given by (4.47). As,

$$(B^{-1})_{i,j} = A_{i,j} = \left(\frac{\partial \Phi(t,\mathbf{X})}{\partial \mathbf{X}}\right)_{i,j} = \delta_{ij} + \frac{\partial u_i}{\partial X_j}(t,\mathbf{X}) = \delta_{ij} + \frac{\partial \overline{u}_i}{\partial \overline{\mathbf{X}}_j}(\overline{t},\overline{\mathbf{X}}), \quad \text{(A.1)}$$

we kept the notation B to refer to $B(\overline{\mathbf{u}})$ in system (A.3). Note that we equally dropped bars on dimensionless variables but kept them on dimensionless parameters. Let us denote

$$J^B_{enz} = \frac{1}{f}\overline{\boldsymbol{\kappa}}\, B\nabla P - \overline{\mathbf{D}^0_{enz}} B\nabla f \quad \text{and} \quad J^B_{drug} = \frac{1}{f}\overline{\boldsymbol{\kappa}}\, B\nabla P - \overline{\mathbf{D}^0_{drug}} B\nabla f. \quad \text{(A.2)}$$

We recall that $g_s = g_{\mathcal{E}} + g_{\mathcal{C}}$.

- **The poroelasticity system**. Let us start with the final form of equations (4.21) and (4.15).

$$
\begin{aligned}
&\boldsymbol{\nabla} \cdot (\varphi_s \boldsymbol{\sigma}_s^E) = \nabla p \\
\iff &\boldsymbol{\nabla} \cdot \left(\varphi_s \frac{1}{J} B^{-1} \mathbf{S}_s^E B^{-T} \right) = \nabla p \\
\iff &B \boldsymbol{\nabla}_{X_1,X_2} \cdot \left(g_s \frac{1}{J} B^{-1} \mathbf{S}_s^E B^{-T} \right) = B \nabla_{X_1,X_2} P \\
\iff &\boldsymbol{\nabla} \cdot \left(g_s \frac{1}{J} B^{-1} (2\mu \boldsymbol{\varepsilon} + \lambda \mathrm{Tr}(\boldsymbol{\varepsilon}) I) B^{-T} \right) = \nabla P \\
\iff &\boldsymbol{\nabla} \cdot \left(g_s \frac{1}{J} B^{-1} (\mu(\nabla \mathbf{u} + \nabla \mathbf{u}^T) + \lambda(\nabla \cdot \mathbf{u}) I) B^{-T} \right) = \nabla P \\
\iff &\frac{1}{l_0} \boldsymbol{\nabla}_{\overline{X_1},\overline{X_2}} \cdot \left(g_s \frac{1}{J} B^{-1} (\mu(\frac{1}{l_0} \nabla (l_0 \overline{\mathbf{u}}) + \frac{1}{l_0} \nabla (l_0 \overline{\mathbf{u}}^T)) + \lambda(\frac{1}{l_0} \nabla \cdot (l_0 \overline{\mathbf{u}})) I) B^{-T} \right) \\
&\quad = \frac{1}{l_0} \nabla_{\overline{X_1},\overline{X_2}} ((\lambda + 2\mu) \overline{P}) \\
\iff &\boldsymbol{\nabla}_{\overline{X_1},\overline{X_2}} \cdot \left(g_s \frac{1}{J} B^{-1} (\overline{\mu}(\nabla \overline{\mathbf{u}} + \nabla \overline{\mathbf{u}}^T) + \overline{\lambda}(\nabla \cdot \overline{\mathbf{u}}) I) B^{-T} \right) = \nabla_{\overline{X_1},\overline{X_2}} \overline{P}
\end{aligned}
$$

  Dropping bars on the dimensionless variables $\mathbf{u}$, P and $\mathbf{x}$, we get equation (A.3b).

$$
\begin{aligned}
&\varphi_s s_0 \left(\frac{\partial p}{\partial t} + \nabla p \cdot \mathbf{v}_s \right) + \nabla \cdot (\mathbf{v}_s + \varphi_f \mathbf{w}) \\
&= \left(1 - \frac{\rho_s^{R,0}}{\rho_f^R} \right) \varphi_{\mathcal{E}} (-K \varphi_f c_{enz} + a_r \left(\varphi_f - \varphi_f(0, \mathbf{x}) \right)) \\
&+ Q_{inj}^{tot} + Q_{vas} - Q_{lym} \\
\iff &\varphi_s s_0 \frac{Dp}{Dt} + \nabla \cdot (\mathbf{v}_s) - \nabla \cdot (\boldsymbol{\kappa} \nabla P) \\
&= \left(1 - \frac{\rho_s^{R,0}}{\rho_f^R} \right) \varphi_{\mathcal{E}} (-K C_{enz} + a_r \left(\varphi_f - \varphi_f(0, \mathbf{x}) \right)) \\
&+ Q_{inj}^{tot} + Q_{vas} - Q_{lym} \\
\iff &\varphi_s s_0 \frac{Dp}{Dt} - \nabla \cdot (\boldsymbol{\kappa} \nabla p) \\
&= \left(1 - \frac{\rho_s^{R,0}}{\rho_f^R} \right) \varphi_{\mathcal{E}} (-K C_{enz} + a_r \left(\varphi_f - \varphi_f(0, \mathbf{x}) \right)) \\
&+ Q_{inj}^{tot} + \gamma (p - p_v) - \nabla \cdot (\mathbf{v}_s) \\
\iff &g_s s_0 \frac{\partial P}{\partial t} - B \nabla_{X_1, X_2} \cdot (\boldsymbol{\kappa} B \nabla_{X_1, X_2} P) \\
&= \left(1 - \frac{\rho_s^{R,0}}{\rho_f^R} \right) g_{\mathcal{E}} (-K h + a_r \left(f - f(0, \mathbf{x}) \right)) \\
&+ Q_{inj}^{tot} + \gamma (P - P_v) - B \nabla_{X_1, X_2} \cdot (\mathbf{V}_s) \\
\iff &g_s s_0 \frac{\kappa(\lambda + 2\mu)}{l_0^2} \frac{\partial (\lambda + 2\mu) \overline{P}}{\partial \overline{t}} - \frac{1}{l_0} B \nabla_{\overline{X_1}, \overline{X_2}} \cdot \left(\boldsymbol{\kappa} \frac{1}{l_0} B \nabla_{\overline{X_1}, \overline{X_2}} ((\lambda + 2\mu) \overline{P}) \right) \\
&= \left(1 - \frac{\rho_s^{R,0}}{\rho_f^R} \right) g_{\mathcal{E}} (-K c_0 \overline{h} + a_r \left(f - f(0, \mathbf{x}) \right)) \\
&+ Q_{inj}^{tot} + \gamma (\lambda + 2\mu) (\overline{P} - \overline{P}_v) - \frac{1}{l_0} B \nabla_{\overline{X_1}, \overline{X_2}} \cdot \left(\frac{\kappa(\lambda + 2\mu)}{l_0} \overline{\mathbf{V}}_s \right) \\
\iff &g_s \overline{s_0} \frac{\partial \overline{P}}{\partial \overline{t}} - B \nabla_{\overline{X_1}, \overline{X_2}} \cdot \left(\overline{\boldsymbol{\kappa}} B \nabla_{\overline{X_1}, \overline{X_2}} \overline{P} \right) \\
&= \left(1 - \frac{\rho_s^{R,0}}{\rho_f^R} \right) g_{\mathcal{E}} (-\overline{K h} + \overline{a_r} \left(f - f(0, \mathbf{x}) \right)) \\
&+ \alpha Q_{inj}^{tot} + \overline{\gamma} (\overline{P} - \overline{P}_v) - B \nabla_{\overline{X_1}, \overline{X_2}} \cdot \left(\overline{\mathbf{V}}_s \right)
\end{aligned}
$$

Dropping bars on the dimensionless variables P, h, $\mathbf{V}_s$, t and $\mathbf{x}$, we get equation (A.3c).

- **The equations on the volume fractions of the different components of the mixture**. Let us look at the final form of system (4.13). First, equation (4.2) in the reference domain writes

$$g_{\mathcal{E}} + g_{\mathcal{C}} + f = 1,$$

which is exactly equation (A.3a). As we already have this equation, we only need two equations from system (4.13) to close the problem on $\varphi_f, \varphi_{\mathcal{E}}, \varphi_{\mathcal{C}}$.

$$\begin{aligned}
&\frac{\partial}{\partial t}(\rho_s^R \varphi_{\mathcal{E}}) + \nabla \cdot (\rho_s^R \varphi_{\mathcal{E}} \mathbf{v}_s) = \rho_s^R \varphi_{\mathcal{E}}(-K\varphi_f c_{enz} + a_r\,(\varphi_f - \varphi_f(0,\mathbf{x})))\\
\iff &\rho_s^{R,0}\left(\frac{\partial \varphi_{\mathcal{E}}}{\partial t} + \nabla\varphi_{\mathcal{E}} \cdot \mathbf{v}_s\right) + \rho_s^{R,0}\varphi_{\mathcal{E}}\left(s_0\left(\frac{\partial p}{\partial t} + \nabla p \cdot \mathbf{v}_s\right) + \boldsymbol{\nabla} \cdot \mathbf{v}_s\right)\\
&= \rho_s^{R,0}\varphi_{\mathcal{E}}(-KC_{enz} + a_r\,(\varphi_f - \varphi_f(0,\mathbf{x})))\\
\iff &\frac{D\varphi_{\mathcal{E}}}{Dt} + \varphi_{\mathcal{E}}\left(s_0\frac{Dp}{Dt} + \boldsymbol{\nabla} \cdot \mathbf{v}_s\right) = \varphi_{\mathcal{E}}(-KC_{enz} + a_r\,(\varphi_f - \varphi_f(0,\mathbf{x})))\\
\iff &\frac{\partial g_{\mathcal{E}}}{\partial t} + g_{\mathcal{E}}\left(s_0\frac{\partial P}{\partial t} + B\boldsymbol{\nabla}_{X_1,X_2} \cdot \mathbf{V}_s\right) = g_{\mathcal{E}}(-Kh + a_r\,(f - f(0,\mathbf{x})))\\
\iff &\frac{\kappa(\lambda+2\mu)}{l_0^2}\frac{\partial g_{\mathcal{E}}}{\partial \bar{t}} + g_{\mathcal{E}}\left(s_0\frac{\kappa(\lambda+2\mu)}{l_0^2}\frac{\partial(\lambda+2\mu)\overline{P}}{\partial \bar{t}} + \frac{1}{l_0}B\boldsymbol{\nabla}_{\overline{X_1},\overline{X_2}}\frac{\kappa(\lambda+2\mu)}{l_0}\overline{\mathbf{V}_s}\right)\\
&= g_{\mathcal{E}}(-Kc_0\bar{h} + a_r\,(f - f(0,\mathbf{x})))\\
\iff &\frac{\partial g_{\mathcal{E}}}{\partial \bar{t}} + g_{\mathcal{E}}\left(\overline{s_0}\frac{\partial \overline{P}}{\partial \bar{t}} + B\boldsymbol{\nabla}_{\overline{X_1},\overline{X_2}}\overline{\mathbf{V}_s}\right) = g_{\mathcal{E}}(-\overline{Kh} + \overline{a_r}\,(f - f(0,\mathbf{x})))
\end{aligned}$$

Dropping bars on the dimensionless variables P, h, $\mathbf{V}_s$, t and $\mathbf{x}$, we get equation (A.3f). The same method applies for equation (4.13b) to get equation (A.3e).

- **The equations on the concentration of species**. Finally, let us look at

the final form of equations (4.25) and (4.29).

$$
\begin{aligned}
&\frac{\partial C_{\text{enz}}}{\partial t} + \nabla \cdot (C_{\text{enz}} \mathbf{v}_f) = \nabla \cdot \left(\varphi_f^2 \mathbf{D}^0_{enz} \nabla \left(\frac{C_{\text{enz}}}{\varphi_f} \right) \right) - \frac{k_d^{enz}}{\varphi_f} C_{\text{enz}} + \mathcal{S}_{enz} \\
\iff &\frac{\partial C_{\text{enz}}}{\partial t} + \nabla \cdot \left(C_{\text{enz}} \left(-\frac{1}{\varphi_f} \boldsymbol{\kappa} \nabla p + \mathbf{v}_s \right) \right) \\
&= \nabla \cdot \left(\varphi_f^2 \mathbf{D}^0_{enz} \nabla \left(\frac{C_{\text{enz}}}{\varphi_f} \right) \right) - \frac{k_d^{enz}}{\varphi_f} C_{\text{enz}} + \mathcal{S}_{enz} \\
\iff &\frac{\partial C_{\text{enz}}}{\partial t} + \nabla C_{\text{enz}} \cdot \mathbf{v}_s - \nabla \cdot \left(C_{\text{enz}} \left(\frac{1}{\varphi_f} \boldsymbol{\kappa} \nabla p - \mathbf{D}^0_{enz} \nabla \varphi_f \right) \right) \\
&= \nabla \cdot \left(\varphi_f \mathbf{D}^0_{enz} \nabla C_{\text{enz}} \right) - \left(\frac{k_d^{enz}}{\varphi_f} + \nabla \cdot \mathbf{v}_s \right) C_{\text{enz}} + \mathcal{S}_{enz} \\
\iff &\frac{DC_{\text{enz}}}{Dt} = \nabla \cdot \left(\varphi_f \mathbf{D}^0_{enz} \nabla C_{\text{enz}} \right) + \nabla \cdot \left(C_{\text{enz}} \left(\frac{1}{\varphi_f} \boldsymbol{\kappa} \nabla p - \mathbf{D}^0_{enz} \nabla \varphi_f \right) \right) \\
&- \left(\frac{k_d^{enz}}{\varphi_f} + \nabla \cdot \mathbf{v}_s \right) C_{\text{enz}} + \mathcal{S}_{enz} \\
\iff &\frac{\partial h}{\partial t} = B \nabla_{X_1, X_2} \cdot \left(f \mathbf{D}^0_{enz} B \nabla_{X_1, X_2} h \right) \\
&+ B \nabla_{X_1, X_2} \cdot \left(h \left(\frac{1}{f} \boldsymbol{\kappa} B \nabla_{X_1, X_2} P - \mathbf{D}^0_{enz} B \nabla_{X_1, X_2} f \right) \right) \\
&- \left(\frac{k_d^{enz}}{f} + B \nabla_{X_1, X_2} \cdot \mathbf{V}_s \right) h + \mathcal{S}_{enz} \\
\iff &\frac{\kappa(\lambda + 2\mu)}{l_0^2} \frac{\partial c_0 \overline{h}}{\partial \overline{t}} = \frac{1}{l_0} B \nabla_{\overline{X_1}, \overline{X_2}} \cdot \left(f \mathbf{D}^0_{enz} \frac{1}{l_0} B \nabla_{\overline{X_1}, \overline{X_2}} (c_0 \overline{h}) \right) \\
&+ \frac{1}{l_0} B \nabla_{\overline{X_1}, \overline{X_2}} \cdot \left(c_0 \overline{h} \left(\frac{1}{f} \boldsymbol{\kappa} \frac{1}{l_0} B \nabla_{\overline{X_1}, \overline{X_2}} ((\lambda + 2\mu) \overline{P}) - \mathbf{D}^0_{enz} \frac{1}{l_0} B \nabla_{\overline{X_1}, \overline{X_2}} f \right) \right) \\
&- \left(\frac{k_d^{enz}}{f} + \frac{1}{l_0} B \nabla_{\overline{X_1}, \overline{X_2}} \cdot \frac{\kappa(\lambda + 2\mu)}{l_0} \overline{\mathbf{V}_s} \right) c_0 \overline{h} + \mathcal{S}_{enz} \\
\iff &\frac{\partial \overline{h}}{\partial \overline{t}} = B \nabla_{\overline{X_1}, \overline{X_2}} \cdot \left(f \overline{\mathbf{D}^0_{enz}} B \nabla_{\overline{X_1}, \overline{X_2}} \overline{h} \right) \\
&+ B \nabla_{\overline{X_1}, \overline{X_2}} \cdot \left(\overline{h} \left(\frac{1}{f} \overline{\boldsymbol{\kappa}} B \nabla_{\overline{X_1}, \overline{X_2}} \overline{P} - \overline{\mathbf{D}^0_{enz}} B \nabla_{\overline{X_1}, \overline{X_2}} f \right) \right) \\
&- \left(\overline{\frac{k_d^{enz}}{f}} + B \nabla_{\overline{X_1}, \overline{X_2}} \cdot \overline{\mathbf{V}_s} \right) \overline{h} + \frac{\alpha}{c_0} \mathcal{S}_{enz}
\end{aligned}
$$

Dropping bars on the dimensionless variables h, P, $\mathbf{V}_s$, t and $\mathbf{x}$, we get equa-

tion (A.3d). The same method applies for equation (4.29) to get equation (A.3g).

The equivalent system in Ω_0 in dimensionless form reads

$$
\begin{cases}
g_{\mathcal{E}} + g_{\mathcal{C}} + f = 1, & \text{(A.3a)}\\
\boldsymbol{\nabla} \cdot \left((g_{\mathcal{E}} + g_{\mathcal{C}}) \dfrac{1}{J} B^{-1} (\overline{\mu}(\nabla \overline{\mathbf{u}} + \nabla \overline{\mathbf{u}}^T) + \overline{\lambda}(\nabla \cdot \overline{\mathbf{u}}) I) B^{-T} \right) = \nabla P, & \text{(A.3b)}\\
(g_{\mathcal{E}} + g_{\mathcal{C}}) \overline{s_0} \dfrac{\partial P}{\partial t} - B\nabla \cdot (\overline{\boldsymbol{\kappa}} B \nabla P) \\
\qquad = \left(1 - \dfrac{\rho_s^{R,0}}{\rho_f^R} \right) g_{\mathcal{E}} (-\overline{K} h + \overline{a_r} (f - f(0, \mathbf{x}))) \\
\qquad\quad + \alpha Q_{inj}^{tot} + \overline{\gamma}(\overline{P_v} - P) - B\nabla \cdot \left(\dfrac{\partial \mathbf{u}}{\partial t} \right), & \text{(A.3c)}\\
\dfrac{\partial h}{\partial t} = B\nabla \cdot \left(f \overline{\mathbf{D}_{enz}^0} B \nabla h \right) + B\nabla \cdot \left(h J_{enz}^B \right) \\
\qquad - \left(\dfrac{\overline{k_d^{enz}}}{f} + B\nabla \cdot \left(\dfrac{\partial \mathbf{u}}{\partial t} \right) \right) h + \dfrac{\alpha}{c_0} \mathcal{S}_{enz}, & \text{(A.3d)}\\
\dfrac{\partial g_{\mathcal{C}}}{\partial t} + g_{\mathcal{C}} \left(\overline{s_0} \dfrac{\partial P}{\partial t} + B\boldsymbol{\nabla} \cdot \left(\dfrac{\partial \mathbf{u}}{\partial t} \right) \right) = 0, & \text{(A.3e)}\\
\dfrac{\partial g_{\mathcal{E}}}{\partial t} + g_{\mathcal{E}} \left(\overline{s_0} \dfrac{\partial P}{\partial t} + B\boldsymbol{\nabla} \cdot \left(\dfrac{\partial \mathbf{u}}{\partial t} \right) \right) = g_{\mathcal{E}} (-\overline{K} h + \overline{a_r} (f - f(0, \mathbf{x}))), & \text{(A.3f)}\\
\dfrac{\partial c}{\partial t} = B\nabla \cdot \left(f \overline{\mathbf{D}_{drug}^0} B \nabla c \right) + B\nabla \cdot \left(c J_{drug}^B \right) \\
\qquad - \left(\dfrac{\overline{k_d^{drug}}}{f} + B\nabla \cdot \left(\dfrac{\partial \mathbf{u}}{\partial t} \right) \right) c + \dfrac{\alpha}{c_0} \mathcal{S}_{drug}, & \text{(A.3g)}
\end{cases}
$$

Writing the system with $B = I_d$ using Remark 9, we recover system (4.55).

Appendix B

Axisymmetric variational formulation of the poroelastic model

Writing an axisymmetric variational formulation of the problem allows to analyze a 3D domain which is rotationally symmetric about an axis. The input is 2D, but because of the rotational symmetry, you are in fact analyzing a symmetric 3D problem. While modeling a speroid or a tumor by a sphere, solving the problem in axisymmetry allows us to consider the 2D input shown in Figure 4.18 while in fact analyzing a sphere. To simplify the governing equations of the axisymmetric problem, it is natural to use a global cylindrical coordinate system (r, z, θ) where r is the radial coordinate, z is the axial coordinate and θ is the circumferential coordinate.

The displacement field is a function of r and z only, defined by two components:

$$\mathbf{u}(r, z) = \begin{pmatrix} u_r(r, z) \\ u_z(r, z) \end{pmatrix}.$$

The circumferential displacement component u_θ is zero on account of rotational symmetry. The nonvanishing components of the infinitesimal strain tensor and the stress tensor in cylindrical coordinates are, as usual in preparation for finite

element work, arranged as 4×1 vectors:

$$\boldsymbol{\varepsilon}(\mathbf{u}) = \begin{pmatrix} e_{rr} \\ e_{zz} \\ e_{\theta\theta} \\ 2e_{rz} \end{pmatrix} \text{ and } \boldsymbol{\sigma} = \begin{pmatrix} \sigma_{rr} \\ \sigma_{zz} \\ \sigma_{\theta\theta} \\ \sigma_{rz} \end{pmatrix}.$$

The strain-displacement equations for the axysymmetric problem are, in matrix form:

$$\boldsymbol{\varepsilon}(\mathbf{u}) = \begin{pmatrix} e_{rr} \\ e_{zz} \\ e_{\theta\theta} \\ 2e_{rz} \end{pmatrix} = \begin{pmatrix} \frac{\partial}{\partial r} & 0 \\ 0 & \frac{\partial}{\partial z} \\ \frac{1}{r} & 0 \\ \frac{\partial}{\partial z} & \frac{\partial}{\partial r} \end{pmatrix} \begin{pmatrix} u_r(r,z) \\ u_z(r,z) \end{pmatrix}.$$

For an isotropic material of Lamé 's constants λ and μ, the constitutive equation between stress and strain takes the form

$$\boldsymbol{\sigma} = \begin{pmatrix} \lambda + 2\mu & \lambda & \lambda & 0 \\ \lambda & \lambda + 2\mu & \lambda & 0 \\ \lambda & \lambda & \lambda + 2\mu & 0 \\ 0 & 0 & 0 & \mu \end{pmatrix} \times \boldsymbol{\varepsilon}(\mathbf{u}).$$

The calculus of $\boldsymbol{\nabla} \cdot \boldsymbol{\sigma}$ in cylindrical coordinates gives

$$\boldsymbol{\nabla} \cdot \boldsymbol{\sigma} = \begin{pmatrix} \frac{1}{r}\frac{\partial(r\sigma_{rr})}{\partial r} + \frac{\partial \sigma_{rz}}{\partial z} - \frac{1}{r}\sigma_{\theta\theta} \\ 0 \\ \frac{\partial \sigma_{zr}}{\partial r} + \frac{\partial \sigma_{zz}}{\partial z} + \frac{1}{r}\sigma_{zr} \end{pmatrix}$$

Thus, the variational formulation in axisymmetry of equation (4.55b) with boundary conditions (4.74a) is: $\forall \mathbf{w}$

$$\int_{\Omega_0} \left(r\sigma_{rr}\frac{\partial w_r}{\partial r} + r\sigma_{rz}\left(\frac{\partial w_z}{\partial r} + \frac{\partial w_r}{\partial z}\right) + r\sigma_{zz}\frac{\partial w_z}{\partial z} + \sigma_{\theta\theta} w_r \right) \mathrm{dV} = \int_{\Omega_0} \left(rP\left(\frac{\partial w_r}{\partial r} + \frac{\partial w_z}{\partial z}\right) + P w_r \right) \mathrm{dV}$$

with

$$\begin{cases} \sigma_{rr} = (\lambda + 2\mu)\dfrac{\partial u_r}{\partial r} + \lambda\dfrac{\partial u_z}{\partial z} + \lambda\dfrac{u_r}{r} \\ \sigma_{zz} = \sigma_{rr} = \lambda\dfrac{\partial u_r}{\partial r} + (\lambda + 2\mu)\dfrac{\partial u_z}{\partial z} + \lambda\dfrac{u_r}{r} \\ \sigma_{\theta\theta} = \sigma_{rr} = \lambda\dfrac{\partial u_r}{\partial r} + \lambda\dfrac{\partial u_z}{\partial z} + (\lambda + 2\mu)\dfrac{u_r}{r} \\ \sigma_{rz} = \mu\left(\dfrac{\partial u_r}{\partial z} + \dfrac{\partial u_z}{\partial r}\right) \end{cases}$$

For the equations on the scalar variables P, h and c, the variational formulations in axisymmetry are derived easily, taking into account the fact that for any vector A, the divergence in cylindrical coordinates writes

$$\boldsymbol{\nabla} \cdot A = \frac{\partial A_r}{\partial r} + \frac{\partial A_z}{\partial z} + \frac{A_r}{r},$$

as A_θ is zero on account of rotational symmetry. The variational formulation in axisymmetry of equation (4.55c) with boundary conditions (4.74b) is: $\forall Q$

$$\int_{\Omega_0} (r g_s s_0(P)_t Q)\ \mathrm{dV} + \int_{\Omega_0} \left(r\kappa\left(\frac{\partial P}{\partial r}\frac{\partial Q}{\partial r} + \frac{\partial P}{\partial z}\frac{\partial Q}{\partial z}\right)\right)\ \mathrm{dV} = \int_{\Omega_0} \left(\alpha Q_{inj}^{tot} + \gamma(P_v - P)\right) Q\,\mathrm{dV}$$
$$+ \int_{\Omega_0} \left(r\left(\frac{\rho_s^{R,0}}{\rho_f^R} - 1\right) g_{\mathcal{E}}(Kh + a_r(f(0,\mathbf{x}) - f)) - \left(r\left(\frac{\partial (u_r)_t}{\partial r} + \frac{\partial (u_z)_t}{\partial z}\right) + (u_r)_t\right)\right) Q\,\mathrm{dV}$$

The variational formulation in axisymmetry of equation (4.55d) with boundary conditions (4.74c) is: $\forall \psi$

$$\int_{\Omega_0} (h)_t \psi\,\mathrm{dV} + \int_{\Omega_0} \left(r f D^0_{enz}\left(\frac{\partial h}{\partial r}\frac{\partial \psi}{\partial r} + \frac{\partial h}{\partial z}\frac{\partial \psi}{\partial z}\right)\right)\ \mathrm{dV}$$
$$+ \int_{\Omega_0} \left(r\left(\frac{\partial (h(J_{enz})_r)}{\partial r} + \frac{\partial (h(J_{enz})_z)}{\partial z}\right) + h(J_{enz})_r\right)\psi\,\mathrm{dV}$$
$$= -\int_{\Omega_0} h\left(r\left(\frac{\partial (u_r)_t}{\partial r} + \frac{\partial (u_z)_t}{\partial z} + \frac{k_d^{enz}}{f}\right) + (u_r)_t\right)\psi\,\mathrm{dV} + \int_{\Omega_0} \frac{\alpha}{c_0}\mathcal{S}_{enz}\psi\,\mathrm{dV}$$

The variational formulation in axisymmetry of equation (4.55g) with boundary conditions (4.74d) is obtained with the same calculus.

Bibliography

[1] T. Akerstrom, K. Vedel, J. Needham, P. Hojman, E. Kontou, Y. Hellsten, and J. F. Wojtaszewski. Optimizing hyaluronidase dose and plasmid dna delivery greatly improves gene electrotransfer efficiency in rat skeletal muscle. *Biochemistry and Biophysics Reports*, 4:342 – 350, 2015.

[2] G. Alì, V. Furuholt, R. Natalini, and I. Torcicollo. A mathematical model of sulphite chemical aggression of limestones with high permeability. Part I. Modeling and qualitative analysis. *Transport in Porous Media*, 69:109–122, 2007.

[3] G. Allaire. Homogenization and two-scale convergence. *SIAM Journal on Mathematical Analysis*, 23(6):1482–1518, 1992.

[4] G. Allaire, A. Damlamian, and U. Hornung. Two-scale convergence on periodic surfaces and applications. *Mathematical Modelling of Flow through Porous Media*, 09 1995.

[5] G. Allaire and F. Murat. Homogenization of the Neumann problem with non-isolated holes. *Asymptotic Analysis*, 7:81–95, 1993.

[6] P. M. Altrock, L. L. Liu, and F. Michor. The mathematics of cancer: integrating quantitative models. *Nature Reviews Cancer*, 15(12):730–745, Dec. 2015.

[7] M. Amar, D. Andreucci, P. Bisegna, and R. Gianni. On a hierarchy of models for electrical conduction in biological tissues. *Mathematical Methods in the Applied Sciences*, 29(7):767–787, 2006.

[8] D. Ambrosi. Infiltration through deformable porous media. *ZAMM. Zeitschrift für Angewandte Mathematik und Mechanik. Journal of Applied Mathematics and Mechanics*, 82(2):115–124, 2002.

[9] F. André and L. M. Mir. DNA electrotransfer: its principles and an updated review of its therapeutic applications. *Gene therapy*, 11 Suppl 1:S33–42, Oct. 2004.

[10] S. Astanin and L. Preziosi. *Selected Topics in Cancer Modeling: Genesis, Evolution, Immune Competition, and Therapy*, chapter Multiphase Models of Tumour Growth, pages 1–31. Birkhäuser Boston, 2008.

[11] J. L. Au, S. H. Jang, J. Zheng, C. T. Chen, S. Song, L. Hu, and M. G. Wientjes. Determinants of drug delivery and transport to solid tumors. *Journal of controlled release : official journal of the Controlled Release Society*, 74(1-3):31–46, July 2001.

[12] Y. H. Bae, R. J. Mrsny, and K. Park. *Cancer targeted drug delivery*. Springer, 2013.

[13] Y. H. Bae, R. J. Mrsny, and K. Park. Cancer targeted drug delivery, 2013.

[14] S. I. Barry and G. K. ALDIS. Unsteady-Flow Induced Deformation of Porous Materials. *International Journal of Non-Linear Mechanics*, 26(5):687–699, 1991.

[15] S. I. Barry and G. N. Mercer. Flow and deformation in poroelasticity. I. Unusual exact solutions. *Mathematical and Computer Modelling*, 30(9-10):23–29, 1999.

[16] P. J. Basser. Interstitial pressure, volume, and flow during infusion into brain tissue. *Microvascular research*, 44(2):143–165, Sept. 1992.

[17] R. C. Batra. Linear constitutive relations in isotropic finite elasticity. *Journal of Elasticity. The Physical and Mathematical Science of Solids*, 51(3):243–245, 1998.

[18] G. Baumgartner. The impact of extracellular matrix on chemoresistance of solid tumors–experimental and clinical results of hyaluronidase as additive to cytostatic chemotherapy. *Cancer letters*, 131(1):1–2, Sept. 1998.

[19] L. T. Baxter and R. K. Jain. Transport of fluid and macromolecules in tumors. i. role of interstitial pressure and convection. *Microvascular Research*, 37(1):77 – 104, 1989.

[20] J. Bear and Y. Bachmat. *Introduction to Modeling of Transport Phenomena in Porous Media*. Kluwer Academic Publishers, 1990.

[21] M. A. Biot. General theory of three-dimensional consolidation. *Journal of applied physics*, 12(2):155, 1941.

[22] L. H. Bookbinder, A. Hofer, M. F. Haller, M. L. Zepeda, G. A. Keller, J. E. Lim, T. S. Edgington, H. M. Shepard, J. S. Patton, and G. I. Frost. A recombinant human enzyme for enhanced interstitial transport of therapeutics. *Journal of controlled release : official journal of the Controlled Release Society*, 114(2):230–241, Aug. 2006.

[23] A. Bottaro and T. Ansaldi. On the infusion of a therapeutic agent into a solid tumor modeled as a poroelastic medium. *Journal of biomechanical engineering*, 134(8):084501, Aug. 2012.

[24] Y. Boucher, L. T. Baxter, and R. K. Jain. Interstitial Pressure Gradients in Tissue-isolated and Subcutaneous Tumors: Implications for Therapy. *Cancer research*, 50(15):4478–4484, Aug. 1990.

[25] Y. Bourgault, Y. Coudière, and C. Pierre. Existence and uniqueness of the solution for the bidomain model used in cardiac electrophysiology. *Nonlinear Analysis: Real World Applications*, 10(1):458–482, Feb. 2009.

[26] R. M. Bowen. Incompressible porous media models by use of the theory of mixtures. *International Journal of Engineering Science*, 18(9):1129–1148, Jan. 1980.

[27] C. Brekken and C. de Lange Davies. Hyaluronidase reduces the interstitial fluid pressure in solid tumours in a non-linear concentration-dependent manner. *Cancer letters*, 131(1):65–70, Sept. 1998.

[28] M. Breton, F. Buret, and L. Krähenbühl. Non-Linear Steady-State Electrical Current Modeling for the Electropermeabilization of Biological Tissue. *IEEE Transactions ...*, 51(3):1–4, 2015.

[29] B. A. Buhren, H. Schrumpf, N.-P. Hoff, E. Bölke, S. Hilton, and P. A. Gerber. Hyaluronidase: from clinical applications to molecular and cellular mechanisms. *European journal of medical research*, 21(1):5, 2016.

[30] M. Bureau, S. Naimi, R. T. Ibad, J. Seguin, C. Georger, E. Arnould, L. Maton, F. Blanche, P. Delaere, and D. Scherman. Intramuscular plasmid dna electrotransfer: biodistribution and degradation. *Biochimica et Biophysica Acta (BBA) - Gene Structure and Expression*, 1676(2):138 – 148, 2004.

[31] J. F. R. C Geuzaine. Gmsh: a three-dimensional finite element mesh generator with built-in pre- and post-processing facilities. *International Journal for Numerical Methods in Engineering*, 79(11):1309–1331, 2009.

[32] M. A. J. Chaplain, L. Graziano, and L. Preziosi. Mathematical modelling of the loss of tissue compression responsiveness and its role in solid tumour development. *Mathematical medicine and biology : a journal of the IMA*, 23(3):197–229, Sept. 2006.

[33] Z. Chen, G. Huan, and Y. Ma. *Computational methods for multiphase flows in porous media*. Computational Science & Engineering. Society for Industrial and Applied Mathematics (SIAM), Philadelphia, PA, 2006.

[34] I.-K. Choi, R. Strauss, M. Richter, C.-O. Yun, and A. Lieber. Strategies to increase drug penetration in solid tumors. *Frontiers in oncology*, 3:193, 2013.

[35] G. G. Cleveland, D. C. Chang, C. F. Hazlewood, and H. E. Rorschach. Nuclear magnetic resonance measurement of skeletal muscle: anisotrophy

of the diffusion coefficient of the intracellular water. *Biophysical journal*, 16(9):1043–1053, Sept. 1976.

[36] G. M. Cooper and D. Ganem. *The Cell: A Molecular Approach*. Nature Medicine, 1997.

[37] D. Cukjati, D. Batiuskaite, F. André, D. Miklav**v**ci**v**c, and L. M. Mir. Real time electroporation control for accurate and safe in vivo non-viral gene therapy. *Bioelectrochemistry (Amsterdam, Netherlands)*, 70(2):501–507, May 2007.

[38] K. A. D. P. D and W. K. P. D. Modeling Electroporation in a Single Cell. I. Effects of Field Strength and Rest Potential. *Biophysical journal*, 77(3):1213–1224, Sept. 1999.

[39] B. M. Damon, A. K. W. Buck, and Z. Ding. Diffusion-Tensor MRI Based Skeletal Muscle Fiber Tracking. *Imaging in medicine*, 3(6):675–687, Nov. 2011.

[40] R. V. Davalos, B. Rubinsky, and L. M. Mir. Theoretical analysis of the thermal effects during in vivo tissue electroporation. *Bioelectrochemistry (Amsterdam, Netherlands)*, 61(1):99–107, Oct. 2003.

[41] H. Delingette. Towards realistic soft-tissue modeling in medical simulation. *Proceedings of the IEEE*, 86:512 – 523, 1998.

[42] A. Denzi, L. Strigari, F. Di Filippo, C. Botti, S. Di Filippo, L. Perracchio, M. Ronchetti, R. Cadossi, and M. Liberti. Modeling the positioning of single needle electrodes for the treatment of breast cancer in a clinical case. *BioMedical Engineering OnLine*, 14 Suppl 3(Suppl 3):S1, 2015.

[43] M. Deville, R. Natalini, and C. Poignard. A continuum mechanics model of enzyme-based tissue degradation in cancer therapies. Research Report RR-9030, Inria Bordeaux Sud-Ouest ; IMB - Institut de Mathématiques de Bordeaux ; Université de Bordeaux ; IAC - Istituto per le Applicazioni del Calcolo "M. Picone", Consiglio Nazionale delle Ricerche, Feb. 2017.

[44] J. F. Edd and R. V. Davalos. Mathematical modeling of irreversible electroporation for treatment planning. *Technology in Cancer Research and Treatment*, 6(4):275–286, Aug. 2007.

[45] L. Eikenes, Ø. S. Bruland, C. Brekken, and C. d. L. Davies. Collagenase increases the transcapillary pressure gradient and improves the uptake and distribution of monoclonal antibodies in human osteosarcoma xenografts. *Cancer research*, 64(14):4768–4773, July 2004.

[46] L. Eikenes, M. Tari, I. Tufto, Ø. S. Bruland, and C. de Lange Davies. Hyaluronidase induces a transcapillary pressure gradient and improves the distribution and uptake of liposomal doxorubicin (Caelyx) in human osteosarcoma xenografts. *British journal of cancer*, 93(1):81–88, July 2005.

[47] L. Eikenes, I. Tufto, E. A. Schnell, A. Bjørkøy, and C. De Lange Davies. Effect of collagenase and hyaluronidase on free and anomalous diffusion in multicellular spheroids and xenografts. *Anticancer research*, 30(2):359–368, Feb. 2010.

[48] A. Erikson, I. Tufto, A. B. Bjønnum, Ø. S. Bruland, and C. d. L. Davies. The impact of enzymatic degradation on the uptake of differently sized therapeutic molecules. *Anticancer research*, 28(6A):3557–3566, Nov. 2008.

[49] J.-M. Escoffre, J. Teissie, and M.-P. Rols. Gene transfer: how can the biological barriers be overcome? *The Journal of membrane biology*, 236(1):61–74, July 2010.

[50] X. Feng, Z. Ge, and Y. Li. Multiphysics Finite Element Methods for a Poroelasticity Model. *arXiv.org*, Nov. 2014.

[51] C. Frantz, K. M. Stewart, and V. M. Weaver. The extracellular matrix at a glance. *Journal of cell science*, 123(Pt 24):4195–4200, Dec. 2010.

[52] Y. C. Fung. Biomechanics: mechanical properties of living tissues, 1981.

[53] L. Fusi, A. Farina, and D. Ambrosi. Mathematical Modeling of a Solid–Liquid Mixture with Mass Exchange Between Constituents. *Mathematics and Mechanics of Solids*, 11(6):575–595, Dec. 2006.

[54] S. Ganesh, M. Gonzalez-Edick, D. Gibbons, M. Van Roey, and K. Jooss. Intratumoral coadministration of hyaluronidase enzyme and oncolytic adenoviruses enhances virus potency in metastatic tumor models. *Clinical cancer research : an official journal of the American Association for Cancer Research*, 14(12):3933–3941, June 2008.

[55] J. Garnier, L. Giovangigli, H. Ammari, W. Jing, and J. K. Seo. Spectroscopic imaging of a dilute cell suspension. *Journal de Mathématiques Pures et Appliquées*, 105(5):603–661, Jan. 2016.

[56] L. Giovangigli. *Modélisation mathématique pour l'imagerie membranaire*. PhD thesis, Université Paris VII, 2014.

[57] K. S. Girish and K. Kemparaju. The magic glue hyaluronan and its eraser hyaluronidase: a biological overview. *Life sciences*, 80(21):1921–1943, May 2007.

[58] A. Gothelf, L. M. Mir, and J. Gehl. Electrochemotherapy: results of cancer treatment using enhanced delivery of bleomycin by electroporation. *Cancer Treatment Reviews*, 29(5):371 – 387, 2003.

[59] R. Grantab, S. Sivananthan, and I. F. Tannock. The penetration of anticancer drugs through tumor tissue as a function of cellular adhesion and packing density of tumor cells. *Cancer research*, 66(2):1033–1039, Jan. 2006.

[60] M. F. K. Happel, H. Niekisch, L. L. Castiblanco Rivera, F. W. Ohl, M. Deliano, and R. Frischknecht. Enhanced cognitive flexibility in reversal learning induced by removal of the extracellular matrix in auditory cortex. *Proceedings of the National Academy of Sciences of the United States of America*, 111(7):2800–2805, Feb. 2014.

[61] F. Hecht. New development in freefem++. *Journal of Numerical Mathematics*, 20, 12 2012.

[62] A. Ivorra, J. Villemejane, and L. M. Mir. Electrical modeling of the influence of medium conductivity on electroporation. *Physical chemistry chemical physics : PCCP*, 12(34):10055–10064, Sept. 2010.

[63] R. K. Jain and L. T. Baxter. Mechanisms of Heterogeneous Distribution of Monoclonal Antibodies and Other Macromolecules in Tumors: Significance of Elevated Interstitial Pressure. *Cancer research*, 48(24 Part 1):7022–7032, Dec. 1988.

[64] P. Joseph Phillips and M. Wheeler. Overcoming the problem of locking in linear elasticity and poroelasticity: An heuristic approach. *Computational Geosciences*, 13:5–12, 01 2009.

[65] L. Juhlin. Reconstitution of dermal connective tissue barrier after testicular or bacterial hyaluronidase. *Acta Pharmacologica et Toxicologica*, 12(1):96–108, 1956.

[66] M. Kanduser and D. Miklavcic. Electroporation in biological cell and tissue: an overview. *In book: Electrotechnologies for Extraction from Food Plants and Biomaterials*, pages 1–37, 02 2009.

[67] O. Kavian, M. Leguèbe, C. Poignard, and L. Weynans. "Classical" electropermeabilization modeling at the cell scale. *Journal of Mathematical Biology*, 68(1-2):235–265, Jan. 2014.

[68] I. A. Khawar, J. H. Kim, and H.-J. Kuh. Improving drug delivery to solid tumors: priming the tumor microenvironment. *Journal of controlled release : official journal of the Controlled Release Society*, 201:78–89, Mar. 2015.

[69] N. Kohno, T. Ohnuma, and P. Truog. Effects of hyaluronidase on doxorubicin penetration into squamous carcinoma multicellular tumor spheroids and its cell lethality. *Journal of cancer research and clinical oncology*, 120(5):293–297, 1994.

[70] G. E. Lang, D. Vella, S. L. Waters, and A. Goriely. Mathematical modelling of blood-brain barrier failure and oedema. *Mathematical medicine and biology : a journal of the IMA*, June 2016.

[71] J. Langus, M. Kranjc, B. Kos, T. **v**Su**v**star, and D. Miklavcic. Dynamic finite-element model for efficient modelling of electric currents in electroporated tissue. *Scientific reports*, 6:26409, May 2016.

[72] M. Leguèbe. *Modélisation de l'électroperméabilisation à l'échelle cellulaire*. PhD thesis, Université de Bordeaux, 2014.

[73] M. Leguèbe, M. G. Notarangelo, M. Twarogowska, R. Natalini, and C. Poignard. Mathematical model for transport of DNA plasmids from the external medium up to the nucleus by electroporation. *Mathematical Biosciences*, 285:1–13, Nov. 2016.

[74] C. Lelli, R. Sacco, P. Causin, and M. T. Raimondi. A poroelastic model of mechanobiological processes in tissue engieering. part i : Mathematical formulation. *doi: arXiv:1512.02182 (2015). Under review in Journal of Mathematical Biology*, 2015.

[75] G. Lemon, J. R. King, H. M. Byrne, O. E. Jensen, and K. M. Shakesheff. Mathematical modelling of engineered tissue growth using a multiphase porous flow mixture theory. *Journal of Mathematical Biology*, 52(5):571–594, May 2006.

[76] S. F. Levinson. Ultrasound propagation in anisotropic soft tissues: the application of linear elastic theory. *Journal of biomechanics*, 20(3):251–260, 1987.

[77] M. Magzoub, S. Jin, and A. S. Verkman. Enhanced macromolecule diffusion deep in tumors after enzymatic digestion of extracellular matrix collagen and its associated proteoglycan decorin. *FASEB journal : official publication of the Federation of American Societies for Experimental Biology*, 22(1):276–284, Jan. 2008.

[78] C. A. R. Martínez, A. L. V. Tizatl, C. E. V. Tizatl, P. R. H. Rodríguez, A. V. Hernández, L. L. Salas, M. I. G. Velasco, and S. A. R. Cuevas. Modeling of electric field and Joule heating in breast tumor during electroporation. In *2016 13th International Conference on Electrical Engineering, Computing Science and Automatic Control (CCE*, pages 1–4. IEEE, 2016.

[79] C. O. McAtee, J. J. Barycki, and M. A. Simpson. Emerging roles for hyaluronidase in cancer metastasis and therapy. *Advances in cancer research*, 123:1–34, 2014.

[80] H. R. Mellor and R. Callaghan. Accumulation and distribution of doxorubicin in tumour spheroids: the influence of acidity and expression of P-glycoprotein. *Cancer chemotherapy and pharmacology*, 68(5):1179–1190, Nov. 2011.

[81] D. Miklavcic, D. **v**Semrov, H. Mekid, and L. M. Mir. A validated model of in vivo electric field distribution in tissues for electrochemotherapy and for DNA electrotransfer for gene therapy. *Biochimica et Biophysica Acta (...*, 1523(1):73–83, 2000.

[82] D. Miklav**v**ci**v**c, M. Snoj, A. **v**Zupani**v**c, B. Kos, M. Cemazar, M. Kropivnik, M. Bracko, T. Pecnik, E. Gadzijev, and G. Sersa. Towards treatment planning and treatment of deep-seated solid tumors by electrochemotherapy. *BioMedical Engineering OnLine*, 9(1):10–8, 2010.

[83] A. I. Minchinton and I. F. Tannock. Drug penetration in solid tumours. *Nature Reviews Cancer*, 6:583–592, Aug. 2006.

[84] L. M. Mir, M. F. Bureau, R. Rangara, B. Schwartz, and D. Scherman. Long-term, high level in vivo gene expression after electric pulse-mediated gene transfer into skeletal muscle. *Comptes rendus de l'Academie des sciences. Serie III, Sciences de la vie*, 321(11):893–899, Nov. 1998.

[85] L. M. Mir, C. Poignard, R. Scorretti, and A. Silve. Dynamic Modeling of Electroporation for the Computation of the Electric Field Distribution Inside

Biological Tissues during the Application of the Pulse Voltage. *1st World Congress on ...*, 2015.

[86] V. C. Mow, M. H. Holmes, and W. M. Lai. Fluid transport and mechanical properties of articular cartilage: a review. *Journal of biomechanics*, 17(5):377–394, 1984.

[87] M. A. Murad and A. F. D. Loula. Improved accuracy in finite element analysis of Biot's consolidation problem. *Computer Methods in Applied Mechanics and Engineering*, 95(3):359–382, 1992.

[88] M. A. Murad and A. F. D. Loula. On stability and convergence of finite element approximations of Biot's consolidation problem. *International Journal for Numerical Methods in Engineering*, 37(4):645–667, 1994.

[89] S. Muro. *Drug Delivery Across Physiological Barriers*. CRC Press, Mar. 2016.

[90] H. Namazi, V. V. Kulish, A. Wong, and S. Nazeri. Mathematical Based Calculation of Drug Penetration Depth in Solid Tumors. *BioMed research international*, 2016:8437247, 2016.

[91] P. A. Netti, L. T. Baxter, Y. Boucher, R. Skalak, and R. K. Jain. Macro- and microscopic fluid transport in living tissues: Application to solid tumors. *AIChE Journal*, 43(3):818–834, Mar. 1997.

[92] P. A. Netti, D. A. Berk, M. A. Swartz, A. J. Grodzinsky, and R. K. Jain. Role of extracellular matrix assembly in interstitial transport in solid tumors. *Cancer research*, 60(9):2497–2503, May 2000.

[93] J. C. Neu and W. Krassowska. Asymptotic model of electroporation. *Physical review E*, 59(3):3471–3482, Mar. 1999.

[94] M. G. Notarangelo. *A Mathematical model of intracellular transport: role of microtubules and Ran cycle in the nucleocytoplasmic plasmids transport*

in gene therapy anti-tumor. PhD thesis, Universitá degli studi di Roma, Sapienza, 2014.

[95] D. Peri and INSEAN. Self-learning metamodels for optimization. *Ship Technology Research*, 56(3):95–109, 2009.

[96] R. Perrussel and C. Poignard. Asymptotic expansion of steady-state potential in a high contrast medium with a thin resistive layer. *Applied Mathematics and Computation*, 221:48–65, 2013.

[97] C. Poignard, A. Silve, and L. Wegner. Different Approaches used in Modeling of Cell Membrane Electroporation. In D. M. ci**v**c, editor, *Handbook of electroporation*. Springer, July 2017.

[98] L. Preziosi and A. Tosin. Multiphase modelling of tumour growth and extracellular matrix interaction: mathematical tools and applications. *Journal of Mathematical Biology*, 58(4-5):625–656, Oct. 2008.

[99] P. P. Provenzano, C. Cuevas, A. E. Chang, V. K. Goel, D. D. Von Hoff, and S. R. Hingorani. Enzymatic Targeting of the Stroma Ablates Physical Barriers to Treatment of Pancreatic Ductal Adenocarcinoma. *Cancer Cell*, 21(3):418–429, Mar. 2012.

[100] F. A. Radu, I. S. Pop, A. Muntean, and I. Berre. Simulation of reactive flow in porous media with variable porosity as appears when modelling concrete carbonation. In *11th World Congress on Computational Mechanics (WCCM XI), 5th European Conference on Computational Mechanics (ECCM V), 6th European Conference on Computational Fluid Dynamics (ECFD VI)*, Barcelona, Spain, 2014.

[101] K. A. Rejniak, V. Estrella, T. Chen, A. S. Cohen, M. C. Lloyd, and D. L. Morse. The role of tumor tissue architecture in treatment penetration and efficacy: an integrative study. *Frontiers in oncology*, 3:111, 2013.

[102] M. P. Rols, C. Delteil, M. Golzio, P. Dumond, and S. Cros. In vivo electrically mediated protein and gene transfer in murine melanoma. *Nature ...*, 16(2):168–171, 1998.

[103] C. Rosazza, A. Buntz, T. Rieß, D. Wöll, A. Zumbusch, and M.-P. Rols. Intracellular Tracking of Single-plasmid DNA Particles After Delivery by Electroporation. *Molecular therapy : the journal of the American Society of Gene Therapy*, 21(12):2217–2226, Aug. 2013.

[104] J. Rosler, H. Harders, and M. Baker. Mechanical behaviour of engineering materials, 2007.

[105] D. Royer, J.-L. Gennisson, T. Deffieux, and M. Tanter. On the elasticity of transverse isotropic soft tissues (L). *The Journal of the Acoustical Society of America*, 129(5):2757–5, 2011.

[106] B. Rubinsky. Irreversible electroporation in medicine. *Technology in Cancer Research & Treatment*, 6(4):255–259, 2007.

[107] M. B. Sano, R. E. Fan, and L. Xing. Asymmetric Waveforms Decrease Lethal Thresholds in High Frequency Irreversible Electroporation Therapies. *Scientific reports*, 7:40747, Jan. 2017.

[108] J. D. Schertzer, D. R. Plant, and G. S. Lynch. Optimizing plasmid-based gene transfer for investigating skeletal muscle structure and function. *Molecular therapy : the journal of the American Society of Gene Therapy*, 13(4):795–803, Apr. 2006.

[109] H. P. Schwan. Electrical properties of tissues and cell suspensions: mechanisms and models. *Engineering in Medicine and Biology Society*, pages A70–A71 vol.1, 1994.

[110] D. Sel, D. Cukjati, D. Batiuskaite, T. Slivnik, L. M. Mir, and D. Miklavcic. Sequential Finite Element Model of Tissue Electropermeabilization. *IEEE Transactions on Biomedical Engineering*, 52(5):816–827, May 2005.

[111] G. Sersa, T. Jarm, T. Kotnik, A. Coer, M. Podkrajsek, M. Sentjurc, D. Miklavcic, M. Kadivec, S. Kranjc, A. Secerov, and M. Cemazar. Vascular disrupting action of electroporation and electrochemotherapy with bleomycin in murine sarcoma. *British journal of cancer*, 98(2):388–398, Jan. 2008.

[112] D. Signori, R. Lancellotta, and L. Preziosi. Mathematical models for soil consolidation problems : a state of the art report. *Chapter 6 of Modeling and Mechanics of Granular and Porous Materials*, pages 159–180, 2002.

[113] E. Signori, K. Wells, V. Fazio, and D. Wells. Optimisation of electrotransfer of plasmid into skeletal muscle by pretreatment with hyaluronidase - increased expression with reduced muscle damage. *Gene Therapy*, 8:1264–1270, 2001.

[114] M. Soltani and P. Chen. Effect of tumor shape and size on drug delivery to solid tumors. *Journal of biological engineering*, 2012.

[115] M. Spiegelman. Flow in deformable porous media. Part 1 Simple analysis. *Journal of Fluid Mechanics*, 247(-1):17–38, Feb. 1993.

[116] M. Spiegelman. Flow in deformable porous media. Part 2 Numerical analysis – the relationship between shock waves and solitary waves. *Journal of Fluid Mechanics*, 247(-1):39–63, Feb. 1993.

[117] B. St Croix, S. Man, and R. S. Kerbel. Reversal of intrinsic and acquired forms of drug resistance by hyaluronidase treatment of solid tumors. *Cancer letters*, 131(1):35–44, Sept. 1998.

[118] K. H. Støverud, M. Darcis, R. Helmig, and S. M. Hassanizadeh. Modeling Concentration Distribution and Deformation During Convection-Enhanced Drug Delivery into Brain Tissue. *Transport in Porous Media*, 92(1):119–143, Oct. 2011.

[119] R. M. Sutherland, H. A. Eddy, B. Bareham, K. Reich, and D. Vanantwerp. Resistance to adriamycin in multicellular spheroids. *International journal of radiation oncology, biology, physics*, 5(8):1225–1230, Aug. 1979.

[120] T. Suzuki, B. C. Shin, K. Fujikura, T. Matsuzaki, and K. Takata. Direct gene transfer into rat liver cells by in vivo electroporation. *FEBS letters*, 425(3):436–440, Apr. 1998.

[121] M. A. Swartz and M. E. Fleury. Interstitial flow and its effects in soft tissues. *Annual review of biomedical engineering*, 9:229–256, 2007.

[122] O. Trédan, C. M. Galmarini, K. Patel, and I. F. Tannock. Drug resistance and the solid tumor microenvironment. *Journal of the National Cancer Institute*, 99(19):1441–1454, Oct. 2007.

[123] D. Voyer, A. Silve, L. M. Mir, R. Scorretti, and C. Poignard. Dynamic modeling of electroporation in biological tissues. To appear in Bioelectrochemistry Journal, 2017.

[124] S. R. Ward and R. L. Lieber. Density and hydration of fresh and fixed human skeletal muscle. *Journal of biomechanics*, 38(11):2317–2320, Nov. 2005.

[125] C. J. Whatcott, H. Han, R. G. Posner, G. Hostetter, and D. D. Von Hoff. Targeting the tumor microenvironment in cancer: why hyaluronidase deserves a second look. *Cancer discovery*, 1(4):291–296, Sept. 2011.

[126] J. A. Wolff, R. W. Malone, P. Williams, W. Chong, G. Acsadi, A. Jani, and P. L. Felgner. Direct gene transfer into mouse muscle in vivo. *Science (New York, N.Y.)*, 247(4949 Pt 1):1465–1468, Mar. 1990.

[127] L. Wu and J. Ding. Effects of porosity and pore size on in vitro degradation of three-dimensional porous poly (D, L-lactide-co-glycolide) scaffolds for tissue engineering. *Journal of Biomedical Materials Research Part A*, 2005.

[128] W. Yao, Y. Li, and G. Ding. Interstitial fluid flow: the mechanical environment of cells and foundation of meridians. *Evidence-based complementary and alternative medicine : eCAM*, 2012:853516, 2012.

[129] J. S. Young, C. E. Llumsden, and A. L. Stalker. The significance of the "tissue pressure" of normal testicular and of neoplastic (Brown-Pearce carcinoma) tissue in the rabbit. *The Journal of pathology*, 62(3):313–333, July 1950.

[130] A. M. Zöllner, O. J. Abilez, M. Böl, and E. Kuhl. Stretching skeletal muscle: chronic muscle lengthening through sarcomerogenesis. *PloS one*, 7(10):e45661, 2012.

[131] A. Zupanic, B. Kos, and D. Miklavcic. Treatment planning of electroporation-based medical interventions: electrochemotherapy, gene electrotransfer and irreversible electroporation. *Physics in Medicine & Biology*, 57(17):5425, 2012.